

Microsystems and Nanosystems

Joseph C. Doll
Beth L. Pruitt

Piezoresistor Design and Applications

Microsystems and Nanosystems

Series Editors

Roger T. Howe

Antonio J. Ricco

For further volumes:
<http://www.springer.com/series/11483>

Joseph C. Doll · Beth L. Pruitt

Piezoresistor Design and Applications



Springer

Joseph C. Doll
Beth L. Pruitt
Mechanical Engineering Department
Stanford University
Stanford, CA
USA

Cover image is a scanning electron microscopy image of carbon nanotube-based digital circuits, by Max Shulaker from the Carbon Group at Stanford University, led by Professors Subhasish Mitra and Philip Wong.

ISBN 978-1-4614-8516-2 ISBN 978-1-4614-8517-9 (eBook)
DOI 10.1007/978-1-4614-8517-9
Springer New York Heidelberg Dordrecht London

Library of Congress Control Number: 2013944553

© Springer Science+Business Media New York 2013

This work is subject to copyright. All rights are reserved by the Publisher, whether the whole or part of the material is concerned, specifically the rights of translation, reprinting, reuse of illustrations, recitation, broadcasting, reproduction on microfilms or in any other physical way, and transmission or information storage and retrieval, electronic adaptation, computer software, or by similar or dissimilar methodology now known or hereafter developed. Exempted from this legal reservation are brief excerpts in connection with reviews or scholarly analysis or material supplied specifically for the purpose of being entered and executed on a computer system, for exclusive use by the purchaser of the work. Duplication of this publication or parts thereof is permitted only under the provisions of the Copyright Law of the Publisher's location, in its current version, and permission for use must always be obtained from Springer. Permissions for use may be obtained through RightsLink at the Copyright Clearance Center. Violations are liable to prosecution under the respective Copyright Law. The use of general descriptive names, registered names, trademarks, service marks, etc. in this publication does not imply, even in the absence of a specific statement, that such names are exempt from the relevant protective laws and regulations and therefore free for general use.

While the advice and information in this book are believed to be true and accurate at the date of publication, neither the authors nor the editors nor the publisher can accept any legal responsibility for any errors or omissions that may be made. The publisher makes no warranty, express or implied, with respect to the material contained herein.

Printed on acid-free paper

Springer is part of Springer Science+Business Media (www.springer.com)

Preface

Piezoresistive sensors are among the oldest and most widely used silicon microsystems. Yet a book dedicated to their design is strangely lacking and most introductory MEMS textbooks dedicate a single chapter to the subject. After designing and fabricating piezoresistors for a number of years, we can vouch that a single chapter is not sufficient room to develop the models and optimization methods required for the design of high-performance sensors. We wrote this book to address the need for a comprehensive guide to piezoresistor design.

This book grew out of a 2009 review paper written by members of the Stanford Microsystems Group [1]. Around the same time, we were developing new models and optimization techniques for the development of nanomechanical piezoresistive cantilevers [2]. This work combines the historical material, high-level overview, and notation fundamentals introduced in the review paper with the in-depth performance models and optimization techniques developed in the dissertation. Interested readers are referred to the dissertation for experimental, fabrication, and circuit details that are beyond the scope of this book.

This book can be divided into three parts. In the first part ([Chaps. 1–3](#)), we develop the fundamental tools required for piezoresistor design. After briefly discussing the history of piezoresistive and micromachined sensors ([Chap. 1](#)), we present notation and analyze several possible signal conditioning circuits ([Chap. 2](#)). Models for calculating noise, sensitivity, and resolution are developed in [Chap. 3](#).

In the second part ([Chaps. 4 and 5](#)), we discuss practical issues in piezoresistor development. Fabrication processes are discussed in [Chap. 4](#) with an emphasis on accurate models for the dopant concentration profiles and electrical properties of ion implanted, diffused, and epitaxial grown piezoresistors. Thermal effects are a major challenge in practical piezoresistor design, and in [Chap. 5](#) we discuss temperature compensation and the effects of Joule heating.

In the final part of the book ([Chaps. 6 and 7](#)), we focus on the performance limits of piezoresistive sensing. Design optimization is the focus of [Chap. 6](#). Numerical design optimization is the glue that allows our mechanical, electrical, thermal, and fabrication process models to be integrated. In [Chap. 7](#), we conclude by comparing piezoresistive transduction with alternative MEMS transduction technologies using design optimization and present piezoresistive materials beyond single crystal silicon.

Several appendices follow the main text. In particular, Appendix B provides lookup tables for the design optimization of ion implanted piezoresistors and Appendix C describes the numerical modeling and optimization code that Chaps. 6 and 7 are based upon.

The intended audience includes design engineers, process engineers, and researchers. Piezoresistive device design encompasses a broad range of engineering disciplines from heat transfer and solid mechanics to semiconductor physics and electronics. We assume some background in MEMS and microfabrication and limit the discussion of fabrication to piezoresistor-specific processes. Some background knowledge of each of these four fields will prove helpful in designing piezoresistors, and we refer the interested reader to works by Plummer et al. [3], Jaeger [4], Pierret [5], and Senturia [6] for additional reading.

One of the defining features of piezoresistor design is its cross-disciplinary nature and complexity. Analytical models are simply not sufficient for accurate design work. We developed an open source tool (piezoD) for modeling and numerical optimization of piezoresistive sensors in 2008 to address this complexity. Since then we have continued to add new features (e.g. piezoelectric sensor design, ion implantation support, thermal models) and the tool has been downloaded hundreds of times. Rather than reprinting thousands of lines of code here, we refer the reader to the piezoD website and repository: <http://microsystems.stanford.edu/piezod> <http://github.com/jcdoll/piezod>

We hope that the code and this book will aid you in designing your next generation of piezoresistive sensors.

Stanford, CA, May 2013

Joseph C. Doll
Beth L. Pruitt

References

1. A.A. Barlian, W.-T. Park, J.R. Mallon, A.J. Rastegar, B.L. Pruitt Review: Semiconductor piezoresistance for microsystems. *Proc. IEEE*, **97**(3),513–552 (2009)
2. J.C. Doll Advances in high bandwidth nanomechanical force sensors with integratedactuation. Ph.D. dissertation, Stanford University, 2012
3. J.D. Plummer, M.D. Deal, P.B. Griffin, *Silicon VLSI Technology Fundamentals,Practice, and Modeling*. (Prentice Hall, New Jersey, 2000)
4. R. Jaeger, *Introduction to Microelectronic Fabrication*. (Prentice Hall, New Jersey, 2002)
5. R.F. Pierret, *Semiconductor Device Fundamentals*. (Addison Wesley, Reading, MA, 1996)
6. S. Senturia, *Microsystem Design*. (Springer, New York, 2000)

Acknowledgments

This book would not have been possible without the help and feedback of our colleagues in the field, especially those who have designed piezoresistive sensors for a wide range of applications in the Stanford Microsystems Laboratory over the past 10 years. In particular, we would like to thank the co-authors of the 2009 piezoresistor review paper: A. Alvin Barlian, Woo-Tae Park, Joseph R. Mallon Jr., and Ali J. Rastegar. Portions of Chaps. 1–3, and 7 are adapted from the review paper. This book would not have been possible without the foundation that their work provided. The discussions and background research leading to that review provided the genesis for subsequent studies in design, modeling, and optimization and ultimately this book.

Two additional colleagues stand out for their contributions to the book: Sung-Jin Park and Nahid Harjee. They helped in getting the book project started and defining its overall structure. They also aided in developing and validating the models for piezoresistor operation utilized here. In particular, Sung-Jin developed the ion implantation optimization scheme and the theory behind β^* , β_1^* , and β_2^* . JCD is indebted to Sung-Jin and Nahid for their mentorship in the cleanroom and in the laboratory.

We are grateful to the students of the MEMS design courses at Stanford who not only fabricated and tested hundreds of process variations but were also the audience for evolving class note versions of the materials leading to this text. We would like to thank the many talented researchers and students with whom we have had the privilege to explore the topics in this book. That list is too long to enumerate, but it should start with BLP’s doctoral advisor T. W. Kenny and design mentors J. Harley and A. Partridge for introducing her to the wide-ranging potential for piezoresistive transducers.

Finally, we thank the many dedicated researchers and designers who have brought the field to its current state and collectively have provided mountains of useful data and insights to inform better models for piezoresistor design.

JCD thanks Cassie for her proofreading, advice, and patience.

BLP thanks Matt for the same.

The authors also gratefully acknowledge support for the research that served as a foundation for our work on piezoresistor design and made this book possible. Research support included grants from the Stanford Center for Integrated Systems,

Stanford Bio-X, the National Science Foundation (CAREER ECS-0449400, NSEC PHY-0830228, NSEC ECCS-0832819), DARPA (YFA N66001-09-1-2089), and the National Institutes of Health NIBIB (R01 EB006745).

Contents

1	Introduction	1
1.1	Early Piezoresistor History	2
1.2	Device and Technology Timeline	4
1.2.1	Strain Gauges	4
1.2.2	Pressure Sensors	6
1.2.3	Cantilever Beams	10
1.2.4	Inertial Sensing	14
1.2.5	Resonators	17
1.2.6	Shear Stress Sensing	19
1.3	Summary and Roadmap	20
2	Piezoresistance Fundamentals	21
2.1	Notation Fundamentals	22
2.1.1	Crystal Structure	22
2.1.2	Stress, Strain and Tensors	23
2.2	Piezoresistivity	25
2.2.1	Crystallographic Orientation	25
2.2.2	Piezoresistance Factor	29
2.2.3	Nonlinearity	35
2.2.4	Theoretical Models	38
2.3	Signal Conditioning	41
2.3.1	Process Variation and Temperature Compensation	44
2.3.2	Heterodyne Biasing	48
2.4	Summary	49
3	Sensitivity, Noise and Resolution	51
3.1	Noise	51
3.1.1	A Brief Introduction to Noise	52
3.1.2	Johnson Noise	55
3.1.3	1/f Noise	56
3.1.4	Amplifier Noise	63
3.1.5	Thermomechanical Noise	65
3.1.6	Noise Summary	67

3.2	Sensitivity	70
3.2.1	Resistance Factor (γ)	71
3.2.2	Sensitivity Factor (β^*)	71
3.2.3	Transverse Loading Factor (ϕ)	76
3.3	Resolution Example	80
3.4	Summary	82
4	Fabrication and Process Modeling	85
4.1	Model Assumptions	87
4.2	Concentration Limits	88
4.3	Predeposition	90
4.4	Ion Implantation	96
4.5	Epitaxy	104
4.6	Polysilicon	108
4.7	Electrical Modeling	109
4.8	Experimental Validation Techniques	111
4.9	Practical Notes	113
4.9.1	Wafer Selection	113
4.9.2	Dopant-Induced Lattice Strain	114
4.9.3	Piezoresistor Surface Damage	119
4.9.4	Lateral Dopant Diffusion	121
4.9.5	Excess Electrical Resistance	122
4.10	Summary	124
5	Temperature Effects	127
5.1	Temperature Coefficient of Sensitivity	128
5.2	Temperature Coefficient of Resistance	129
5.3	Piezoresistor Self-Heating	130
5.3.1	A Qualitative Example	131
5.3.2	Thermal Conductivity of Typical Materials	132
5.3.3	Heat Transfer Fundamentals	135
5.3.4	Convective Heat Transfer	137
5.3.5	Example Experimental and Modeling Results	138
5.3.6	Analytical Temperature Approximations	142
5.4	Power Dissipation and Sensor Resolution	144
5.5	Summary	147
6	Design Optimization	149
6.1	Optimization Fundamentals	151
6.2	Analytical Optimization	153
6.3	Numerical Optimization	154
6.4	Example: Fabrication Process Selection	157
6.4.1	Problem Definition	157
6.4.2	Dopant Concentration	162

6.4.3	Dopant Type	163
6.4.4	Fabrication Method	164
6.5	Final Thoughts on Design.	167
6.6	Summary	168
7	Alternative Materials and Transduction Methods	171
7.1	Alternative Piezoresistive Materials	171
7.1.1	Silicon Carbide	171
7.1.2	Diamond	173
7.1.3	Nanotubes and Nanowires	175
7.1.4	Metals	179
7.2	Alternative Transduction Mechanisms	181
7.2.1	Optical	181
7.2.2	Capacitive	183
7.2.3	Piezoelectric	186
7.2.4	Pseudo-Hall and Piezojunction Effects.	192
7.3	Summary	193
Appendix A: Glossary of Mathematical Symbols		195
Appendix B: Ion Implantation Lookup Tables		199
Appendix C: Code		221
References		223

Chapter 1

Introduction

Piezoresistive sensors were among the earliest micromachined silicon devices. The exceptionally large change in resistivity of strained silicon and germanium was first discovered in 1954 by Charles Smith at Bell Laboratories. Since then, researchers have produced increasingly complex piezoresistive strain gauges, pressure sensors, accelerometers and force/displacement sensors, including many commercially successful products. The need for smaller, less expensive, higher performance sensors helped drive early micromachining technology, a precursor to microsystems or microelectromechanical systems (MEMS). Today, piezoresistive sensors comprise a substantial portion of the MEMS sensors market [9, 10] and are found in everything from automobiles to smartphones to interstellar probes [11].

All piezoresistive sensors operate upon the principle of a mechanical load deforming a sensor structure (Fig. 1.1). In silicon sensors the deformation is transduced into a resistance change by embedding a doped resistor in the structure. The resistance change is converted to a voltage signal using a measurement circuit, typically a Wheatstone bridge. The signal is conditioned by amplifiers and filters before it is acquired. Depending on the physical quantity being measured, the physical form of the sensor will vary. For example, the piezoresistor may be embedded in the surface of a thin membrane for detecting pressure, while it may compose the entirety of a linear bar for sensing strain.

In this chapter we review the history of strain sensing resistors, from the initial discovery of resistance changes in elongated metal wires in 1856 to present day silicon piezoresistors. Next, we discuss the history of MEMS piezoresistive sensors, organized by measurement type. Finally, we provide a roadmap for the remainder of the book.

Portions of this chapter were adapted from an earlier review of piezoresistance [1]. We would also like to thank A. Alvin Barlian, Nahid Harjee, Joseph R. Mallon Jr., Sung-Jin Park, Woo-Tae Park and Ali J. Rastegar for extensive and productive discussions and their contributions to the concepts presented in this chapter.

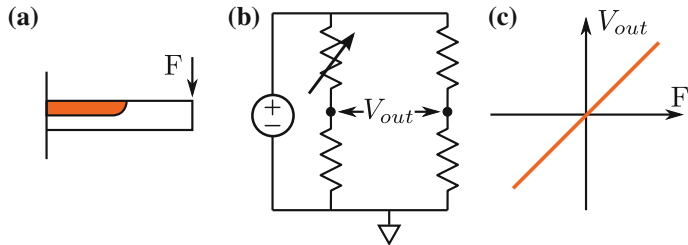


Fig. 1.1 Piezoresistive sensing principles. **a** A doped silicon resistor is embedded in a mechanical structure. **b** When the structure is mechanically loaded, the resistance of the piezoresistor changes, and the resistance change is transduced into a voltage using a Wheatstone bridge. **c** The output voltage varies linearly with the mechanical load

1.1 Early Piezoresistor History

William Thomson (Lord Kelvin) first reported on the change in resistance with elongation in iron and copper in 1856 [12]. Telegraph wire signal propagation changes and time-related conductivity changes were nuisances to telegraph companies and motivated further observations of conductivity under strain. In his Bakerian lecture to the Royal Society of London, Kelvin reported an elegant experiment where joined, parallel lengths of copper and iron wires were stretched with a weight and the difference in their resistance change was measured with a modified Wheatstone bridge. Kelvin determined that, since the elongation was the same for both wires, “the effect observed depends truly on variations in their conductivities.” Observation of these small differences was remarkable, given the precision of available instrumentation.

Motivated by Lord Kelvin’s work, Tomlinson confirmed this strain-induced change in conductivity and made measurements of temperature and strain dependent elasticity and conductivity of metals under mechanical loads and electrical currents (Fig. 1.2), [13, 14].

The steady-state displacement measurement techniques of Thomson and Tomlinson were replicated, refined, and applied to other polycrystalline and amorphous conductors by several researchers [15–18]. In 1930, Rolnick presented a dynamic technique to quantify the resistance change in vibrating wires and reported data for 15 different metals [19]. Two years later, Allen presented the first measurements of direction-dependent conductivity with strain in *single crystals* of bismuth, antimony, cadmium, zinc and tin [20–23]. Based on her work, Bridgman developed a tensor formulation for the general case of homogeneous mechanical stress on the electrical resistance of single crystals [15, 16]. We elaborate on this essential notation for handling the complexity of directional material properties in Chap. 2.

In 1935, Cookson first applied the term piezoresistance to the change in conductivity with stress, as distinct from the total fractional change of resistance, which includes both geometric and material property dependent changes [24]. The term was

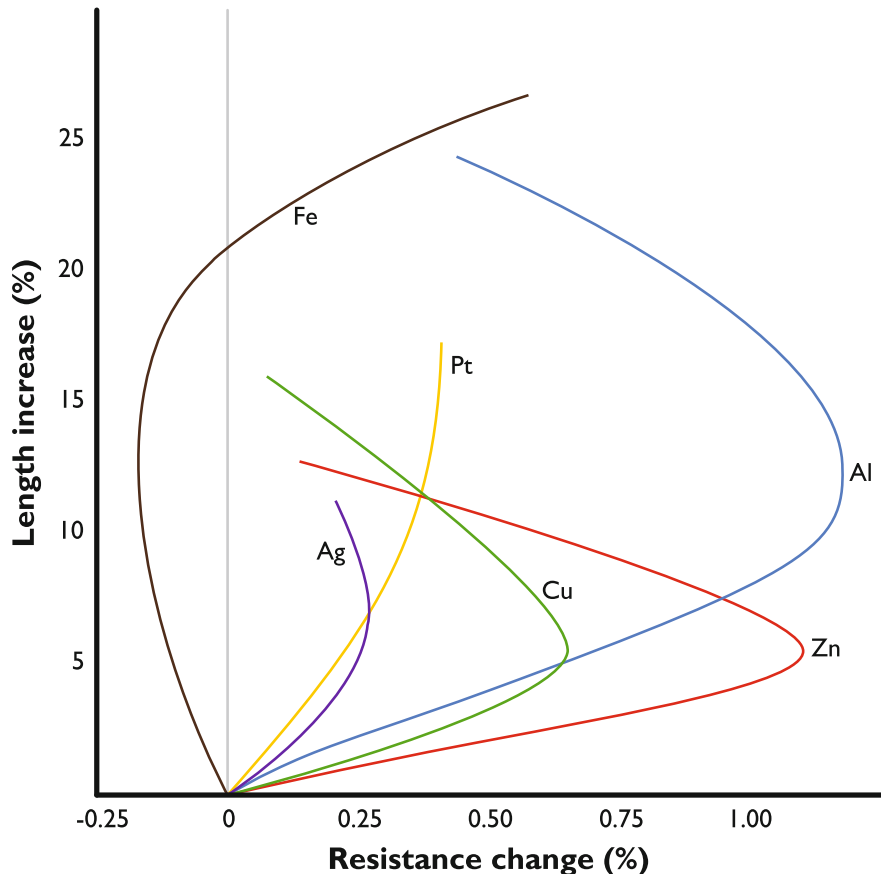


Fig. 1.2 The resistance change of several metals with length change as reported by Tomlinson in 1883. The measurement techniques pioneered by Lord Kelvin and Tomlinson were applied to numerous other materials in the following decades. (Source Redrawn from Tomlinson [13])

most likely coined after piezoelectricity, the generation of charge with applied stress, a ferroelectric-mediated effect quite different from piezoresistivity. Hanke coined the term piezoelectricity in 1881 after “piezen”, from the Greek “to press” [25, 26]. The now standard notation for piezoresistivity was also adapted from analogous work on piezoelectricity [27]. Voigt first formalized the tensor notations for stress and strain in crystals, and then formulated tensor expressions for generalized Hooke’s Law and piezoelectricity [28]. He adapted this notation following from the works of Curie and Kelvin [27, 29–32].

In 1938, more than 80 years after the discovery of piezoresistance in metal wires, Clark and Datwyler used a bonded wire to monitor strain in a stressed member [33]. In the same year, Arthur Ruge independently demonstrated the bonded metallic strain gauge which had been first suggested by Edward Simmons Jr. in 1936 [34–36].

In 1950, Bardeen and Shockley first predicted relatively large conductivity changes with deformation in single crystal semiconductors [37]. In his seminal paper on semiconductor piezoresistance four years later, Charles S. Smith (a Bell Laboratories visiting researcher from Case Western Reserve University interested in anisotropic electrical properties of materials), reported the first measurements of the exceptionally large piezoresistive shear coefficient in silicon and germanium [8]. A detailed discussion of Smith's measurement apparatus and results will wait until Chap. 2.

1.2 Device and Technology Timeline

Within a few years of Smith's discovery, silicon piezoresistors were being utilized to build transducers. In this section, we will briefly review the most common types of piezoresistive sensing structures and their development histories. More general reviews of advances in MEMS, microstructures, and Microsystems are available in the literature [38, 39].

1.2.1 Strain Gauges

The measurement of strain is important in numerous applications in science and engineering and metallic strain gauges are widely used. The measurement principle is based on the change in electrical conductance and geometry of a stretched conductor. Metal and semiconductor strain gauges are functionally equivalent, with the semiconductor gauge exhibiting greater sensitivity to strain and temperature.

In 1957, Mason and Thurston first reported silicon strain gauges applied to measuring displacement, force, and torque [40]. Semiconductor strain gauges, with sensitivity more than fifty times higher than conventional metal strain gauges, were considered a leap forward in sensing technology. Early silicon strain gauges were fabricated by sawing and chemical etching to form a bar shaped strain gauge [41]. The gage was then attached to a material surface with cement.

Using this technique, the first commercial piezoresistive silicon strain gauges and pressure sensors started to appear in the late 1950's. Kulite Semiconductor, founded in 1958 to exploit piezoresistive technology, became the first licensee under the Bell piezoresistive patents [7]. By 1960 there were at least two commercial suppliers of bulk silicon strain gauges: Kulite-Bytrex and Microsystems [7]. Examples of modern bar and U-shaped strain gauges sold by Micron Instruments are shown in Fig. 1.3. Micron Instruments produces gauges that are less than 0.5 mm long for medical applications, allowing four gauges to fit inside of a 2.5 mm diameter pressure sensor.

Higson reviewed advances in mechanical bonded resistance strain gauges, from their introduction in 1938–1964 [42]. These first-generation semiconductor strain gauges were used for making stress measurements and were bonded to metal

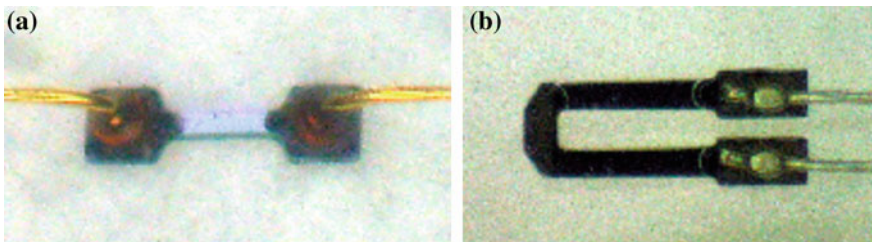


Fig. 1.3 Modern micromachined, precision-etched silicon gages. **a** Bar shaped strain gauge with a length of 0.75 mm and ball bonded Au leads. **b** U-shaped strain gauge with a length of 1.2 mm and wedge bonded Al leads. (*Source* Reprinted with permission from Herb Chelner, Micron Instruments, Simi Valley, CA)

flexural elements to make pressure sensors, load cells and accelerometers. With improvements in silicon micromachining (particularly lithography and patterning advances) it became possible to integrate piezoresistive strain gauges directly into mechanical sensor structures. We will trace the timeline of these process advances in the next section.

A simplified representation of a micromachined uniaxial strain gauge is presented in Fig. 1.4. A linear silicon resistor is patterned and formed before an insulating layer of silicon dioxide is grown. Vias are opened in the oxide before metal is deposited and patterned to define electrical contacts. The p-type piezoresistor is isolated from the n-type substrate by a depletion region. Practical piezoresistive sensors typically include multiple piezoresistors to reduce their temperature sensitivity (Chap. 5). For example, four linear strain gauges can be combined in a square arrangement with two gauges oriented with their electrical current flow parallel to the direction of applied stress (longitudinal loading) and two oriented perpendicular to the applied stress (transverse loading). These issues will be discussed at length in Chaps. 2 and 5.

More recently stress sensitive rosette patterns have been integrated onto silicon die to measure integrated circuit packaging stresses, wire bonding forces and flip

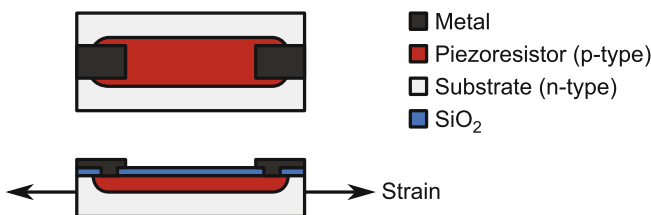


Fig. 1.4 Example uniaxial strain gauge layout and fabrication. A linear silicon resistor is formed through ion implantation or diffusion doping before a passivation oxide is grown. Vias are opened in the oxide, metal is deposited and lithographically patterned, and the sensor is diced from the wafer. The p-type piezoresistor is isolated from the n-type substrate by a depletion region. Four linear strain gauges can be combined in a square pattern forming a full Wheatstone bridge for temperature compensation and maximum strain sensitivity

chip solder ball process parameters [43–45]. As an alternative to rosette patterns, researchers have also used circular piezoresistors to map stresses using a single resistive structure [46, 47]. The pseudo-Hall effect, a piezoresistive sensing technique based upon shear loading (Sect. 7.2.4), has been used for 3D force sensing when coupled to a joystick input arm [48, 49].

1.2.2 Pressure Sensors

Pressure sensors are among the most successful micromachined sensors. Although we will focus on the history of piezoresistive pressure sensors, we recommend Esashi et al. for a more general review of pressure sensor technology and principles [50].

In the late 1950s, Kulite-Bytrex and Microsystems leveraged their strain gauge expertise to commercially introduce metal-diaphragm pressure sensors [7]. Silicon strain gauges were epoxy-bonded to the surface of a machined metal diaphragm. Typically, four semiconductor strain gauges were employed, two at the diaphragm center and two at the edge, allowing configuration into a four active arm Wheatstone bridge which: provided a voltage output proportional to $\Delta R/R$, increased sensitivity, nulled the output, and provided a first order correction for zero shift with temperature. These sensors were intended for high-cost, low-volume industrial, aerospace, and biomedical applications.

These miniature devices had relatively low performance by todays standards. They suffered especially from poor zero stability due to the mismatch between the thermal expansion coefficients of the silicon strain gauge and the stainless steel diaphragm and the relatively poor stress transmission characteristics of the metal-epoxy-silicon interface, which caused creep and hysteresis. The performance of piezoresistive pressure sensors would improve dramatically within just a few years. Incidentally, the first piezoresistive microphones were designed around the same time and closely paralleled the development of pressure sensors. In 1959, Burns patented one of the earliest diaphragm-based piezoresistive semiconductor microphones [51]. Although intended as acoustic transducers, the operation principles were similar to those of piezoresistive pressure sensors.

Developments in the manufacture of semiconductors, especially Hoerni's invention of the planar transistor in 1959, resulted in improved methods of manufacturing piezoresistive sensors [52]. In their classic 1961 paper, Pfann and Thurston proposed the integration of diffused piezoresistive elements with a silicon force collecting element [53]. In 1962, Tufte et al. [54] demonstrated this concept by reporting the first silicon pressure sensors with piezoresistors integrated with the diaphragm using dopant diffusion. Integration removed the need for the epoxy bonding and replaced the metal diaphragm with single-crystal silicon, both of which improved performance and reliability. Following this, Peake et al. [55] demonstrated monolithic integration by combining a digital circuit and diffused pressure sensor onto the same silicon die for air data applications in 1969.

In the late 1960s and early 1970s, three important microfabrication techniques were developed: anisotropic chemical etching of silicon, ion implantation, and anodic

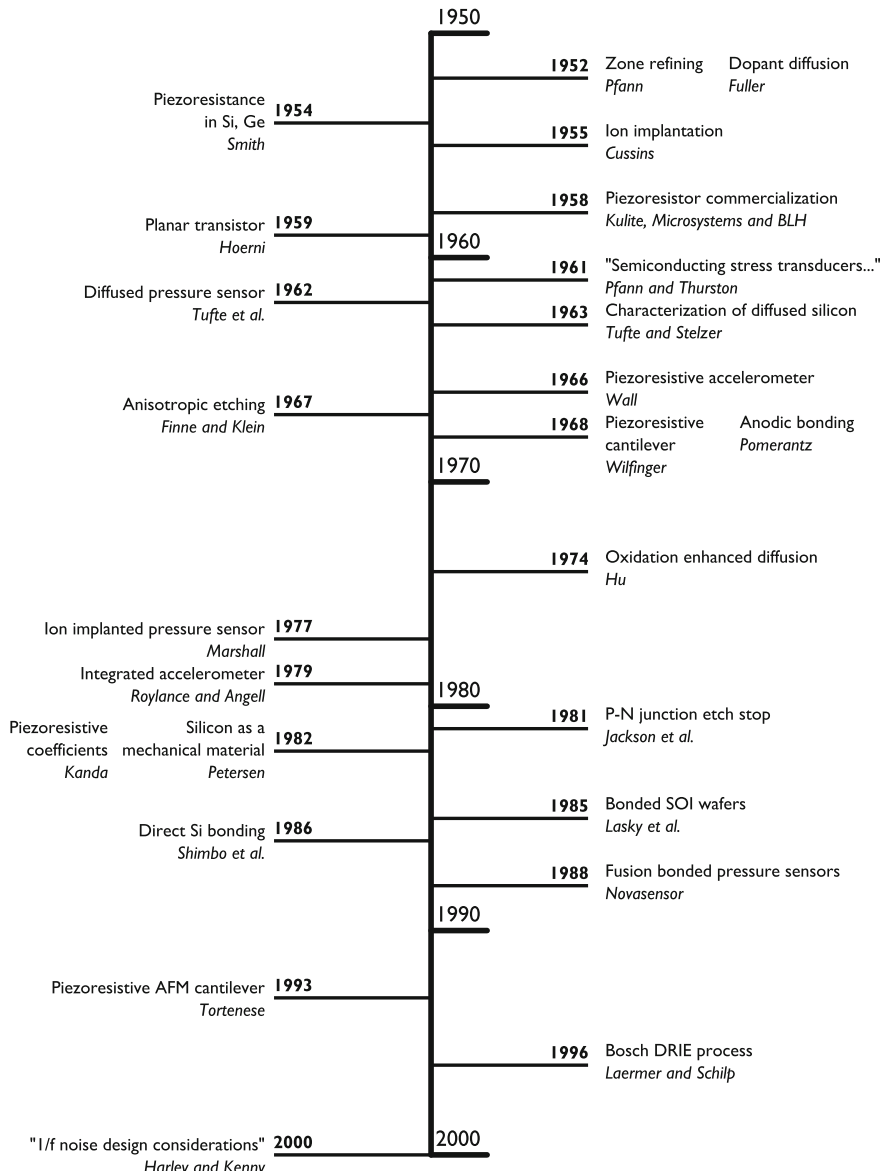


Fig. 1.5 Prominent technological and theoretical advances in the development of IC fabrication, MEMS and piezoresistive transduction over the last five decades

bonding. These techniques played a major role in improving the performance of piezoresistive pressure sensors and MEMS at large. A timeline of significant developments in ICs, piezoresistors and MEMS is presented in Fig. 1.5 and highlights the interplay between advances in the broader IC industry and piezoresistive sensors.

In 1967, Stedman pioneered bossed-diaphragm pressure sensors [56]. Samaun et al. used anisotropic etching in 1971 to form the silicon diaphragm and showed a significant increase in sensitivity of the sensor [57]. Wilner further improved sensitivity and linearity in 1977 by placing piezoresistors in the transverse direction at the concentrated stress locations and introduced sculptured diaphragms [58, 59].

Around the same time, Marshall at Honeywell patented the first silicon-based pressure sensor using ion implantation [60]. In 1978, Kurtz et al. at Kulite Semiconductor invented a low pressure, bossed-diaphragm, pressure transducer with good sensitivity and linearity at low pressure [61]. These developments led to the commercial introduction of modern piezoresistive pressure sensors by Kulite Semiconductor and Honeywell. Clark and Wise enabled refined pressure sensor designs in 1979 with their derivation of the governing electromechanical equations of thin diaphragm silicon pressure sensors using finite difference methods [62].

Piezoresistive sensors were the first commercial devices requiring three dimensional micromachining of silicon. Consequently, this technology was a singularly important precursor to the MEMS technology that emerged in the 1980s [63]. Figure 1.6 shows how these process developments impacted pressure sensor design, as discussed in detail by Eaton and Smith [64]. Piezoresistor process and design tradeoffs that accompany miniaturization are discussed in Chap. 4.

One of the critical parameters in pressure sensor performance is diaphragm thickness. Several microfabrication techniques have been developed and employed to precisely control diaphragm thickness. The first technique for controlling membrane thickness was the boron etch stop, reported in 1969 by Greenwood [65]. The etch

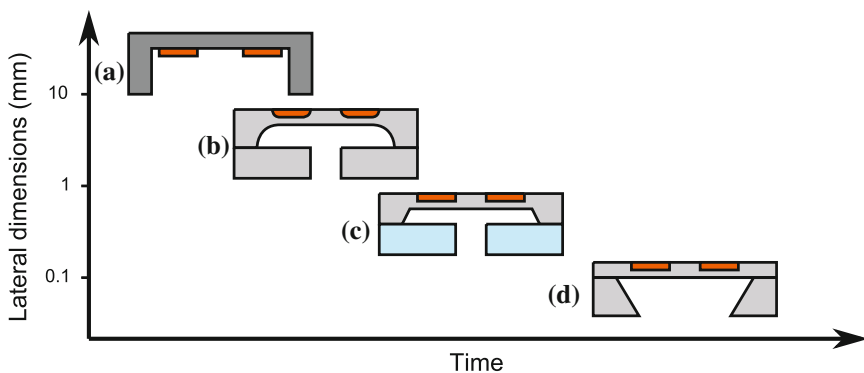


Fig. 1.6 Piezoresistive pressure sensors illustrate the enormous advances in micromachining technology with time. **a** Early pressure sensors combined a machined metal diaphragm with bonded silicon strain gauges. **b** The introduction of diffused strain gauges enabled single crystal silicon diaphragms. The diaphragms were isotropically wet etched before being bonded to a silicon support with a Si/Au eutectic bond. **c** The development of ion implantation, anodic bonding, and anisotropic wet etching enabled further size reductions. **d** Improvements in etching and bonding techniques, including direct silicon bonding, enabled further reductions in sensor size. (Source Adapted with permission from [64]. ©1997 IOP Publishing)

rates of EDP and KOH, aqueous anisotropic silicon etchants, drop significantly for boron concentrations greater than 10^{19} cm^{-3} . The electrochemical etch stop was subsequently developed which allowed for precise membrane thicknesses without the need for degenerate doping [66–68]. Novasensor combined silicon fusion bonding and boron etch stops in the late 1980s to introduce high performance commercial pressures sensors [66, 67, 69]. Novasensor pioneered many generations of piezoresistive pressure sensors [70–73].

More recent approaches to controlling diaphragm thickness are the use of silicon on insulator (SOI) wafers and the porous silicon process. An example of the latter is the Bosch piezoresistive pressure sensor shown in Fig. 1.7. This sensor is used to measure atmospheric and manifold pressure in electronic engine control systems. The porous silicon process enables the formation of a single crystal silicon membrane and vacuum cavity without any bonding steps [74, 75]. Etch stop techniques are reviewed in more detail in Ref. [76].

In 1987, Chau and Wise [77] provided scaling limits for ultra-miniature and ultra-sensitive silicon pressure sensors based on Brownian noise, electrical noise, electrostatic pressure variations, and pressure offset errors due to resistance mismatch. Spencer et al. [78] compared noise limits for piezoresistive and capacitive pressure sensors integrated with typical signal conditioning for varying diaphragm thickness,

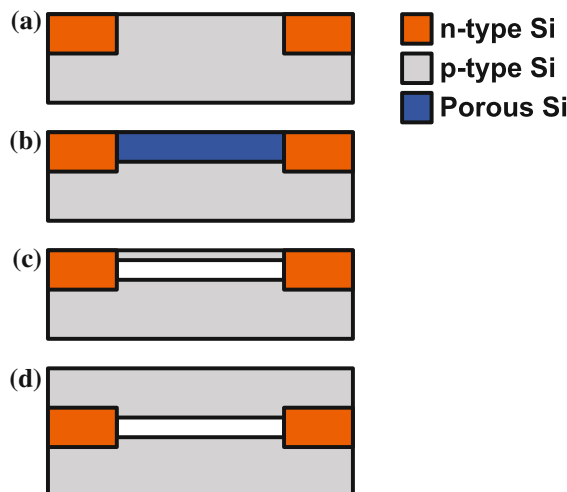


Fig. 1.7 Overview of the Bosch advanced porous silicon membrane (APSM) process. **a** Deep n-type wells are formed in a p-type wafer to define the extent of the membrane. **b** The exposed p-type silicon is anodized to form a porous silicon layer. A two-step etching process is typically used to form a fine porous region at the surface and a coarse porous region in the bulk. **c** A high temperature hydrogen anneal (e.g. 1100°C) sinters the porous silicon, forming a cavity in the coarse porous silicon region and a thin membrane in the fine porous region. **d** The thickness of the membrane is increased through epitaxy. The anneal and epitaxy steps are usually performed sequentially in an epitaxial reactor

diameter, and gap. Regardless of the sensor dimension, piezoresistive sensors configured in a Wheatstone bridge achieved the best resolution. Sun et al. [79] presented a theoretical model of the reverse current (leakage current across the piezoresistor-substrate p-n junction) and its effect on thermal drift of the bridge offset voltage. They found cleaner processing, gettering of metal impurities, and contamination control reduced the reverse current and offset errors.

Some of the first piezoresistor optimization work was performed for pressure sensors. Kanda and Yasukawa worked on the design optimization of pressure sensors in 1997 and considered the effect of numerous second order effects such as diaphragm thickness uniformity [80]. They used signal-to-noise ratio as a figure of merit to optimize the crystal planes of the diaphragm and the crystal directions of the piezoresistors. They found that a square diaphragm with a center boss was the optimal geometry and that orienting p-type piezoresistors in the $<111>$ direction on a (110) plane wafer resulted in a 1.4x resolution improvement over the more conventional (and more manufacturable) approach of aligning the piezoresistors in the $<110>$ direction on a (100) wafer.

Similarly, Bae et al. [81] reported a design optimization of a piezoresistive pressure sensor considering the piezoresistor lengths and number of turns and showed that the optimal design from a resolution standpoint is significantly different than from a sensitivity maximization standpoint. We agree wholeheartedly with this view based upon our own optimization work (Chap. 6). Bharwadj et al. reported on signal-to-noise ratio optimization of piezoresistive microphones and took into account the placement of piezoresistors, geometry, process condition, and bias voltage [82].

Most pressure sensors manufactured today still use piezoresistive transduction. Advantages of piezoresistive sensing compared with capacitive sensing include ease of differential pressure sensing configurations and freedom from the film stress related errors and failures of surface micromachining.

1.2.3 Cantilever Beams

Cantilever beams are a ubiquitous micromachined structure. End loaded cantilever beams are widely used to sense force and displacements in scanning probe microscopy [83, 84]. The deposition of a chemically responsive film transforms a cantilever beam into a surface stress sensor [85, 86]. A cantilever beam can be driven on resonance to transduce the added mass of individual atoms into an electrical signal for portable chemical sensing, gas chromatography or mass spectroscopy [87, 88]. The addition of a proof mass to the end of the cantilever beam transforms it into an accelerometer [89, 90]. In this section we will briefly summarize the history of piezoresistive cantilevers and their applications to force, displacement and surface stress sensing, leaving inertial sensing for the following section.

Silicon piezoresistive cantilevers were first developed in the late 1960s by Wilfinger, Bardell and Chhabra [91], who used a silicon cantilever with diffused piezoresistive elements to fabricate a “resonistor” (Fig. 1.8). The resonistor was actuated

via Joule heating and the piezoresistors were used to measure the deflection. They utilized a sustaining circuit to build an oscillator from the resonistor. Subsequently, Fulkerson integrated a Wheatstone bridge and amplifier circuit with a piezoresistive cantilever and pioneered the concept of signal conditioning integration [92].

Perhaps the best-known application of cantilevers as force and displacement sensors is in Atomic Force Microscopy (AFM) [93]. In 1993, Tortonese et al. first used piezoresistive transduction to detect AFM cantilever displacement [83]. Piezoresistive transduction is attractive in its simplicity and reliability because: (1) the absence of external sensing elements simplifies the design of an AFM for large samples and adverse environments (high vacuum, etc.) and reduces the cost of the experimental setup; (2) the operation of the microscope is further simplified by eliminating the need for precise optical alignment; (3) piezoresistive AFM requires low voltages and simple circuitry for operation. However, implementing a piezoresistor on the cantilever adds fabrication cost and piezoresistive cantilevers are not widely produced today. At least one of the reasons is the tip wear experienced by all silicon cantilevers when scanning hard samples; the frequent replacement of AFM cantilevers amplifies the additional cost of incorporating piezoresistive sensing.

Piezoresistive AFM cantilevers can address many specialized applications that are beyond the capabilities of optical transduction. Individually actuated piezoresistive cantilevers have been developed for parallel high-speed imaging [94, 95]. Integrated actuators (thermal or piezoelectric) allow for increased imaging bandwidth (up to several hundred kHz) by reducing the effective mass of the system [96–98]. Brugger et al. demonstrated lateral force measurements using surface piezoresistors on AFM cantilevers [99]. Brugger et al. also fabricated and tested ultra-sensitive piezoresistive cantilevers for torque magnetometry [100]. Hagleitner et al. fabricated the first

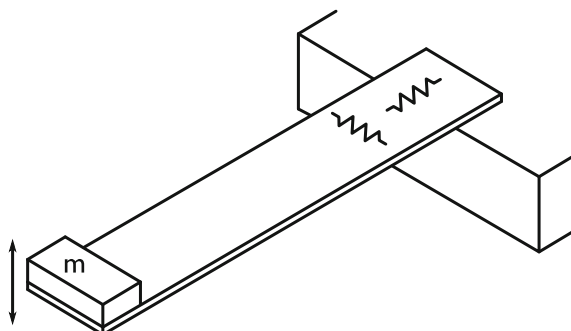


Fig. 1.8 Example of an early resonator based upon a cantilever beam developed by Wilfinger, Bardell and Chhabra [91]. The beam ($0.2\text{ mm thick} \times 0.75\text{ mm wide} \times 8.9\text{ mm long}$) was cut from the source wafer and gold eutectic bonded to a gold plated pedestal before being thermally actuated and piezoresistively sensed at 1.4 kHz . A full Wheatstone bridge with both longitudinal and transverse piezoresistors was integrated into the base of the beam to provide the highest possible sensitivity and thermal compensation

parallel scanning, piezoresistive AFM cantilevers integrated with on-chip complementary metal-oxide-semiconductor (CMOS) electronics [101].

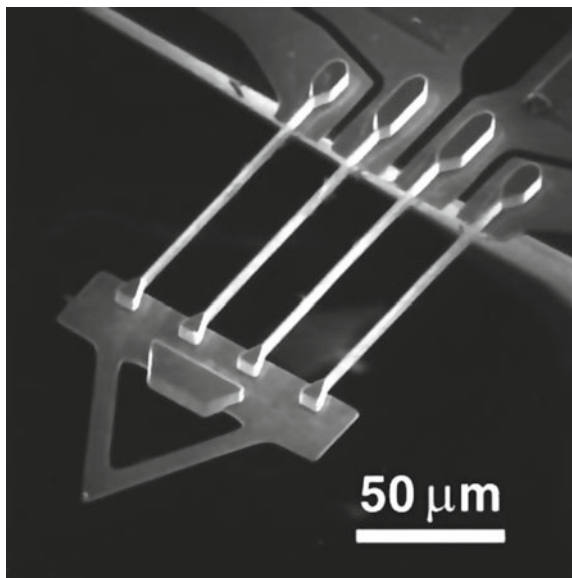
Chui et al. [102] later introduced sidewall-implant fabrication for dual-axis piezoresistive AFM cantilever applications. The dual-axis AFM cantilevers utilize regions with orthogonal compliance to reduce mechanical crosstalk when an AFM cantilever is operated in a torsional bending mode and allow improved measurement of lateral forces at the tip (Fig. 1.9).

Piezoresistive cantilevers have also been widely used for environmental, chemical and biological sensing [103–106]. Boisen et al. developed AFM probes with integrated piezoresistive read-out for environmental sensing [107]. Franks et al. fabricated piezoresistive CMOS-based AFM cantilevers for nanochemical surface analysis application [108]. Baselt et al. reviewed micromachined biosensors and demonstrated the use of piezoresistive AFM cantilevers for the study of interactions between biomolecules and chemical sensors [109].

Piezoresistive cantilevers have also been used for materials characterization [110–112], liquid or gas flow velocity sensing [113, 114] and data storage applications [115–117]. Aeschimann et al. developed piezoresistive scanning-probe arrays for operation in liquids [118]. Their cantilevers were passivated with 50-nm silicon nitride films over the piezoresistors and 500-nm silicon oxide films over the metal lines.

Researchers have also pushed the limits of microfabrication to make ultra thin cantilevers. Harley and Kenny fabricated 89 nm thick single crystal silicon cantilevers using epitaxial deposition with sensitivity of 5.6×10^{-15} N-Hz $^{-0.5}$ in air [84]. Liang et al. showed 70 nm thick n-type piezoresistive cantilevers with sensitivity of

Fig. 1.9 SEM of a dual-axis AFM cantilever. Piezoresistors are formed on the sidewalls of the tall, narrow tethers for in-plane sensing while conventional piezoresistors are formed on the V-shaped end of the cantilever beam for out-of-plane sensing. (Source Reprinted with permission from [102]. ©1998 American Institute of Physics)



1.6×10^{-15} N-Hz $^{-0.5}$ at 1 kHz [119]. Harley and Kenny and Liang et al. formed the piezoresistors by growing doped epitaxial layers, which allowed the fabrication of ultra thin piezoresistors and cantilevers. However, Bergaud et al. showed that ion implantation could also be used to fabricate ultra-thin piezoresistors (90 nm) by implanting BF₂ into germanium-preamorphized silicon [120]. Arlett et al. developed a family of sub-100 nm thick piezoresistive cantilevers via oxidation thinning and epitaxial growth of the piezoresistor [121, 122].

Piezoresistive cantilevers have also been scaled to the radio frequency (RF) domain. Bargatin et al. developed a novel method to detect displacement and resonance up to 71 MHz using piezoresistors as signal downmixers [123]. They tested their scheme using nanoscale silicon and AlGaAs piezoresistive cantilevers and demonstrated that the downmixed signal is approximately 1,000 times larger than in the standard scheme. The same group later reported nanoscale silicon carbide (SiC) cantilevers with piezoresistive gold films for very high frequency applications [87]. Reviews of nanomechanical resonators and other device types, piezoresistive or otherwise, are available in Refs. [106, 124, 125].

The design of piezoresistive cantilevers has been investigated numerous times over the past several decades. Hansen and Boisen provided design criteria considering noise for piezoresistive AFM cantilevers [126]. Harley and Kenny reported optimization of thin, power-limited piezoresistive cantilevers fabricated using epitaxy for AFM applications [127]. Yu et al. performed a similar analysis for piezoresistive cantilevers used in micro-channels [128]. Yang et al. reported design and optimization of piezoresistive cantilevers for biosensing applications using finite element analysis, and analyzed the change in relative resistivity in the presence of a chemical reaction [104]. Other notable publications include Rasmussen et al. [129], Bhardwaj et al. [82] and Wang et al. [130].

These design optimization investigations were targeted at particular application needs and based upon analytical optimization techniques, which prevented them from accounting for complex phenomena such as ion implantation-based fabrication, Joule heating or fluid damping. In 2009 we used a numerical optimization approach to eliminate these limitations and experimentally validated the results [131, 132]. In the following year we extended the design optimization to ion-implanted piezoresistors [133]. In 2011 we extended our numerical optimization work to thermal effects and experimentally demonstrated that piezoresistive cantilever performance actually improves when operated in water rather than air [134].

We subsequently designed and fabricated a second generation of 300 nm thick piezoresistive cantilevers that were integrated with thermal and piezoelectric actuators (Fig. 1.10) [97, 98]. Operation in ionic media was enabled through parylene passivation. Piezoelectric actuation enabled a rise time of <10 μs while the piezoresistor was capable of resolving 1–100 pN depending on the measurement bandwidth, a 10–20 fold improvement over prior cantilevers (largely due to numerical optimization). The cantilevers were used for the study of mammalian hair cells which transduce sound into electrical impulses.

Another application of piezoresistive cantilevers is surface stress sensing. Coating a cantilever beam with a chemically response film yields a chemical sensor. The

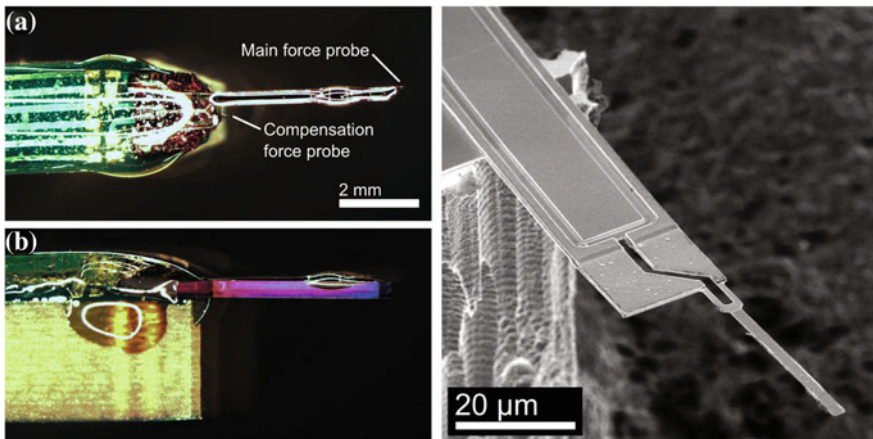


Fig. 1.10 Piezoresistive cantilevers with integrated actuation for biomolecular force measurements. *Left* A cantilever is wirebonded to a printed circuit board before being passivated with epoxy and a thin layer of parylene to enable operation in ionic media. *Right* SEM of a 300 nm thick cantilever beam that integrates piezoresistive sensing with piezoelectric actuation. (*Source* Reprinted with permission from Ref. [2])

adsorption of molecules into the film generates biaxial stress and the cantilever stress can be modeled using Stoney's formula or more recent versions [136, 137].

However, the operation and design optimization of piezoresistive cantilevers for surface stress sensing is very different from force or displacement sensors [38, 85]. The relative resistance change of end-loaded and surface stress-loaded cantilever beams is shown in Fig. 1.11. The stress along the longitudinal axis of the cantilever beam is equal to the stress in the transverse direction everywhere except for near the base. The problem with this loading configuration is that the resistivity change from longitudinal and transverse stress are opposite in sign for the most common piezoresistor configurations (Sect. 2.2).

One approach to the clamping effect for surface stress sensors is to use a short and wide beam [86]. An alternative approach, introduced by Yoshikawa et al. [135], utilizes a membrane suspended at the end of four cantilever beams. The membrane collects surface stress and concentrates it into a longitudinal deflection of the cantilever beams.

1.2.4 Inertial Sensing

Accelerometers and gyroscopes are both heavily commercialized MEMS applications. A comprehensive review of micromachined inertial sensors, including piezoresistive accelerometers, can be found in Ref. [139]. Accelerometers are widely used in automotive, biomedical, consumer electronics, robotics, structural health monitoring

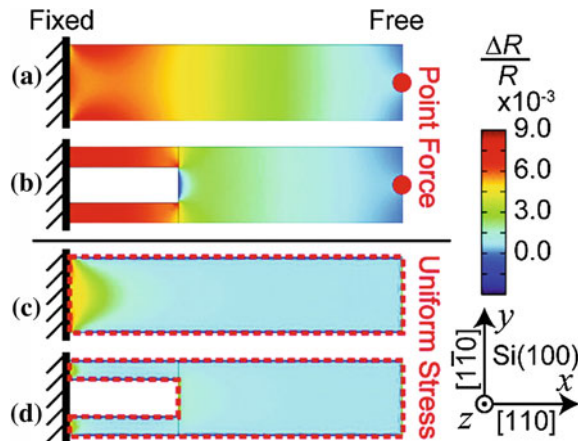


Fig. 1.11 Distribution of the relative resistance change over p-type, $<110>$ oriented end loaded and surface stress loaded cantilevers. **a, b** The relative resistance change varies smoothly over the length of end loaded cantilever beams with constant width and a constriction at the base. **c, d** In contrast, the relative resistance change of surface stress loaded cantilevers is nearly zero everywhere except for near the base due to a clamping effect. (Source Reprinted with permission from [135]. ©2011 American Chemical Society)

and military applications. Gyroscopes can be used together with accelerometers to provide additional information on angular velocity for navigation purposes in automotive, robotics, and military applications.

The first piezoresistive inertial sensor was reported in 1969 by Gravel and Brosh [140]. Their sensor was based upon a diffused piezoresistor and a chemically micro-machined cantilever. Roylance and Angell subsequently introduced the first fully integrated piezoresistive micromachined accelerometers in 1978 for biomedical applications [141]. The accelerometer consisted of a piezoresistive cantilever with an integrated micromachined lumped mass at the end and a diffused piezoresistor at the root of the flexure. Barth et al. introduced the first commercialized piezoresistive accelerometer using silicon fusion bonding to provide an integrated package and over-pressure stop [142].

Monolithic integration of piezoresistive accelerometers with CMOS circuitry subsequently improved the output readout and accommodated temperature compensation circuitry [143, 144]. Allen demonstrated piezoresistive accelerometers with self-test features [145]. Chen et al. integrated a novel vertical beam structure in a piezoresistive accelerometer to allow in-plane and out-of-plane acceleration measurements [146]. Kwon and Park [147] fabricated a three axis piezoresistive accelerometer using bulk micromachining and silicon direct bonding technology using a polysilicon layer.

Partridge et al. [89] and Park et al. [148] used oblique ion-implantation for the piezoresistors with DRIE to fabricate devices designed for lateral acceleration sensing. These devices also incorporated a novel wafer-level packaging technique using a

thick polysilicon epitaxial cap to seal the devices and protect the piezoresistors from harsh plasma processing. This protection reduced the noise and package footprint [149]. Park et al. also reported using fully packaged sub-mm scale piezoresistive accelerometers for vibration measurements in middle ear ossicles (Fig. 1.12). This technology was intended to provide an alternative sensing method for implantable hearing aids [148]. Lynch et al. integrated piezoresistive planar accelerometers with wireless sensing unit for structural monitoring [150].

While capacitive transduction dominates the commercial MEMS inertial sensing market, piezoresistive transduction remains a popular alternative. Many Japanese accelerometer manufacturers use piezoresistive transduction (e.g. Hitachi Metals, Matsushita, Fujitsu and Hokuriku), while manufacturers from the US and Europe focus mainly on capacitive sensing (e.g. Bosch, Freescale, Kionix, STMicroelectronics and Analog Devices). Other companies, such as Infineon and Novasensor have also demonstrated piezoresistive accelerometers in production. Both sensing mechanisms utilize CMOS integrated circuits for amplification and compensation, typically using a hybrid integration approach with a separate MEMS and CMOS die combined into an injection molded package. Large manufacturers of automotive sensors prefer capacitive sensing with integrated self-test by electrostatic actuation. Three-axis sensing capability, size, power consumption and cost are important factors for mobile consumer applications which are driving the growth of most MEMS-based sensors.

A related class of inertial sensors, MEMS gyroscopes were first developed in the late 1980s by Draper Laboratory. Inertial gyroscopes measure rate of rotation and operate by detecting inertial resistance to changes in velocity. Most micromachined gyroscopes are based on vibration and use the transfer of energy between two orthogonal vibration modes via the Coriolis force. The Coriolis force, F_C , induces

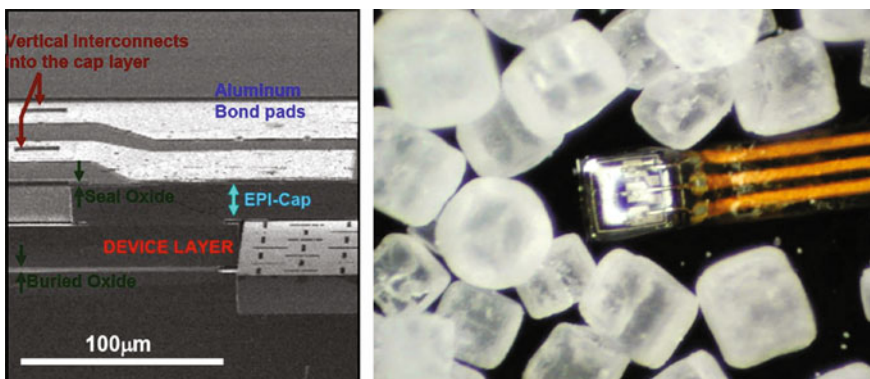


Fig. 1.12 Piezoresistive inertial sensing. *Left* Oblique-view SEM of a sidewall-implanted piezoresistive accelerometer with a 20 μm thick polysilicon cap. *Right* Optical micrograph of the packaged table salt crystals for scale. (*Source* Reprinted with permission from Ref. [148]. ©2007 Springer Science and Business Media)

acceleration (in y) of the mass proportional to the vibration velocity (in x) and angular rate of rotation (about z) (Fig. 1.13). Micromachined gyroscopes are difficult to manufacture because they require a high performance resonator and an accelerometer coupled in a high-vacuum hermetic package. Manufacturers of MEMS gyroscopes include Invensense, STMicroelectronics, Bosch and Analog Devices.

In most commercial MEMS gyroscopes, the same transduction scheme is preferred for both resonator actuation and acceleration sensing for ease of integration. This is one reason why piezoresistive gyroscopes are seen more frequently in research than in commercial production [151–153]. Although thermal actuation can be integrated with piezoresistive sensing, piezoelectric and capacitive transduction have historically provided lower power and simpler integration. Thermally actuated and piezoresistively sensed resonators are under active development in research labs [154, 155].

In most gyroscope applications, the sensor is used to calculate angular position by integrating the rate of rotation over time. Thus, gyroscope sensor performance is especially degraded by low frequency drift and offset errors. Capacitive transduction adds negligible 1/f noise to the system in contrast with piezoresistive sensing. Unlike the 1/f noise and zero stability in the signal conditioning circuit, which can be reduced using a chopper stabilized amplifier and heterodyning, transducer 1/f noise can not be eliminated. However, it is possible to design and fabricate very low 1/f noise piezoresistors with some tradeoffs in size [156], and piezoresistive gyroscopes may be commercially produced some day.

1.2.5 Resonators

Gyroscopes are based upon resonant mechanical systems—the other major commercial applications of MEMS resonators are frequency references and filters. Piezoresistive transduction can be used to efficiently transduce resonator motion into an electrical signal. For certain operating conditions, piezoresistive sensing can even be

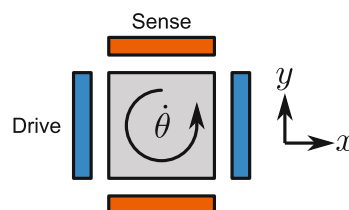


Fig. 1.13 MEMS gyroscopes measure the angular rate of rotation ($\dot{\theta}$) via the Coriolis force. A proof mass is driven in the x -direction and its movement in the y -direction is measured. The angular rate of rotation is integrated over time to determine heading, making long-term stability critical. In this example, the proof mass is driven and sensed capacitively by a pair of electrodes on each axis

used to amplify rather than attenuate the electrical input to the resonator [157] and generate resonator motion without any external sustaining circuit [158].

Frequency references are at the heart of every electronic device, serving as everything from low power real time clocks in microcontrollers to local oscillators for RF systems. Major design issues with MEMS-based frequency references include initial frequency accuracy, stability over temperature and phase noise [159]. MEMS-based resonators provide several advantages over quartz, the incumbent technology, and are beginning to gain traction commercially. Resonators, like gyroscopes, require integrated actuation and sensing. As one might expect, capacitive transduction is the dominant technology today [159].

However, both piezoelectric [160] and piezoresistive [161] resonators have been developed in order to address the shortcoming of capacitive transduction, primarily its high motional impedance. Piezoelectric resonators enable the lowest possible motional impedance [162] but the inclusion of multiple metal layers can degrade their frequency stability and prevent high temperature encapsulation [163, 164]. Piezoresistive sensing enables a significant reduction in motional impedance over capacitive transduction, up to two orders of magnitude [165], while remaining compatible with high temperature encapsulation technologies. An example of a capacitively actuated and piezoresistively sensed resonator is shown in Fig. 1.14. Oscillators based upon piezoresistive resonators have been developed as frequency references [166]. Capacitive actuation requires a high voltage (>10 V) for most applications. Resonators that combine electrothermal actuation with piezoresistive sensing have been developed in order to address this issue [154, 155], although their power efficiency is typically less than capacitive actuation except at very high frequencies (>500 MHz) [167].

The dominant MEMS filter technology today is the thin film bulk acoustic resonator (FBAR), developed in the 1990s at HP, Agilent and now Avago [168, 169]. The FBAR utilizes the thickness vibrational mode of a piezoelectric film,

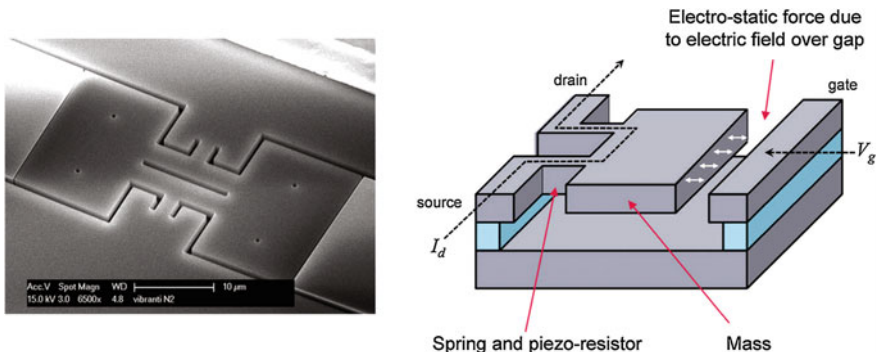


Fig. 1.14 Example of a capacitively actuated, piezoresistively sensed resonator. The enlarged ends of the dogbone structure are actuated electrostatically by two fixed electrodes, inducing mechanical stress in the piezoresistor legs. Current is passed through the legs to transduce the stress into an electrical signal. (Source Reprinted with permission from [159]. ©2012 IOP Publishing)

predominantly aluminum nitride (AlN), sandwiched between metal electrodes to provide a high Q, low motional impedance resonator at 1–2 GHz. Multiple resonators with slightly detuned resonant frequencies are coupled to filter signals at RF frequencies. The FBAR has been adapted for frequency reference applications [170] although it has not been commercialized for this purpose yet. Recent developments in MEMS filter technology include piezoelectric contour mode resonators with lithographically- rather than thickness-defined resonant frequencies for single chip filter banks [171]. Piezoresistive MEMS filters have not been developed to date due to the need for low insertion loss (e.g. $<10\ \Omega$ motional impedance), although the ability of piezoresistive resonators to amplify input signals may change this in the future [157].

1.2.6 Shear Stress Sensing

A final application of piezoresistive sensors is the detection of shear stress. From improving the aerodynamic design of a vehicle body to understanding the formation of atherosclerosis on the wall of human blood vessels [172], shear stress measurement provides key input to understanding the fluid flow physics. Piezoresistive shear stress sensors commonly utilize a floating-element anchored to the substrate via four piezoresistive tethers [173, 174]. The displacement of the floating element due to the integrated shear stress (force) is detected as bending stress in the piezoresistors.

Ng et al. [175] and Shajii et al. [176] used wafer-bonding technology to fabricate floating-element sensors. Piezoresistors were fabricated on the top surface of the tethers using ion implantation. In operation, the fluid flow direction was parallel to the tethers such that a shear force over the element loads two of the tethers in axial compressive stress and the other two in axial tensile stress.

Barlian et al. used oblique ion-implantation to form piezoresistors on the sidewall of two tethers and a normal surface implant for two other tethers (Fig. 1.15), [178, 177]. The sidewall piezoresistors are sensitive to lateral deflections, while the normal piezoresistors are sensitive to flow fluctuations producing out-of-plane deflections. Thus, each sensor enabled simultaneous measurements of normal and shear stresses.

Li et al. also developed piezoresistive shear stress sensors using oblique ion-implantation technique [179, 180]. Other piezoresistive 3D stress sensors have been used to measure multi-axis tactile or traction forces for biological [181, 182], robotic [183], and device packaging applications [47, 184, 185]. Noda et al. fabricated 2-D shear stress sensors for tactile sensing with standing piezoresistive cantilevers embedded in polydimethylsiloxane (PDMS) [186]. Fan et al. and Chen et al. have designed, fabricated, and characterized biomimetic piezoresistive flow sensors for underwater applications [187, 188].

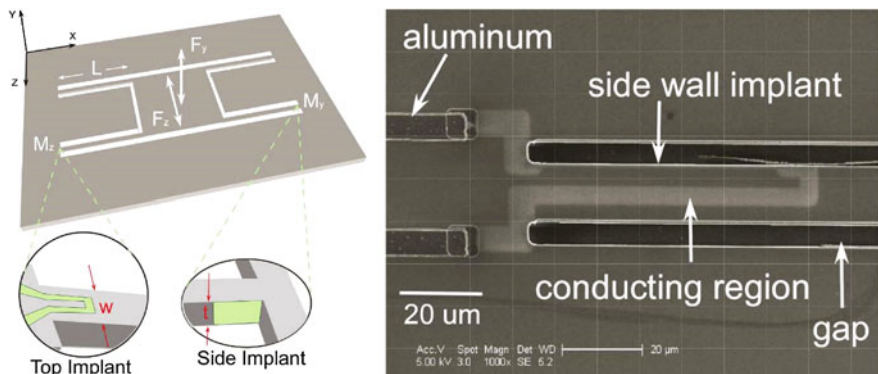


Fig. 1.15 Shear stress sensing. *Left* Piezoresistive floating-element MEMS shear stress sensor. Each sensor consists of two top-implanted and two sidewall-implanted piezoresistors. The sidewall-implanted piezoresistors are sensitive to in-plane stress while the top-implanted piezoresistors are sensitive to out-of-plane stress. *Right* SEM image of one of the tethers with a sidewall-implanted piezoresistor. (*Source* Reprinted with permission from [177]. ©2007 Elsevier)

1.3 Summary and Roadmap

The focus of this chapter has been on the evolution of piezoresistive sensors over time, the interplay between fabrication process and performance, and an overview of the many applications where piezoresistive sensors are used. The rest of the book will emphasize design optimization and the accurate electrical, thermal and mechanical models necessary for successful optimization.

Chapters 2 through 5 will each dive into the details of a particular aspect of piezoresistor operation. We will begin with the notation and modeling fundamentals of piezoresistance (Chap. 2) before moving onto models for the noise and resolution of a sensor (Chap. 3). In Chap. 4 we will discuss piezoresistor fabrication options and present models to calculate electrical characteristics from fabrication process parameters for epitaxy, diffusion and ion implantation. Temperature effects, particularly important for high performance sensor design, will be described in Chap. 5.

We will bring all of these models together in Chap. 6 in describing and demonstrating the application of analytical and numerical optimization methods. An in-depth understanding of piezoresistor design will allow the reader to tailor a sensor design to match the required performance specifications. Design optimization can be used to maximize performance, minimize cost, or balance the desired tradeoff between the two. By the end, we hope that you will be ready to design high performance piezoresistor sensors using realistic design models, understand the strengths and limitations of piezoresistive sensing, and have an intuitive sense of the design tradeoffs that are fundamental to piezoresistor design. With a good understanding of silicon-based piezoresistive sensing in hand, we will conclude by discussing alternative transduction technologies and materials in Chap. 7.

Chapter 2

Piezoresistance Fundamentals

The core concepts for piezoresistive sensing will be presented in this chapter. We will open by discussing resistive strain sensing in general before moving on to the piezoresistive effect in particular. Variation in piezoresistive coefficients with crystallographic orientation, dopant concentration, strain and temperature will be considered, with an emphasis on accurate analytical models for each effect. We will close by presenting the transduction and signal conditioning approaches that can be used to transduce a resistance change into a usable signal.

Consider a homogenous resistor in the shape of a square prism (Fig. 2.1). The electrical resistance (R) measured between its ends is

$$R = \frac{\rho l}{w^2}. \quad (2.1)$$

where l is the length, w is the width of each side, and ρ is the electrical resistivity.

A mechanical load applied to one face of the resistor while holding the other end stationary will mechanically strain the material. For an elastic change in length equal to Δl , the longitudinal strain in the material is $\varepsilon_l = \Delta l / l$ to first-order approximation.

The width will also change due to contraction of material in the transverse direction in proportion to the Poisson's ratio of the material (ν). For a sufficiently small strain the change in width is $\Delta w = -\nu \varepsilon_l w$. ν ranges from 0.20 to 0.35 for most polycrystalline metals. For single crystal silicon, which is anisotropic, the Poisson's ratio ranges from 0.06 to 0.36 depending on the crystal orientation [189, 190]. The fundamental lower and upper limits for ν of an isotropic material are -1.0 and 0.5 [191]. Examples include rubber (+0.5) and polymer foams (-0.7) [192].

Portions of this chapter were adapted from an earlier review of piezoresistance [1]. We would also like to thank A. Alvin Barlian, Nahid Harjee, Joseph R. Mallon Jr., Sung-Jin Park, Woo-Tae Park and Ali J. Rastegar for extensive and productive discussions and their contributions to the concepts presented in this chapter.

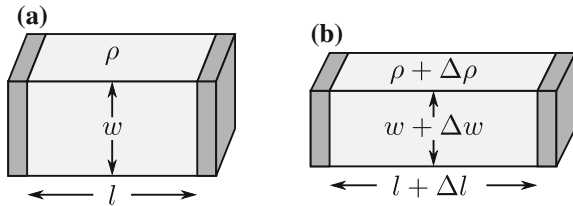


Fig. 2.1 **a** The electrical resistance of a homogenous square prism depends on its dimensions (l and w) and resistivity (ρ). **b** When subjected to mechanical loading, all three can potentially change, leading to a change in the measured electrical resistance (Source Reprinted with permission from [2])

We can take the natural log and partial derivatives of both sides of (2.1) to obtain

$$\frac{\partial R}{R} = \frac{\partial \rho}{\rho} + \frac{\partial l}{l} - 2 \frac{\partial w}{w}. \quad (2.2)$$

The relative resistance change can be written in terms of the strain [19] as

$$\frac{\Delta R}{R} = \frac{\Delta \rho}{\rho} + (1 + 2\nu)\varepsilon_l. \quad (2.3)$$

The gauge factor (GF) of a strain gauge is defined as

$$GF = \frac{\Delta R/R}{\varepsilon_l}. \quad (2.4)$$

Combining (2.3) and (2.4) we see that geometric effects alone provide a gauge factor of approximately 1.4–2.0 depending on the Poisson's ratio. Metals experience a small resistivity change with strain, which typically increases the gauge factor by an additional 0.3 or so. However, for silicon and other semiconductors, $\Delta \rho / \rho$ can be 50–100 times larger than the geometric term due to the piezoresistive effect. Models for calculating the piezoresistive coefficients and gauge factor of silicon will be developed in this chapter as a first step towards the design of piezoresistive sensors.

2.1 Notation Fundamentals

2.1.1 Crystal Structure

Crystals are periodic arrangements of atoms arranged in one of 14 lattice types. The Miller indices specify crystal planes by n-tuples. The direction index $[hkl]$ denotes a vector normal to a plane described by (hkl) . Angle-bracketed indices,

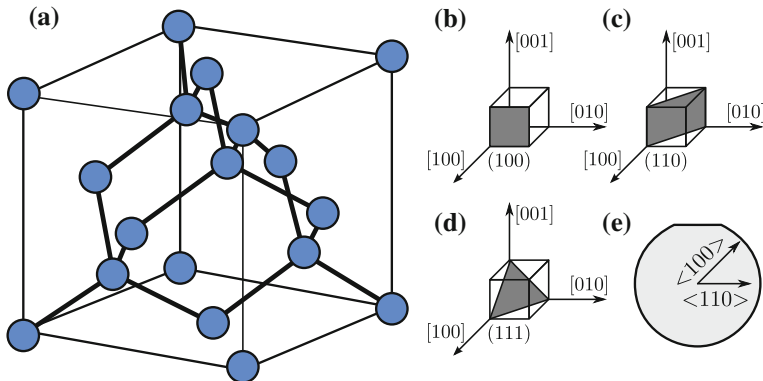


Fig. 2.2 **a** Single crystal silicon forms a diamond cubic lattice with each atom covalently bonded to its four neighbors. **b–d** Important crystal planes of silicon are the (100), (110) and (111) planes. **e** Wafers smaller than 200 mm in diameter have a major flat that indicates the <110> direction, whereas larger wafers have a notch (Source Reprinted with permission from [2])

like $\langle hkl \rangle$, represent all directions equivalent to $[hkl]$ by symmetry. The family of planes normal to $[hkl]$ are denoted with curly brackets as $\{hkl\}$. Complete reviews are available elsewhere [193, 194].

Crystalline silicon forms a covalently bonded diamond-cubic structure with lattice constant $a = 5.43 \text{ \AA}$ (Fig. 2.2a). The diamond-cubic structure is equivalent to two interpenetrating face-centered-cubic (FCC) lattices with basis atoms offset by $\frac{1}{4}a$ in the three orthogonal directions [193]. Silicon's diamond-cubic lattice is relatively sparse (34 % packing density) compared to a regular face-centered-cubic (FCC) lattice (74 % packing density).

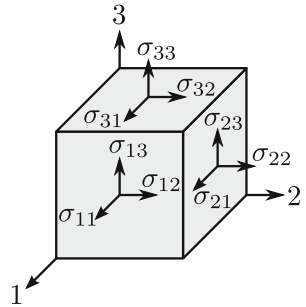
Commonly used wafer surface orientations in micromachining include (100), (111), and (110) (Fig. 2.2b). The $\{111\}$ planes, oriented 54.74° from $\{100\}$ planes, are the most densely packed. As alluded to earlier, the magnitude of the piezoresistive effect varies with the crystal orientation of the resistor. In order to maximize sensitivity piezoresistors are typically oriented in the <100> direction for n-type doping and <110> direction for p-type doping. Variation in piezoresistive coefficients with orientation will be discussed in more detail shortly.

2.1.2 Stress, Strain and Tensors

To define the state of stress for a unit element (Fig. 2.3), nine components, σ_{ij} , must be specified, as in:

$$\boldsymbol{\sigma} = \begin{pmatrix} \sigma_{11} & \sigma_{12} & \sigma_{13} \\ \sigma_{21} & \sigma_{22} & \sigma_{23} \\ \sigma_{31} & \sigma_{32} & \sigma_{33} \end{pmatrix}. \quad (2.5)$$

Fig. 2.3 General stress elements on a unit cell. The stress component σ_{ij} represents the stress on face i in direction j . Both normal ($i = j$) and shear ($i \neq j$) stress components are generally present and play a role in piezoresistive transduction (Source Reprinted with permission from [2])



The first index (i) denotes the direction of the vector normal to the surface that the stress is applied to, while the second index (j) indicates the direction of the force or stress. If $i = j$, the stress is normal to the specified surface, while $i \neq j$ indicates a shear stress on face i . Assuming static equilibrium, the stress tensor will always be symmetric, i.e. $\sigma_{ij} = \sigma_{ji}$. Thus the stress tensor contains only six independent components. Strain, ε_{ij} , is also directional. For an isotropic, homogeneous material, stress is related to strain by Hooke's Law, $\sigma = E\varepsilon$ [195].

Although effective values of Young's modulus and Poisson's ratio for a single direction are often employed for simple loading situations, a tensor is required to fully describe the mechanics of an anisotropic material such as silicon [6, 63, 196]. The stress and strain are related by the elastic stiffness matrix, C , where $\sigma_{ij} = C_{ijkl}\varepsilon_{kl}$, or equivalently by the compliance matrix, S , where $\varepsilon_{ij} = S_{ijkl}\sigma_{kl}$.

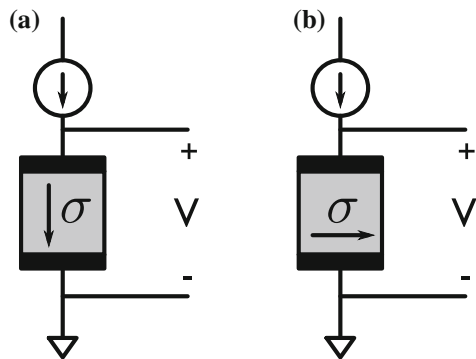
For simplicity, collapsed notation is often used. Collapsed notation reduces each pair of subscripts to one number: 11→1, 22→2, 33→3, 23→4, 13→5, 12→6, e.g. σ_{11} becomes σ_1 , ε_{12} becomes ε_6 , c_{1111} becomes c_{11} and s_{2323} becomes s_{44} . In other words,

$$\begin{pmatrix} \sigma_{11} \\ \sigma_{22} \\ \sigma_{33} \\ \sigma_{23} \\ \sigma_{13} \\ \sigma_{12} \end{pmatrix} = \begin{pmatrix} c_{11} & c_{12} & c_{13} & c_{14} & c_{15} & c_{16} \\ c_{12} & c_{22} & c_{23} & c_{24} & c_{25} & c_{26} \\ c_{13} & c_{23} & c_{33} & c_{34} & c_{35} & c_{36} \\ c_{14} & c_{24} & c_{34} & c_{44} & c_{45} & c_{46} \\ c_{15} & c_{25} & c_{35} & c_{45} & c_{55} & c_{56} \\ c_{16} & c_{26} & c_{36} & c_{46} & c_{56} & c_{66} \end{pmatrix} \begin{pmatrix} \varepsilon_{11} \\ \varepsilon_{22} \\ \varepsilon_{33} \\ 2\varepsilon_{23} \\ 2\varepsilon_{13} \\ 2\varepsilon_{12} \end{pmatrix} \quad (2.6)$$

and

$$\begin{pmatrix} \varepsilon_{11} \\ \varepsilon_{22} \\ \varepsilon_{33} \\ 2\varepsilon_{23} \\ 2\varepsilon_{13} \\ 2\varepsilon_{12} \end{pmatrix} = \begin{pmatrix} s_{11} & s_{12} & s_{13} & s_{14} & s_{15} & s_{16} \\ s_{12} & s_{22} & s_{23} & s_{24} & s_{25} & s_{26} \\ s_{13} & s_{23} & s_{33} & s_{34} & s_{35} & s_{36} \\ s_{14} & s_{24} & s_{34} & s_{44} & s_{45} & s_{46} \\ s_{15} & s_{25} & s_{35} & s_{45} & s_{55} & s_{56} \\ s_{16} & s_{26} & s_{36} & s_{46} & s_{56} & s_{66} \end{pmatrix} \begin{pmatrix} \sigma_{11} \\ \sigma_{22} \\ \sigma_{33} \\ \sigma_{23} \\ \sigma_{13} \\ \sigma_{12} \end{pmatrix}. \quad (2.7)$$

Fig. 2.4 Schematic of Smith's test configurations for extracting **a** longitudinal and **b** transverse piezoresistive coefficients [8]. Lightly doped p- and n-type samples of Ge and Si were characterized. Uniaxial stress (σ) was applied by hanging weights on the sample bars of silicon. Longitudinal and piezoresistive coefficients were measured in both the $<100>$ and $<110>$ directions, allowing the extraction of the π_{11} , π_{12} and π_{44} coefficients



2.2 Piezoresistivity

Single crystal germanium and silicon were the first materials widely used as piezoresistors. Smith reported the first measurements of large piezoresistive coefficients in these semiconductor crystals in 1954 noting that work by Bardeen and Shockley, and later Herring, could explain the phenomena [8]. Smith applied Bridgman's tensor notation [17] in defining the piezoresistive coefficients and geometry of his test configurations (Fig. 2.4).

2.2.1 Crystallographic Orientation

The piezoresistive coefficients (π) require four subscripts because they relate two second-rank tensors (stress and resistivity). In the most general case, electrical current is forced across the piezoresistor in one direction, the voltage drop is measured along another, and the stress is applied in a third arbitrary direction.

The first subscript refers to the direction of electrical potential measurement, the second to the direction of current flow, in the resistor, and the third and fourth to the stress (recall that stress has two directional components). For conciseness, the subscripts of each tensor are also collapsed [40], e.g. $\pi_{1111} \rightarrow \pi_{11}$, $\pi_{1122} \rightarrow \pi_{12}$, $\pi_{2323} \rightarrow \pi_{44}$. Kanda later generalized these relations for a fixed voltage and current orientation (ω) as a function of stress direction (λ) [197]:

$$\frac{\Delta\rho_\omega}{\rho} = \sum_{\lambda=1}^6 \pi_{\omega\lambda} \sigma_\lambda. \quad (2.8)$$

Smith determined these coefficients for relatively lightly doped silicon and germanium samples with resistivities ranging from 1.5 to 22.7 $\Omega\text{-cm}$ [8]. He measured the piezoresistive coefficients for (100) samples along the $<100>$ and $<110>$ crystal directions. Longitudinal and transverse coefficients for the fundamental crystal axes were determined directly. Shear piezoresistive coefficients were inferred. By these measurements and considering the crystal symmetry, Smith fully characterized the piezoresistive tensor of 7.8 $\Omega\text{-cm}$ p-type silicon as

$$\pi = \begin{pmatrix} 6.6 & -1.1 & -1.1 & 0 & 0 & 0 \\ -1.1 & 6.6 & -1.1 & 0 & 0 & 0 \\ -1.1 & -1.1 & 6.6 & 0 & 0 & 0 \\ 0 & 0 & 0 & 138.1 & 0 & 0 \\ 0 & 0 & 0 & 0 & 138.1 & 0 \\ 0 & 0 & 0 & 0 & 0 & 138.1 \end{pmatrix} \times 10^{-11} \quad (2.9)$$

where π has units of Pa^{-1} and takes the general form of

$$\pi = \begin{pmatrix} \pi_{11} & \pi_{12} & \pi_{12} & 0 & 0 & 0 \\ \pi_{12} & \pi_{11} & \pi_{12} & 0 & 0 & 0 \\ \pi_{12} & \pi_{12} & \pi_{11} & 0 & 0 & 0 \\ 0 & 0 & 0 & \pi_{44} & 0 & 0 \\ 0 & 0 & 0 & 0 & \pi_{44} & 0 \\ 0 & 0 & 0 & 0 & 0 & \pi_{44} \end{pmatrix}. \quad (2.10)$$

As illustrated in Fig. 2.4, there are four particularly important piezoresistive measurement configurations. The direction of current flow and applied stress can be parallel (longitudinal) or perpendicular (transverse) to each other, and they can be oriented in the $<100>$ or $<110>$ directions of the crystal lattice.

The net relative resistivity change is usually written as a sum of the longitudinal and transverse effects as

$$\frac{\partial \rho}{\rho} = \pi_l \sigma_l + \pi_t \sigma_t \quad (2.11)$$

where σ_l is the stress parallel to the current flow (longitudinal direction), σ_t is the stress perpendicular to the current flow (transverse direction), and π_l and π_t are the longitudinal and transverse piezoresistive coefficients.

The relationship between π_l , π_t and the fundamental piezoresistive coefficients depends on the crystallographic orientation of the resistor. In the $<100>$ direction, the relationships are

$$\pi_l = \pi_{11} \quad (2.12)$$

$$\pi_t = \pi_{12} \quad (2.13)$$

while in the $<110>$ direction they are

Table 2.1 Piezo resistive tensor components for lightly doped (10^{16} cm^{-3}) silicon in the (100) plane near room temperature as reported by Smith [8]

Doping type	$\pi_{11} (10^{-11} \text{ Pa}^{-1})$	$\pi_{12} (10^{-11} \text{ Pa}^{-1})$	$\pi_{44} (10^{-11} \text{ Pa}^{-1})$
n-type	-102.2	53.4	-13.6
p-type	6.6	-1.1	138.1

Table 2.2 Longitudinal and transverse piezo resistive coefficients for lightly doped (10^{16} cm^{-3}) single crystal silicon in the $<100>$ and $<110>$ directions near room temperature based upon measurements by Smith [8]

Doping type	Orientation	$\pi_l (10^{-11} \text{ Pa}^{-1})$	$\pi_t (10^{-11} \text{ Pa}^{-1})$
n-type	$<100>$	-102	53.4
	$<110>$	-31.6	-17.6
p-type	$<100>$	6.6	-1.1
	$<110>$	71.8	-66.3

$$\pi_l = 1/2(\pi_{11} + \pi_{12} + \pi_{44}) \quad (2.14)$$

$$\pi_t = 1/2(\pi_{11} + \pi_{12} - \pi_{44}). \quad (2.15)$$

The piezo resistive tensor coefficients for lightly doped (10^{16} cm^{-3}), room temperature single crystal silicon piezoresistors are summarized in Table 2.1. Note the large π_{11} and π_{44} coefficients for n- and p-type silicon, respectively. The longitudinal and transverse piezo resistive coefficients in the $<100>$ and $<110>$ directions are summarized in Table 2.2.

Note that the $<110>$ orientation with transverse tensile stress can be used to reduce the resistivity of both n-type ($\pi_t = -17.6 \times 10^{-11} \text{ Pa}^{-1}$) and p-type ($\pi_t = -66.3 \times 10^{-11} \text{ Pa}^{-1}$) resistors. In CMOS devices, where mobility enhancement is desired, the $<110>$ orientation is often used to stress engineer both n- and p-type channels [198]. A more complex alternative which maximizes the mobility enhancement for both transistor types is to orient n- and p-type devices in the $<100>$ and $<110>$ directions with longitudinal tensile and compressive stresses, respectively [199].

The coefficients illustrate why n- and p-type resistors should be oriented in the $<100>$ and $<110>$ directions, respectively, in order to maximize the magnitude of the piezo resistive effect. Notably, $\pi_l \approx -\pi_t$ for p-type piezoresistors, while $\pi_l \approx -2\pi_t$ for n-type piezoresistors. In certain applications, the large transverse effect of p-type piezo resistance can be utilized to improve sensitivity (e.g. full Wheatstone bridge devices) while in others the transverse effect leads to reduced sensitivity (e.g. surface stress sensors).

It is important to emphasize that the polarity of the piezo resistive effects differs for n-type and p-type silicon. A longitudinal tensile stress decreases the resistivity of n-type resistors and increases the resistivity of p-type resistors, while a transverse stress leads to the opposite effects.

Although the $\langle 100 \rangle$ and $\langle 110 \rangle$ directions are optimal, the longitudinal and transverse piezoresistive coefficients can be calculated for an arbitrary direction from [40, 197]

$$\pi_l = \pi_{11} - 2(\pi_{11} - \pi_{12} - \pi_{44})(l_1^2 m_1^2 + m_1^2 n_1^2 + n_1^2 l_1^2) \quad (2.16)$$

$$\pi_t = \pi_{12} + (\pi_{11} - \pi_{12} - \pi_{44})(l_1^2 l_2^2 + m_1^2 m_2^2 + n_1^2 n_2^2) \quad (2.17)$$

where l_i , m_i , and n_i are the direction cosines between the crystallographic coordinate system and the direction of current flow and stress. The general form for computing the direction cosines is described in Ref. [197]. In the case of (100) plane wafers, which includes most piezoresistor applications, the direction cosines are

$$\begin{pmatrix} l_1 & m_1 & n_1 \\ l_2 & m_2 & n_2 \\ l_3 & m_3 & n_3 \end{pmatrix} = \begin{pmatrix} \cos(\phi) & \sin(\phi) & 0 \\ -\sin(\phi) & \cos(\phi) & 0 \\ 0 & 0 & 1 \end{pmatrix} \quad (2.18)$$

where ϕ is the angle between the direction of current flow in the piezoresistor and the $\langle 100 \rangle$ direction. Most applications are best suited by orienting the piezoresistors in either the $\langle 100 \rangle$ or $\langle 110 \rangle$ direction to maximize the piezoresistive coefficients, although a handful of applications require the sensor structure to be oriented in a particular off-axis angle. When utilizing off-axis orientations, care should be taken to properly compute the stiffness matrix of the lattice following Ref. [200]. A graphical representation of the longitudinal and transverse coefficients as a function of direction and dopant type is presented in Fig. 2.5.

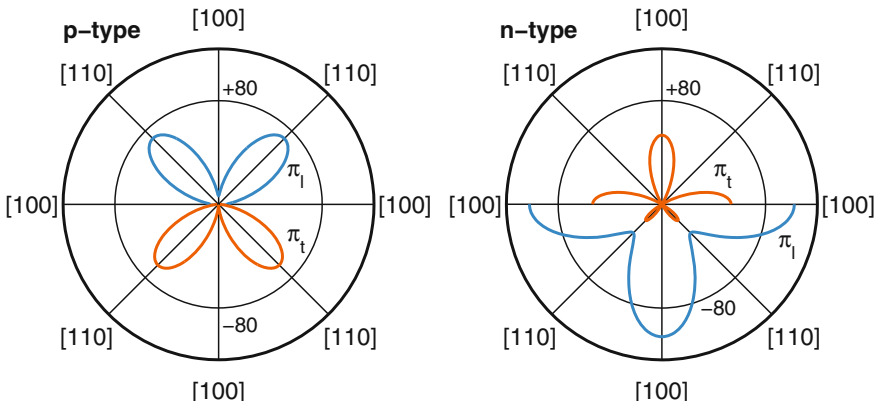


Fig. 2.5 Room temperature piezoresistive coefficients of lightly doped silicon in the (100) plane for (left) p-type doping and (right) n-type doping. Computed from (2.16), (2.17), (2.18) and Table 2.1. The longitudinal and transverse piezoresistive coefficients, plotted as radial distance from the origin, have units of 10^{-11} Pa^{-1} . Note that the longitudinal coefficient is positive in p-type silicon and negative in n-type silicon

There are two common arrangements for measuring piezo resistive coefficients. Smith [8], Tufte and Stelzer [202] and others used a tensile test bar (Fig. 2.4). This method works particularly well for uniformly doped samples. More recent experiments have used four-point bending to apply a known stress to the piezo resistors [198, 203–205]. Four-point bending applies uniform stress to any piezo resistors located between the two inner supports, and can be used to test arbitrary samples without the need for sample gripping. An additional benefit of four-point bending is that the π_{11} , π_{12} and π_{44} coefficients can be readily determined from the same sample by orienting piezo resistors along the $<100>$ and $<110>$ directions.

An alternative method for determining the piezo resistive coefficients in arbitrary directions was developed by Richter [46, 47, 201]. A circular piezo resistor with multiple contacts along the resistor annulus was used to arbitrarily set the current flow orientation. A photograph of the circular piezo resistor and schematic of the contact are shown in Fig. 2.6.

Richter also developed a more conventional test chip for measuring the π_{11} , π_{12} and π_{44} coefficients (Fig. 2.7) [201, 206]. The piezo resistors were formed via boron ion implantation at multiple doses in order to accurately extract the piezo resistive coefficients at multiple concentrations and temperatures. Each test chip included six piezo resistors with varying crystallographic orientations and test structures for accurately measuring sheet resistance (Van der Pauw) and contact resistance (six-terminal Kelvin cross bridge). The piezo resistive coefficients and theory that Richter presented in [206] and [201] will be featured prominently in the next section.

2.2.2 *Piezoresistance Factor*

Variation in the resistivity of silicon with respect to strain and temperature depends on dopant concentration. Initial experiments by Smith used bars of silicon cut from wafers that were doped while growing the single-crystal ingot [8]. Smith's samples were relatively lightly doped, ranging from 5×10^{14} to 10^{16} cm^{-3} in dopant concentration.

Later, Pfann and Thurston [53] proposed diffusion techniques to integrate doped piezo resistors on the sensor surface. Tufte and Stelzer [202] fabricated diffused piezo resistors and investigated their properties, observing a large reduction in strain sensitivity at high concentration. In contrast with Smith, their dopant concentrations varied from 3×10^{18} to $2 \times 10^{21} \text{ cm}^{-3}$. Tufte and Stelzer reported empirical data on piezo resistive coefficients as a function of both dopant concentration and temperature, which they varied from -200 to 100°C . Kurtz and Gravel replotted their data and noted that the piezo resistive coefficients decreased approximately with the logarithm of the surface concentration [207].

Kanda presented a theoretical model for variation in piezo resistive coefficients with dopant concentration and temperature (Fig. 2.8) [197]. He also introduced the piezo resistance factor notation for calculating piezo resistive coefficients for arbitrary dopant concentration and temperature,

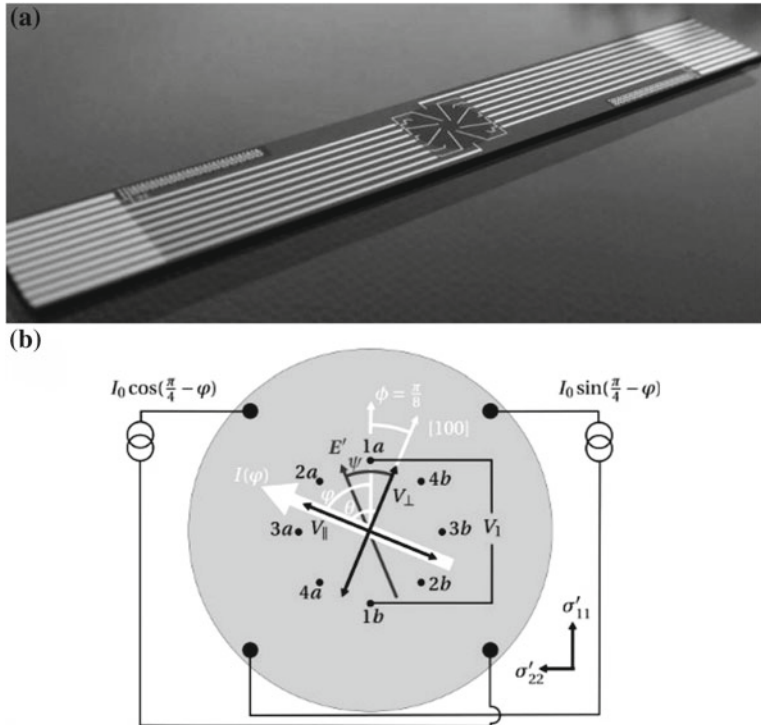


Fig. 2.6 Example of a circular piezoresistor for piezoresistive coefficient extraction and stress sensing. **a** Photograph of a circular piezoresistor with eight contacts at the perimeter for forcing an electrical current through the piezoresistor and eight contacts near the center for measuring the induced potential drops. The chip is 4 cm long and 5.3 mm wide with a 3.6 mm diameter resistor. **b** Schematic of the circular piezoresistor. Four of the outside electrical contacts are shown. The outside contacts apply time varying currents that generate a spinning electrical potential drop in the center of the circle (Source Reprinted with permission from [201] courtesy of Jacob Richter)

$$\pi(N, T) = P(N, T)\pi^{\text{ref}} \quad (2.19)$$

where π^{ref} is the value of the piezoresistive coefficient of interest for lightly doped silicon (10^{16} cm^{-3}) at 300 K. All of the piezoresistive coefficients ($\pi_{11}, \pi_{12}, \pi_{44}, \pi_l$ and π_t) can be scaled linearly using the piezoresistance factor, which follows from (2.16) and (2.17).

The piezoresistance factor, P , accounts for variation in the piezoresistive coefficients with concentration and temperature, and in Kanda's model is calculated from

$$P = \frac{300}{T} \frac{F'_{s+(1/2)}}{F_{s+(1/2)}} \quad (2.20)$$

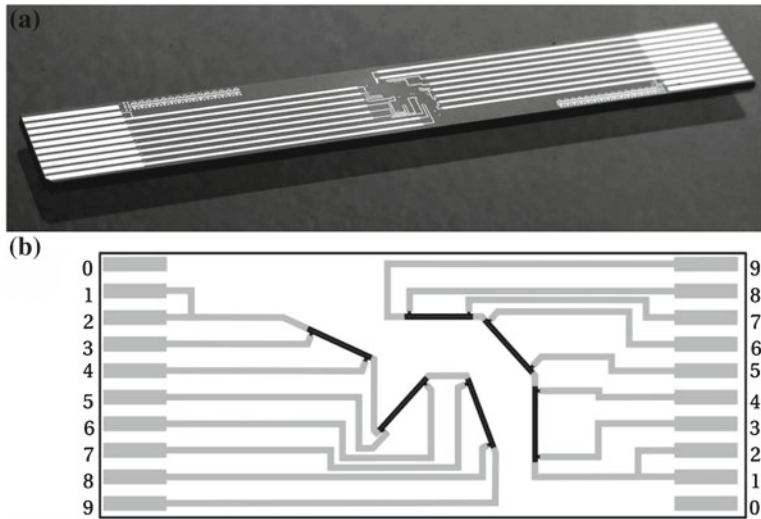


Fig. 2.7 Test chip for extracting piezo resistive coefficients from four point bending tests. **a** Photograph of a test chip with six piezoresistors in four-wire configurations. Test structures for measuring the sheet and contact resistances are included along the edges of the chip. **b** Schematic of the piezoresistor layout (Source Reprinted with permission from [201] courtesy of Jacob Richter)

where F_s and F'_s are the Fermi integral and its derivative with respect to the Fermi energy, E_F .

Kanda considered the case where carriers are predominantly scattered by phonons rather than ionized impurities; impurity scattering becomes important at high concentration ($>10^{19} \text{ cm}^{-3}$). Phonon-limited scattering corresponds to $s = -\frac{1}{2}$. In general, the Fermi integral is

$$F_{s+(1/2)} = (k_b T)^{s+(3/2)} \int_0^\infty \frac{E^{s+(1/2)}}{1 + \exp((E - E_F)/k_b T)} dE. \quad (2.21)$$

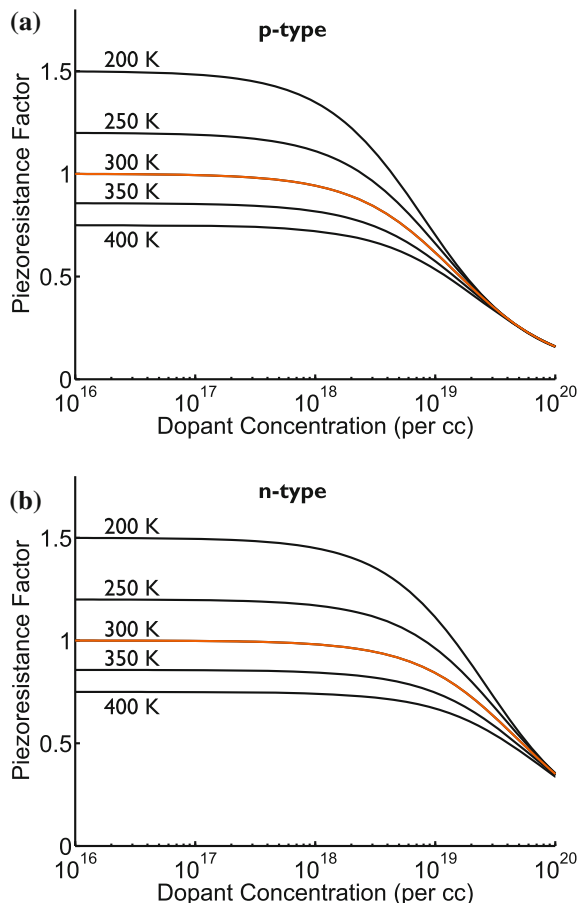
In order to properly account for the density of states available for conduction, the Fermi level is calculated from

$$n = v\sqrt{2} \left(\frac{m_d^* k_b T}{\pi h} \right)^{3/2} F_{s+(1/2)}(E_F/k_b T) \quad (2.22)$$

where n is the carrier concentration, h is Planck's constant, v is the number of carrier valleys, and m_d^* is the density of states effective mass [208]. There are 6 valleys for both n-type and p-type silicon, while m_d^* is 1.08 or 0.49 for electrons (n-type) or holes (p-type), respectively [208, 209].

In this problem, n is known and we are solving for E_F . Solving (2.22) for E_F when $s = -\frac{1}{2}$ would normally require iterative numerical integration, but accurate

Fig. 2.8 Theoretical predictions for the piezoresistance factor of p- and n-type silicon from Kanda's model, calculated from (2.20). The piezoresistance factor is plotted as a function of dopant concentration for several operating temperatures, and it decreases with increasing dopant concentration and temperature. The piezoresistance factor decreases more quickly with dopant concentration for p-type than n-type silicon in Kanda's model (*Source* Reprinted with permission from [2])



analytical approximations for the inverse Fermi integral have been developed. We use the method from Nilsson, which is accurate to within 0.5 % for $-10 < E_F/k_b T < 20$ [210, 211]. E_F is calculated from

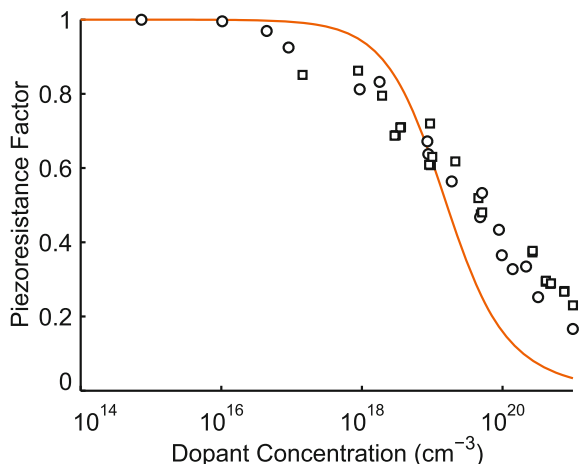
$$\frac{E_F}{k_b T} = \frac{\ln(u)}{1 - u^2} + v - \frac{v}{1 + (0.24 + 1.08v)^2} \quad (2.23)$$

where

$$u = \frac{\pi^2 N_d}{v\sqrt{2}} \left(\frac{m_d^* k_b T}{h} \right)^{-3/2} \quad (2.24)$$

$$v = \left(\frac{3\sqrt{\pi}u}{4} \right)^{2/3}. \quad (2.25)$$

Fig. 2.9 Comparison between Kanda's theoretical piezo resistance factor and experimental data at 300 K. The theory, plotted for p-type silicon, overpredicts P at intermediate dopant concentrations (10^{17} – 10^{18} cm^{-3}) and underpredicts P for high concentrations (10^{19} cm^{-3}). Experimental data are drawn from Refs. [202, 206, 207, 212–214]. Data from p-type (squares) and n-type (circles) silicon are plotted as distinct symbols (Source Reprinted with permission from [2])



Kanda's piezo resistance factor, calculated from (2.20), is plotted in Fig. 2.8. The model predicts a reduction in the piezo resistance factor with increasing temperature and dopant concentration. Additionally, it predicts a more rapid reduction in P with dopant concentration for p-type silicon than for n-type silicon. The model also predicts that the temperature coefficient of sensitivity (TCS), $\partial P / \partial T$, decreases with increasing dopant concentration, which will be discussed in more detail later.

Comparing Kanda's model with experimental data (Fig. 2.9) we see two things. First, the model significantly underpredicts P at high concentration. Second, there is no substantial difference in P between p- and n-type silicon. Kanda's calculated values of P agreed well with the experimental values obtained by Mason [213] for doping concentrations less than $1 \times 10^{17} \text{ cm}^{-3}$ from -50 to 150°C , but they are 21% lower than experimental results at $3 \times 10^{19} \text{ cm}^{-3}$. His calculations only consider carrier scattering with lattice vibrations (phonons), and the deviation from experimental data can be attributed to additional scattering by ionized dopants at high concentrations.

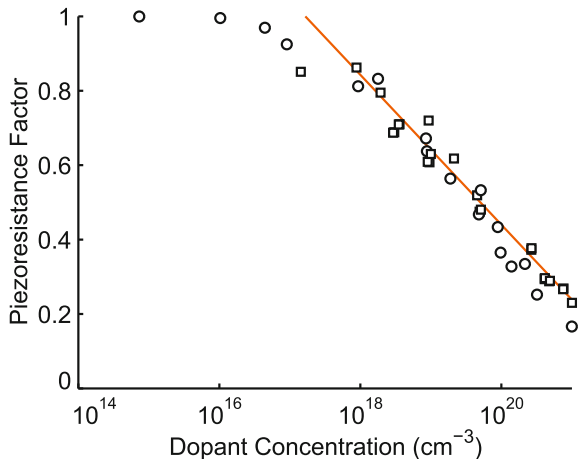
The experimental data in Fig. 2.9 is drawn from Tufte and Stelzer [202, 212], Mason [213], Kerr [214], Kurtz and Gravel [207], and Richter [206]. Both Tufte and Kurtz used diffusion doping to form their piezo resistors, so the coefficients are plotted against the surface dopant concentration. This can lead to an error of up to 15% due to contributions from the more lightly doped silicon deeper in the sample [214]. In contrast, Richter used an SOI structure with uniform doping throughout the device layer to eliminate this effect.

In 2000, Harley developed an empirical fit for the piezo resistance factor based upon the p-type data from Tufte and Stelzer, Mason, and Kerr [127]. In Harley's fit, P is calculated from

$$P = \log_{10} \left(\left[\frac{b}{n} \right]^a \right) \quad (2.26)$$

where $a = 0.2014$, $b = 1.53 \times 10^{22} \text{ cm}^{-3}$, and n is the dopant concentration.

Fig. 2.10 Comparison between Harley's empirical fit and experimental data at 300 K. The fit is accurate for dopant concentrations greater than $1 \times 10^{18} \text{ cm}^{-3}$ but overpredicts the piezoresistance factor for lower concentrations. The fit does not include any temperature dependency (Source Reprinted with permission from [2])



Harley's fit is plotted against the experimental data in Fig. 2.10. The fit is accurate for dopant concentrations above $1 \times 10^{18} \text{ cm}^{-3}$ but overpredicts P for lower concentrations. Additionally, the fit is only for $P(N)$ and not $P(N, T)$, so can't be used for devices operating at temperatures above or below 300 K and does not provide information about the temperature coefficient of sensitivity.

Richter et al. presented an updated model in 2008 for the piezoresistance factor of p-type silicon as a function of dopant concentration and temperature [206]. The model was developed from first principles and included both phonon and ionized impurity scattering, in contrast with Kanda's model, which only included phonon scattering. The complete model was reduced to an approximate analytical formula at the end of the 2008 paper,

$$P = \frac{T_n^{-\theta}}{1 + \left(\frac{N}{N_b}\right)^\alpha T_n^{-\beta} + \left(\frac{N}{N_c}\right)^\gamma T_n^{-\eta}} \quad (2.27)$$

where $T_n = T/300$ is the normalized temperature. The fitting coefficients θ , N_b , N_c , α , β , γ and η are presented in Table 2.3.

Richter's model is compared with the experimental data at 300 K in Fig. 2.11a. The fit is excellent at high concentrations and $P \rightarrow 1$ at low concentrations. Although the model was developed specifically for p-type silicon it fits n-type accurately as well.

However, most piezoresistive sensors do not operate at room temperature. Commercial devices are typically designed to meet a particular temperature specification, such as commercial grade (0–70 °C) or industrial grade (−40 to 85 °C). In contrast with Harley's fit, Richter's model is temperature dependent. Experimental data for temperatures other than 300 K is available from Richter et al. (300, 325 and 350 K) and Tufte and Stelzer (77, 125, 160, 200, 250, 300 and 350 K) [206, 212]. The Richter

Table 2.3 Fitting parameters for the Richter model and the modified Richter model to calculate the piezo resistance factor as a function of dopant concentration as temperature

Parameter	Richter model [206]	Modified Richter model
θ (-)	0.9	0.95
N_b (cm^{-3})	6×10^{19}	4.9×10^{19}
N_c (cm^{-3})	7×10^{20}	2.6×10^{20}
α (-)	0.43	0.39
β (-)	1.6	1.35
γ (-)	0.1	0.94
η (-)	3	4.55

model is plotted against the experimental piezo resistance factor data in Fig. 2.11b for the temperatures investigated by Tufte and Stelzer.

The piezo resistance factor predicted by Richter's model is accurate over the entire temperature range for dopant concentrations below 10^{16} cm^{-3} . As in Kanda's theory, the piezo resistance factor scales as roughly $1/T$ for lightly doped silicon. However, the predicted value is too large for higher dopant concentrations when the temperature is below 200 K.

In order to provide a more accurate model for low temperature piezo resistor operation, we fit Richter's model (2.27) to the experimental data in Refs. [206, 212] by minimizing the squared sum of the residual error between the theory and data. The resulting modified Richter model is plotted in Fig. 2.12 at 300 K and the same temperatures plotted in Fig. 2.11. The fit is substantially improved at low temperature without any reduction in accuracy at higher temperatures. We will use the modified Richter model throughout the book to calculate the piezo resistance factor as a function of dopant concentration and temperature.

For applications below 77 K, Harjee reported a longitudinal coefficient of $-31 \times 10^{-11} \text{ Pa}^{-1}$ at 2 K for an n-type piezo resistor doped to $1.3 \times 10^{20} \text{ cm}^{-3}$ [215]. It would also be worth visiting the data from Morin et al. who measured the piezo resistance factor of p- and n-type silicon of very lightly doped silicon ($< 10^{14} \text{ cm}^{-3}$) at temperatures as low as 5 K [216].

2.2.3 Nonlinearity

Piezo resistive sensors are linear for small mechanical loads. However, several sources of nonlinearity become significant as the load increases: piezo resistive nonlinearity, circuit nonlinearity, and structural nonlinearity. These nonlinear effects have been characterized and can be accounted for when designing precision sensors. Circuit and structural nonlinearity depend greatly on application specifics, but nonlinearity in the piezo resistance coefficients is a fundamental design issue.

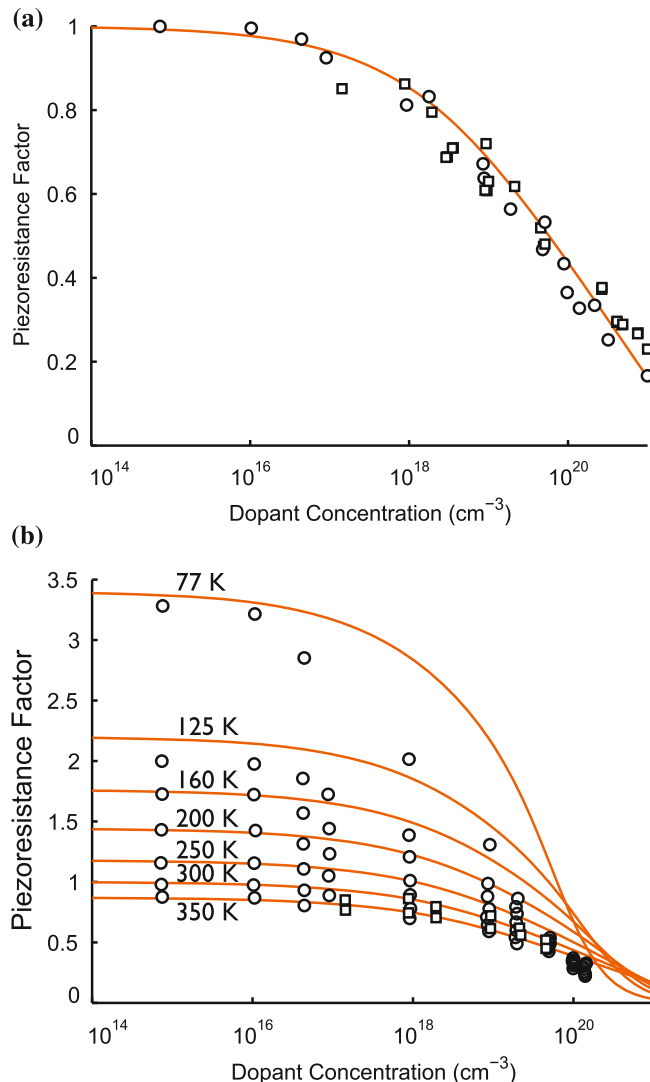


Fig. 2.11 **a** Comparison between Richter's theoretical model and experimental data at 300 K. The fit is excellent over the entire range of dopant concentrations. **b** Richter's model compared with experimental data from 77 to 350 K (77, 125, 160, 200, 250, 300 and 350 K). Data from Tufte and Stelzer is for diffusion doped n-type silicon and is plotted as *circles* [212], while data from Richter et al. is for uniformly doped p-type silicon and is plotted as *squares* [206]. The model overpredicts the piezoresistance factor for dopant concentrations greater than 10^{16} cm^{-3} and temperatures below 200 K (Source Reprinted with permission from [2])

The change in resistance with longitudinal stress can be expanded from a linear model to a third order polynomial of the form

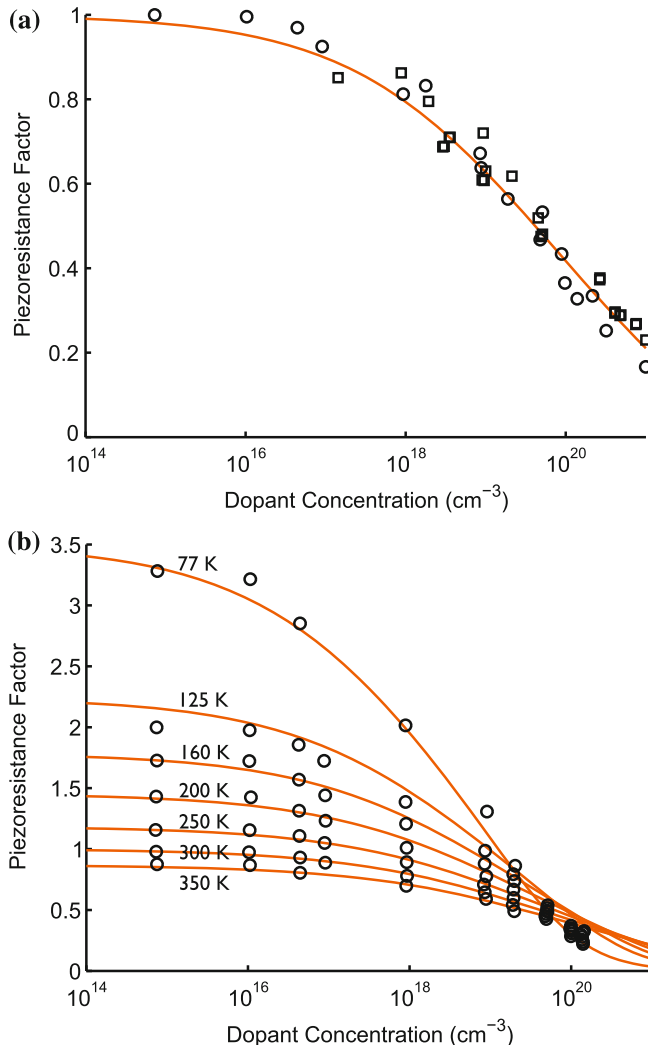


Fig. 2.12 Comparison between the modified Richter model and experimental data at **a** 300 K and **b** 77–350 K. The model predicts the piezo resistance factor relatively accurately over the entire temperature and concentration range, while continuing to accurately predict the performance at 300 K (Source Reprinted with permission from [2])

$$\frac{\Delta R}{R} = \pi_1 \sigma_1 + \pi_2 \sigma_1^2 + \pi_3 \sigma_1^3 \quad (2.28)$$

where π_1 , π_2 and π_3 are the first-, second- and third-order coefficients.

Matsuda et al. [218, 219] calculated and measured the piezo resistive coefficients and third-order effects for both p-type and n-type silicon for the three major crystallographic orientations with strain up to 0.1 %. Higher strain levels were difficult

to measure at the time due to surface defects in the silicon. Measuring higher strain values is necessary to accurately quantify the second- and third-order coefficients.

Addressing this problem, Chen and MacDonald [217] co-fabricated a microactuator and a 150 μm long, 150 nm diameter single-crystal silicon fiber, allowing larger strains to be measured. With the increased range of strain, the second and third order fit for piezoresistive coefficients were quantified more accurately. The fiber was $<110>$ oriented and doped to $2 \times 10^{20} \text{ cm}^{-3}$ with phosphorus. Their best-fit coefficients were $\pi_1 = 1.86 \pm 0.01 \times 10^{-10} \text{ Pa}^{-1}$, $\pi_2 = 0.12 \pm 0.01 \times 10^{-19} \text{ Pa}^{-2}$ and $\pi_3 = 0.100 \pm 0.003 \times 10^{-28} \text{ Pa}^{-3}$.

Similarly, Suthram et al. measured the mobility enhancement in $<110>$ oriented nMOS channels doped to $1 \times 10^{18} \text{ cm}^{-3}$ up to 1.5 GPa of tensile stress [198]. They used a four-point bending system to apply large strains to their samples, and corrected for metal interconnect resistance changes in calculating the silicon mobility enhancement.

The relative resistance changes ($\Delta R/R$) measured by Chen and Suthram are plotted in Fig. 2.13a. Suthram et al measured substantially larger resistance changes due to the lower doping of their samples. As noted earlier, $<110>$ oriented n-type silicon does not maximize the piezoresistive coefficients (Table 2.2).

The first-order coefficient (π_1) varies substantially with dopant concentration and temperature, so we can normalize the expansion to obtain

$$\frac{\Delta R}{R} \frac{1}{\pi_1} = \sigma_1 + \pi'_2 \sigma_1^2 + \pi'_3 \sigma_1^3 \quad (2.29)$$

where $\pi'_2 = \pi_2/\pi_1$ and $\pi'_3 = \pi_3/\pi_1$. The relative second- and third-order coefficients can be used to approximate the magnitude of nonlinearity regardless of variations in dopant concentration and temperature. Using Chen and McDonald's best-fit parameters, $\pi'_2 = 6.45 \times 10^{-11} \text{ Pa}^{-1}$ and $\pi'_3 = 5.38 \times 10^{-20} \text{ Pa}^{-2}$.

The normalized resistance changes ($\Delta R/R/\pi_1$) measured by Chen and Suthram are presented in Fig. 2.13b. No substantial deviation from linearity was observed by Suthram et al. for strains up to 0.8 % (1.35 GPa). Substantially greater deviation was observed by Chen and McDonald, and a 24 % decrease in the longitudinal piezoresistive coefficient was observed at 1 % strain. Possible explanations for the results include increased piezoresistive or mechanical nonlinearity at high concentration.

2.2.4 Theoretical Models

The discovery of such large piezoresistive effects demanded a theory of the underlying physics. This section discusses the prevailing theories at the time of Smith's measurements as well as more recent advances.

The theories of semiconductor piezoresistance are grounded in one-dimensional descriptions of electron and hole transport in crystalline structures under strain, with some extensions to three dimensions, crystal defects, electric potentials and temperature effects. The various models require some understanding of bandgap

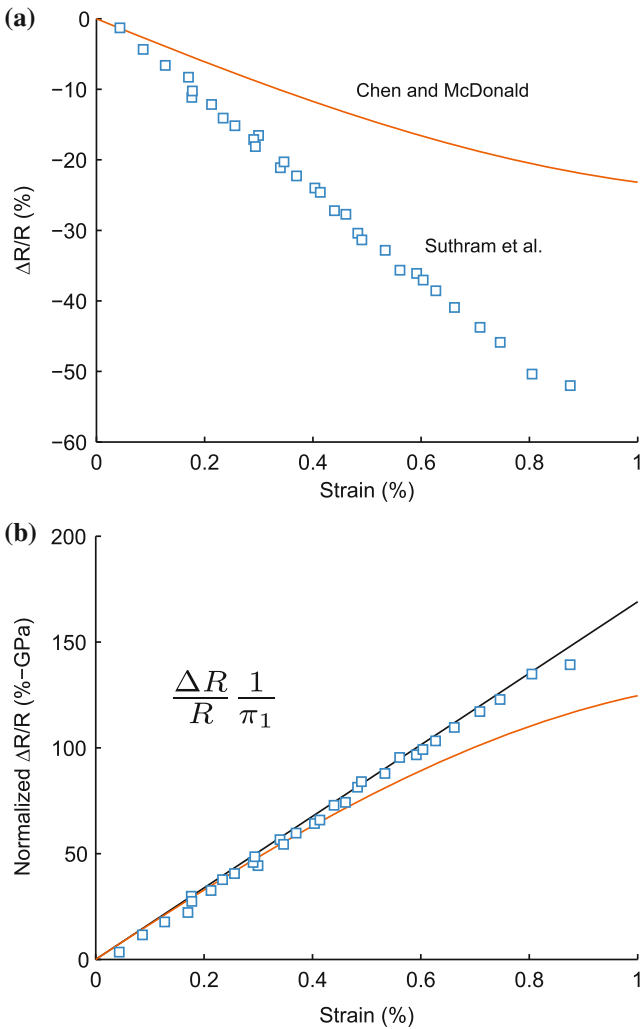


Fig. 2.13 Piezoconductive nonlinearity. **a** Relative resistance changes for n-type (phosphorus), $<110>$ oriented silicon as a function of strain. The samples were doped to 1×10^{18} and $2 \times 10^{20} \text{ cm}^{-3}$ by Suthram and Chen, respectively [198, 217]. **b** By normalizing the resistance change to the first-order piezoconductive coefficient (π_1), we can account for the substantial difference in dopant concentration and illustrate the deviation from linearity, which increases with dopant concentration (Source Reprinted with permission from [2])

energy models, wave mechanics, and quantum effects; the interested reader is referred to [5, 193, 220, 221].

At the time of Smith's piezoconductive measurements, existing theories were based on shifts in bandgap energies. The band structure of diamond was first calculated by Kimball in 1935 [222], and that of silicon by Mullaney in 1944 [223].

In 1950, Bardeen and Shockley presented a model for mobility changes in semiconductors subjected to deformation potentials and compared both predicted and measured conductivity changes in the bandgap with dilation [37]. This work served as the basis for later analyses, such as that of Herring [224, 225] and Long [226].

The mobilities and effective masses of electrons and holes are significantly different from one another and fluctuate under strain. Piezoresistors with n- and p-type doping exhibit opposite trends in resistivity change with strain and different direction-dependent resistivity change magnitudes under stress (Tables 2.1 and 2.2). The magnitudes and signs of the piezoresistive coefficients depend on a number of factors including dopant concentration, temperature, crystallographic direction, and the relative directions of the voltage, current and stress to one another and the crystallographic axes.

The relationship between carrier characteristics and strain has been investigated both experimentally [8, 40, 202] and analytically [37, 53, 197, 225, 227, 228]. Focusing on n-type silicon, these early studies utilized either effective mass or energy band calculations with wave propagation in one direction at a time. The change in mobility (and thus, conductivity) with lattice strain is attributed to band warping or bending and the non-uniform density of states.

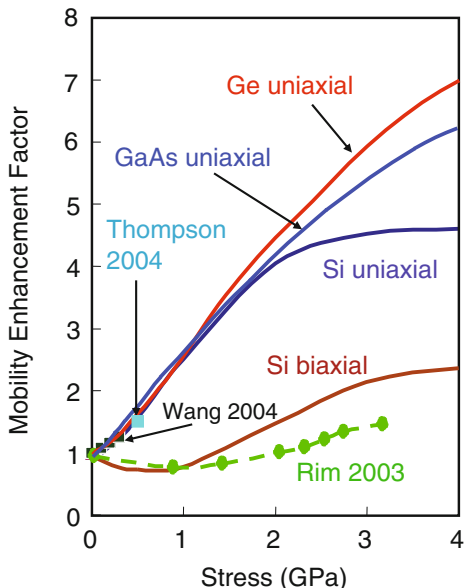
The implications of the large mobility and resistance changes were not realized prior to Smith's discovery [229, 230]. Following Bardeen and Shockley's models for mobility changes with deformation potentials, more refined models of transport and energy band structure based on new experimental work became available. In 1955, Herring proposed his many-valley model, which adequately explained piezoresistance for n-type silicon and germanium [37, 53, 225, 227, 228, 231–234].

In unstrained n-type silicon, the lowest conduction band energies (valleys) or highest mobility orientations are aligned with the $\langle 100 \rangle$ directions. The conduction electrons are thus imagined to be lying in six equal groups aligned with the three $\langle 100 \rangle$ directions. For any valley, the mobility is the lowest when parallel to the valley direction, and the highest when perpendicular to the valley. For example, an electron in the z valley has higher mobility in the x and y directions than in the z direction. The effective mobility is the average from the three valleys [234]. Net electron conductivity is the sum of the conductivity components along the three valley orientations and is independent of direction in the unstrained crystal.

Uniaxial elongation increases the band energy of the valley parallel to the strain and transfers electrons to perpendicular valleys, where they have higher mobility in the strain direction. Tension shifts the electron distribution amongst the valleys, increasing the conductivity in the direction of the tension (longitudinal effect) and reducing the conductivity in the directions perpendicular to the tension (transverse effect). Compression has the opposite effect. The many-valley model accurately models n-type silicon, and recent extensions improve the accuracy at high transverse electric fields and low temperature [235].

The piezoresistance theory for n-type semiconductors continued to be refined from 1954 onward, but until recently piezoresistance in p-type silicon was not fully understood [239, 240]. However, recent computational advances have enabled an improved understanding of p-type piezoresistance [221, 241–243]. This is important

Fig. 2.14 Hole mobility enhancement in semiconductors as a function of stress. Sun et al. compared their experimental results with those from several other research groups [236–238] and noted hole mobility enhancements up to 2 GPa in Si and up to 4 GPa in Ge and GaAs. (*Source* Reprinted with permission from [221]. ©2007 American Institute of Physics)



because most research and commercial piezoresistive devices are p-type and models had been largely based on empirical results. Theoretical studies based on the strain Hamiltonian [244–246], deformation potentials in strained silicon, and cyclotron resonance results have revealed several factors that affect hole mobilities in semiconductors, such as band warping, splitting, and effective mass changes [247–251].

Historically, piezoresistive technology drew from mainstream IC research and continues to do so. Now, with the strong interest in strain engineering to increase carrier mobility in ICs, the situation has reversed and mainstream semiconductor technology is drawing on findings of piezoresistive research. Strain engineered materials, such as silicon-germanium ($\text{Si}_{1-x}\text{Ge}_x$), can increase the channel mobility in metal-oxide-semiconductor field effect transistor (MOSFET) devices [198, 221, 252, 253]. As described earlier, Suthram et al. [198] applied large uniaxial stress to nMOS transistors and showed that piezoresistive coefficients were constant while the electron mobility enhancement increased linearly for stresses up to 1.5 GPa. Figure 2.14 shows plotted hole mobility enhancement factor for several semiconductors as a function of stress.

2.3 Signal Conditioning

The electrical resistance of a piezoresistor can be monitored using a variety of techniques. The most direct method is to force a known current through the piezoresistor (R_{pr}) and measure the voltage drop. This is typically accomplished using a

four-wire measurement (Fig. 2.15a), where one pair of the wires is connected to a current source and the other pair is connected to a voltmeter. As long as the input impedance of the voltmeter is much larger than the piezoresistor resistance, negligible current will flow in the sensing wires and their resistance will not affect the measurement.

The resistance of the piezoresistor depends upon the temperature and stress according to

$$R_{pr} = R_0(1 + \alpha \Delta T + \pi_l \Delta \sigma_l + \pi_t \Delta \sigma_t) \quad (2.30)$$

where R_0 is the resistance for a reference temperature and stress, α is the temperature coefficient of resistance (TCR), π_l and π_t are the longitudinal and transverse piezoresistive coefficients of the piezoresistor, and ΔT , $\Delta \sigma_l$ and $\Delta \sigma_t$ are the changes in temperature, longitudinal stress and transverse stress from their reference values.

The initial output voltage of the circuit is $V_{out} = I R_0$, while the output change can be calculated from $\Delta V_{out} = I R_{pr} - I R_0 = I R_0(1 + \alpha \Delta T + \pi_l \Delta \sigma_l + \pi_t \Delta \sigma_t)$. Assuming that the piezoresistor is uniaxially loaded along its longitudinal axis ($\sigma_t = 0$) then the relative change in output voltage is

$$\frac{\Delta V_{out}}{V_{out}} = 1 + \alpha \Delta T + \pi_l \Delta \sigma_l. \quad (2.31)$$

The relative change in output voltage due to temperature and stress changes can be calculated by taking the partial derivatives of (2.31), yielding

$$\frac{\partial}{\partial T} \left(\frac{\Delta V_{out}}{V_{out}} \right) = \alpha \quad (2.32)$$

$$\frac{\partial}{\partial \sigma_l} \left(\frac{\Delta V_{out}}{V_{out}} \right) = \pi_l. \quad (2.33)$$

Depending on the magnitude of temperature fluctuations, the temperature induced change in output may be substantially larger than that due to mechanical loading.

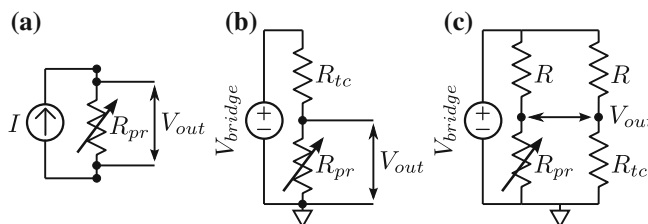


Fig. 2.15 A resistance change can be transduced into a voltage change using a **a** four-wire resistance measurement, **b** voltage divider or **c** Wheatstone bridge. The Wheatstone bridge allows circuit output nulling and temperature compensation (Source Reprinted with permission from [2])

Temperature compensation can be improved by modifying the circuit layout. The most common temperature compensation technique is to use two identical piezoresistors in a configuration where the common-mode resistance change is rejected. For example, the piezoresistor that experiences mechanical loading (R_{pr}) can be placed in a voltage divider with an identical, temperature compensation resistor that does not experience any loading (R_{tc}) as shown in Fig. 2.15b.

The output from the voltage divider is $V_{\text{out}} = V_{\text{bridge}} R_{\text{pr}} / (R_{\text{pr}} + R_{\text{tc}})$, and assuming that R_{pr} and R_{tc} are perfectly matched the initial output will be $V_{\text{bridge}}/2$. The relative change in output voltage, assuming uniaxial longitudinal loading once more, is

$$\frac{\Delta V_{\text{out}}}{V_{\text{out}}} = \frac{1 + \alpha \Delta T + \pi_1 \Delta \sigma_1}{1 + \alpha \Delta T + \frac{1}{2} \pi_1 \Delta \sigma_1}. \quad (2.34)$$

Taking partial derivatives of (2.34) with respect to T and σ_1 , we obtain

$$\frac{\partial}{\partial T} \left(\frac{\Delta V_{\text{out}}}{V_{\text{out}}} \right) = \frac{\alpha(1 + \alpha \Delta T + \frac{1}{2} \pi_1 \Delta \sigma_1) - \alpha(1 + \alpha \Delta T + \pi_1 \Delta \sigma_1)}{(1 + \alpha \Delta T + \frac{1}{2} \pi_1 \Delta \sigma_1)^2} \quad (2.35)$$

$$\frac{\partial}{\partial \sigma_1} \left(\frac{\Delta V_{\text{out}}}{V_{\text{out}}} \right) = \frac{\pi_1(1 + \alpha \Delta T + \frac{1}{2} \pi_1 \Delta \sigma_1) - \frac{1}{2} \pi_1(1 + \alpha \Delta T + \pi_1 \Delta \sigma_1)}{(1 + \alpha \Delta T + \frac{1}{2} \pi_1 \Delta \sigma_1)^2}. \quad (2.36)$$

For small changes in temperature and stress ($\alpha \Delta T \ll 1$ and $\pi_1 \Delta \sigma_1 \ll 1$) we can simplify the results to obtain

$$\frac{\partial}{\partial T} \left(\frac{\Delta V_{\text{out}}}{V_{\text{out}}} \right) = 0 \quad (2.37)$$

$$\frac{\partial}{\partial \sigma_1} \left(\frac{\Delta V_{\text{out}}}{V_{\text{out}}} \right) = \frac{1}{2} \pi_1. \quad (2.38)$$

The voltage divider circuit eliminates first-order output voltage temperature changes, although the sensitivity is a factor of two smaller. The fact that $\pi_1 \approx -\pi_t$ for p-type silicon piezoresistors can be utilized by placing both piezoresistors on the mechanically loaded element, one oriented in the longitudinal direction and the other in the transverse direction, to restore the original stress sensitivity of the sensor.

However, in both the 4-wire and voltage divider circuits the initial output offset is usually much larger than the stress-induced voltage changes. If data acquisition circuits had infinite resolution this would not pose a problem, but it is desirable to null the initial output voltage in most practical applications.

The most common measurement circuit, which achieves temperature compensation and allows nulling of the initial output offset is the Wheatstone bridge (Fig. 2.15c). If only one resistor in the bridge is mechanically loaded (quarter-active configuration) then the stress sensitivity of the sensor is reduced by a factor of four from the 4-wire configuration (2.33). As in the voltage divider case, the sensitivity can be increased by using a half- or full-bridge configuration with either two or four

piezoresistors placed on the mechanically loaded element. In the half-bridge configuration the temperature and stress sensitivities are identical to (2.37) and (2.38). We emphasize that voltage divider and Wheatstone bridge circuits are inherently nonlinear, with the magnitude depending on how many resistors in the circuit change resistance with strain, and both circuit and piezoresistive nonlinearity may need to be compensated for precision applications [254].

The Wheatstone bridge can be biased with either a voltage or current source, and feedback resistors can be added to the bridge for improved temperature compensation [255]. Additionally, a pair of differential amplifiers can be used instead of a Wheatstone bridge [256] at the cost of additional complexity and increased noise depending on the particular design of the piezoresistors and differential amplifiers.

Pfann and Thurston [53] recognized the benefits of using transverse and shear piezoresistance effects in conjunction with longitudinal piezoresistance for devices. Many of their geometries employed a full Wheatstone bridge with two longitudinal and two transverse piezoresistors to increase sensitivity and compensate for resistance changes due to temperature. Notably, they proposed integrating the piezoresistors with the force collecting structure and discussed the advantages and disadvantages of a number of geometries for various types of measurements. They anticipated most of the geometries widely employed today.

2.3.1 Process Variation and Temperature Compensation

In practice, fabrication process variations give rise to mismatch in R_0 , α and π_1 between nominally identical silicon resistors so perfect temperature compensation is never achieved. Mismatch can be minimized by placing all of the resistors as close as possible to each other. Additionally, the output from the signal conditioning circuit can be calibrated and compensated to achieve high accuracy. Signal conditioning electronics typically perform amplification, filtering, additional temperature compensation and nonlinearity correction, and can be monolithically integrated with the piezoresistive sensors or fabricated separately.

Modern electronics can ultimately correct all repeatable errors. If a piezoresistive sensor is heated and then cooled to the initial temperature, then the output should be the same for the same input. However, small differences are usually observed between temperature cycles. This thermal non-repeatability is one of the fundamental limits of sensor accuracy, not correctable with signal conditioning circuits.

Prior to 1980 most of the temperature compensation circuits for piezoresistive sensors employed trim resistors with or without low noise bipolar junction transistor (BJT) based amplifiers. Laser-trimmed resistors were used to adjust the offset, span, nonlinearity and other errors of piezoresistive sensors.

CMOS circuitry became the dominant source of signal conditioning after 1990. The need for even smaller, more accurate, and cheaper sensors was an impetus for the transition to CMOS. Analog technologies do not offer the functionality of a digital technology measured in terms of cost per power per functionality. The push

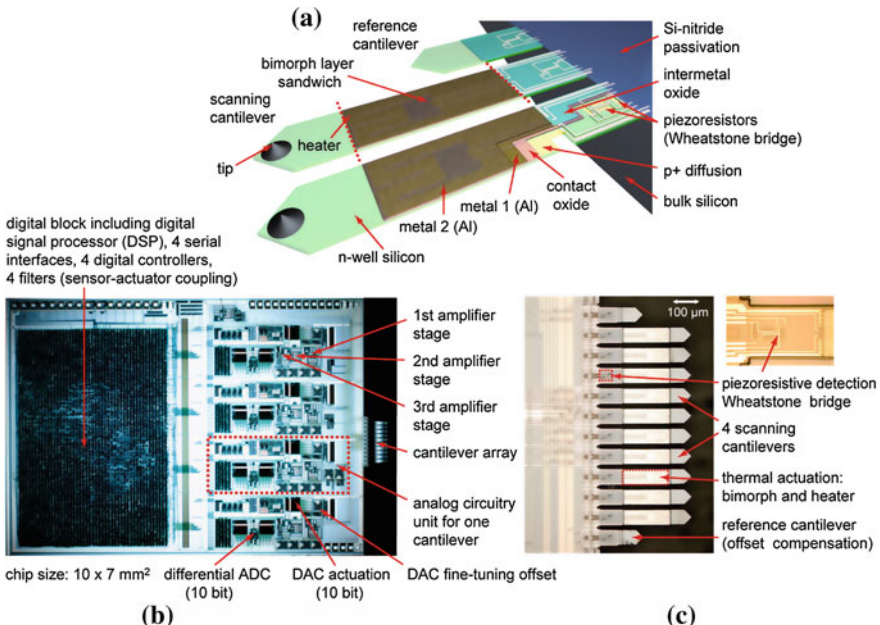


Fig. 2.16 **a** CMOS integrated piezoresistive cantilever array (two scanning cantilevers and one reference cantilever). **b** Micrograph of the overall sensor CMOS signal conditioning circuit. **c** Array of 12 cantilevers (the inner ten can be used for scanning while the outer two serve as a reference). The dimensions of the scanning cantilevers are $500 \times 85 \mu\text{m}$ (*Source* Reprinted with permission from [260]. ©2004 National Academy of Sciences, USA)

toward CMOS evolved with the availability of non-volatile memory (NVM). The laser-trimmed resistors were then replaced with digital-to-analog converters (DAC) and memory. By use of double correlated sampling, offset and low frequency noise of the CMOS circuit are sampled and stored on a capacitor and in the next cycle they are subtracted from the original signal. Hence rendering the CMOS amplifier almost ideal in the low frequency region relative to the sampling frequency.

In CMOS, the need for digital output is easily addressed by integrating the analog-to-digital converter (ADC) with the sensor. A majority of integrated designs incorporate sigma-delta converters (Fig. 2.16) as the primary ADC architecture due to its inherent robustness [257, 258]. Through the combination of CMOS integration and NVM, the need for laser trimming as a means of sensor compensation was eliminated and the power of digital technology was used to compensate and calibrate the piezoresistive sensors. This technology enabled unprecedented sensor accuracy at very low cost [259].

There are two main architectures for piezoresistor temperature compensation: fully digital compensation and digitally controlled analog compensation [261]. The digital signal path architecture uses an ADC to digitize the Wheatstone bridge signal and a temperature sensor signal, then uses a predefined model to perform

signal compensation. If an analog output is needed then the compensated digital data are fed to a DAC.

This architecture is the most flexible but has some inherent problems that limit its use in control loops. One of the main drawbacks is the delay time from the input to output. The ADC, the microprocessor, and the DAC all need processing time, this dead time may not be tolerated in feedback control.

In contrast, the digitally controlled analog path architecture takes advantage of the fact that temperature is a slow signal so that latency is not generally a problem. The digitized temperature signal is mathematically processed in the slow digital path to adjust parameters in the primary purely analog signal path, such as the gain and offset of wide-band amplifiers.

Ishihara et al. developed the first CMOS integrated silicon diaphragm pressure sensors in 1987 [262]. Since then, CMOS circuitry has been integrated with several piezoresistive MEMS devices, such as AFM [101, 105, 108, 260, 263–266] and force or stress sensors [48, 183, 184, 267–272]. Baltes et al. reviewed advances in the CMOS-based MEMS until 2002, including microsensors and packaging, and discussed some key challenges and applications for the future [273, 274].

Generic signal conditioning circuitry consists of an excitation circuit, a bridge circuit, an amplifier, and a filter [6]. These components can all potentially contribute to the system noise spectrum (Fig. 2.17). The noise contribution from amplifiers and

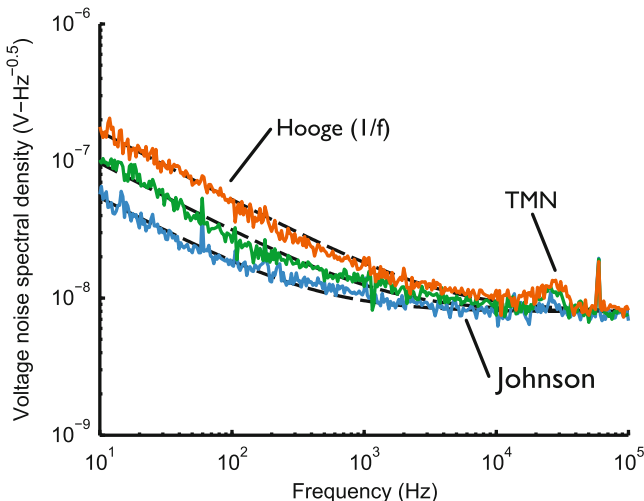


Fig. 2.17 Example voltage noise spectra of a piezoresistive cantilever for bridge bias voltages of 1, 1.5 and 2 V. The readout circuit consists of a Wheatstone bridge and two stages of amplification, yielding a -3 dB bandwidth of 800 kHz. The noise spectra are dominated by the Johnson noise and Hooge (1/f) noise of the piezoresistive cantilever. The cantilever force noise is low enough to enable self-detection of its thermomechanical response in air ($f_0 = 30$ kHz and $Q = 3.6$). The sharp peak at 60 kHz is from external electromagnetic interference (Source Reprinted with permission from [2])

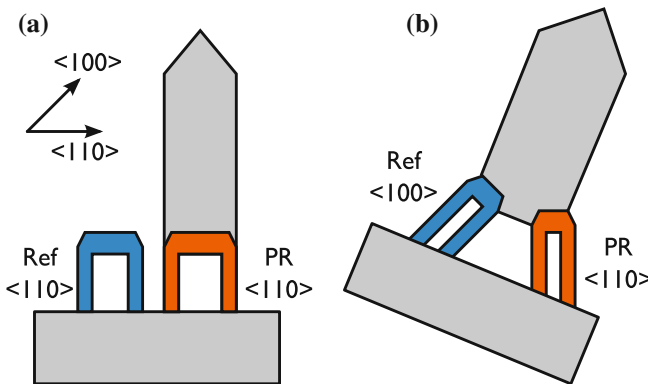


Fig. 2.18 Temperature compensation in piezoresistive cantilevers. **a** Conventionally, two separate piezoresistive cantilevers are included in a Wheatstone bridge to compensate for changes in the ambient temperature and self-heating. However, the piezoresistors are not thermally coupled, leading to poor compensation of thermal gradients. **b** The thermal coupling between the two piezoresistors can be improved substantially by combining them into a single mechanical structure. Both piezoresistors have the same temperature sensitivity, but the $<110>$ oriented piezoresistor has 12-times higher stress sensitivity than its $<100>$ counterpart (Source Redrawn with permission from [275]. ©2007 American Institute of Physics)

filters can be made insignificant with proper piezoresistor design and component selection. Amplifier voltage and current noise spectra are particularly important to consider during design and will be discussed in Sect. 3.1.4.

When there is sufficient room on the sensor (such as in pressure sensors and accelerometers which benefit from a large force collection membrane or proof mass), a full-bridge configuration is typically used with four active piezoresistors. This approach provides the highest possible sensitivity and first-order temperature compensation. However, other piezoresistive sensors (such as force sensing cantilevers) should typically be made as small as possible, making it challenging to optimize performance while placing all four piezoresistors on the cantilever. If only one piezoresistor can fit on the cantilever, an off-cantilever temperature compensation is typically used in a quarter-active Wheatstone bridge [2, 97].

More recently, Chui et al. [275] fabricated a p-type cantilever with two separate piezoresistors serving as the legs (Fig. 2.18). One of the legs is oriented in the $<100>$ direction and the other is oriented in the $<110>$ direction. Both piezoresistors have the same temperature sensitivity, but the $<110>$ oriented piezoresistor has 12-times higher stress sensitivity than its $<100>$ counterpart (Table 2.1). This approach enables a half Wheatstone bridge to be formed out of a single cantilever beam structure so that the output signal is sensitive to mechanical stress but relatively insensitive to temperature. The improved matching and thermal contact between the two resistors in the bridge improved the thermal disturbance rejection of the cantilever by an order of magnitude compared with the conventional cantilever beam approach.

2.3.2 Heterodyne Biasing

In most measurement systems the piezoresistor noise is larger than the amplifier noise at all frequencies (Fig. 2.19a). However, for long-term measurement applications (e.g. chemical sensing) it is desirable to use a relatively large and highly doped piezoresistor that has a lower 1/f corner frequency than the amplifier [156]. If the Wheatstone bridge is DC biased then the noise of the system at low frequencies will be limited by the amplifier rather than the piezoresistive sensor (Fig. 2.19b).

One solution to this problem is to use a modulation-demodulation circuit in which the Wheatstone bridge is sinusoidally biased at a frequency well above the 1/f corner frequency of the amplifier (e.g. 1 kHz). This shifts the signal amplification to a frequency where the amplifier noise is set by Johnson rather than 1/f noise (Fig. 2.19c). After amplification the signal is bandpass-filtered, demodulated and lowpass filtered before data acquisition (Fig. 2.19d). The amplitude of the AC sensor signal after amplification but before demodulation is proportional to the piezoresistor resistance change.

With the modulation-demodulation circuit the noise floor of the system is limited by the uncorrelated sum of the piezoresistor noise (both Johnson and 1/f) and the amplifier noise (only Johnson). In addition to eliminating amplifier noise, the modulation-demodulation approach can eliminate any other noise sources present within a limited range of the frequency spectrum.

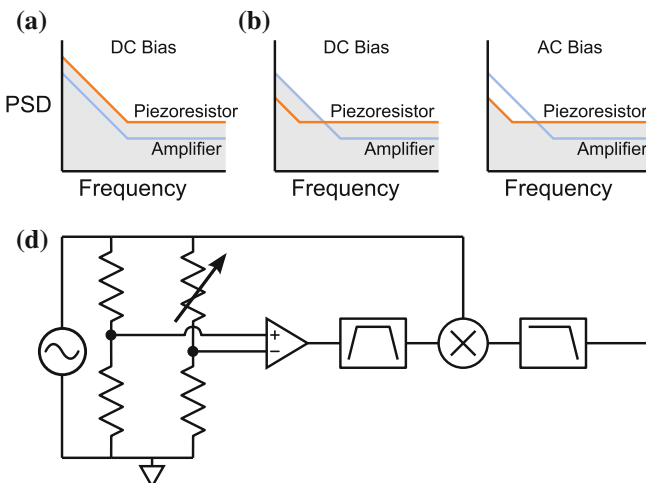


Fig. 2.19 Signal conditioning for low 1/f noise piezoresistors. **a** In most applications the piezoresistor noise is greater than the amplifier noise at all frequencies and defines the noise floor of the system (shaded). **b** If the piezoresistor 1/f noise is decreased below that of the amplifier then the noise floor is limited by the amplifier at low frequencies. **c** The amplifier 1/f noise can be bypassed by modulating the Wheatstone bridge bias at a higher frequency before demodulating the signal. **d** The modulation-demodulation circuit consists of an AC bias, Wheatstone bridge, bandpass filter, demodulator and lowpass filter

2.4 Summary

This chapter established the fundamental concepts and models that underly every piezoresistive device. We began by introducing the concept of using the piezoresistive effect to transduce mechanical stress into a resistivity change, as described by

$$\frac{\partial \rho}{\rho} = \pi_l \sigma_l + \pi_t \sigma_t. \quad (2.11)$$

The longitudinal (π_l) and transverse (π_t) piezoresistive coefficients vary with crystal direction (Fig. 2.5) and are a simplified representation of the piezoresistive tensor. The tensor is required to completely describe the piezoresistive effect in any crystal orientation of single crystal silicon. The piezoresistive tensor for silicon is described by just three piezoresistive coefficients due to symmetry, π_{11} , π_{12} and π_{44} , and takes the form

$$\pi = \begin{pmatrix} \pi_{11} & \pi_{12} & \pi_{12} & 0 & 0 & 0 \\ \pi_{12} & \pi_{11} & \pi_{12} & 0 & 0 & 0 \\ \pi_{12} & \pi_{12} & \pi_{11} & 0 & 0 & 0 \\ 0 & 0 & 0 & \pi_{44} & 0 & 0 \\ 0 & 0 & 0 & 0 & \pi_{44} & 0 \\ 0 & 0 & 0 & 0 & 0 & \pi_{44} \end{pmatrix}. \quad (2.10)$$

Piezoresistive coefficients for lightly doped single crystal silicon at room temperature are summarized in Tables 2.1 and 2.2.

The magnitude of the piezoresistive effect varies with dopant concentration and temperature in addition to crystallographic orientation. The piezoresistance factor (P) is used to model variations in piezoresistive coefficients (i.e. π_{11} , π_{12} , π_{44} , π_l or π_t) with dopant concentration and temperature according to

$$\pi(N, T) = P(N, T)\pi^{\text{ref}}. \quad (2.19)$$

Our preferred model for the piezoresistance factor was developed by Richter and takes the form

$$P = \frac{T_n^{-\theta}}{1 + \left(\frac{N}{N_b}\right)^\alpha T_n^{-\beta} + \left(\frac{N}{N_c}\right)^\gamma T_n^{-\eta}}. \quad (2.27)$$

Parameters for the Richter model and a modified version based upon a larger experimental data set are summarized in Table 2.3.

The piezoresistive effect is sufficiently linear for most applications up to strains on the order of 1% (Sect. 2.2.3). Nonlinearity in a typical piezoresistive sensor is dominated by other electrical or mechanical sources of nonlinearity.

Section 2.3 introduced fundamental signal conditioning and temperature compensation concepts. The most common circuit topology for piezoresistive sensors is the Wheatstone bridge, which can provide excellent rejection of common-mode signals such as temperature by including multiple matched piezoresistors in the circuit.

Chapter 3

Sensitivity, Noise and Resolution

In this chapter we will develop models for calculating the noise, sensitivity and resolution of arbitrary piezoresistive sensors. Sensor resolution is defined as the smallest signal that can be reliably detected. The minimum detectable signal without averaging multiple trials is commonly equated to the root mean square (RMS) noise of the measurand according to

$$\text{Resolution} = \frac{V_{\text{noise}}}{S} \quad (3.1)$$

where V_{noise} is the RMS voltage noise and S is the voltage-referred sensitivity with respect to the measurand (e.g. force, displacement or pressure) of the sensor.

The crux of piezoresistor design is that the noise and sensitivity are simultaneously affected by changes in piezoresistor design parameters. Although sensitivity and noise are presented separately in this chapter, they will be treated holistically in Chap. 6.

3.1 Noise

Noise is any unwanted disturbance that interferes with the signal being measured. A variety of noise sources lead to random fluctuations in the output of a piezoresistive sensor. The dominant noise sources in piezoresistive sensors are electrical, although there are exceptions. For example, temperature fluctuations typically limit resolution for measurements that are hours to days in length, while Brownian motion of the

Portions of this chapter were adapted from an earlier review of piezoresistance [1]. We would also like to thank A. Alvin Barlian, Nahid Harjee, Joseph R. Mallon Jr., Sung-Jin Park, Woo-Tae Park and Ali J. Rastegar for extensive and productive discussions and their contributions to the concepts presented in this chapter.

atoms in the piezoresistive sensor (thermomechanical noise) provides a fundamental lower limit for optimized nanomechanical sensors.

We will divide piezoresistor noise into intrinsic and extrinsic sources. Intrinsic sources, which depend solely on the design of the piezoresistive sensor and signal conditioning circuitry, are the focus of our design methods because they are readily quantified. Extrinsic sources are associated with the specific measurement environment, such as inductive or capacitive line pickup [6], carrier injection due to high intensity light illumination, and variation in the ambient temperature or humidity [276]. Extrinsic noise sources can vary enormously with the measurement situation so are not included in our piezoresistor performance models.

Noise processes are stochastic, but can be modeled using statistical methods in both the time and frequency domains. The goal of our noise analysis will be to determine amplitude and spectral distributions of the noise sources for a general piezoresistive sensor and signal conditioning circuit. We will discuss a generic noise source in order to introduce these concepts before moving onto piezoresistive sensor and signal conditioning noise sources.

3.1.1 A Brief Introduction to Noise

Consider a random voltage noise source, v_N , that is passed through an ideal bandpass filter with center frequency f_0 and bandwidth Δf . We expect the noise to have a mean value of zero and a standard deviation of σ . If we assume that the noise is normally distributed, then its probability density function (PDF) is

$$p(x) = \frac{1}{\sigma\sqrt{2\pi}} \exp\left(-\frac{x^2}{2\sigma^2}\right) \quad (3.2)$$

where $p(x)$ is the probability of observing $v_N = x$. We assume that the noise source is stationary so that the PDF doesn't change with time. In order to verify the PDF, we measure the noise amplitude a large number of times and compute the mean and mean-square values as

$$\bar{v}_N = \frac{1}{N} \sum_{t=1}^N v_N(t) = 0 \quad (3.3)$$

$$\bar{v}_N^2 = \frac{1}{N} \sum_{t=1}^N v_N^2(t) = \sigma^2. \quad (3.4)$$

We can compare these values with the PDF model by computing the mean and mean-square values as

$$\overline{v_N} = \int_{-\infty}^{\infty} xp(x) dx = 0 \quad (3.5)$$

$$\overline{v_N^2} = \int_{-\infty}^{\infty} x^2 p(x) dx = \sigma^2. \quad (3.6)$$

to find that the PDF model does in fact accurately describe the noise source.

The RMS noise amplitude, equal to the square root of the mean-square value, can then be calculated as σ . In general, any noise source with a Gaussian probability distribution will have an RMS amplitude equal to the probability distribution's standard deviation. The peak-to-peak amplitude of the same signal is usually estimated to be 6σ , because the chance of observing a voltage outside of that range is small (0.3%).

Now suppose that we discovered v_N is actually the sum of two independent noise sources, v_{N1} and v_{N2} each with their own standard deviations, σ_1 and σ_2 . The mean and mean-square values of the total noise can be recalculated in terms of the noise components from

$$\overline{v_N} = \overline{v_{N1}} + \overline{v_{N2}} \quad (3.7)$$

$$\overline{v_N^2} = \overline{v_{N1}^2} + \overline{v_{N2}^2} + 2\overline{v_{N1}v_{N2}}. \quad (3.8)$$

The third term in (3.8) depends on the correlation between the two smaller noise sources. If they are uncorrelated, then the average value of their product is equal to zero and the term drops out. Most noise sources are uncorrelated, for example the thermal noise of two separate resistors. Correlated noise sources can arise when there is coupling between noise sources (e.g. capacitive, inductive or thermal coupling) or when the noise is due to a external source that affects a circuit in multiple locations simultaneously. The dominant noise sources in piezoresistive sensors are uncorrelated.

Noise is often expressed in units of power (which is proportional to V^2), because the total noise power increases linearly with the addition of uncorrelated noise sources. Assuming that v_{N1} and v_{N2} are uncorrelated, the RMS noise is

$$v_N^{\text{RMS}} = \sqrt{\overline{v_{N1}^2} + \overline{v_{N2}^2}}. \quad (3.9)$$

An important concept in adding noise sources is that the RMS noise mainly depends on the largest noise source. For example, if $\overline{v_{N1}} = \overline{v_{N2}} = 10 \text{ nV}$ then both contribute equally to the total noise and $v_N^{\text{RMS}} = 14.1 \text{ nV}$. But if $\overline{v_{N2}}$ decreases by a factor of five, the total noise only decreases slightly (from 14.1 to 10.2 nV) because it is limited by the largest noise source. The fact that piezoresistive sensor noise is the sum of several uncorrelated noise sources (e.g. Johnson and 1/f noise) has broad implications for piezoresistor design. We will discuss this in more detail later, but for now we note that balancing the contribution of each noise source typically leads to optimal sensor resolution.

We have kept the center frequency (f_0) and bandwidth (Δf) of the bandpass filter constant so far. However, both will change depending on the frequency response of the

amplifiers and filters in the signal conditioning circuit. In general, noise is generated by broadband sources over a wide frequency range, and by applying a narrow-band filter we have selected a small frequency range to observe. The mean-square amplitude of our noise source can be normalized to the measurement bandwidth to yield its power spectral density:

$$S_N(f) = \frac{\overline{v_N^2}}{\Delta f} = \frac{\sigma^2}{\Delta f}. \quad (3.10)$$

The power spectral density (PSD) has units of power per unit frequency, such as V^2/Hz or A^2/Hz . The RMS amplitude of any noise source can be calculated from

$$v_N^{\text{RMS}} = \sqrt{\int_{f_{\min}}^{f_{\max}} S_N(f) df} \quad (3.11)$$

for an arbitrary frequency range if $S(f)$ of the noise source is known, where f_{\min} and f_{\max} are the lower and upper measurement frequency limits. Multiple uncorrelated noise sources can be treated by summing their power spectral densities. By integrating the power spectral density over frequency, we are effectively treating the noise at each frequency as an independent noise source and adding their mean-square values.

Assuming that the power spectral density of our example noise source is constant and independent of frequency (3.10), then its integrated RMS noise from f_{\min} to f_{\max} will be

$$v_N^{\text{RMS}} = \sqrt{S_N(f_{\max} - f_{\min})}, \quad (3.12)$$

scaling with the square root of the measurement bandwidth.

The noise source we have discussed in this section is an example of white noise, which has a flat power spectral density, typical of Johnson noise or shot noise. Other noise sources, such as $1/f$ noise, have power spectral densities that vary with frequency. The first step in designing any sensor is determining the measurement bandwidth because the results from piezoresistive sensor design will vary depending on the measurement bandwidth. The measurement bandwidth should always be limited to the frequency range over which the signal of interest is distributed through the use of filters.

We will often discuss noise sources in terms of their voltage or current spectral densities rather than their power spectral densities. Voltage spectral density, V_N , is equivalent to the square root of the power spectral density, and has units of $\text{V}/\sqrt{\text{Hz}}$. The noise performance of integrated circuits is typically quoted in terms of voltage and current spectral densities by manufacturers.

Noise spectra can be measured using either a signal/spectrum analyzer or by taking the Fourier transform of time-domain data (Fig. 3.1). In the time-domain case, special care must be taken in choosing the sampling rate (see Nyquist-Shannon sampling theorem) and inserting antialiasing filters into the signal path. The measurement circuit in Fig. 3.1 includes two silicon resistors in a Wheatstone bridge for temperature

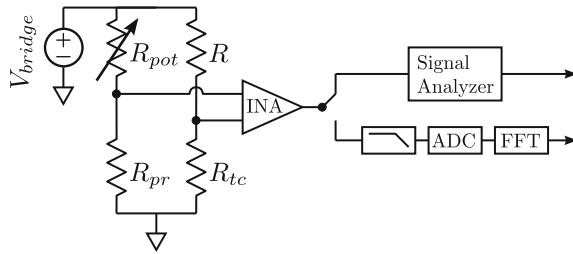


Fig. 3.1 Example noise measurement system. The Wheatstone bridge is balanced using a single potentiometer, the output is amplified using an instrumentation amplifier (INA) and the spectral content of the noise signal is measured using a signal analyzer. Alternatively the signal is passed through an antialiasing filter, sampled with an analog-to-digital converter (ADC) and analyzed using the fast Fourier transform (FFT) method. (*Source* Reprinted with permission from [2])

compensation (R_{pr} and R_{tc}) and one potentiometer (R_{pot}). The potentiometer is used to null the Wheatstone bridge output before it is amplified and measured.

We will now discuss the particular noise sources that affect piezoresistive sensors.

3.1.2 Johnson Noise

Thermal noise, also referred to as Johnson or Johnson-Nyquist noise, is universal to electrical resistors [277]. It was first observed in 1928 by Johnson [278] and theoretically explained later that year by Nyquist [279]. Johnson noise is caused by the thermal agitation of charge carriers within a conductor. Similarly, Brownian motion and thermomechanical noise are caused by the thermal agitation of atoms. Johnson noise is fundamental, exists in all resistors and modern electronic devices, and cannot be eliminated.

The power spectral density of Johnson noise is independent of frequency and can be calculated from

$$S_J = 4k_b T_{pr} R_{pr} \quad (3.13)$$

where k_b (J/K) is Boltzmann's constant, T_{pr} (K) is the average piezoresistor temperature and R_{pr} (Ω) is the electrical resistance of the piezoresistor. We will generally model Johnson noise as a voltage noise source in series with an ideal resistor, although it can equivalently be modeled as a current noise source in parallel with the resistor with a current noise power spectral density of $4k_b T_{pr} / R_{pr}$.

The RMS voltage noise in a given circuit can be calculated by integrating the Johnson noise power spectral density over the measurement bandwidth to obtain

$$V_J = \sqrt{4k_b T_{pr} R_{pr} (f_{max} - f_{min})}. \quad (3.14)$$

Thus, in order to minimize Johnson noise, the resistance, temperature and measurement bandwidth should be minimized. The temperature and measurement bandwidth are typically determined by the sensor application, so reducing the piezoresistor resistance is the main design option for minimizing Johnson noise.

Although (3.13) holds for a single resistor, a Wheatstone bridge contains four resistors. Assuming that the bridge is balanced and all four resistors have resistance R , then the impedance looking out from each amplifier input is $R/2$ and the Johnson noise PSD due to the resistors will be $2k_b T R$ at each amplifier input. However, the noise power of uncorrelated sources adds linearly, so the total Johnson noise of the Wheatstone bridge is $4k_b T_{\text{pr}} R_{\text{pr}}$. In short, the Johnson noise of a balanced Wheatstone bridge is equal to the Johnson noise of one of the resistors in the bridge.

3.1.3 1/f Noise

The power spectral density of 1/f noise, as its name implies, is inversely proportional to frequency. First discovered due to excess low frequency noise in vacuum tubes, 1/f noise is found in a wide variety of systems, from noise in field effect transistors to the resonant frequency of quartz crystal oscillators to annual variations in rainfall and temperature [280]. 1/f noise in semiconductor electronics is not completely understood and remains an active research topic [281 – 286]. Despite many decades of research, the underlying sources of 1/f noise are still debated [287].

The most widely used models for 1/f noise today are attributed to McWhorter and Hooge. These views are currently the leading explanations for the origin of 1/f noise in semiconductors. The McWhorter model attributes the 1/f noise to surface factors [288,289], while the Hooge model implicates bulk defects [290, 291] (Fig. 3.2). 1/f noise can be caused by fluctuations in the number of carriers (McWhorter model) or carrier mobility (Hooge model).

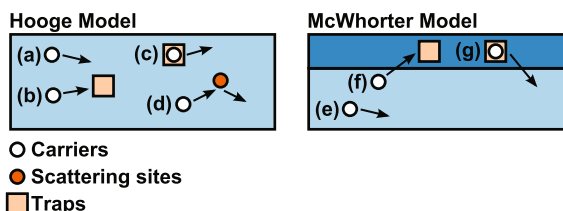


Fig. 3.2 Models for semiconductor 1/f noise. The Hooge model assumes that scattering sites and traps exist in the bulk of the material. Carriers may (a) drift unimpeded in the electric field, (b) enter and (c) exit traps, or (d) scatter. Post-ion implantation annealing reduces the density of scattering sites and traps. In the McWhorter model, traps exist at material interfaces, such as between Si and SiO_2 . (e) Carriers generally drift unimpeded within the bulk of the semiconductor, but may (f) enter and (g) exit trapping sites at the material interface. (Source Reprinted with permission from [2])

One point that all experiments and models agree upon is that 1/f noise in resistors is caused by conductivity fluctuations [286, 291]. Hooge showed that 1/f noise modulates Johnson noise even with no current flowing through a resistor [292]. This experiment demonstrated that 1/f noise is not current-generated, and that rather, current flow is only needed to transduce conductivity fluctuations into voltage noise. Attempts to observe the lower limit of 1/f, below which the spectrum theoretically flattens, have not been successful [291]. Measurements down to 3 μ Hz (or approximately 4 days per cycle) show a noise spectrum that is still 1/f [293].

Hooge's empirical 1/f noise model predicts that the voltage power spectral density of a resistor with uniform current density is

$$S_H = V_{\text{bias}}^2 \frac{\alpha}{N_{\text{eff}} f} \quad (3.15)$$

where f , N_{eff} , and V_{bias} are the frequency, the effective number of carriers in the resistor, and the bias voltage across the resistor, respectively. A non-dimensional fitting parameter, α , is ascribed to the crystal lattice quality and typically ranges from 10^{-3} to 10^{-7} depending on the fabrication process details [127, 128, 156]. Note that the total number of carriers in the resistor is not equal to the effective number of carriers when the current density is not constant throughout the resistor. We will discuss calculating the effective number of carriers shortly.

The RMS 1/f noise in a measurement bandwidth from f_{\min} to f_{\max} , rewritten in terms of V_{bridge} rather than V_{bias} , is equal to

$$V_H = \frac{V_{\text{bridge}}}{2} \sqrt{\frac{\alpha}{N_{\text{eff}}} \ln \frac{f_{\max}}{f_{\min}}} \quad (3.16)$$

Note that (3.16) and (3.15) only apply to a single resistor. Although a Wheatstone bridge could contain just a single silicon piezoresistor, either two or four silicon resistors are typically used for temperature compensation (Chap. 5). The 1/f noise from discrete resistors is uncorrelated, so the integrated noise increases by a factor of $\sqrt{2}$ for every additional (nominally identical) silicon resistor in the bridge.

We emphasize that the integrated 1/f noise power spectral density is constant for every decade of measurement bandwidth, whereas the Johnson noise power spectral density scales linearly with bandwidth. The result is that 1/f noise tends to be limiting factor for low frequency measurements while Johnson noise limits wide bandwidth measurements.

Is 1/f noise in silicon piezoresistors due to surface or bulk defects? Harley and Kenny showed that resistors with different surface to volume ratios have the same 1/f noise characteristics, and that 1/f noise scales with the resistor volume, consistent with Hooge's empirical equation [127]. The Hooge model has been applied to accurately model 1/f noise in silicon piezoresistors for diffused [132, 294], ion implanted [89,295] and epitaxial piezoresistors [84,296]. In summary, 1/f noise in

silicon piezoresistors is predominantly due to bulk defects located near the wafer surface and we will use the Hooge model for all modeling and optimization work.

Hooge defines 1/f noise as only those spectra described by $1/f^n$ where the frequency exponent n ranges from 0.9 to 1.1. Noise with a different power spectral density and other frequency exponents, sometimes referred to as 1/f-like noise, is often confused with 1/f noise and is not predicted by the Hooge equation. According to Hooge, noise with a higher exponent (e.g. 1.5 or 2), indicates noise mechanisms other than mobility fluctuations that should not be considered 1/f noise.

Abnormal 1/f noise characterization can give insights into piezoresistor reliability and failure analyses. For example, Neri [297] found that the 1/f exponent is closer to two in metal traces that exhibit electromigration. Similarly, Vandamme [298] showed that excess 1/f noise in semiconductors can be attributed to small constrictions and current crowding. Constrictions can also lead to a nonlinear sensor response due to localized heating, generating higher order harmonics in the signal output.

Another source of excess low frequency noise is Joule heating. Park showed that piezoresistive cantilevers generate excess low frequency noise when self-heated significantly above the ambient temperature [133]. Unreleased silicon resistors did not exhibit excess low frequency noise for the same Joule heating power due to their much smaller temperature increase. When the temperature of the silicon resistor is significantly above the ambient temperature, air flow modulates the resistor temperature and resistance. Elevated temperature also leads to an increase in sensor noise and a reduction in sensitivity, so is important to consider during design optimization and will be addressed in Chap. 5.

Polysilicon resistors have higher 1/f noise than their single crystal counterparts [299]. At grain boundaries, small constrictions are present, thus reducing the effective number of carriers due to current crowding. The reduction in the number of carriers depends on the polysilicon processing history due to its dependence on grain size.

As noted earlier in (3.15), the 1/f noise depends on the effective number of carriers, not the total number. When the current density varies over the resistor volume, the effective number of carriers will always be less than the total number. Examples include polysilicon and metal-silicon contacts, where current crowding is well known, but also any resistor where the dopant concentration varies throughout the thickness (e.g. ion implanted and diffused resistors). The general expression for the Hooge noise power spectral density is [291, 300]

$$S_H = \frac{\alpha}{I^2 f} \int \frac{J^4 \rho^2}{n} dV \quad (3.17)$$

where I is the total current and J , ρ and n are the spatially varying current density, resistivity and carrier concentration. Current density contributes to the noise power by the fourth power, and local constrictions, sharp changes in current direction, or abrupt changes in dopant concentration can substantially increase the 1/f noise. The integral for arbitrary geometries can be evaluated using finite element analysis.

Any piezoresistor that varies in dopant concentration throughout its depth has some degree of current crowding. This occurs because the carrier mobility varies

with dopant concentration; as dopant concentration increases the mobility decreases and the current carried per dopant atom decreases. The total number of carriers per unit area (N_z^{total}) can be calculated directly from the carrier profile as

$$N_z^{\text{total}} = \int_0^{t_j} n(z) dz. \quad (3.18)$$

The total number of carriers is essentially equal to the effective number of carriers for epitaxial piezoresistors, but the total number of carriers is often erroneously applied to other fabrication methods [301]. The effective number of carriers per unit area (N_z^{eff}) can be calculated from (3.17) following [302] as

$$N_z^{\text{eff}} = \frac{\left(\int_0^{t_j} n \mu dz \right)^2}{\int_0^{t_j} n \mu^2 dz}. \quad (3.19)$$

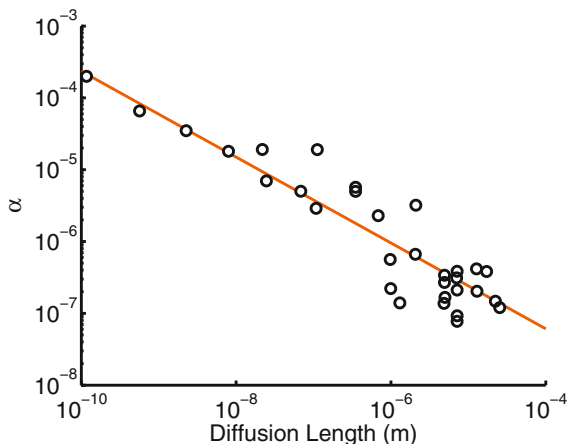
For a typical diffusion dopant profile (e.g. POCl_3 at 800°C for 60 minutes) the effective number of carriers per unit area is 80 % of the total number. Using the total rather than the effective number of carriers would lead to a 20 % overestimate of α during noise analysis. Current crowding should also be considered when laying out devices with doped silicon traces, which will contribute to the overall 1/f noise. Current crowding is not an issue for epitaxial profiles. For the ion implanted profiles we will investigate (Sect. 4.4) the effective number of carriers ranges from 54 to 99 % of the total number and is 90 % on average.

A defining characteristic of Hooge-type 1/f noise is that the voltage spectral density increases linearly with the applied bias and the power spectral density scales with the bias squared. If the noise amplitude scales in another manner, then it is likely that other mechanisms, such as current crowding or temperature fluctuations, are present.

1/f noise can be reduced by either increasing N_{eff} or decreasing α . Vandamme showed that α depends on crystal lattice disorder and that α can be reduced for ion implanted resistors by increasing the time and temperature of the post-implantation anneal [303]. He later showed that the α for a MOSFET channel varies with the gate voltage due to variation in α through the channel depth [304]. The 1/f noise was lower when the channel was operated in depletion mode than in accumulation mode because the current flow was further away from the surface where the ion implantation damage was greatest even after a high temperature anneal.

Thus, the post-ion implantation anneal performs three functions: dopant activation, lattice repair and shifting conduction away from the surface. Several groups have investigated the dependence of α on the diffusion length of the dopant atoms during the anneal, \sqrt{Dt} , and shown that longer diffusion length anneals decrease the 1/f noise of silicon piezoresistive cantilevers [127, 156]. The Hooge noise parameter (α) is plotted in Fig. 3.3 as a function of the dopant diffusion length during the post-ion implantation anneal based upon data from Refs. [83, 127, 156, 303, 305].

Fig. 3.3 The Hooge noise parameter, α , decreases for ion implanted piezoresistors as the diffusion length of dopant atoms during the post-implantation anneal, \sqrt{Dt} , increases. Data were compiled from Refs. [83, 127, 156, 303, 305]. (Source Reprinted with permission from [2])



It is important to note that a surface passivation oxide layer is not necessary to achieve low 1/f noise. Harley measured the noise spectra of resistors with and without passivation oxide layers and observed no difference in 1/f noise [84]. The data suggest that the post-implantation anneal decreases 1/f noise by eliminating defects in the bulk of the resistor and driving dopants further into the bulk, not by passivating the resistor surface. Although surface passivation is not critical to Hooge noise, surface passivation improves long-term stability by reducing susceptibility to moisture and outgassing [306].

The best-fit line plotted in Fig. 3.3 is

$$\alpha = 2.469 \times 10^{-10} (\sqrt{Dt})^{-0.598} \quad (3.20)$$

which is slightly different from the fit presented in 2000 by Harley [301] because it includes subsequent data from Mallon and Yu [156, 128].

The diffusion length in (3.20) is calculated as

$$D = D_0 \exp\left(-\frac{E_a}{k_b T}\right) \quad (3.21)$$

where D_0 and E_a for common silicon dopants are summarized in Table 3.1. The coefficients assume intrinsic, vacancy-dominated diffusion. These assumptions are fairly accurate for sufficiently high anneal temperatures and low dopant concentrations. In reality, prescribing a single diffusion length to an ion implanted (or even a diffused) piezoresistor is a coarse approximation of reality due to lattice damage, dopant clustering, oxidation enhanced diffusion and other effects [307]. However, (3.20) in Fig. 3.3 was calculated using the coefficients in Table 3.20 and can be used to reasonably approximate α over a wide range of fabrication processes.

Table 3.1 Diffusivity coefficients for common silicon dopants assuming intrinsic, vacancy-dominated diffusion

Dopant	D_0 (cm ² /s)	E_a (eV)
As	22.9	4.10
B	0.76	3.46
P	3.85	3.66

Coefficients taken from Ref. [307]

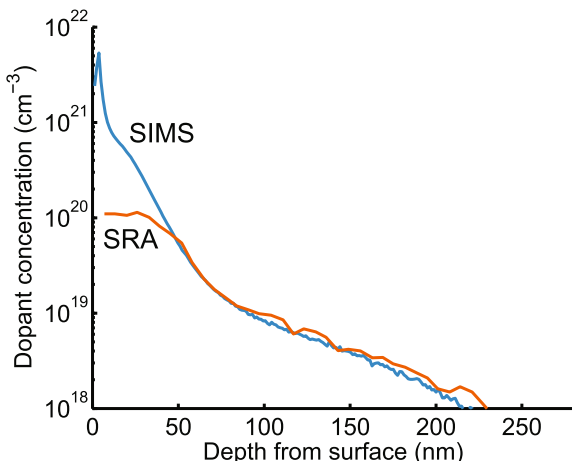
We note several points of caution with regards to the empirical fit. First, there is substantial uncertainty in calculating α due to the difficulty in calculating the effective number of carriers in the piezoresistor. Errors can be introduced either through an inaccurate estimate of the dopant concentration profile, error in calculating the resistor volume, or not accounting for current crowding in the resistor. For example, using simulated dopant profiles rather than a direct measurement of the electrically active dopant concentration profile (via spreading resistance analysis) could account for some error. However, the calculated α values are from multiple research groups spanning several decades, so random errors should presumably average out. There are several possible sources of systematic error in the data as well. In particular, using N_{total} rather than N_{eff} would lead to overestimates of 10–50 % in calculating α depending on the degree of current crowding.

Second, there is probably a lower bound on α . Harley initially predicted a lower bound of 10^{-6} based upon the data available at the time [301]. Jevtic theoretically investigated variation in α with dopant concentration and predicted minimum values of 1×10^{-5} and 3×10^{-5} for n- and p-type single crystal silicon, respectively [308]. However, silicon piezoresistors with significantly lower α values have been demonstrated for both dopant types [2, 83, 156, 303]. Applying (3.20) to diffusion lengths greater than 10^{-5} m without preliminary tests is not advised.

Third, the data fit only applies to ion implanted piezoresistors and all of the data points are for boron doping. This leads to two major assumptions. First, we will assume that the relationship between α and the dopant diffusion length holds for phosphorus and arsenic as well. Due to the lower diffusivities of phosphorus and especially arsenic, this assumption leads to very different optimization results than if we had assumed that α depends on the diffusion length of the silicon atoms. Second, we will assume that $\alpha = 10^{-5}$ for diffused and epitaxial piezoresistors without any subsequent annealing.

Harley measured an α of 2×10^{-5} for his epitaxial piezoresistors [301]. We measured α values ranging from 2×10^{-7} to 5×10^{-5} for diffused phosphorus piezoresistors with a mean value of 1.05×10^{-5} [132]. Neither technique introduces as much lattice damage as ion implantation, but defects are still generated. For example, predeposition introduces electrically inactive dopants, dislocations and precipitates [309, 310]. We have experimentally observed interstitial phosphorus near the surface of POCl_3 doped piezoresistors which is probably a major factor in limiting α (Fig. 3.4) [2, 97]. Similarly, epitaxy can introduce grain boundaries and various lattice defects depending on the growth conditions.

Fig. 3.4 Example dopant concentration profiles from secondary ion mass spectroscopy (SIMS) and spreading resistance analysis (SRA). The piezoresistor was formed via POCl_3 predeposition at 825°C for 30 min. Most of the dopants are present within the first 50 nm from the surface and excess electrically inactive phosphorus is present. (Source Reprinted with permission from [2])



Vandamme's results in Ref. [304] suggest that lattice quality is higher in the bulk of the silicon than near its surface, and that shifting electrical conduction away from the surface may be an important role of the post-implantation anneal. If the sole purpose of the anneal was to reduce implantation-induced crystal lattice damage, then piezoresistors formed from different dopant atoms (e.g. boron vs. arsenic) would exhibit the same value of α for an identical annealing process. If this were true then arsenic piezoresistors would yield much higher performance than boron or phosphorus doped piezoresistors due to its dramatically lower diffusivity.

However, the variation in 1/f noise with MOSFET gate voltage suggests that dopant diffusion length, not the time and temperature of the anneal, is critical in determining the 1/f noise parameter [304]. Without clear experimental data on the subject, we will assume that the dopant diffusion length defines the 1/f noise parameter and that arsenic-doped piezoresistors would need to be annealed much longer in order to achieve the same 1/f noise parameter as boron- and phosphorus-doped piezoresistors. In other words, we recommend employing (3.20) regardless of the dopant species.

In summary, 1/f noise is fundamentally different from Johnson noise. Johnson noise is present regardless of the current density flowing through the resistor and depends only on its electrical resistance. In contrast, 1/f noise is a conductivity noise, and the voltage noise measured across the resistor scales linearly with the current flowing through the resistor. Additionally, 1/f noise depends on the dimensions and processing history of the resistor. Any residual damage from ion implantation or ion bombardment during reactive ion etching will increase the 1/f noise, but will only affect the Johnson noise to the extent that any lattice damage increases the overall electrical resistance.

3.1.4 Amplifier Noise

The Wheatstone bridge output is amplified before being filtered and acquired (Fig. 3.1). Throughout our discussion of piezoresistor design we will assume that the signal is amplified by an instrumentation amplifier, but the noise analysis can be extended to any signal conditioning configuration.

Instrumentation amplifiers typically consist of three operational amplifiers (op-amps). The first two op-amps present a high input impedance and amplify the signal at each amplifier input. This eliminates loading effects on the circuit and improves the rejection of common mode signals. The final op-amp differentially amplifies the buffered signals. A single resistor, integrated on-chip or provided by the designer, determines the amplifier gain. The high input impedance, high common mode rejection ratio, and precision with which the gain can be set make instrumentation amplifiers ideal for piezoresistor signal conditioning.

The instrumentation amplifier, which provides the first-stage of gain, is usually the dominant signal conditioning noise source. The noise contribution from second-stage elements such as filters and variable gain amplifiers should be small compared to the first-stage if the instrumentation amplifier gain, G , is large.

This effect is illustrated in Fig. 3.5. There are five noise sources that contribute to the amplifier input signal: Johnson noise (V_J), Hooge noise (V_H), thermomechanical noise (V_{TMN}), amplifier noise (V_A) and electromagnetic coupling noise (V_{EM}). The noise sources sum at the amplifier input and are amplified by G , before the amplifier output is filtered and acquired. The filter contributes additional noise at the system output (V_{filter}) due to either active or passive filtering elements.

The overall noise for the configuration in Fig. 3.5 is $V_{noise} = G(V_J + V_H + V_{TMN} + V_A + V_{EM}) + V_{filter}$. If the first term is much larger than the second term (i.e. $G \gg 1$) then signal conditioning operations after the initial signal amplification don't substantially increase the noise. If the filter were erroneously placed before the first-stage amplifier or a particularly noisy filter were used, this assumption would no longer hold.

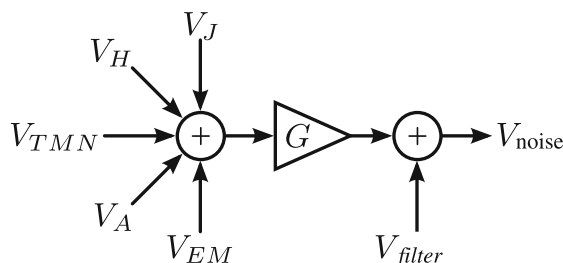


Fig. 3.5 Schematic representation of noise cascading through amplifier stages. When the first stage gain is large ($G \gg 1$), noise from filters and other components after the first stage can be safely neglected with negligible error. (Source Reprinted with permission from [2])

Amplifiers contribute both voltage and current noise to the system. Both forms of noise have Johnson and 1/f spectral components. The voltage noise is independent of the amplifier source impedance; it remains the same whether the amplifier inputs are left open or shorted together. In contrast, the current noise is transduced into a voltage noise by the Wheatstone bridge. As in the case of Johnson noise, the impedance seen looking out from each amplifier input is $R/2$ for a balanced Wheatstone bridge. The voltage spectral density contributed by each amplifier input is then $A_{IJ} R/2$ where A_{IJ} is the magnitude of the Johnson component of the current noise in units of A/ $\sqrt{\text{Hz}}$. The current noise at each of the amplifier inputs is uncorrelated, so the voltage spectral density is increased by a factor of $\sqrt{2}$ and the power spectral density is increased by a factor of two. The same analysis holds true for the amplifier's 1/f-type current noise.

The overall voltage power spectral density contributed by the instrumentation amplifier can be calculated from

$$S_A = A_{VJ}^2 + 2A_{IJ}^2 \left(\frac{R}{2} \right)^2 + \frac{1}{f} \left(A_{VF}^2 + 2A_{IF}^2 \left[\frac{R}{2} \right]^2 \right) \quad (3.22)$$

where A_{VJ} , A_{IJ} , A_{VF} and A_{IF} quantify the Johnson and 1/f components of the voltage and current noise from the amplifier. We used the subscript H for piezoresistor 1/f (Hooge) noise, but we use F to describe the amplifier 1/f noise because it is not necessarily due to bulk mobility fluctuations. The 1/f noise coefficients, A_{VF} and A_{IF} , are equal to the voltage and current noise spectral density at 1 Hz, respectively. The integrated amplifier voltage noise is

$$V_A = \left[\left(A_{VJ}^2 + 2A_{IJ}^2 \left[\frac{R}{2} \right]^2 \right) (f_{\max} - f_{\min}) + \left(A_{VF}^2 + 2A_{IF}^2 \left[\frac{R}{2} \right]^2 \right) \ln \left(\frac{f_{\max}}{f_{\min}} \right) \right]^{1/2}. \quad (3.23)$$

The amplifier noise coefficients can be calculated from the amplifier data sheet provided by the manufacturer. Example coefficients for several instrumentation amplifiers manufactured by Texas Instruments and Analog Devices are tabulated in Table 3.2. Note that BJT-based amplifiers have relatively low voltage noise and high current noise coefficients, while the converse is generally true for FET-based amplifiers.

An accurate description of amplifier noise is essential for sensor design and optimized designs will vary substantially depending on the amplifier noise characteristics. For example, the high current noise of the INA103 (Table 3.2) would lead to a lower optimal piezoresistor resistance than if the sensor were designed for the low current noise INA111. The optimal amplifier for a particular application will depend upon bandwidth, cost and performance requirements as well as the sensor design

Table 3.2 Noise coefficients for common instrumentation amplifier options

Amplifier	Technology	Bandwidth (kHz)	A_{VJ} (nV/ $\sqrt{\text{Hz}}$)	A_{VF} (nV)	A_{IJ} (fA/ $\sqrt{\text{Hz}}$)	A_{IF} (fA)
INA103	BJT	80	1.2	6	2000	2500
INA111	FET	50	10	68	0.8	8
INA116	FET	7	28	300	0.1	1
AD622	BJT	12	9	23	100	600
AD623	BJT	2	30	130	100	590
AD8220	FET	14	14	50	1	10
AD8221	BJT	15	8	11	40	540

The noise coefficients and other performance parameters were manually extracted from the manufacturer-provided data sheets. The -3 dB bandwidth and voltage noise coefficients are for $G = 1000$. The 1/f noise coefficients, A_{VF} and A_{IF} , are equal to the voltage and current noise spectral density at 1 Hz assuming that the corner frequency occurs at a higher frequency. Amplifier characteristics vary with the input stage transistor type, bandwidth and cost

constraints. When numerical optimization is used for sensor design (Chap. 6) it is advantageous and straightforward to evaluate several possible amplifier options.

3.1.5 Thermomechanical Noise

All atoms possess thermal energy at temperatures greater than absolute zero. Brownian motion of the atoms in the sensor is an additional noise source (thermomechanical noise) and places a lower limit on the resolution of all mechanical sensors [311]. Thermomechanical noise is directly analogous to Johnson noise. The motion of a simple harmonic oscillator (SHO) is described by

$$m \frac{\partial^2 x}{\partial t^2} + b \frac{\partial x}{\partial t} + kx = F. \quad (3.24)$$

Similarly, the charge in an RLC oscillator circuit can be written as

$$L \frac{\partial^2 Q}{\partial t^2} + R \frac{\partial Q}{\partial t} + \frac{1}{C} Q = V \quad (3.25)$$

where Q is the charge. In the case of the electrical circuit, the equivalent voltage noise spectral density due to thermal equilibrium is $\sqrt{4k_b T R}$ (Sect. 3.1.2). By direct analogy, the equivalent force noise spectral density in a mechanical system is [311]

$$F_{TMN} = \sqrt{4k_b T b} \quad (3.26)$$

which has units of N/ $\sqrt{\text{Hz}}$. The greater the damping force on a mechanical structure, the greater the thermomechanical force noise.

It is common to rewrite (3.26) so that it depends on more easily measurable experimental parameters. The damping coefficient of the SHO can be written in terms of the spring constant, resonant frequency and quality factor of the oscillator as $b = k/\omega_0 Q$, allowing the thermomechanical force noise spectral density to be written as

$$F_{\text{TMN}} = \sqrt{\frac{4k k_b T}{\omega_0 Q}} \quad (3.27)$$

where k , ω_0 and Q are the spring constant, resonant frequency and quality factor of the oscillator, respectively. When the spring constant varies with respect to position on the mechanical structure, which is true for most situations, then the equivalent force and displacement noise also varies with position.

Note that thermomechanical force noise is independent of frequency up to extremely high frequencies as in the case of Johnson noise. Also, the interactions between the SHO and any surrounding fluid are completely accounted for by (3.27) except in the case of significant nonlinear damping.

Thermomechanical noise is transduced into a voltage noise by the force sensitivity of the sensor according to

$$S_{\text{TMN}} = S_{\text{FV}} F_{\text{TMN}} \quad (3.28)$$

where S_{FV} is the force sensitivity of the sensor (with units of V/N). As the force sensitivity increases, the magnitude of the thermomechanical noise at the circuit output increases. We will discuss sensitivity in the next section in detail, but briefly, force sensitivity increases as the sensor size is reduced making thermomechanical noise particularly important for nanomechanical devices.

As with the other noise sources, we can calculate the RMS thermomechanical noise voltage from

$$V_{\text{TMN}} = S_{\text{FV}} \sqrt{\frac{4k k_b T}{\omega_0 Q} \sqrt{f_{\max} - f_{\min}}} \quad (3.29)$$

Although the thermomechanical force noise is flat with respect to frequency, the induced displacement noise is not. The thermomechanical displacement noise is equal to

$$x_{\text{TMN}} = F_{\text{TMN}} G \quad (3.30)$$

where G is the SHO transfer function from force to displacement. The transfer function can be calculated by taking the Laplace transform of (3.24), resulting in

$$G(s) = \frac{1}{ms^2 + bs + k}. \quad (3.31)$$

Substituting $s = i\omega = i2\pi f$ we obtain

$$G(f) = \frac{1/k}{\left(1 - \frac{f^2}{f_0^2}\right) + i \frac{f}{f_0 Q}}. \quad (3.32)$$

For example, on resonance the displacement noise of the SHO will be equal to $F_{TMN}Q/k$ and 90° out of phase with the driving force due to mechanical amplification.

Another way of looking at thermomechanical noise can be obtained from the Equipartition Theorem [193], which states that if a set of eigenmodes is in thermal equilibrium with a thermal reservoir, the average energy of each mode will be $\frac{1}{2}k_b T$ where k_b is Boltzmann's constant and T is the absolute temperature. Each eigenmode must be capable of storing energy, e.g. kinetic energy ($\frac{1}{2}mv^2$), elastic energy ($\frac{1}{2}kx^2$) or electrostatic energy ($\frac{1}{2}CV^2$). Accordingly, the mean-square displacement of our SHO can be calculated from $\frac{1}{2}k\langle x^2 \rangle = \frac{1}{2}k_b T$ as

$$\langle x^2 \rangle = \frac{k_b T}{k} \quad (3.33)$$

which can be equivalently calculated by integrating the thermomechanical displacement noise spectral density over each eigenmode.

3.1.6 Noise Summary

We have discussed the most important noise sources for piezoresistive sensors: Johnson, Hooge, amplifier and thermomechanical noise. Before moving on, we will illustrate typical noise spectra and discuss practical noise measurement issues.

Figure 3.6 presents the noise spectrum of a simulated piezoresistive cantilever sensor. The simulated cantilever is $1\text{ }\mu\text{m}$ thick, $10\text{ }\mu\text{m}$ wide and $10\text{ }\mu\text{m}$ long. Two piezoresistors are included in the Wheatstone bridge, and the bridge bias voltage is 2 V. The piezoresistor extends 30 % of the cantilever length, and is an epitaxially grown phosphorus resistor with a 333 nm junction depth and $n = 10^{20}\text{ cm}^{-3}$. The electrical impedance of the piezoresistor is low ($580\text{ }\Omega$), making an INA103 a good choice for amplifying the Wheatstone bridge output. The noise is input referred, i.e. the noise at the output of the amplifier is measured and divided by the gain of the amplifier.

The piezoresistor noise consists of Johnson and Hooge noise. The corner frequency ($\approx 120\text{ Hz}$) indicates the frequency below which $1/f$ noise dominates the noise spectrum. Dashed lines in Fig. 3.6 illustrate the contribution of each noise source. The relative magnitudes of the piezoresistor, amplifier and thermomechanical noise is typical for most applications. The thermomechanical noise would be $20\text{ pV/Hz}^{0.5}$ in air ($Q \approx 160$) and $215\text{ pV/Hz}^{0.5}$ in water ($Q \approx 3.9$) following Ref. [312]. Thermomechanical noise can become comparable to amplifier noise when the motion of the sensor is highly damped and it has a high force sensitivity.

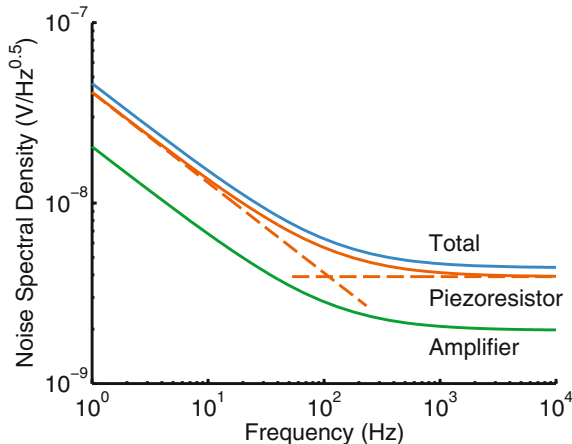


Fig. 3.6 Typical noise spectrum. Piezoresistor noise is substantially larger than amplifier noise. Johnson noise and Hooge noise for the piezoresistor are shown as dashed lines. Noise is dominated by Hooge noise at frequencies below the 1/f corner frequency. Thermomechanical noise is 1–2 orders of magnitude smaller than the other noise sources depending on the damping experienced by the sensor. The relative magnitude of the noise sources will vary depending on the precise design of the sensor. (Source Reprinted with permission from [2])

The noise spectral density varies with the bias applied to the Wheatstone bridge, as illustrated in Fig. 3.7. The simulation conditions are identical to those used in Fig. 3.6. The Hooge noise spectral density increases linearly with the bridge bias, while the Johnson and amplifier noise are approximately independent of it if Joule heating is neglected. In reality, Joule heating of the piezoresistor is an important consideration and it is discussed at length in Sects. 5.3 and 5.4. As the bridge bias approaches zero, the Hooge noise goes to zero but the 1/f noise of the amplifier remains constant. The only way to eliminate the amplifier 1/f noise is to use a heterodyne measurement technique (Sect. 2.3.2) in order to shift the piezoresistor noise signal to a frequency above the amplifier’s 1/f corner frequency before amplification.

There are a number of experimental issues that can confound noise measurements and, in some cases, add additional noise to the system:

Potentiometer noise: Certain types of potentiometers can add excess noise to the measurement system. Wirewound potentiometers have negligible 1/f noise, but ceramic-based potentiometers (e.g. Cermet) can contribute excess 1/f noise. Care should be taken in potentiometer selection.

Noise floor verification: The noise floor of the system should be verified by grounding the Wheatstone bridge bias, shorting the amplifier inputs, and/or inserting a precision test resistor in the place of the piezoresistor in the bridge. The noise should also be measured over a range of bias voltages to ensure that the noise isn’t limited by a system noise floor and that other devices (e.g. potentiometers) are not limiting the system noise.

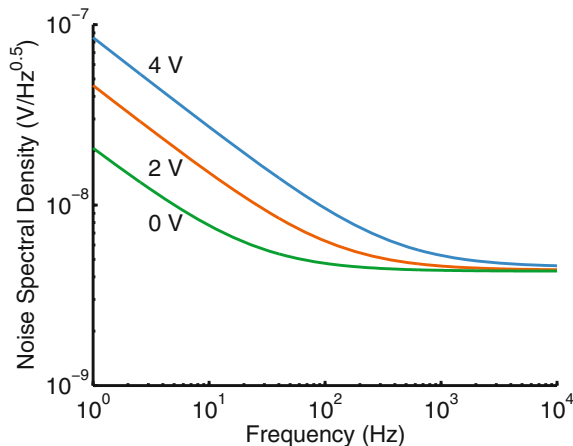


Fig. 3.7 Idealized noise spectra for varying bridge bias voltages. The Hooge noise spectral density increases linearly with the bridge bias, while the Johnson and amplifier noise are independent of the bridge bias (excluding Joule heating of the piezoresistor). When the bridge bias goes to zero, the 1/f noise is limited by the amplifier rather than the piezoresistor. When the amplifier 1/f noise floor is larger than the piezoresistor noise, a modulation-demodulation technique can be utilized (Sect. 2.3.2). (Source Reprinted with permission from [2])

Noise cascading: This is a straightforward but important point. When multiple signal conditioning stages are used, the highest gain stages should be closest to the initial signal. The noise that a signal conditioning stage effectively adds to the system is reduced by the cumulative system gain to that stage.

Gain accuracy: The amplifier gain is set by 1 or 2 feedback resistors depending on the circuit topology. The gain accuracy will vary from 0.1-1% depending on the accuracy of the resistors and will vary with temperature. The gain of the system should be directly measured by applying a test signal to the amplifier inputs and measuring its output.

Line noise: Noise in the bridge bias signal will couple into the circuit output due to imperfect matching between resistors in the bridge and a finite amplifier common mode rejection ratio (CMRR). In particular, noise peaks at 50 or 60 Hz and higher harmonics are often present. Noise from the power supply can be reduced by using a voltage reference (e.g. the ADR44x from Analog Devices), which improves the power supply rejection ratio of the system. A voltage reference can be combined with a potentiometer controlled voltage divider and buffer to provide an adjustable, low noise bridge bias voltage [2].

3.2 Sensitivity

Piezoresistive sensors transduce a mechanical signal into an electrical one according to

$$\frac{\Delta R}{R} = \pi_l \sigma_l + \pi_t \sigma_t \quad (3.34)$$

as discussed in Sect. 2.2.1. A Wheatstone bridge transduces a resistance change into a voltage change according to

$$\Delta V_{\text{out}} = N_{\text{pr}} \frac{V_{\text{bridge}}}{4} \frac{\Delta R}{R} \quad (3.35)$$

where N_{pr} is the number of piezoresistors in the Wheatstone bridge that are mechanically loaded and V_{bridge} is the potential drop across the bridge. This expression assumes that the bridge is balanced (i.e. all four quadrants of the bridge have the same nominal resistance) and that the relative resistance change ($\Delta R/R$) of each of the piezoresistors is equal in magnitude. If the bridge is not balanced, then the voltage change will be attenuated due to the nonlinear response of the bridge.

Sensitivity is typically reported as either a fractional change in resistance or voltage change with respect to the mechanical signal. For example, the sensitivity of a pressure sensor may be reported with units of ppm/kPa or mV/kPa for the former and latter cases, respectively. Sensitivity should be reported for the signal at the input to the amplifier inputs (input referred) because signal conditioning gain can be arbitrarily adjusted.

Sensitivity is calculated by integrating the relative resistance change over the piezoresistor volume. However, the stress and piezoresistive coefficients will almost always vary spatially. In this section we will discuss three important general sensitivity concepts: the resistance factor (γ), sensitivity factor (β^*) and transverse loading factor (ϕ). The resistance factor accounts for excess resistances in the device that reduces the relative resistance change. The sensitivity factor will allow us to calculate sensitivity by multiplying the maximum stress by a correction factor, simplifying the calculation process substantially. The transverse loading factor accounts for regions of the piezoresistor that are loaded in an orthogonal direction from the rest of the resistor.

We have discussed variations in the piezoresistance factor with dopant concentration and temperature (Sect. 2.2.2) and variation in dopant concentration with depth through the device (Chap. 4). In this section we will discuss how to calculate sensitivity while accounting for spatially varying dopant concentration and stress profiles. The stress profile is always either constant (e.g. strain gauges) or varies linearly (e.g. cantilevers and other flexural mode devices), and we will discuss the two cases in depth.

3.2.1 Resistance Factor (γ)

Piezoresistive sensors function by measuring a relative resistance change, and sensor sensitivity is always of the form

$$S \propto \frac{\Delta R}{R}. \quad (3.36)$$

Until now, we have assumed that the resistance is composed entirely of the piezoresistor resistance, i.e. $R = R_{\text{pr}}$. However, additional resistances will always be present in a real sensor and measurement system (e.g. contact resistance, conducting traces, wirebonds), and the total resistance should actually be written as $R = R_{\text{pr}} + R_{\text{excess}}$. Clearly, the sensitivity in (3.36) will be decreased by any excess resistance that does not vary in response to a mechanical load.

We can define a resistance factor as

$$\gamma = \frac{R_{\text{pr}}}{R} \quad (3.37)$$

where γ is the ratio of the piezoresistor resistance to the total resistance, so that the relative change in resistance can be written as

$$\frac{\Delta R}{R} = \frac{\Delta R_{\text{pr}}}{R_{\text{pr}}} \gamma. \quad (3.38)$$

Combining (3.36) and (3.38), we can write the sensitivity in terms of the piezoresistor resistance and resistance factor as

$$S \propto \frac{\Delta R_{\text{pr}}}{R_{\text{pr}}} \gamma. \quad (3.39)$$

We will include the resistance factor, γ , in all sensitivity calculations to account for this resistance effect. During design optimizations we will typically define γ by assuming a fixed value of R_{excess} such as 200Ω .

The total resistance, $R = R_{\text{pr}}/\gamma$ is used to calculate Johnson and amplifier noise. Excess resistance decreases the sensitivity and increases the noise of the sensor, so should clearly be avoided. Conductive traces should be made short and from low resistivity materials (e.g. aluminum rather than doped silicon) and oxide vias should be as large as possible given the area constraints of the device to minimize excess resistance (Sect. 4.9.5).

3.2.2 Sensitivity Factor (β^*)

We will use a simple, end loaded cantilever beam to demonstrate how to calculate sensor sensitivity before generalizing the approach. The example beam is shown in

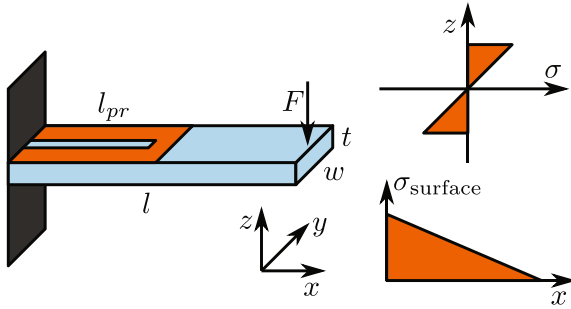


Fig. 3.8 An end loaded cantilever beam. The beam has overall length, width and thickness of l , w , and t , respectively. The piezoresistor extends l_{pr} from the clamped base of the beam and is divided by an infinitesimal width gap to form a resistive loop. The material in the gap should generally be removed rather than diode isolated in order to limit shunted leakage currents. The orientation of the reference axis is shown. (Source Reprinted with permission from [2])

Fig. 3.8. The overall dimensions of the beam are noted (l , w , t and l_{pr}), and the beam is subjected to a point load at its tip of magnitude F .

Assuming a linear elastic beam that obeys Euler-Bernoulli beam theory, the longitudinal stress in the beam varies linearly along the x - and z - axes according to

$$\sigma_l = \frac{12z(l-x)}{wt^3} F. \quad (3.40)$$

We will assume that the transverse stress in the beam is negligible because $l \gg w$. The average longitudinal stress, $\bar{\sigma}_l$, will be used frequently in this section and is calculated as

$$\bar{\sigma}_l = \frac{1}{l_{pr}} \int_0^{l_{pr}} \sigma_l \, dx. \quad (3.41)$$

For this particular case, the average longitudinal stress is

$$\bar{\sigma}_l = \frac{12z(l - l_{pr}/2)}{wt^3} F. \quad (3.42)$$

The surface of the cantilever experiences the maximum stress level, $\bar{\sigma}_l^{\max}$, for $z = t/2$. The average maximum stress level is

$$\bar{\sigma}_l^{\max} = \frac{6(l - l_{pr}/2)}{wt^2} F. \quad (3.43)$$

We will first calculate the sensitivity assuming that the piezoresistor is of infinitesimal thickness and situated at the top surface of the beam, before performing

the more realistic and complex calculation, following the approach taken by Harley [301].

Consider a thin, short slice of the piezoresistor with length dx and thickness dz . The resistance of this slice is

$$dR_{\text{slice}} = 2 \frac{\rho}{w} \frac{dx}{dz} \quad (3.44)$$

where ρ is the resistivity of the material and the factor of two assumes that each leg of the piezoresistor is one half of the cantilever width as in Fig. 3.8. We can integrate the differential slice resistance along the length of the piezoresistor to calculate the total resistance of the slice with thickness dz ,

$$R_{\text{slice}} = \frac{4\rho l_{\text{pr}}}{w dz} \quad (3.45)$$

where the additional factor of two comes from the addition of the two piezoresistor legs in series. The resistance change in the region defined by dR_{slice} is

$$\Delta(dR_{\text{slice}}) = 2 \frac{\Delta\rho}{w} \frac{dx}{dz}. \quad (3.46)$$

This can be integrated along the length of the piezoresistor using (3.40) and the fact that $\Delta\rho = \rho\pi_1\sigma_1$ to obtain

$$\Delta R_{\text{slice}} = 4 \int_0^{l_{\text{pr}}} \frac{\rho\pi_1\sigma_1}{w} \frac{1}{dz} dx \quad (3.47)$$

$$= \frac{4\rho\pi_1\bar{\sigma}_1 l_{\text{pr}}}{w dz}, \quad (3.48)$$

where π_1 is the effective piezoresistive coefficient of the slice. The additional factor of two again comes from integrating along both piezoresistor legs. We can calculate the relative resistance change in the slice by combining (3.42), (3.45) and (3.48) to obtain

$$\frac{\Delta R_{\text{slice}}}{R_{\text{slice}}} = \pi_1 \bar{\sigma}_1 \quad (3.49)$$

$$= \frac{12\pi_1 z(l - l_{\text{pr}}/2)}{wt^3} F. \quad (3.50)$$

If we assume that piezoresistor consists of a single slice located at the surface ($z = t/2$), then the force sensitivity of the cantilever beam is

$$\frac{\Delta R_{\text{pr}}}{R_{\text{pr}}} = \frac{6\pi_1(l - l_{\text{pr}}/2)}{wt^2} F. \quad (3.51)$$

However, (3.51) does not account for the finite thickness of the piezoresistor or piezoresistive coefficient variations through its thickness.

We can generalize the sensitivity derivation by integrating (3.45) and (3.48) over the beam thickness rather than assuming that a single slice exists at the surface. The slices through the piezoresistor are connected in parallel, so their conductivities add linearly. The conductance of each slice, G_{slice} , is equal to $1/R_{\text{slice}}$, and relative changes in resistance and conductance are related by

$$\frac{\Delta R_{\text{slice}}}{R_{\text{slice}}} = -\frac{\Delta G_{\text{slice}}}{G_{\text{slice}}}. \quad (3.52)$$

The denominator of (3.52) is calculated from

$$G_{\text{slice}} = \int_{-t/2}^{t/2} \frac{1}{R_{\text{slice}}} dz \quad (3.53)$$

$$= \int_{-t/2}^{t/2} \frac{w}{4\rho l_{\text{pr}}} dz \quad (3.54)$$

$$= \frac{w}{4l_{\text{pr}}} \int_{-t/2}^{t/2} q\mu n dz. \quad (3.55)$$

Here, we have substituted $\rho = 1/q\mu n$, where q is the elementary charge, μ is the carrier mobility and n is the carrier density. As in the simplified example, the factor of four follows from the width ($w/2$) and overall length ($2l_{\text{pr}}$) of the piezoresistor.

To calculate ΔG_{slice} , we can rearrange (3.52) to find

$$\Delta G_{\text{slice}} = -\frac{\Delta R_{\text{slice}}}{R_{\text{slice}}^2}. \quad (3.56)$$

We previously calculated both ΔR_{slice} and R_{slice} in (3.45) and (3.48). Combining them, we obtain

$$\Delta G_{\text{slice}} = -\frac{w}{4l_{\text{pr}}} \int_{-t/2}^{t/2} \pi_l \bar{\sigma}_l q\mu n dz. \quad (3.57)$$

Finally, we can calculate the relative resistance change of the piezoresistor using (3.55) and (3.57) as

$$\frac{\Delta R_{\text{pr}}}{R_{\text{pr}}} = \pi_l^{\text{ref}} \frac{\int_{-t/2}^{t/2} P \bar{\sigma}_l \mu n dz}{\int_{-t/2}^{t/2} \mu n dz}. \quad (3.58)$$

We have used the relationship $\pi_l = P \pi_l^{\text{ref}}$ from (2.19) where P is the piezoresistance factor.

The relative resistance change of any piezoresistive sensor can be calculated using (3.58) assuming that the piezoresistor electrical properties only vary in the z -direction. This is a reasonable assumption for piezoresistors that are much wider

than they are deep. Otherwise lateral diffusion of the piezoresistor should be considered (see Sect. 4.9.4).

It is important to emphasize that the overall resistance change is calculated as

$$\frac{\Delta R}{R} = \gamma \frac{\Delta R_{\text{pr}}}{R_{\text{pr}}} \quad (3.59)$$

due to excess resistances in the measurement circuit. We can apply (3.58) to the specific case of an end loaded piezoresistive cantilever by substituting (3.42) for $\bar{\sigma}_l$, which yields

$$\frac{\Delta R_{\text{pr}}}{R_{\text{pr}}} = \frac{12F(l - l_{\text{pr}}/2)\pi_l^{\text{ref}}}{wt^3} \frac{\int_{-t/2}^{t/2} P \mu n z dz}{\int_{-t/2}^{t/2} \mu n dz}. \quad (3.60)$$

We can simplify (3.60) significantly using (3.43) to obtain

$$\frac{\Delta R_{\text{pr}}}{R_{\text{pr}}} = \bar{\sigma}_l^{\max} \pi_l^{\text{ref}} \left(\frac{2}{t} \frac{\int_{-t/2}^{t/2} P \mu n z dz}{\int_{-t/2}^{t/2} \mu n dz} \right) \quad (3.61)$$

where $\bar{\sigma}_l^{\max}$ is the average stress at the surface of the piezoresistor from (3.43).

Multiple piezoresistors of varying size and shape are often fabricated using the same doping process on a particular wafer. We can lump the process dependent terms in (3.61) into a single parameter called the sensitivity factor, β^* (beta star), following Park et. al. [295]. The sensitivity factor is calculated from

$$\beta^* = \frac{2}{t} \frac{\int_{-t/2}^{t/2} P \mu n z dz}{\int_{-t/2}^{t/2} \mu n dz}. \quad (3.62)$$

Combining (3.61) and (3.62), we obtain our final result for the relative resistance change of a piezoresistive cantilever,

$$\frac{\Delta R_{\text{pr}}}{R_{\text{pr}}} = \bar{\sigma}_l^{\max} \pi_l^{\text{ref}} \beta^*. \quad (3.63)$$

The overall relative change in resistance, accounting for excess resistance that does not change with the applied load and the effect of transverse stress, is obtained by combining (2.11), (3.63) and (3.38) to yield

$$\frac{\Delta R}{R} = (\bar{\sigma}_l^{\max} \pi_l^{\text{ref}} + \bar{\sigma}_t^{\max} \pi_t^{\text{ref}}) \gamma \beta^*. \quad (3.64)$$

The sensitivity factor varies from 0 to 1 and defines the ratio of the actual relative resistance change of the piezoresistor to the maximum that is theoretically possible if the piezoresistor were infinitely thin, located at the surface and lightly doped.

Tortonese introduced an earlier version of the sensitivity factor, β , in 1993 to account for the finite piezoresistor thickness [313]. However, he included the piezoresistance factor in both the numerator and denominator so that β represented the conductivity and piezoresistivity weighted stress which is correct only if the piezoresistance factor does not vary with dopant concentration. In contrast, β^* only includes the piezoresistance factor in the numerator so defines the conductivity weighted product of the stress and piezoresistance factor.

In summary, (3.64) can be used to accurately calculate the sensitivity of any piezoresistive sensor where the stress varies linearly across its thickness. The integral in (3.62) extends from the bottom to the top of the device. For devices that are junction isolated, the integral should only extend to the junction, however the difference is minor if the piezoresistor is much more highly doped than the background.

Devices with a constant stress, such as strain gauges or extensional mode resonators, must be handled slightly differently. Following Tufte and Stelzer [314], we can define a conductivity weighted, average piezoresistance factor as

$$\bar{P} = \frac{\int_0^t P \mu n dz}{\int_0^t \mu n dz} \quad (3.65)$$

so that the sensitivity of strain gauges can be calculated as

$$\frac{\Delta R}{R} = \sigma \pi_l^{\text{ref}} \gamma \bar{P}. \quad (3.66)$$

3.2.3 Transverse Loading Factor (ϕ)

Most piezoresistive sensors are designed to exploit the longitudinal piezoresistive factor by orienting the mechanical stress and electrical current in the same direction. This approach maximizes the relative resistance change and sensor resolution because the longitudinal and transverse coefficients are opposite in sign for the most widely used crystallographic orientations (Table 2.2). The sign difference between the longitudinal and transverse coefficients leads to a degradation in performance whenever the mechanical stress is perpendicular to the direction of the electrical current flow.

There are two mechanisms by which transverse loading can reduce the relative resistance change: the application of transverse stress directly to the piezoresistor (Fig. 3.9a) or the application of longitudinal stress to the loop at the end of the piezoresistor (Fig. 3.9b). The former effect is relatively complex and depends on the sensor geometry. For example, thick or wide cantilever beams can develop significant transverse stress in response to a point load. However, even if the stress field is perfectly longitudinal any transverse portions of the piezoresistor will degrade the relative resistance change. We will focus on the latter effect in this section and develop a sensitivity reduction factor to account for transverse loading.

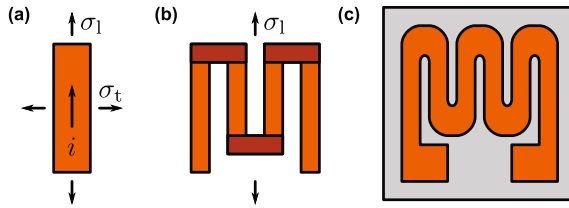


Fig. 3.9 The transverse piezoresistive effect becomes important when **a** the longitudinal and transverse stress fields are comparable in magnitude or **b** there are transverse portions of the resistor (highlighted). **c** Transverse loading similarly degrades the sensitivity of conventional strain gauges, which require many loops to reach a convenient impedance. All resistive strain sensors, whether silicon or metal, should be designed to minimize the ratio of the transverse to longitudinal resistance

First though, we want to emphasize that transverse loading also degrades the performance of conventional wire and foil strain gauges [315]. Metal strain gauges require many turns of the resistor to achieve a convenient resistance (e.g. 120–700 Ω) to reduce the impact of parasitic resistances and for ease of readout circuit integration. Each turn introduces a short transverse section which opposes the resistance change of the longitudinal portions of the gauge due to the Poisson effect. The impact of the end loops can be minimized by making them wider than the rest of the gauge and maximizing the length to width ratio of the foil or wire gauge (Fig. 3.9c).

Silicon piezoresistors do not typically require multiple turns to reach a practical resistance due to their higher sheet resistance. Due to the fact that every transverse portion of the resistor degrades sensitivity (whether the stress field is purely longitudinal or more complex), the ideal piezoresistor would consist of a single straight section (Fig. 3.10a). Unfortunately, piezoresistors are two-port devices and placing a second bondpad in the middle of a pressure sensor diaphragm or at the end of a cantilever beam is not usually possible. Without delving into more complex geometries that combine silicon piezoresistors and low resistance metal interconnects, this leaves us with a piezoresistor consisting of two longitudinally oriented legs connected by a short transverse loop (Fig. 3.10b). We will analyze the performance of this structure in more detail to derive a transverse loading factor.

The relative resistance change of the structure in Fig. 3.10c is

$$\frac{\Delta R}{R} = \frac{\Delta R_l + \Delta R_t}{R_l + R_t} \quad (3.67)$$

$$= \frac{(\Delta R/R)_l R_l + (\Delta R/R)_t R_t}{R_l + R_t} \quad (3.68)$$

$$= \frac{\pi_l \bar{\sigma}_l R_l + \pi_t \bar{\sigma}_t R_t}{R_l + R_t} \quad (3.69)$$

where $\bar{\sigma}_l$ and $\bar{\sigma}_t$ are the average stress levels experienced by the longitudinal and transverse portions of the piezoresistor. In the case of an end loaded cantilever beam

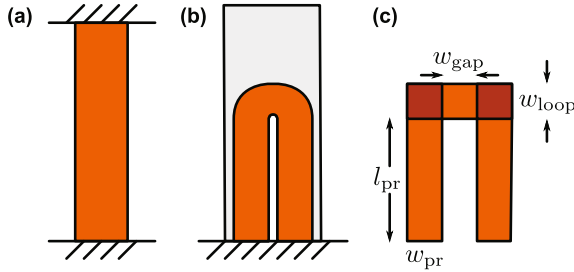


Fig. 3.10 Piezoresistor geometry. **a** Considering the detrimental effect of transverse loading, a piezoresistor designed to exploit the longitudinal piezoresistive effect should consist of a simple straight resistor. **b** However, the simplest piezoresistor geometry for most micromachined sensors consists of two longitudinal legs connected by a short transverse loop. **c** We will analyze this case assuming that the width and length of each piezoresistor leg is \$w_{pr}\$ and \$l_{pr}\$ while the legs are separated by \$w_{gap}\$ with a loop width of \$w_{loop}\$

that is relatively long and thin the stress field is purely longitudinal and \$\overline{\sigma_t}\$ is the longitudinal stress evaluated at the midpoint of the transverse loop.

The relative resistance change can be rewritten as

$$\frac{\Delta R}{R} = \frac{\overline{\sigma_l} \pi_l R_l (1 + \overline{\sigma_t} \pi_t R_t / \overline{\sigma_l} \pi_l R_l)}{R_l (1 + R_t / R_l)} \quad (3.70)$$

$$= \overline{\sigma_l} \pi_l \phi \quad (3.71)$$

where

$$\phi = \frac{1 + \overline{\sigma_t} \pi_t R_t / \overline{\sigma_l} \pi_l R_l}{1 + R_t / R_l} \quad (3.72)$$

is the transverse loading factor and, like the resistance and sensitivity factors introduced in Sects. 3.2.1 and 3.2.2, ranges from zero to one. The transverse loading factor approaches one as \$R_t / R_l \rightarrow 0\$ or \$\pi_t / \pi_l \rightarrow 0\$.

As an example, we will calculate \$\phi\$ for the case of an end loaded cantilever beam. The ratio of the average loop stress to the average leg stress can be calculated following Sect. 3.2.2 as

$$\frac{\overline{\sigma_t}}{\overline{\sigma_l}} = \frac{l - (l_{pr} + w_{loop}/2)}{l - l_{pr}/2} \quad (3.73)$$

where \$l\$ and \$l_{pr}\$ are the lengths of the cantilever beam and piezoresistor leg while the transverse stress is computed from (3.40) for a distance \$l_{pr} + w_{loop}/2\$ from the base of the beam.

The ratio of the transverse resistance to the longitudinal resistance for the resistive loop illustrated in Fig. 3.10c is

$$\frac{R_t}{R_l} = \frac{w_{gap}/w_{loop}}{2l_{pr}/w_{pr}} \quad (3.74)$$

where l_{pr} and w_{pr} are the dimensions of each piezoresistor leg and the dimensions of the loop are defined by w_{gap} and w_{loop} . We neglect the connections between the longitudinal and transverse resistances (shaded in Fig. 3.10c) for simplicity but note that each corner will contribute approximately half of a square to the overall resistance and contribute negligibly to the change in resistance if $\pi_t \approx -\pi_l$.

Finally, we will assume an n-type <100> oriented piezoresistor so that

$$\frac{\pi_t}{\pi_l} = -1. \quad (3.75)$$

Combining (3.72), (3.73), (3.74) and (3.75), the transverse loading factor for a cantilever beam is

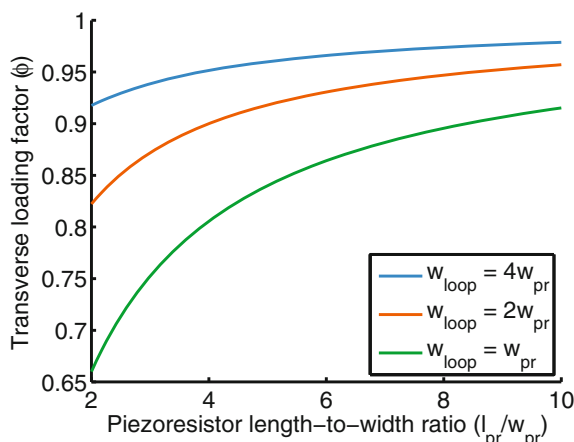
$$\phi = \frac{2l_{\text{pr}}w_{\text{loop}}/w_{\text{pr}}w_{\text{gap}} - (l - l_{\text{pr}} - w_{\text{loop}}/2)/(l - l_{\text{pr}}/2)}{1 + 2l_{\text{pr}}w_{\text{loop}}/w_{\text{pr}}w_{\text{gap}}}. \quad (3.76)$$

Figure 3.11 plots the transverse loading factor as a function of the piezoresistor's length-to-width ratio assuming that $l = 3l_{\text{pr}}$ and $w_{\text{gap}} = w_{\text{pr}}$. Increasing the width of the transverse loop (w_{loop}) has an outsized effect on the transverse loading factor, particularly when the piezoresistor is relatively short. For example, when $l_{\text{pr}} = 2w_{\text{pr}}$, increasing the width of the loop from w_{pr} to $4w_{\text{pr}}$ increases the piezoresistor sensitivity by 50 %.

The impact of the transverse loop width (w_{loop}) is smaller if the piezoresistor is relatively long (e.g. $l_{\text{pr}} = 10w_{\text{pr}}$) but in general w_{loop} should be maximized. If the effect of transverse loading is neglected during piezoresistor design then it will introduce an error between the calculated and measured sensitivity ranging from 5 to 35 % depending on the aspect ratio of the piezoresistor.

In discussing piezoresistor Joule heating (Sect. 5.3), we will show that piezoresistor performance improves for a given temperature increase as its length decreases.

Fig. 3.11 Variation in the transverse loading factor with the piezoresistor length-to-width ratio ($l_{\text{pr}}/w_{\text{pr}}$) and loop width to piezoresistor width ratio ($w_{\text{loop}}/w_{\text{pr}}$). As the length of the piezoresistor decreases the overall sensitivity decreases due to the transverse loading effect. Increasing the width of the loop decreases both its resistance and the average stress that it experiences



However, Fig. 3.11 shows that the transverse loading factor will degrade as the piezoresistor aspect ratio decreases. Thus, the optimal piezoresistor length is a trade-off between minimizing the temperature rise for a given power dissipation (which favors a short piezoresistor) and maximizing the transverse loading factor (which favors a long piezoresistor).

Regardless of the piezoresistor dimensions, maximizing the width of the transverse portion of the loop with respect to the piezoresistor legs and minimizing the gap between the legs will minimize the effect of transverse loading.

3.3 Resolution Example

We can calculate the resolution for any sensor by combining (3.1) with expressions for the sensor noise and sensitivity. We will use a piezoresistive cantilever force and displacement sensor as a brief example to illustrate how to calculate resolution.

The noise sources for the cantilever include Johnson, Hooge, amplifier and thermomechanical noise sources. Combining (3.14), (3.16), (3.23) and (3.29), the RMS voltage noise of the sensor is

$$V_{\text{noise}} = \sqrt{V_J^2 + V_H^2 + V_A^2 + V_{\text{TMN}}^2} \quad (3.77)$$

which can be expanded into

$$V_{\text{noise}} = \left[(f_{\max} - f_{\min}) \left(4k_b T R + A_{VJ}^2 + 2A_{IJ}^2 \left(\frac{R}{2} \right)^2 + S_{FV}^2 \frac{4k_b T}{\omega_0 Q} \right) + \ln \left(\frac{f_{\max}}{f_{\min}} \right) \left(V_{\text{bridge}}^2 \frac{\alpha}{2N_{\text{eff}}} + A_{VF}^2 + 2A_{IF}^2 \left(\frac{R}{2} \right)^2 \right) \right]^{1/2}. \quad (3.78)$$

The noise expression assumes a balanced Wheatstone bridge (Sect. 3.1.2) and two silicon piezoresistors in the bridge, one for measurement and one for temperature compensation (Sect. 3.1.3).

Assuming that only one of the piezoresistors is mechanically loaded, we can adapt (3.35) to calculate the force and displacement sensitivity as

$$S_{FV} = \frac{V_{\text{bridge}}}{4} \frac{\Delta R}{R} \frac{1}{F} \quad (3.79)$$

and

$$S_{XV} = \frac{V_{\text{bridge}}}{4} \frac{\Delta R}{R} \frac{1}{x} \quad (3.80)$$

where F and x are the force or displacement applied to the tip of the cantilever beam, respectively. The overall relative resistance change can be found by applying

the transverse loading factor to (3.64), yielding

$$\frac{\Delta R}{R} = \overline{\sigma_l^{\max}} \pi_l^{\text{ref}} \gamma \beta^* \phi \quad (3.81)$$

where γ , β^* and ϕ are the resistance factor (3.37), sensitivity factor (3.62) and transverse loading factor (3.72) while $\overline{\sigma_l^{\max}}$ is the average longitudinal surface stress experienced by the piezoresistor, which we previously calculated as

$$\overline{\sigma_l^{\max}} = \frac{6(l - l_{\text{pr}}/2)}{wt^2} F. \quad (3.43)$$

The average maximum longitudinal stress can be rewritten in terms of displacement by combining $F = kx$ and the spring constant of a cantilever beam ($k = Ewt^3/4l^3$) to yield

$$\overline{\sigma_l^{\max}} = \frac{3Et(2 - l_{\text{pr}}/l)}{4l^2} x. \quad (3.82)$$

The maximum longitudinal piezoresistive coefficient (π_l^{ref}) can be found in Table 2.2. We can combine all of these expressions to calculate the force and displacement sensitivities of an end-loaded cantilever beam as

$$S_{\text{FV}} = \frac{V_{\text{bridge}}}{4} \frac{6(l - l_{\text{pr}}/2)}{wt^2} \pi_l^{\text{ref}} \gamma \beta^* \phi \quad (3.83)$$

and

$$S_{\text{XV}} = \frac{V_{\text{bridge}}}{4} \frac{3Et(2 - l_{\text{pr}}/l)}{4l^2} \pi_l^{\text{ref}} \gamma \beta^* \phi. \quad (3.84)$$

The RMS force and displacement noise, which we will equate to the minimum detectable force (MDF) and displacement (MDD) can finally be calculated following (3.1) as

$$\text{MDF} = \frac{V_{\text{noise}}}{S_{\text{FV}}} \quad (3.85)$$

and

$$\text{MDD} = \frac{V_{\text{noise}}}{S_{\text{XV}}}. \quad (3.86)$$

The piezoresistive cantilever is a useful canonical example. Other piezoresistive sensors (e.g. pressure, surface stress or acceleration) differ in their geometry and loading conditions but the piezoresistor itself is typically still a resistive loop. Thus, the sensitivity equations differ between sensor types but the noise equations change relatively little.

3.4 Summary

This chapter established the concept of sensor resolution as described by

$$\text{Resolution} = \frac{V_{\text{noise}}}{S} \quad (3.1)$$

and introduced models for both the sensitivity and noise of piezoresistive sensors. For nearly all applications the overall sensor resolution should be optimized rather than focusing on the sensitivity or noise independently.

There are four principal sources of noise in piezoresistive sensors: Johnson, 1/f, amplifier and thermomechanical. The 1/f noise in piezoresistors is accurately predicted using the Hooge model. Of the four noise sources, well-optimized systems are limited by the combination of Johnson and 1/f noise. Their RMS voltage noise over the measurement bandwidth of f_{\min} to f_{\max} can be calculated from

$$V_J = \sqrt{4k_b T_{\text{pr}} R_{\text{pr}} (f_{\max} - f_{\min})} \quad (3.14)$$

and

$$V_H = \frac{V_{\text{bridge}}}{2} \sqrt{\frac{\alpha}{N_{\text{eff}}} \ln \frac{f_{\max}}{f_{\min}}}. \quad (3.16)$$

Johnson noise primarily depends upon the electrical resistance of the piezoresistor. Hooge noise depends upon its volume and degree of crystal lattice disorder, as empirically described by the Hooge parameter (α) which depends on the piezoresistor fabrication process.

One of the first and most critical steps in designing a piezoresistive sensor (or any sensor for that matter) is defining the measurement bandwidth and developing filters to limit the noise contribution from frequencies beyond the desired bandwidth. Other practical issues with piezoresistor noise are summarized in Sect. 3.1.6.

Sensitivity describes the relationship between a mechanical input (e.g. force) and the electrical output of the sensor (e.g. Wheatstone bridge output voltage). The sensitivity of a Wheatstone bridge where one of the four resistors is a mechanically loaded piezoresistor can be calculated from

$$\Delta V_{\text{out}} = \frac{V_{\text{bridge}}}{4} \frac{\Delta R}{R} \quad (3.35)$$

where the relative resistance change is

$$\frac{\Delta R}{R} = (\overline{\sigma_1^{\max}} \pi_1^{\text{ref}} + \overline{\sigma_t^{\max}} \pi_t^{\text{ref}}) \gamma \beta^*. \quad (3.64)$$

Piezoresistive sensors typically use longitudinal mechanical loading with the mechanical stress and electrical current flowing in the same direction. In that case,

the fractional resistance change reduces to

$$\frac{\Delta R}{R} = \overline{\sigma_l^{\max}} \pi_l^{\text{ref}} \gamma \beta^* \phi \quad (3.81)$$

where γ , β^* and ϕ are the resistance factor, sensitivity factor and transverse loading factor, respectively. The factors are discussed in Sects. 3.2.1, 3.2.2 and 3.2.3 and models are presented to calculate the factors from the piezoresistor design parameters.

Chapter 4

Fabrication and Process Modeling

A necessary precondition for successful piezoresistor design is an accurate model for the fabrication process. In particular, we require a model that can predict the dopant concentration profile of the piezoresistor in terms of fabrication input parameters (e.g. predeposition time and temperature). The dopant concentration profile, $N(z)$, determines the charge carrier and electrical resistivity profiles, $n(z)$ and $\rho(z)$. As we saw in the last section, these quantities determine the noise, sensitivity and resolution of a sensor. This chapter will focus on accurately modeling the most common piezoresistor fabrication techniques.

The three most common techniques for doping silicon to form piezoresistive sensors are ion implantation, epitaxy and diffusion (also commonly known as pre-deposition). The typical dopant concentration profile varies significantly between each technique (Fig. 4.1), leading to relative strengths and weaknesses for each. A complete review of doping techniques is available elsewhere [3]. We also highly recommend Ref. [307] for a general introduction to diffusion processes in silicon. The three main techniques are summarized in Table 4.1.

Ion implantation is the most common technique for fabricating piezoresistors. Advantages of ion implantation are the precise control of the dopant dose, concentration and depth. Ion implantation also exhibits the best cross-wafer uniformity of the three techniques. Downsides of ion implantation are the lattice damage intrinsic to the process and the accompanying need to anneal the wafer to activate the dopants and reduce lattice damage. Shallow piezoresistors are difficult to fabricate using ion implantation due to the post-implantation anneal step. Ion implanted piezoresistors have achieved the lowest Hooge factors to date as seen in Fig. 3.3 [156], although data for the other two techniques are more limited.

Predeposition is a batch process while the other two techniques are generally serial processes, and it can be used to fabricate very shallow piezoresistors. It is

We would like to thank Sung-Jin Park for his contributions to the concepts in this chapter. In particular, he developed the concepts of β^* , β_1^* , β_2^* and the concept of ion implantation optimization using lookup tables.

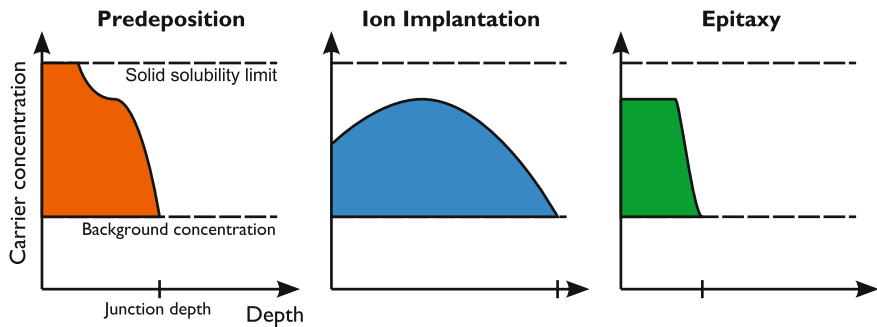


Fig. 4.1 Comparison between the typical dopant concentration profiles produced by predeposition/diffusion, ion implantation and epitaxy. Diffusion (also commonly known as predeposition) is characterized by a high surface concentration and shallow junction depth before an optional drive-in step. Ion implantation can produce lower concentrations with more flexibility and accuracy, but has difficulty doping shallow layers. Epitaxial growth enables precise dopant profile control at the expense of increased system complexity and cost (*Source* Reprinted with permission from [2])

Table 4.1 Summary of the most common piezoresistor fabrication techniques: predeposition/diffusion, ion implantation and epitaxy

	Predeposition	Ion implantation	Epitaxy
Temperature (°C)	750–1100	750–1100	600–1100
Pressure	Atmospheric	High vacuum	Low vacuum
Throughput	High	High	Low
Lattice damage	Minimal	Substantial	Minimal
Concentration (cm ⁻³)	10 ²⁰ –10 ²¹	10 ¹⁶ –10 ²⁰	10 ¹⁶ –10 ²⁰
Min. <i>t_j</i> (nm)	<100	>500	<100
Masking materials	Hard mask	Hard/Soft mask	Hard mask
Profile modeling	Less complex	More complex	Less complex

All three processes will be discussed and modeled in depth

also the simplest, most widely available technique of the three due to its longer history. However, predeposition generally (although not always) yields less cross-wafer uniformity than ion implantation and the dopant concentration is fixed at the solid solubility concentration unless a drive-in step is included in the fabrication process. Lattice damage is minimal during predeposition, although excess dopants tend to aggregate at the surface.

Epitaxy is generally a serial process, but provides the most precise control over piezoresistor depth and concentration of the three techniques. Any damage introduced into the lattice during growth is minimal with proper growth conditions, so a post-growth anneal is not generally performed. Epitaxy has been used to fabricate the thinnest piezoresistors to date [84, 119]. However, processing complexity and equipment costs limit the availability of epitaxial reactors.

The most important facet of piezoresistor design and optimization is calculating the dopant concentration profile. Without an accurate predictive model, designs will

Table 4.2 Summary of the dopant/process combinations that will be modeled in this work

	Predeposition	Ion implantation	Epitaxy
Arsenic	No	Yes	Yes
Boron	No	Yes	Yes
Phosphorus	Yes	Yes	Yes

not match experimental results and optimized designs will be inaccurate. Analytical models for diffused and epitaxial piezoresistors will be presented. Ion implantation is significantly more complicated so we have tabulated lookup tables for all of the relevant profile parameters (β_1^* , β_2^* , R_s , N_z^{eff} and t_j) using TSUPREM-4™(Synopsys, Mountain View, CA).

We will present models for the combinations of dopant species and fabrication types listed in Table 4.2. Predeposition dopant profiles were only calculated for phosphorus doping. Boron and arsenic were not investigated due to practical fabrication issues and the lack of accurate, analytical models for their dopant profiles (Sect. 4.3). Epitaxial profiles do not vary significantly between the three dopant species, because we will focus on relatively low temperature epitaxy where diffusion lengths are short. Ion implantation, as noted earlier, will be treated numerically and so the differences in solid solubility, diffusivity, and oxide segregation between the dopant species will be handled by the software.

4.1 Model Assumptions

Throughout this book we assume charge neutrality and complete dopant ionization so that $N(z) \approx n(z)$. Incomplete ionization can become significant for low temperature applications and we refer the interested reader to Sah [316]. The charge neutrality assumption only affects very shallow or narrow geometries. The Debye length, the characteristic distance over which charge screening occurs, is on the order of 10 nm in silicon so does not affect the vast majority of devices [5].

Incomplete dopant ionization, also known as freezeout, occurs when there is insufficient thermal energy to ionize the dopants [317]. Degenerately doped piezoresistors ($>10^{19} \text{ cm}^{-3}$) have operated at temperatures below 4.3 K [318]. Many piezoresistive cantilevers used for cryogenic measurements have not been optimized for low temperature operation, so have dissipated more power than necessary, limiting their utility [319]. With the addition of accurate carrier freezeout modeling, the design techniques in this book could be applied to cryogenic temperatures with relatively little modification.

Finally, we assume that the dopant concentration only varies in the direction orthogonal to the exposed wafer surface (vertically in most but not all cases). There

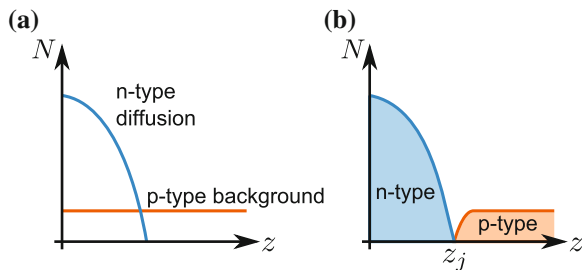


Fig. 4.2 Piezoresistor formation. **a** Dopants are introduced to the wafer surface to define an n-type piezoresistor. The piezoresistor is electrically isolated from the bulk of the wafer by a p-n junction. **b** The net carrier concentration drops sharply at the junction, which is depth z_j from the surface (Source Reprinted with permission from [2])

are several potential design issues related to lateral dopant diffusion, which will be discussed in Sect. 4.9.4.

Piezoresistors should be electrically isolated from the bulk of the wafer using either a low leakage p-n junction, dielectric or vacuum. Leakage is detrimental to both the sensitivity and noise of piezoresistors [215]. During piezoresistor formation, dopants are introduced at the wafer surface to define the piezoresistor. Electrical current is confined to the piezoresistor by forming a p-n junction with the initial wafer material. For example, if the wafer is initially p-type, an n-type dopant would be introduced to the wafer (Fig. 4.2a). Junction fabrication and device physics are treated extensively in [3, 5].

The p-type and n-type dopants cancel one another, so the depth at which the introduced impurities are equal in concentration to the initial background concentration defines the junction depth. The net dopant concentration is shown in Fig. 4.2b. By ensuring that the p-n junction is always reverse biased, the depletion region of the diode can be used to electrically isolate the piezoresistor up to frequencies where the electrical impedance of the depletion region is comparable to the piezoresistive loop (MHz to GHz).

4.2 Concentration Limits

Piezoresistor design optimization generally favors high dopant concentrations (Sect. 6.4.2). Two concentration limits are important to consider: the solid solubility limit and the maximum electrically active concentration. These concentration limits determine the maximum possible dopant concentrations possible with diffused and epitaxial piezoresistors. Concentration limits for ion implanted dopant profiles were handled by TSUPREM-4™ in this book.

Dopants only contribute charge carriers when positioned in substitutional crystal lattice sites; interstitial dopant atoms do not [3]. The total dopant concentration

(substitutional and interstitial sites) is always greater than or equal to the electrically active dopant concentration (substitutional sites only), and the proportion of activated dopants depends on the processing history of a wafer.

The total dopant concentration is bounded by the solid solubility limit. Above the solubility limit, dopant atoms aggregate and begin to come out of solution. The solid solubility limit varies with the dopant atom and maximum wafer processing temperature and is on the order of 10^{20} – 10^{21} cm $^{-3}$ for boron, phosphorus and arsenic at 1000 °C. Solid solubility data of multiple atomic species was first tabulated by Trumbore in 1960 [320], and updated by Borisenko and Yudin in 1987 [321]. The maximum electrically active concentration also varies with temperature and can approach the solid solubility limit. Excess, electrically inactive dopants have been observed for phosphorus in particular [309, 310].

Figure 4.3 plots the solid solubility and electrically active concentration limits for boron and phosphorus as functions of temperature. Solmi et al. measured the total and electrically active concentrations for phosphorus [310]. Their best-fit models for the total and active phosphorus concentrations were

$$N_{\text{total}}^{\text{phos}} = 2.45 \times 10^{23} \text{ cm}^{-3} \exp(-0.62 \text{ eV}/k_b T) \quad (4.1)$$

$$N_{\text{active}}^{\text{phos}} = 9.2 \times 10^{21} \text{ cm}^{-3} \exp(-0.33 \text{ eV}/k_b T). \quad (4.2)$$

Solmi et al. observed the presence of electrically inactive, interstitial phosphorus for processing temperatures above 750 °C. Vick et al. electrically measured the maximum boron concentration achievable by predeposition as a function of temperature

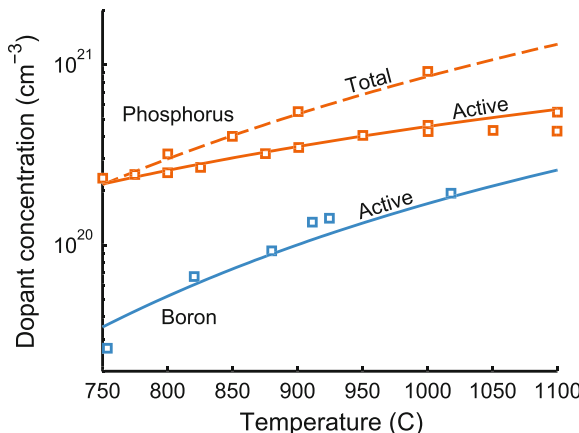


Fig. 4.3 Total and electrically active boron and phosphorus concentrations vary with processing temperature. Solmi et al. measured the total and electrically active concentrations of phosphorus [310], while Vick et al. measured the electrically active boron concentration [322]. The best-fit models in the text are plotted for comparison with the experimental data (Source Reprinted with permission from [2])

[322]. We fit the Arrhenius equation to their data to obtain a best-fit model for the maximum electrically active boron concentration of

$$N_{\text{active}}^{\text{boron}} = 1.9 \times 10^{22} \text{ cm}^{-3} \exp(-0.41\text{eV}/k_b T). \quad (4.3)$$

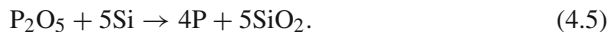
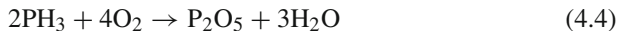
When calculating diffused and epitaxial profiles, we will take these concentration limits into account.

4.3 Predeposition

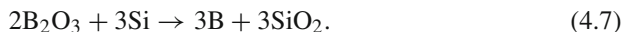
Diffusion is the migration of dopant atoms from a region of high concentration to a region of low concentration. During predeposition (also known as diffusion) a high concentration dopant source is formed on the wafer surface and diffused into the crystal lattice at high temperature.

Predeposition is typically performed at atmospheric pressure in the 750–1100 °C temperature range. The dopant source can be solid-, liquid- or gas-phase [3, 323]. When a gas-phase source is used, such as diborane (B_2H_6), phosphine (PH_3), or arsine (AsH_3), it is carried in an inert gas such as N_2 or Ar. Most modern predeposition systems use liquid- rather than gas-phase sources because they are dramatically safer and provide more consistent dopant profiles [324]. A common approach is to bubble the carrier gas through the liquid-source, most often BBr_3 or POCl_3 ; liquid-phase arsenic sources are not widely available. Solid-phase systems use solid wafer dopant sources, typically P_2O_5 or BN, which are interleaved with the device wafers. When both the wafers are heated, dopant atoms sublime and diffuse from the source wafers to the device wafers. A final option is the use of doped spin-on-glass layers. [325 – 327].

Regardless of the dopant source, dopant atoms diffuse into the silicon lattice during predeposition via a two step process. First, a highly doped oxide is formed at the surface, followed by the silicon diffusion reaction [328]. For example, in the case of phosphorus doping the reaction proceeds according to



In the case of boron doping it proceeds according to



During predeposition, the boundary condition is a constant surface concentration and the doping profile is often approximated by a complementary error function. The surface concentration is equal to the solid dopant solid solubility limit which varies

with temperature, assuming that a high enough concentration of dopants is present in the furnace.

After predeposition, the oxide dopant source is usually (but not always) removed in hydrofluoric acid (HF) and the dopants can be driven in via high temperature annealing in either an inert or oxidizing environment. The drive-in step is performed to reduce the surface concentration and increase the junction depth, although it may be beneficial to skip the drive-in step depending on the piezoresistive sensor design.

One notable issue with boron predeposition is the formation of a $\approx 200\text{\AA}$ thick B:Si layer on the surface that can not be etched in hydrofluoric acid (HF). In this case, a short oxidation step can be performed to oxidize the B:Si layer (e.g. 750°C for 20 min), allowing it to be removed in HF. The complete removal of the oxide and B:Si layer can be easily verified because the oxide and B:Si surfaces are hydrophilic while the bare silicon surface is hydrophobic.

Predeposition profiles are often modeled using a complementary error function. An important assumption in this approach is that the dopant diffusivity does not vary with concentration. Unfortunately, this assumption does not hold for boron, arsenic, or phosphorus when the dopant concentration exceeds the intrinsic carrier concentration, n_i , which can be calculated from (4.31) and is plotted in Fig. 4.4. Above the intrinsic concentration level, the diffusivities of boron and arsenic increase approximately linearly with concentration [4]. In general, diffusivity varies with dopant concentration due to the formation of lattice defects, dopant clustering, and lattice strain [322, 329, 330]. Increased diffusivity at high dopant concentrations leads to more abrupt concentration profiles, and using a complementary error function to model piezoresistive devices will lead to large errors in calculating device performance.

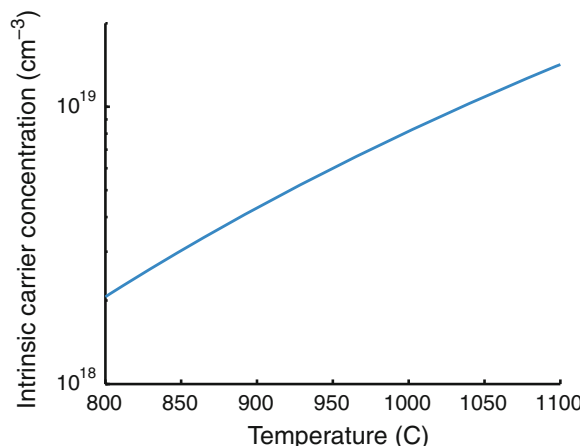


Fig. 4.4 Intrinsic carrier concentration (n_i) as a function of processing temperature. Dopant diffusivity is relatively constant below n_i but increases above it, leading to more abrupt concentration profiles than would otherwise be predicted. Predeposition can only be accurately modeled by a complementary error function for concentrations below n_i (Source Reprinted with permission from [2])

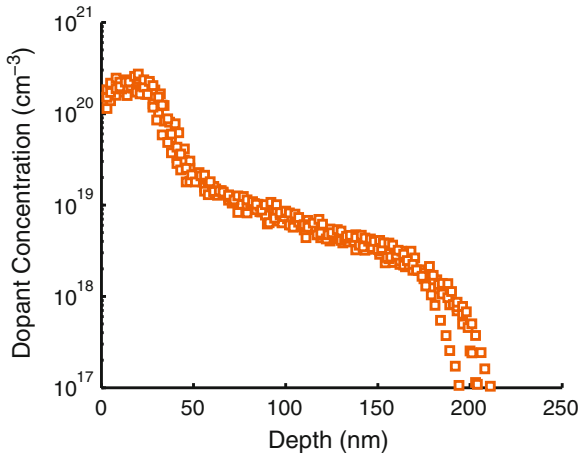


Fig. 4.5 Electrically active dopant concentration profiles for phosphorus predeposition at 800 °C for 35 min. The electrically active concentration was measured via spreading resistance analysis (SRA). The profile consists of a constant concentration surface region, a kink in the transition region, and a fast-diffusing tail due to variation in diffusivity with concentration. Four SRA profiles from separate wafers are plotted for comparison (Source Reprinted with permission from [2])

We will only investigate phosphorus predeposition because a simple, accurate dopant profile model is available and due to the practical issues with boron (B:Si formation) and arsenic (only gas-phase sources). Phosphorus predeposition is widely used and has been researched extensively [330 – 333]. Typical concentration profiles for phosphorus predeposition are shown in Fig. 4.5. Phosphorus predeposition in particular yields concentration profiles with a characteristic plateau and kink, and more sophisticated modeling approaches are required to accurately model diffused piezoresistors.

We calculate dopant concentration profiles for phosphorus predeposition using Tsai's 1969 model [330]. Although more advanced models have since been developed [334, 335], we have used the Tsai model to accurately model dopant concentration and sheet resistance for processing temperatures from 775 to 950 °C. The model is simple to implement, computationally inexpensive, and accurate. In our experience, TSUPREM-4™ did not accurately reproduce the dopant concentration profiles measured experimentally. The Tsai model is implemented in our design optimization and piezoresistor modeling software (Appendix C).

In Tsai's model, the dopant profile consists of three regions: a surface layer, a transition region, and a normal diffusion region. The dopant concentration is constant in the surface region. The dopant profile consists of slow and fast diffusion processes, and the concentration beyond the surface region is determined by their sum. The slow diffusion process, with diffusivity D_A , determines the dopant concentration in the transition region. The fast diffusion process, with diffusivity D_B , determines the dopant concentration in the normal region. More specifically,

$$C(x, t) = C_S \quad \text{for } x \leq x_0 \quad (4.8)$$

$$C(x, t) = C_A(x, t) + C_B(x, t) \quad \text{for } x > x_0. \quad (4.9)$$

The depth of the surface layer is $x_0 = \alpha t$ where t is the time in seconds and α is the growth rate of the surface phase. The surface concentration, C_S , is the total dopant concentration (4.1). The concentration profile is calculated using the total phosphorus concentration before being capped at the electrically active concentration limit (4.2).

The slow and fast diffusing components are calculated from

$$C_A(x, t) = \frac{1 - \kappa}{2} C_S \exp \left[-\frac{\alpha}{2D_A} (x - \alpha t) \right] F_1(x, t) \quad (4.10)$$

$$C_B(x, t) = \frac{\kappa}{2} C_S \exp \left[-\frac{\alpha}{2D_B} (x - \alpha t) \right] F_2(x, t) \quad (4.11)$$

where $\kappa = C_B(x_0)/C_S$ and

$$F_1(x, t) = \operatorname{erfc} \left(\frac{x + \alpha t}{2\sqrt{D_A t}} \right) + \operatorname{erfc} \left(\frac{x - 3\alpha t}{2\sqrt{D_A t}} \right) \quad (4.12)$$

$$F_2(x, t) = \operatorname{erfc} \left(\frac{x + \alpha t}{2\sqrt{D_B t}} \right) + \operatorname{erfc} \left(\frac{x - 3\alpha t}{2\sqrt{D_B t}} \right). \quad (4.13)$$

There are four model parameters: D_A , D_B , α and $C_B(x_0)$. However, they vary with temperature and are modeled via Arrhenius kinetics as

$$D_A = D_{A0} \exp \left(-\frac{E_{DA}}{k_b T} \right) \quad (4.14)$$

$$D_B = D_{B0} \exp \left(-\frac{E_{DB}}{k_b T} \right) \quad (4.15)$$

$$\alpha = \alpha_0 \exp \left(-\frac{E_\alpha}{k_b T} \right) \quad (4.16)$$

$$C_B(x_0) = C_{B0} \exp \left(-\frac{E_{CB}}{k_b T} \right) \quad (4.17)$$

and there are a total of eight fitting parameters. To verify the model and provide fitting parameter estimates, Tsai doped samples from 820 to 1100 °C via POCl₃ predeposition. He measured the electrically active dopant concentration profiles by iteratively anodically oxidizing the samples and measuring their sheet resistances. We have measured phosphorus predeposition dopant concentration profiles using spreading resistance analysis (SRA) and sheet resistance data. Our best fit parameters for POCl₃-based predeposition from 775 to 950 °C and 10–60 min are presented in Table 4.3.

Figure 4.6 compares the computed and measured electrically active concentration profiles for predeposition at 800 °C for 35 min. The agreement between the model

Table 4.3 Best fit parameters for the Tsai model of phosphorus predeposition obtained by fitting to experimentally measured spreading resistance profiles

Prefactor	Activation energy
D_A	$200 \text{ cm}^2/\text{sec}$
D_B	$2.3 \times 10^{-5} \text{ cm}^2/\text{sec}$
α	0.12 cm/sec
C_B	$3 \times 10^{23} \text{ cm}^{-3}$
	$1.65 \text{ eV} + 0.05 \text{ eV} \exp[-0.015 \frac{1}{K}(T - 1073 \text{ K})]$
	0.88 eV

The α activation energy varies with temperature to accurately model low temperature predeposition processes ($< 820^\circ\text{C}$) where phosphorus diffusion through a surface oxide layer can become the rate limiting step

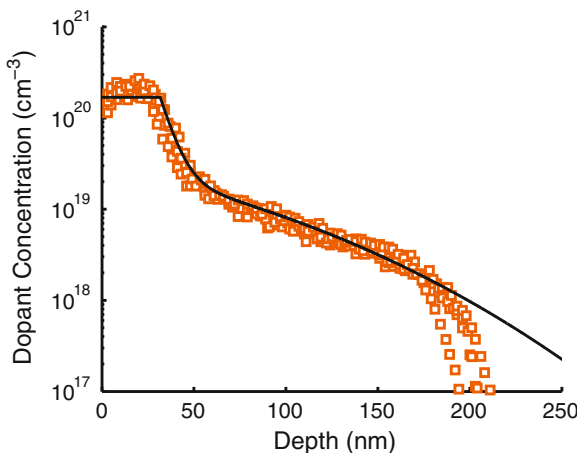


Fig. 4.6 Comparison between experimental and modeled dopant profiles for phosphorus predeposition 800°C for 35 min. The plateau, kink, and tail regions of the profile are captured. The model overestimates the dopant concentration beyond 200 nm ($< 10^{18} \text{ cm}^{-3}$), however there is no impact on piezoresistor modeling accuracy because the vast majority of the current is carried near the surface (Source Reprinted with permission from [2])

and experiments is excellent, and the three profile regions (plateau, kink, and tail) are captured by the model. Figure 4.7 compares the modeled and measured sheet resistance values from 775 to 950°C . The model error is less than 10 % for all of the measured data points.

We found that α decreases more than expected for processing temperatures below 825°C . Tsai also noted lower than expected values of α at low temperatures, and did not use the 820°C data in calculating the model parameter estimates. The most likely mechanism is that the diffusivity of phosphorus in SiO_2 is relatively slow and varies dramatically with temperature. Most phosphorus predeposition processes include an initial oxidation step (e.g. 2–5 min) to prevent surface pitting and roughness. Thus, diffusion through surface SiO_2 can become the rate limiting diffusion process at temperatures below 825°C .

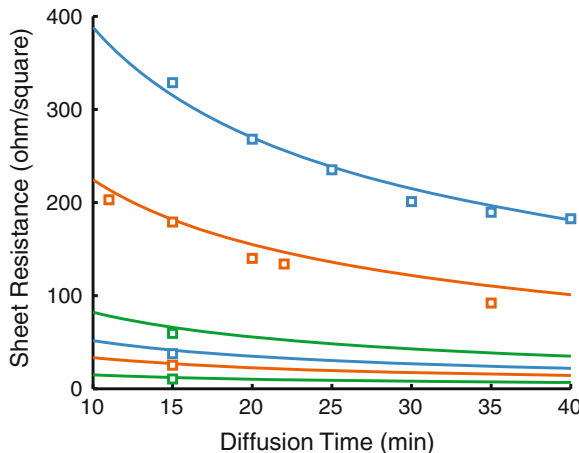


Fig. 4.7 Comparison between experimental and modeled sheet resistance data. Phosphorus predeposition was performed at temperatures from 775 to 950 °C and the sheet resistance was measured via 4-point probe. The model error is less than 10 % for all of the measured data points. The curves in the plot correspond to 775, 800, 850, 875, 900 and 950 °C, from top to bottom (Source Reprinted with permission from [2])

The relatively slow diffusion of phosphorus through SiO₂ makes it an excellent masking material. Sah et al. measured the diffusivity of phosphorus in SiO₂ in 1959 [336]. Their data was later reanalyzed by Ghezzo and Brown and tabulated with other common silicon dopants [337]. The diffusivity of other dopants in SiO₂ and other materials can be found in an unpublished book chapter by Jones [307].

Phosphorus diffusion in SiO₂ obeys Arhenius kinetics with $E_a = 2.3\text{eV}$ and $D_0 = 5.73 \times 10^{-5}\text{cm}^2/\text{s}$ [337]. The diffusion length of phosphorus in SiO₂ is plotted in Fig. 4.8. Our own experimental measurements indicate a 60 nm phosphorus diffusion length during a 900 °C, 20 min diffusion. We measured the diffusion length by measuring the thickness of the thermal oxide mask before the diffusion, and then afterwards removing the deposited PSG and doped oxide layer in 50:1 hydrofluoric acid before measuring the remaining oxide thickness. Dilute HF etches undoped oxide exceedingly slowly (50 Å/min) compared to phosphorus doped oxide (>3000 Å/min). The minimum required oxide mask thickness (or maximum diffusion time) can be calculated by equating the diffusion length and oxide thickness, $2\sqrt{Dt} = t_{\text{oxide}}$, with a safety factor of at least three. Note that the diffusion of phosphorus in PSG is significantly slower than in SiO₂, yielding a diffusion length on the order of 60 nm after an anneal at 1100 °C for several hours [307].

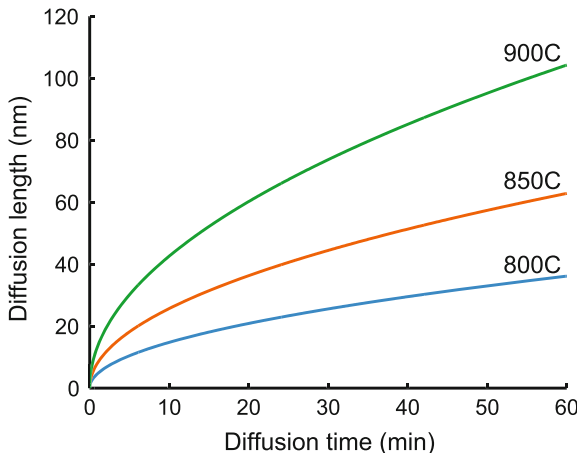


Fig. 4.8 Calculated phosphorus diffusion lengths in SiO_2 as a function of predeposition time and temperature. Calculated results agree well with our experimental observations of the thickness of phosphosilicate glass (PSG) removed with a brief hydrofluoric acid (HF) dip (*Source* Reprinted with permission from [2])

4.4 Ion Implantation

Two important downsides of predeposition are its high surface dopant concentration, fixed at the dopant solid solubility limit, and its relatively high dose nonuniformity due to the strong variation in diffusivity with temperature. Ion implantation was researched extensively in the 1950s and 1960s as an alternative to predeposition that could provide better dose uniformity and lower dopant concentrations [338 – 340]. The depth distribution of implanted ions and their electrical properties were studied extensively using the Hall effect and analytical theories [341 – 344].

The lattice damage induced by ion implantation was recognized early on [345, 346]. There are several excellent reviews on the history of ion implantation [347, 348] and modern ion implantation theory and simulation tools are discussed extensively by Plummer et al. [3]. Ion implantation gained wide use in the 1980s and remains the preferred method in commercial production today, although advanced CMOS nodes primarily rely on plasma-immersion ion implantation rather than conventional beamline ion implantation to form ultrashallow junctions [349].

In ion implantation, dopant atoms are ionized and accelerated at high energy (keV to MeV) into the substrate. The substrate is grounded, which allows the implanted dose to be measured and accurately controlled by integrating the ion current [3]. Additionally, grounding the substrate allows the ionized atoms to be neutralized immediately. The ions also leave a cascade of damage in the crystal structure[345]. Any layer thick or dense enough to block the implanted ions can be used to mask the implantation such as photoresist, silicon dioxide, silicon nitride, or metal. Typical silicon piezoresistor doses range from 1×10^{14} to $5 \times 10^{16} \text{ cm}^{-2}$, with energy

ranges from 30 to 150 keV [6]. The typical sheet resistance nonuniformity is <0.5 % in modern ion implanters [350]. Most implants are performed with a 7° tilt of (100) silicon wafers to avoid ion channeling, a phenomenon where ions deeply traverse gaps in the lattice without scattering. Larger implant angles (7–45°) are sometimes used to form piezoresistors on etched sidewalls to enable in-plane strain measurements [89, 90, 102, 177, 179].

The major disadvantage of ion implantation is lattice damage and the increase in 1/f noise that accompanies it. A short high temperature anneal after ion implantation is required to activate the implanted dopants [345]. A longer anneal is required to restore lattice order and improve the 1/f noise characteristics of the device (Sect. 3.1.3). However, shallow junctions are difficult to obtain with high crystal quality, so ion implantation is problematic for flexural piezoresistive sensors where conduction needs to be tightly confined to the surface. Some researchers have used low energy [305], higher mass ions [120], or intentional lattice damage [351] to extend ion implantation to shallower piezoresistors. Parameters that affect the junction depth include the acceleration energy, the ion mass, and the stopping power of the material [342].

The damage induced by ion implantation can lead to complex dopant activation and diffusion behavior, making a numerical approach necessary [352]. Other issues that make a numerical approach necessary are oxidation enhanced diffusion, dopant segregation at the oxide interface, and diffusivities that vary with dopant concentration and lattice defect densities. We will present tabulated ion implantation results for quickly and efficiently calculating the electrical properties of ion implanted piezoresistors.

Numerical design optimization requires a large number of computational steps. Finding the design optimum from a random initial design might require 5,000 iterations of the optimization algorithm. At each step, the algorithm determines how to improve the design by computing the gradient of the target function in the basis defined by the design parameters. If two of the parameters affect the dopant profile (e.g. predeposition temperature and time), then the dopant profile will need to be computed up to 10,000 times. Calculation of the dopant concentration profile should take less than 1 ms to enable fast design optimization.

Thus, we take the approach presented by Park in 2010 of computing a lookup table for dopant profile dependent parameters: β^* , N_z^{eff} , R_s and t_j [133, 295]. For this book we extended the lookup table to include multiple dopant species (only boron was included in the original table) and integrated the results into our open source design software, piezoD (Appendix C). The automatic table generation scripts are included in piezoD so can be used to generate new tables as required.

The most immediate problem with providing a lookup table for β^* is that it depends on sensor thickness. Calculating a β^* lookup table for every possible thickness isn't practical, but β^* can be reformulated to be thickness independent. We do so by shifting the coordinate system in (3.62) from the neutral axis to the sensor surface by introducing $z' = t/2 - z$, yielding

$$\beta^* = \frac{2}{t} \frac{\int_{-t/2}^{t/2} P \mu n(t/2 - z') dz'}{\int_{-t/2}^{t/2} \mu n dz'} \quad (4.18)$$

$$= \beta_1^* - \frac{2}{t} \beta_2^* \quad (4.19)$$

where t is the thickness of the sensor (e.g. cantilever beam or membrane thickness). The two new parameters, β_1^* and β_2^* , are defined by

$$\beta_1^* = \frac{\int_0^{t_j} P \mu n dz'}{\int_0^{t_j} \mu n dz'} \quad (4.20)$$

$$\beta_2^* = \frac{\int_0^{t_j} P \mu n z' dz'}{\int_0^{t_j} \mu n dz'} \quad (4.21)$$

where t_j is the junction depth. The first parameter, β_1^* , does not have any position dependence, so is just a conductivity weighted average of the piezoresistance factor. If the dopant concentration is low then β_1^* will be high. The second parameter, β_2^* , is a stress and conductivity weighted average of the piezoresistance factor. If the dopant atoms are near the surface, then $\beta_2^* \rightarrow 0$ and $\beta^* \rightarrow \beta_1^*$. However, if the dopants are distributed uniformly over the sensor thickness, then $\beta_2^* \rightarrow \beta_1^* t/2$ and $\beta^* \rightarrow 0$.

If we compare (3.65) and (4.20), we note that $\bar{P} = \beta_1^*$. Thus, the data we tabulate for ion implanted piezoresistors can be used to design sensors where the strain is constant over the entire cross-section ($\bar{P} = \beta_1^*$) in addition to cases where the strain varies linearly across the cross-section ($\beta^* = \beta_1^* - 2\beta_2^*/t$).

Separating β^* into β_1^* and β_2^* allows us to precompute β^* for arbitrary sensor thickness. By running a large number of TSUPREM-4™ simulations offline, we calculate a lookup table for all of the parameters that vary with the dopant concentration profile (β_1^* , β_2^* , N_z^{eff} , R_s and t_j) and quickly look them up during numerical optimization.

We computed ion implantation lookup tables for arsenic, boron and phosphorus over a wide range of process conditions using TSUPREM-4™. The basic fabrication process used in the simulations is noted in Table 4.4. After the wafers are ion implanted they are annealed to activate the dopants and reduce lattice damage from

Table 4.4 Process parameters used in the TSUPREM-4™ ion implantation simulations

Process	Parameters
(1) Grow 250 Å screening SiO ₂	Wet O ₂ (850 °C, 17 min)
(2) Ion implantation	B, As, or P, $2 \times 10^{14} - 2 \times 10^{16}$ cm ⁻² , 20–80 keV
(3) Strip screening SiO ₂	N/A
(4) Wet oxidation (optional)	900, 1000, or 1100 °C for 66, 15 or 5 min
(5) Inert N ₂ anneal	900, 1000 or 1100 °C for 15–120 min

A range of conditions are simulated and a lookup table is precomputed to make numerical design optimization viable

the implantation step. The implantation step was modeled within TSUPREM-4™ using a dual Pearson distribution. The implant moment tables used to calculate the profiles included full energy, dose and tilt dependence. The models used for dopant activation and diffusion included dopant-defect clustering, oxidation-enhanced diffusion, concentration and damage effects, transient defect generation, pairing and recombination.

The data were calculated for implantation energies of 20, 50 and 80 keV, doses of 2×10^{14} , 2×10^{15} and $2 \times 10^{16} \text{ cm}^{-2}$, post-implantation anneal temperatures of 900, 1000 and 1100 °C, and anneal times ranging from 15 to 120 min in 15 min increments. A 250 Å thick oxide layer is grown before the implantation step to protect the silicon from contamination. We assumed a wafer tilt of 7° to avoid ion channeling and a background resistivity of 10 Ω-cm. The simulation input file, like the rest of our numerical modeling code, is open source and freely available (Appendix C).

We assumed two different conditions for the anneal. In the first we assumed that the wafers were oxidized in steam to obtain a 1500–2000 Å thick passivation oxide before performing the inert anneal. In the second condition we assumed that the wafers were not oxidized and the anneal was performed only in an inert atmosphere. In the first case, the passivation oxide was grown at 900, 1000, or 1100 °C for 66, 15 or 5 min, respectively. If a passivation oxide will be regrown during the anneal step then the 250 Å thick protection oxide should be stripped first. However, if the wafer will not be reoxidized then the protection oxide should be left in place during the anneal and stripped afterwards to prevent dopant outgassing.

A total of 1296 different process flows were simulated to build the lookup tables. To efficiently compute the data we used two scripts and a Python template for the TSUPREM-4™ input file. The first script inserted the appropriate dopant, energy, dose, temperature and time into the template, generating a set of TSUPREM-4™ input files. After running the simulations, the script saved the concentration profiles, where the second script aggregated the data into a relatively small (3 MB) MATLAB®(Mathworks, Cambridge, MA) data file. The two scripts and template are presented in Appendix C. The lookup tables could be readily extended to an alternative process flow or larger design parameter space. The simulations took about 12 h to run but lookup table operations take less than a millisecond.

There are five process parameters that determine the dopant profile for ion implanted piezoresistors: the dopant, the implanted dose and energy (N_{implant} and E_{implant}), and the time and temperature of the inert anneal (t_{anneal} and T_{anneal}). The lookup tables in Appendix B provide β_1^* , β_2^* , N_z^{eff} , R_s and t_j over a wide process parameter range.

Variations in the initial, as-implanted dopant concentration profile with changes in energy and dose are shown in Fig. 4.9. The simulations were run for boron implanted at energies of 20, 50 and 80 keV at a dose of $2 \times 10^{15} \text{ cm}^{-2}$ and for an energy of 50 keV with doses of 2×10^{14} , 2×10^{15} and $2 \times 10^{16} \text{ cm}^{-2}$. The concentration and mean projected range scale roughly linearly with the dose and ion energy, respectively, over the range that we will simulate for piezoresistor fabrication [342].

Figure 4.10 demonstrates the evolution of the dopant concentration profile over time. For the simulation, phosphorus ions were implanted at 50 keV and a dose of

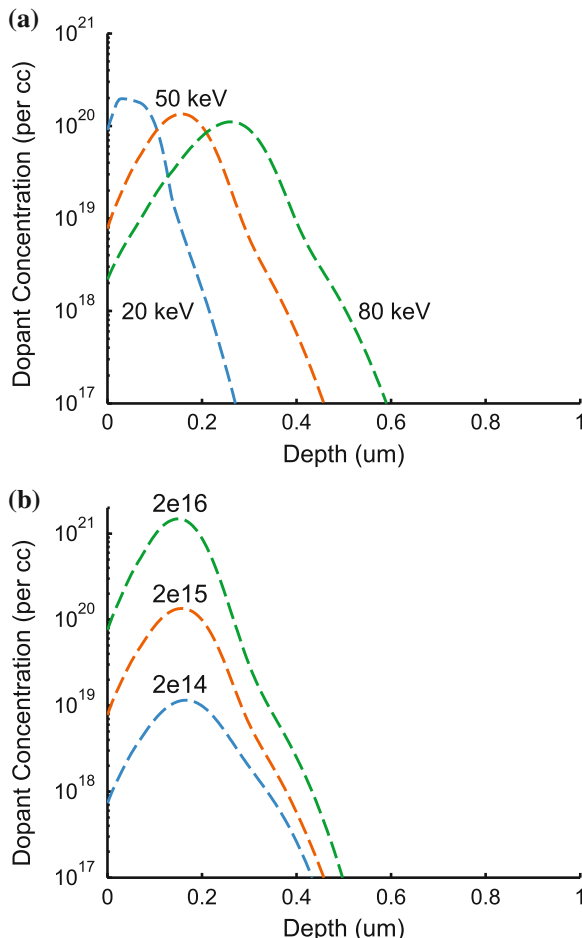


Fig. 4.9 Variation in the as-implanted dopant concentration profile with energy and dose. **a** Results for a boron dose of $2 \times 10^{15} \text{ cm}^{-2}$ at 20, 50 and 80 keV. **b** Results for an implant energy of 50 keV and doses of 2×10^{14} , 2×10^{15} and $2 \times 10^{16} \text{ cm}^{-2}$. The concentration and mean projected range scale roughly linearly with dose and energy, respectively (Source Reprinted with permission from [2])

$2 \times 10^{15} \text{ cm}^{-2}$ before being annealed at 900°C for 15 or 120 min. The passivation oxide was not regrown before the anneal, but the protection oxide from the implantation step was left in place as discussed earlier. The dopant atoms are initially located within the first 200 nm from the surface (dashed line) but they are not electrically active. The anneal is required to activate them and anneal out lattice damage induced by the ion implantation. At high implantation doses (e.g. $2 \times 10^{16} \text{ cm}^{-2}$) the damage can be great enough to make the crystal amorphous. In that case, the anneal restores the crystallinity of the lattice through epitaxial regrowth by using undamaged material as a growth template.

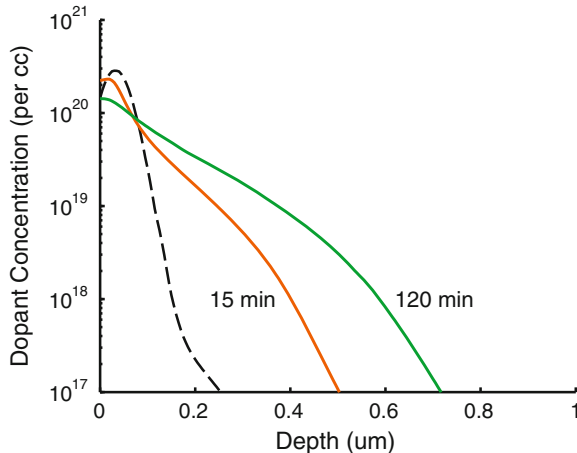


Fig. 4.10 Comparison between the initial phosphorus concentration profile (dashed line) and concentration profiles after 15 and 120 min of annealing at 900 °C. The profiles are calculated for a 50 keV implant with a dose of $2 \times 10^{15} \text{ cm}^{-2}$. The dopants are not electrically active initially, and the anneal integrates them into the crystal lattice and reduces implantation-induced lattice damage. Increasing the temperature or duration of the anneal impacts the noise and sensitivity of the sensor in a variety of ways (Source Reprinted with permission from [2])

The parameters chosen for the anneal affect sensor performance in several ways. Increasing either the time or temperature of the anneal increases the diffusion length, which reduces 1/f noise by reducing the Hooge factor (Sect. 3.1.3). Increasing the temperature leads to an increase in the solid solubility limit (Sect. 4.2), which can increase the dopant concentration near the surface if the dose is high enough that the dopant concentration is limited by solubility. A higher temperature, assuming that the time is reduced to maintain a constant diffusion length, accordingly leads to a smaller piezoresistance factor but shifts conduction closer to the surface, decreasing both β_1^* and β_2^* .

Increasing the duration of the anneal, in contrast, reduces the concentration near the surface and shifts the conduction further from the surface, increasing both β_1^* and β_2^* . Sensors with constant strain through their thickness (e.g. strain gauges) do not depend on β_2^* for their operation, so a longer anneal and lower dopant concentration is good from a sensitivity standpoint but bad from the standpoint of temperature stability. Sensors with a linear strain gradient through their thickness (e.g. pressure sensors) will experience either increased or decreased sensitivity depending on the thickness of the sensor, which determines the relative weighting of β_1^* and β_2^* (4.19).

Figure 4.11 compares dopant concentration profiles for arsenic, boron and phosphorus in processes with and without the growth of a passivation oxide. The profiles are calculated for 50 keV, $2 \times 10^{15} \text{ cm}^{-2}$ implants that are annealed in an inert atmosphere at 900 °C for 60 min. In the passivated process, a 1500–2000 Å thick passivation oxide is grown before the inert anneal. The depth of the piezoresistor

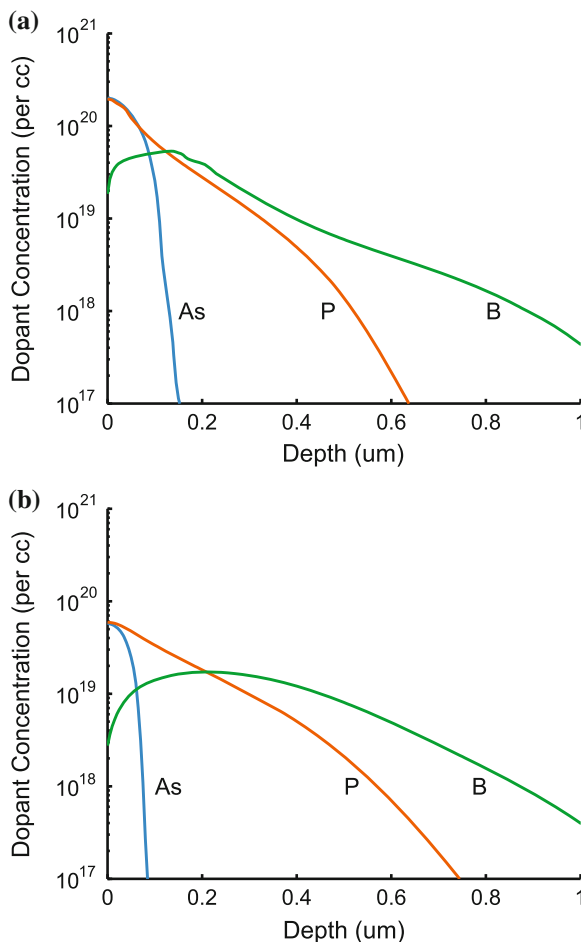


Fig. 4.11 Comparison between As, B and P concentration profiles after implantation and annealing without **a** inert and **b** with a passivation oxide regrowth step. The profiles are calculated for 50 keV, $2 \times 10^{15} \text{ cm}^{-2}$ implants that are annealed in an inert atmosphere at 900 °C for 60 min. The depth of the piezoresistor increases going from arsenic to phosphorus to boron as the atomic mass of the dopant decreases and the dopant diffusivity increases. The oxidation step modifies the concentration profiles through oxidation-enhanced diffusion, dopant segregation and the increased time at high temperature (*Source* Reprinted with permission from [2])

increases going from arsenic to phosphorus to boron as the atomic mass of the dopant decreases (75, 31 and 10.8 amu, respectively) and the dopant diffusivity increases. The peak concentration of boron is lower than either arsenic or phosphorus due to its lower solid solubility limit and higher diffusivity. The oxidation step modifies the concentration profiles through oxidation-enhanced diffusion, dopant segregation at the Si–SiO₂ interface and the increased time at high temperature.

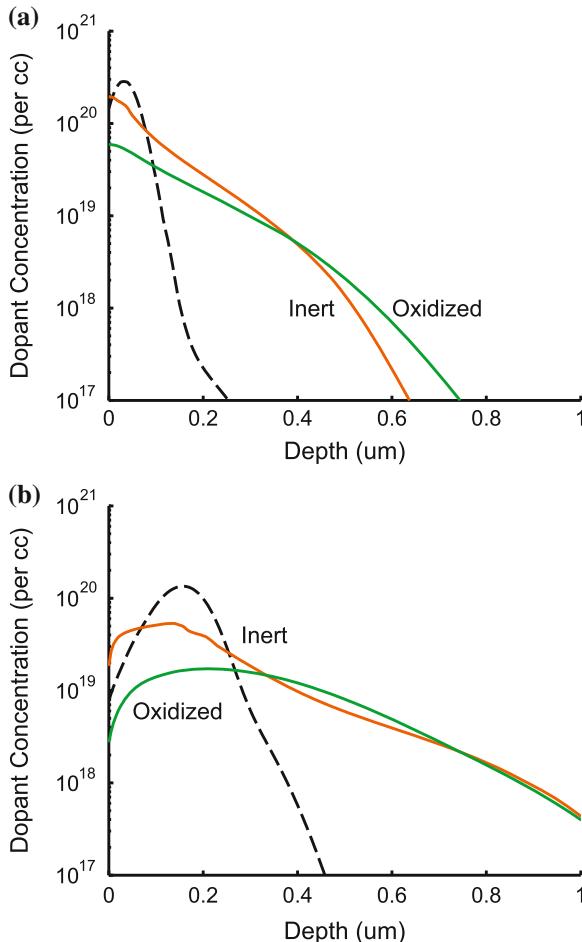


Fig. 4.12 Comparison between **a** phosphorus and **b** boron concentration profiles with and without the regrowth of a passivation oxide immediately before the anneal. The profiles are calculated assuming a 50 keV, $2 \times 10^{15} \text{ cm}^{-2}$ implant and an inert anneal at at 900°C for 60 min. Oxidation modifies the surface concentration due to dopant segregation and the diffusion length increases due to oxidation-enhanced diffusion and the additional time at high temperature (*Source* Reprinted with permission from [2])

Figure 4.12 compares dopant profiles for phosphorus and boron for anneals with and without the growth of a passivation oxide. Both profiles extend slightly deeper into the silicon due to oxidation-enhanced diffusion and the increased time at high temperature. However the difference is particular significant for boron, where the surface concentration has decreased approximately 20-fold.

Oxidation particularly causes the dopants to redistribute at the surface. Silicon at the surface is consumed during the oxidation, and the dopant atoms once contained

in those layers either preferentially shift into the oxide or follow the silicon interface, causing pileup at the surface. A segregation coefficient less than one indicates that the dopants will segregate into the oxide, while a coefficient greater than one indicates that the dopants will pileup at the silicon interface. The segregation coefficient of boron is about 0.3 while the coefficients for arsenic and phosphorus are more than 1000 [307, 353]. Including a reoxidation step reduces the surface concentration of boron 20-fold while only reducing the surface concentrations of arsenic and phosphorus by a factor of two. While the presence of the 250 Å thick protection oxide (in the case where the oxide is not regrown) does modify the profile slightly, the impact is much less than the reoxidation case.

The Tables in Appendix B can be used to calculate β_1^* , β_2^* , N_z^{eff} , R_s and t_j for arsenic, boron and phosphorus implantation over a wide design parameter range. While the printed tables are useful as a reference, actual design and modeling work should be done using the .mat lookup table distributed with our design optimization code. For design optimization, we allow the process parameters to vary continuously by linearly interpolating between the simulated parameter combinations. The lookup table used for optimization also includes the dopant concentration profile up to 5 μm from the wafer surface at 10 nm intervals, allowing the raw simulation data to be recovered.

4.5 Epitaxy

The primary performance limitation of ion implantation for piezoresistor fabrication is the diffusion that necessarily accompanies dopant activation and annealing, which is addressed through epitaxial piezoresistor growth. Conventional epitaxial growth is performed at high temperatures (800–1300 °C) and reduced pressure (10–200 Torr). The four most commonly used silicon gas sources are silicon tetrachloride (SiCl_4), trichlorosilane (SiHCl_3), dichlorosilane (SiH_2Cl_2), and silane (SiH_4) [3]. A clean surface is necessary to obtain a high quality epitaxial layer. Contaminants and native oxide will prevent single-crystal growth. An in-situ HCl clean can remove wafer contaminants and native oxide. Halide source gases are used to grow silicon with the advantage that chlorine is one of the net byproducts. The chlorine removes metal contaminants from the deposited silicon film, resulting in better quality single-crystal silicon.

Selective epitaxy is the deposition of single crystal silicon only on silicon surfaces rather than all exposed surfaces. Joyce and Baldrey first demonstrated the selective deposition of silicon epitaxial layers in 1962 using silicon tetrachloride at 1200 °C and an oxide mask [354]. The presence of hydrochloric acid (HCl), whether from silicon source gas as in silicon tetrachloride or in a separate gas flow, acts to suppress the nucleation of silicon clusters on surfaces less favorable for growth than bare silicon. The HCl continuously etches the silicon, and due to the higher concentration of silicon atoms required on a dielectric surface to nucleate a grain, it is possible to continuously remove silicon from atop a dielectric layer while depositing on the

exposed single crystal silicon. Silicon dioxide is generally used as a masking layer, although silicon nitride has also been demonstrated. Since its initial development, selective epitaxy has been optimized to work at lower temperatures, allowing for less dopant diffusion [3, 335 – 359].

Silicon tetrachloride is widely used because it is stable, has a low vapor pressure and leaves little excess coating on the reaction chamber. However, it requires a high temperature for the reaction to proceed (1100–1300 °C). Silane is widely used for the deposition of polysilicon, but is not favored for epitaxy or selective epitaxy because of its lower deposition rate at any given temperature compared to chlorinated silicon sources [357]. Of the remaining gases, dichlorosilane (DCS) is optimal for selective silicon epitaxy due to its low deposition temperature, high rate of deposition, low nucleation rate on silicon dioxide, and good selectivity at reduced pressure [360]. Epitaxial silicon films may be doped during the deposition by introducing appropriate dopant source gases such as AsH₃, PH₃, or B₂H₆ into the chamber along with the silicon source gases.

The reactions for the deposition of silicon from dichlorosilane are



The second reaction is reversible, and the growth rate is reduced by an increase in the HCl concentration. Selectivity improves as the temperature, pressure, or growth rate are decreased, or as the HCl concentration is increased [356]. Selective epitaxy at atmospheric pressure typically requires the addition of HCl, with a typical combination of gases being DCS, H₂ and HCl. At pressures of less than 100 torr, the addition of HCl is not required because the critical size for grain growth of the silicon on the dielectric is larger [361].

Epitaxial silicon does not require annealing to activate the dopants or reduce lattice disorder. Without an additional annealing step, dopants diffuse less and the dopant concentration profile can approximate a sharp step. Harley [84] and Liang [119] demonstrated the use of epitaxially grown doped silicon to form piezoresistors in ultra-thin cantilevers less than 100 nm thick.

The dopant concentration profile of an epitaxial piezoresistor, including dopant diffusion, can be calculated from

$$N = \frac{N_{\text{epi}}}{2} \operatorname{erfc} \left(\frac{z - t_{\text{pr}}}{2\sqrt{Dt}} \right) + N_{\text{B}} \quad (4.24)$$

where z is the distance from the exposed surface, N_{epi} is the dopant concentration of the epitaxial layer, t_{pr} is the overall piezoresistor thickness, D is the dopant diffusivity, t is the processing time and N_{B} is the background concentration. The piezoresistor thickness is not well defined for diffused or ion implanted piezoresistors, so we will only use t_{pr} in discussing epitaxial piezoresistors.

When the diffusion length is relatively short compared to the piezoresistor thickness, the concentration profile can be approximated as a concentration step where

$$N(z) = N_{\text{epi}} \quad \text{for } z \leq t_{\text{pr}} \quad (4.25)$$

$$= N_B \quad \text{for } z > t_{\text{pr}}. \quad (4.26)$$

However, if there is significant dopant diffusion from either a low epitaxial deposition rate or subsequent high temperature processing, the simplified step model is not accurate and (4.24) should be used instead or the profile should be modeled using TSUPREM-4™ or another numerical modeling package.

Figure 4.13a compares epitaxial boron dopant profiles over a range of deposition rates for a 100 nm thick piezoresistor grown at 900 °C and doped to $5 \times 10^{19} \text{ cm}^{-3}$. Curves are plotted for growth times of 10, 100 and 1000 min. Concentration profiles were calculated from (4.24). The growth rate, diffusion length, sensitivity factor and sheet resistance for each profile are presented in Table 4.5. The growth rates used are all relatively slow; growth rates on the order of 300 nm/min have been reported for selective epitaxy at 900 °C [361].

There is almost no change in β^* until the diffusion length is on the order of the piezoresistor thickness (Fig. 4.13b). Similarly, there is only a small change in the sheet resistance (due to the higher mobility at lower concentrations). Thus, a step profile can be used to model epitaxial piezoresistor with negligible error (<5%). More detailed, numerical models (e.g. TSUPREM-4™) can be used once a design has been optimized using the approximate model. Diffusion during epitaxial growth has an insignificant impact on piezoresistor sensitivity unless the growth rate is exceptionally low or additional thermal processes are performed.

The electrical and piezoresistive properties of an epitaxial piezoresistor with negligible diffusion can be calculated as

$$\beta^* = P(1 - t_{\text{pr}}/t), \quad (4.27)$$

$$\overline{P} = P, \quad (4.28)$$

$$R_s = \rho/t_{\text{pr}}, \text{ and} \quad (4.29)$$

$$N_z^{\text{eff}} = N_{\text{epi}} t_{\text{pr}}. \quad (4.30)$$

where P is calculated as a function of dopant concentration from (2.27). Calculation of the resistivity (ρ) will be discussed in Sect. 4.7. Epitaxial piezoresistors are far simpler to model than their diffused or ion implanted counterparts, which makes them useful for quickly designing a device before shifting to more complicated numerical models.

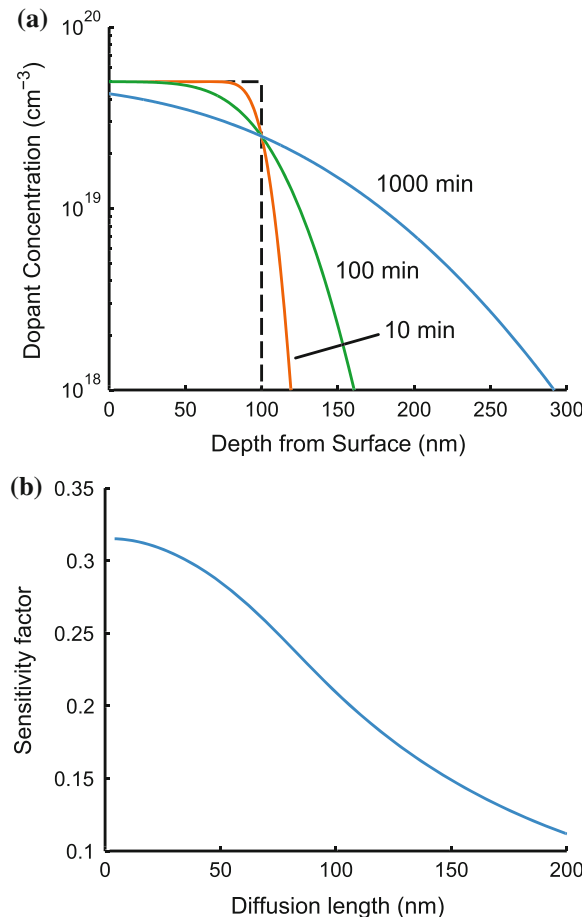


Fig. 4.13 Dopant diffusion during epitaxial growth. **a** Concentration profiles for a phosphorus doped 100 nm thick epitaxial resistors grown at 900 °C for 10, 100 and 1000 min. The dashed line denotes the ideal step concentration profile. **b** The sensitivity factor, β^* , decreases as the diffusion length increases from its maximum possible value of β_0^* if no diffusion occurred (Source Reprinted with permission from [2])

Table 4.5 The sensitivity factor and sheet resistance for three different boron epitaxy growth rates

	10 min	100 min	1000 min
Growth rate (nm/min)	10	1	0.1
Diffusion length (nm)	13	42	132
Sensitivity factor (-)	0.33	0.31	0.17
Sheet resistance (ohm/sq)	185	175	148

The sensitivity factor remains roughly constant until the diffusion length during epitaxial deposition is comparable to the piezoresistor thickness

4.6 Polysilicon

The preceding discussion of diffusion, ion implantation and epitaxy implicitly focused on single crystal silicon. However, piezoresistors are also often fabricated from polycrystalline silicon films, usually referred to as polysilicon or poly. Polysilicon is deposited using the same LPCVD processes as epitaxial silicon, but at lower temperatures or higher rates so that there is insufficient time or thermal energy to eliminate grain boundaries.

Polysilicon can be doped using diffusion, ion implantation, or in-situ doping by introducing gas-phase dopants with the precursor polysilicon gases during the CVD process. However, the introduction of dopant gases affects the polysilicon deposition rate, thickness uniformity, grain size and film stress [3]. Depending upon the polysilicon deposition temperature, it can be amorphous, microcrystalline or polycrystalline. After polysilicon deposition, the wafers are often annealed at a high temperature (800–1100 °C) to relieve stress and alter the grain structure. While the properties of single crystal silicon piezoresistors are well known and reproducible, polysilicon piezoresistor properties vary significantly with the deposition, anneal and doping conditions, because they determine the orientation and size distribution of the grains.

Piezoresistive effects in polysilicon were studied extensively in the 1970 and 1980s. Onuma and Sekiya [362] first reported the piezoresistive properties of polysilicon in 1972. Two years later, Gurtler and Zwernemann filed a patent for polysilicon piezoresistive pressure sensors [363]. Seto further reported on the electrical and piezoresistive properties of polysilicon in 1975 and 1976 [364, 365]. In 1981, Lu and Mandurah separately reported on models for electrical conduction in polysilicon [366 – 369], and Mikoshiba reported on the stress sensitivity of CMOS devices with polysilicon gates [370]. Germer [371] and Erskine [372] reported on piezoresistive devices utilizing polysilicon piezoresistors in 1983. Finally, in 1984 [373] and 1989 [374], French and Evans presented theoretical models for piezoresistance in polysilicon as a function of doping, grain size, and orientation and proposed an optimum set of processing parameters for a given grain size.

We primarily focus on the design of single crystal silicon piezoresistors in this book because they are more widely used in both research and commercial production. Perhaps more importantly, the mechanical, piezoresistive, electrical and thermal properties of single crystal silicon are predictable and can be accurately modeled with less reliance on empirical methods.

However, the models and methods that are presented can be applied to polysilicon piezoresistors once the grain distribution and dopant concentration profile are empirically determined. We recommend Madou [375] and Bao [376] for detailed discussions of polysilicon fabrication and characterization techniques.

4.7 Electrical Modeling

In the last section we calculated the dopant concentration profile, $N(z)$. In this section, we will use the dopant concentration profile to calculate the carrier concentration and resistivity profiles, $n(z)$ and $\rho(z)$. Minority carriers do not affect the operation of piezoresistive sensors, and we will ignore them for the most part.

Both intrinsic and extrinsic carriers can potentially contribute to the carrier concentration. The intrinsic carrier concentration is exceedingly small near room temperature ($\approx 10^{10} \text{ cm}^{-3}$) but contributes to the concentration of carriers at elevated temperatures (e.g. $n_i = 10^{17} \text{ cm}^{-3}$ at $T = 900 \text{ K}$).

The intrinsic carrier concentration is calculated from the empirical fit of Trupke et al. as [377]

$$n_i = 2.9135 \times 10^{15} T^{1.6} \exp\left(\frac{-E_g}{2k_b T}\right) \quad (4.31)$$

where E_g is the bandgap energy, which also varies with temperature and is calculated following Thurmond as [378]

$$E_g = E_g^0 - \frac{\alpha T^2}{T + \beta} \quad (4.32)$$

where $E_g^0 = 1.170 \text{ eV}$, $\alpha = 4.730 \times 10^{-4} \text{ eV/K}$, and $\beta = 636 \text{ K}$. We neglect bandgap narrowing for simplicity.

Assuming complete dopant ionization, the majority carrier concentration is [5]

$$n = \left| \frac{N_D - N_A}{2} \right| + \sqrt{\left(\frac{N_D - N_A}{2} \right)^2 + n_i^2} \quad (4.33)$$

where N_D and N_A are the concentrations of donor and acceptor atoms. This expression is only an approximation for degenerately doped silicon because it is based upon the mass action law ($np = n_i^2$).

We calculate the resistivity from the dopant concentration as

$$\rho = \frac{1}{q\mu n} \quad (4.34)$$

where q is the single electron charge and μ is the carrier mobility. Both the carrier density and mobility vary through the depth of the piezoresistor. We calculate the mobility as a function of the donor and acceptor concentration and temperature following Reggiani et al. [379] as

$$\mu = \mu_0 + \frac{\mu_L - \mu_0}{1 + \left(\frac{N_D}{C_{r1}}\right)^{\alpha_1} + \left(\frac{N_A}{C_{r2}}\right)^{\alpha_2}} - \frac{\mu_1}{1 + \left(\frac{N_D}{C_{s1}} + \frac{N_A}{C_{s2}}\right)^{-2}} \quad (4.35)$$

Table 4.6 Summary of the carrier mobility modeling parameters from Reggiani et al. [379]

Parameters	Phosphorus	Arsenic	Boron
μ_{\max} (cm ² /V-sec)	1441	1441	470.5
c (-)	0.07	0.07	0.0
γ (-)	2.45	2.45	2.16
μ_{0d} (cm ² /V-sec)	$62.2T_n^{-0.7}$	$55T_n^{-0.6}$	$90.0T_n^{-1.3}$
μ_{0a} (cm ² /V-sec)	$132.0T_n^{-1.3}$	$132.0T_n^{-1.3}$	$44.0T_n^{-0.7}$
μ_{1d} (cm ² /V-sec)	$48.6T_n^{-0.7}$	$42.4T_n^{-0.5}$	$28.2T_n^{-2.0}$
μ_{1a} (cm ² /V-sec)	$73.5T_n^{-1.25}$	$73.5T_n^{-1.25}$	$28.2T_n^{-0.8}$
C_{r1} (cm ⁻³)	$8.50 \times 10^{16} T_n^{3.65}$	$8.90 \times 10^{16} T_n^{3.65}$	$1.30 \times 10^{18} T_n^{2.2}$
C_{r2} (cm ⁻³)	$1.22 \times 10^{17} T_n^{2.65}$	$1.22 \times 10^{17} T_n^{2.65}$	$2.45 \times 10^{17} T_n^{3.1}$
C_{s1} (cm ⁻³)	4.00×10^{20}	2.9×10^{20}	$1.1 \times 10^{18} T_n^{6.2}$
C_{s2} (cm ⁻³)	7.00×10^{20}	7.00×10^{20}	6.10×10^{20}
α_1 (-)	0.68	0.68	0.77
α_2 (-)	0.72	0.72	0.719

and

$$\mu_L = \mu_{\max} T_n^{-\gamma + cT_n} \quad (4.36)$$

$$\mu_0 = \frac{\mu_{0d} N_D + \mu_{0a} N_A}{N_D + N_A} \quad (4.37)$$

$$\mu_1 = \frac{\mu_{1d} N_D + \mu_{1a} N_A}{N_D + N_A} \quad (4.38)$$

where μ_L is the lattice mobility due to phonon scattering while μ_0 and μ_1 account for impurity scattering. The model parameters are presented in Table 4.6. The temperature dependencies in Table 4.6 and (4.36) are provided in terms of a normalized temperature, $T_n = T/300$ K.

The resistivity and carrier mobility for phosphorus and boron doped silicon at 300 K are plotted in Fig. 4.14 as functions of dopant concentration. The mobility decreases with dopant concentration due to ionized impurity scattering.

The resistivity profile, $\rho(z)$, is important for calculating the number of carriers, sensitivity factor and sheet resistance of the piezoresistor. The most general approach for calculating the sheet resistance is to integrate the conductivity profile ($\sigma(z) = 1/\rho(z)$) along the direction normal to the piezoresistor surface as

$$R_s = \frac{1}{\int_0^{t_j} \sigma(z) dz} \quad (4.39)$$

where t_j is the junction depth. With the models presented in this work, only diffused piezoresistors need to be calculated this way because a simple analytical expression is available for epitaxial doping (4.29) and ion implantation is complex enough that we have compiled lookup tables (Appendix B). The lateral diffusion of dopants is a negligible effect for most micron-scale piezoresistors and is discussed in more detail in Sect. 4.9.4.

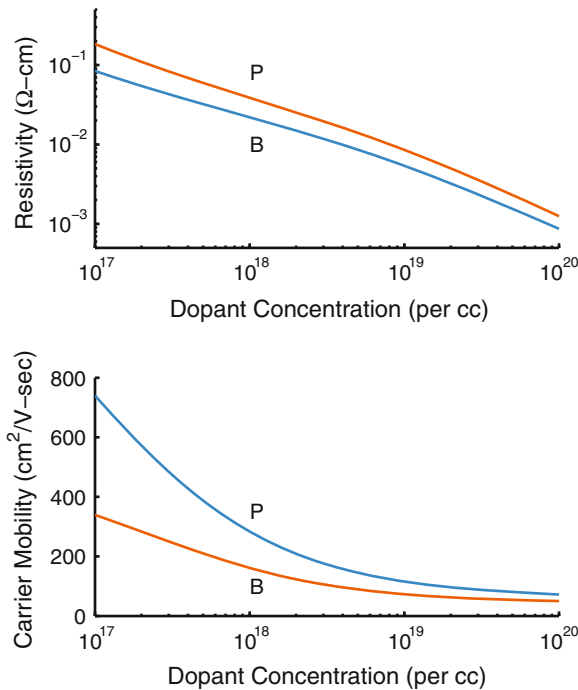


Fig. 4.14 Theoretical resistivity (top) and carrier mobility (bottom) as functions of dopant concentration for room temperature single crystal silicon. Boron (B) and phosphorus (P) show distinct behavior over temperature and are plotted separately. The properties of arsenic-doped silicon closely resemble phosphorus (Source Reprinted with permission from [2])

4.8 Experimental Validation Techniques

There are four common experimental techniques for measuring the dopant concentration profile: secondary ion mass spectrometry, spreading resistance analysis, capacitance voltage profiling, and anodic oxidation. [380 – 383].

Secondary ion mass spectrometry (SIMS) is used to quantify the total concentration of a dopants, including both substitutional and interstitial positions. By directing a beam of ions at the sample, atoms are sputtered from the surface and separated based upon their charge and mass. The initial data obtained from SIMS are the count rates of several ions as a function of time. To quantify the dopant profile, the time must be converted to depth, and the count rate to concentration. The sputtering rate can be measured mechanically using a stylus profilometer or atomic force microscope, or optically using interferometry.

Quantitative concentrations are obtained from the relative count rate of the element of interest compared to that of the major element in the sample, typically silicon [384]. The relative sensitivity factor, used to calculate concentration from the intensity ratio, is calibrated using a reference sample. Ion implantation is typically used to generate

the reference sample, because the integrated count rate can be compared to the implanted dose to calculate the relative sensitivity factor. SIMS has excellent depth resolution, on the order of several nanometers depending on the energy and angle of the primary ion beam, and resolution down to 10^{15} cm^{-3} . We refer the reader to Ref. [385] for a longer review article and Ref. [386] for a comprehensive book on SIMS.

Spreading resistance analysis (SRA) is used to quantify the electrically active dopant concentration profile. SRA reconstructs the dopant profile based upon the resistance measured over the depth of the sample using a four-point probe arrangement. In theory, one could simply cleave the sample and measure the resistance over its cross-section. However, the typical depth of a piezoresistor ranges from nanometers to microns and is far too small to directly probe. In SRA, the sample is first beveled at a shallow angle, θ . This serves two functions; the resistance at a particular depth can now be measured by moving the sample laterally rather than vertically, and size of the features to be probed is magnified by a factor of $1/\sin(\theta)$. This enables a four-point-probe instrument to measure a resistance profile by stepping laterally across the sample. The resistivity profile is calculated from the resistance profile using numerical methods [387, 388], and the resistivity profile is converted to a concentration profile based upon reference standards. SRA directly probes the resistivity profile of the sample, which is of prime importance for piezoresistive sensors, but accurate measurements within the first 20–50 nm of the sample surface can prove challenging due to edge effects.

Capacitance voltage (C-V) profiling infers the dopant concentration profile by measuring the capacitance as a function of voltage between the sample being probed and a surface electrode. As carriers near the surface are depleted, the measured capacitance decreases and the dopant concentration profile is inferred. C-V analysis is widely used in the semiconductor industry to probe gate oxide defects.

The measurement electrode can stationary or mobile. When the sharp tip of a scanning probe is used as the electrode, scanning capacitance microscopy (SCM) allows for sub-micron lateral resolution in addition to nanometer scale depth resolution [389]. One challenge with C-V and SCM measurements is that the field required to deplete highly doped silicon can lead to electrical breakdown. Although both techniques have been used to probe sub-100 nm junctions doped to 10^{20} cm^{-3} , depleting deep, highly doped structures can prove difficult [390]. Additionally, trapped charge or interface states can reduce the measurement accuracy. Scanning Kelvin probe microscopy (SKPM) is a technique related to SCM that infers the surface concentration from the work function difference between a scanned tip and the sample [391].

The final approach, anodic oxidation, encompasses a variety of techniques that use room temperature anodic oxidation for dopant profiling [380]. In the original technique, developed in the 1960s, the silicon wafer is placed in an anodizing solution and electrically biased to induce oxidation. The thickness of the oxide (and the amount of silicon removed) is controlled by applying a constant bias (e.g. 100 V) and terminating the oxidation step once the current reached a predetermined final value. Afterwards, the oxide is removed in HF and the sheet resistance is measured using a conventional four point probe system. By iterating between the oxidation and

measurement steps, the resistivity profile can be assembled. The thickness of silicon removed is controlled by the bias potential and can be quite small, e.g. 194 Å [330]. Although the process is relatively slow, it has been automated [392]. A more recent approach to anodic oxidation is to measure the electrical potential while controlling the current bias, allowing the dopant profile to be measured continuously [393].

4.9 Practical Notes

There are numerous practical issues that affect piezoresistor design and fabrication that we have not addressed yet: wafer selection, doping method selection, lattice strain, piezoresistor surface damage and lateral dopant diffusion.

4.9.1 Wafer Selection

Single crystal silicon piezoresistors are typically fabricated via bulk micromachining, so require the use of double-side polished wafers to allow both frontside- and backside-patterning. Silicon-on-insulator (SOI) wafers are often used because the buried SiO_2 layer can be used for a reliable etch stop and electrical insulation. The sensor thickness can be controlled fairly tightly in SOI wafers as well, although they are more expensive than double-side polished wafers. Although most piezoresistive sensors are bulk micromachined, surface micromachined polysilicon piezoresistors are becoming more popular. Less commonly, single crystal silicon membranes are formed using the porous silicon process [74, 75], enabling the pre-CMOS fabrication of piezoresistive pressure sensors.

SOI wafers come in two varieties: bonded and etched-back SOIs (BESOIs) and ion implantation-based SOIs. Although there are several books on SOI fabrication techniques [394, 395], we are providing a brief summary here with emphasis on issues for piezoresistive sensors.

BESOI wafers are fabricated by bonding a wafer to an oxidized handle wafer and thinning the bonded wafer to the desired device layer thickness through grinding and chemical mechanical planarization (CMP). Variation in the BESOI device layer thickness is typically $0.5 \mu\text{m}$ or more. Accordingly, they are typically used for device layers more than $1 \mu\text{m}$ thick due to the strong thickness dependence of sensor mechanics and sensitivity.

Thinner device layers, used for high performance sensors and fully depleted ICs, require an alternative fabrication method. Rather than polishing back the bonded wafer, a thin layer of oxygen (e.g. the SIMOX process) or hydrogen (e.g. the Smart Cut process) is ion implanted into the oxidized device wafer before it is bonded to the handle wafer. Annealing the bonded wafer stack forms either a buried oxide (SIMOX) or a weakened layer that allows the device layer to be mechanically cleaved before a final CMP cleanup step (Smart Cut). In either case the thickness of the

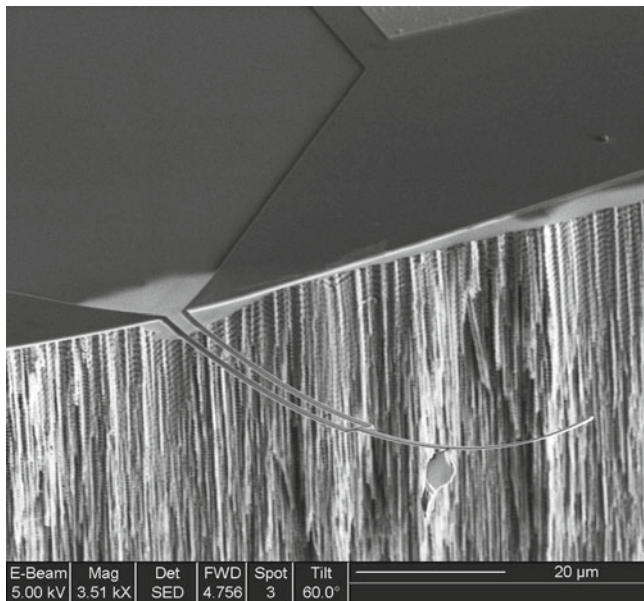


Fig. 4.15 Example of dopant-induced lattice strain leading to device curvature. The high dopant concentration near the device surface, which maximizes piezoresistor sensitivity (β^*) leads to a strain gradient through the device thickness (Source Reprinted with permission from [2])

device layer is set by the projected range of the implanted ions so only relatively thin device layers can be formed (e.g. <500 nm thick). Thickness control is excellent with 3σ thickness variation on the order of 30 nm or less.

Particular care should be taken in the selection of SOI vendor when fabricating piezoresistive sensors, because contamination during the fabrication process can lead to buried impurity layers that interfere with piezoresistor operation. Nafari et al. investigated wafers from three SOI manufacturers and found boron contamination with wafers from one of them [396]. Harjee experienced boron contamination from the same vendor, which shorted out the piezoresistors on his wafers and required another fabrication run to be performed [215]. Nafari et al. recommend ensuring that the SOI vendor oxidizes both the device and handle wafer, using the highest possible background dopant concentration and maximizing the device thickness to avoid contamination issues near the BOX. Wafer quality can be verified by either SIMS or SRA before committing a batch of wafers.

4.9.2 Dopant-Induced Lattice Strain

Piezoresistive sensors tend to be thin, making them susceptible to bending. Bending can be caused by a residual strain or strain gradients within silicon, dielectric or metal layers on the sensor. Strain in sputtered films can be minimized by careful process

development, and strain gradients in the device layer itself can be minimized through a long, high temperature anneal [397]. We typically use a 20h, 1100 °C anneal in an inert atmosphere after the growth of a thin oxide layer for protection from nitridation to reduce residual strain and strain gradients in SOI wafers.

Dopant atoms can add residual strain to the device as well. The addition of smaller or larger dopant atoms to the crystal lattice will induce tensile or compressive strain, respectively. Boron (0.88 Å) and phosphorus (1.10 Å) are both smaller than silicon (1.17 Å) while arsenic (1.20 Å) is slightly larger. Numerous researchers have measured the strain induced by the addition of dopants to the silicon lattice and have observed a linear reduction in average lattice constant with increasing dopant concentration for boron and phosphorus. The lattice strain can be calculated from

$$\epsilon = \beta_1 n \quad (4.40)$$

where n in this case is the total, not just electrically active, dopant concentration and β_1 is the lattice contraction coefficient. Celotti et al. measured contraction coefficients of $4.5 \times 10^{-24} \text{ cm}^3$ and $1.8 \times 10^{-24} \text{ cm}^{-3}$ for boron and phosphorus, respectively, via X-ray diffraction (XRD) rocking curves [398]. Lee et al. measured the contraction coefficient for phosphorus doping via micromachined mechanical test structures and XRD, inferring a contraction coefficient of $4.5 \times 10^{-24} \text{ cm}^{-3}$ [399]. McQuhae and Brown measured contraction coefficients of 5.2×10^{-24} and $1 \times 10^{-24} \text{ cm}^{-3}$ for boron and phosphorus, respectively, via measurements of wafer curvature [400].

We fabricated thin piezoresistive cantilevers using POCl_3 predeposition and also observed substantial lattice strain (Fig. 4.15). A sharp dopant concentration gradient was desirable from a device performance standpoint but introduced a large strain gradient. By measuring the tip deflection of cantilevers with varying lengths we inferred a lattice contraction coefficient of $4 \times 10^{-24} \text{ cm}^{-3}$ (Fig. 4.16). Our measurement technique was based upon the concentration of electrically active dopants rather than their total concentration, but the results are consistent with the other data. We recommend using the data from Celotti et al. in calculating the curvature of boron and phosphorus doped piezoresistive sensors.

Hubbard and Wylde investigated residual strain effects in micromachined cantilever beams and developed a model for calculating the bending due to arbitrary strain profiles [401]. We will briefly summarize their theory here. Two important assumptions are that no additional films are present on the sensor where the piezoresistor is located and that the dopant concentration profile, $n(z)$, is known. Using the concentration profile we can calculate the stress profile,

$$\sigma(z) = E\epsilon(z) = E\beta_1 n(z) \quad (4.41)$$

and calculate the corresponding centroid of the stress distribution as

$$\bar{z} = \frac{\int_0^t z\sigma(z) dz}{\int_0^t \sigma(z) dz} \quad (4.42)$$

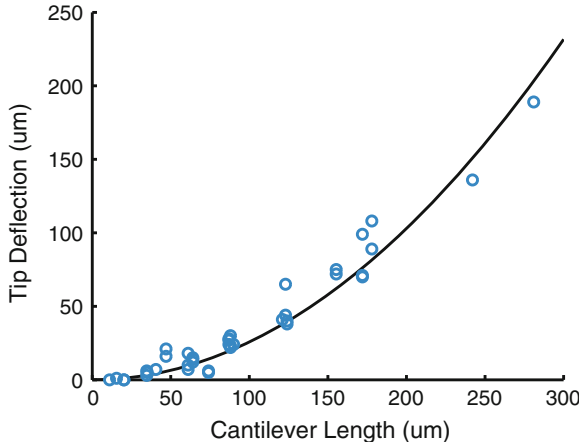


Fig. 4.16 Example measurements of cantilever tip deflection as a function of length due to dopant-induced lattice strain. The entire length of the cantilever was doped via POCl_3 inducing uniform bending along its length. The *best-fit line* is indicated and was used to calculate an effective lattice contraction coefficient (*Source* Reprinted with permission from [2])

where the origin of the coordinate system is at the bottom of the cantilever beam. A schematic of the coordinate system and effective of dopant-induced lattice strain on a cantilever beam are shown in Fig. 4.17. We can treat the beam as a bilayer structure with the interface between the two layers located at \bar{z} . The layer thicknesses are

$$t_1 = t - \bar{z} \quad (4.43)$$

$$t_2 = \bar{z} \quad (4.44)$$

where layer 2 is at the bottom of the cantilever beam, nearest to the origin. The average axial stress of each layer is

$$\sigma_1 = \frac{1}{t_1} \int_{t_2}^t \sigma(z) dz \quad (4.45)$$

$$\sigma_2 = \frac{1}{t_2} \int_0^{t_2} \sigma(z) dz \quad (4.46)$$

and the centroid of the stress for each layer is

$$\bar{z}_1 = \frac{\int_{t_2}^t z \sigma(z) dz}{\int_{t_2}^t \sigma(z) dz} \quad (4.47)$$

$$\bar{z}_2 = \frac{\int_0^{t_2} z \sigma(z) dz}{\int_0^{t_2} \sigma(z) dz}. \quad (4.48)$$

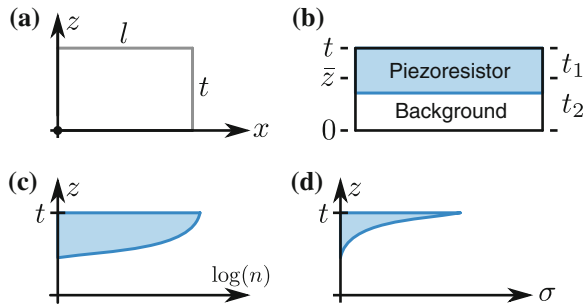


Fig. 4.17 Overview of dopant-induced cantilever beam bending. **a** The origin of the coordinate system is located at the bottom surface of the cantilever beam at its base. The thickness and length of the beam are t and l , respectively. **b** The centroid of the stress distribution (\bar{z}) is denoted and does not generally correspond with the junction depth. The beam is divided into two layers of thickness t_1 and t_2 above and below the stress centroid. **c** The dopant concentration within the piezoresistor varies as a function of depth. A typical profile on a logarithmic concentration scale is shown. **d** The dopant gradient introduces a stress gradient, plotted here on a linear scale. We assume phosphorus doping, which introduces tensile stress

We can calculate the equivalent moment induced by each layer about \bar{z} from

$$M_1 = \sigma_1 t_1 w (\bar{z}_1 - \bar{z}) \quad (4.49)$$

$$M_2 = \sigma_2 t_2 w (\bar{z} - \bar{z}_2) \quad (4.50)$$

where w is the width of the cantilever beam. The curvature of the beam can be calculated, assuming Euler-Bernoulli beam theory and small angular deflections, from

$$C = \frac{M_1 + M_2}{EI} \quad (4.51)$$

where EI is the bending rigidity of the cantilever beam. It is noteworthy that term-cancellation makes the curvature independent of both the beam width and elastic modulus. The curvature can be translated to angle and deflection from

$$\theta(x) = \int_0^x C(x) dx \quad (4.52)$$

$$v(x) = \int_0^x \theta(x) dx \quad (4.53)$$

where x is the distance from the base of the cantilever, θ is the change in angle and v is the deflection. Note that $C(x) = 0$ beyond the end of the piezoresistor so that $\theta(x > l_{pr}) = \theta(l_{pr})$. The deflection at the tip of the cantilever beam, assuming that it is doped along the entire length, is $v(L) = Cl^2/2$. The tip deflection is inversely proportional to the bending rigidity of the beam, so dopant-stress becomes less of an issue as the sensor thickness increases.

Dopant-induced bending can be minimized by minimizing the dopant concentration, dopant concentration gradient, maximizing the bending rigidity of the sensor, minimizing the area that is doped or adding a stress compensation film. Modifying the dopant concentration or bending rigidity are usually sub-optimal solutions, and if the area that is doped is already limited to just the piezoresistors then the only option if bending remains an issue is to add a compensation film. Dopant stress can be compensated by adding a film with compressive (for boron or phosphorus doping) or tensile (for arsenic doping) stress directly above the piezoresistor. The ideal compensation material would have a low elastic modulus, high residual stress, and could be deposited with minimal additional thermal budget so that only a thin layer would be necessary and it would negligibly affect the sensor mechanics or electrical properties.

The thickness of a compensation film can be determined by calculating the sum of the moments at any point on the sensor from

$$\sum M = \sum_i \int (z_i - z_n) \sigma_i dA \quad (4.54)$$

where i is the film number and z_n is the neutral axis of the device cross-section about which the moments are calculated. If thickness of the compensation film (t_{comp}) is much less than the thickness of the silicon (t), then we can approximate the neutral axis as $z_n = t/2$. Assuming that the compensation film has been chosen to ensure a flat sensor we can assume that the bending stress, $E(z - z_n)/R$ is negligible, simplifying the analysis considerably.

We assume that the stress profile in the silicon is an arbitrary function of depth, $\sigma(z) = E\epsilon(z)$, while the stress in the compensation film is a constant value, σ_{comp} . Expanding (4.54),

$$0 = \int_0^t (z - z_n) \sigma(z) dz + \int_t^{t+t_{\text{comp}}} (z - z_n) \sigma_{\text{comp}} dz. \quad (4.55)$$

We can continue to expand the result to obtain

$$t_{\text{comp}}^2 \left(\frac{\sigma_{\text{comp}}}{2} \right) + t_{\text{comp}} \left(\frac{t\sigma_{\text{comp}}}{2} \right) + \int_0^t (z - \frac{t}{2}) \sigma(z) dz = 0 \quad (4.56)$$

which can be solved using the quadratic equation and taking the positive solution for t_{comp} .

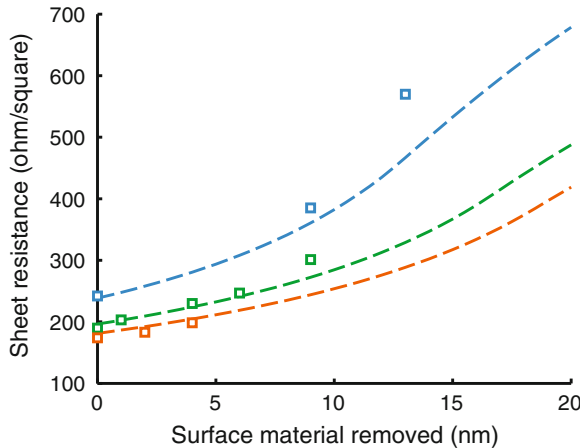


Fig. 4.18 Variation in piezoresistor sheet resistance with surface material removal. SOI samples were doped via phosphorus predeposition at 775 °C for 25, 35 and 40 min (indicated by each *dashed line*) and initial sheet resistance measurements were performed. The samples were subsequently coated with LPCVD SiO₂ at 300–400 °C for 20–60 min. Surface material removal was calculated by measuring the thickness of the SOI device layer before and after the deposition step via ellipsometry. A simple numerical model (*dashed lines*) matches the experimental results quite well (*Source* Reprinted with permission from [2])

4.9.3 Piezoresistor Surface Damage

In addition to being prone to strain effects, thin piezoresistive sensors are prone to surface damage during wafer processing. The sheet resistance of shallow piezoresistors can vary substantially during processing due to surface oxidation or damage. For example, LPCVD deposition of SiO₂ at 300–400 °C usually oxidizes 5–10 nm of surface silicon. The slight reduction in thickness can affect both the mechanics and electrical properties of thin sensors. The sheet resistance and number of carriers are particularly prone to processing variation because the most highly doped silicon is generally located at the top surface of the wafer.

Variation in sheet resistance with surface oxidation can be experimentally measured and modeled as in Fig. 4.18. Wafers were doped with POCl₃ predeposition at 775 °C for 25, 35 and 40 min and initial sheet resistance measurements were performed. The samples were subsequently coated with LPCVD SiO₂ at 300–400 °C for 20–60 min. The changes in silicon thickness were measured via variable angle spectroscopic ellipsometry. Thin SOI device layers (e.g. 300 nm) transmit enough light to enable optical measurements of thickness, enabling the measurement of uniform changes in device layer thickness. The experimental data (squares) and predicted sheet resistance from removing surface material from the modeled dopant concentration profile (dashed lines) in Fig. 4.18 agree reasonably well. Although only several nanometers of material were removed during each step, the impact can be substantial when the piezoresistor is thin. Arlett reported a 25 % sheet resistance increase from

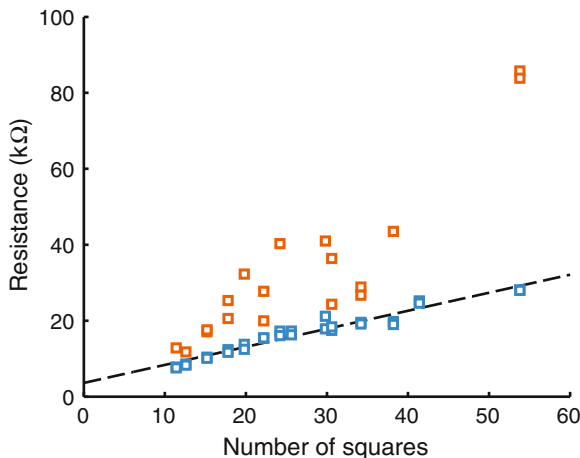


Fig. 4.19 Variation in sheet resistance with reactive ion etching damage. Silicon resistors released from the BOX by a backside RIE step (orange) exhibited much higher resistances and variability than their on-chip counterparts (blue) that were not released. The increased resistance and mismatch lead to reduced performance. Switching to an HF vapor release step alleviated this problem (*Source* Reprinted with permission from [2])

the deposition and patterning of a passivation PECVD oxide layer, corresponding to 12 nm of removed material from her 60 nm thick epitaxial piezoresistors [121].

A second source of electrical variation in thin piezoresistors can come from surface damage during reactive ion etching. We fabricated piezoresistive cantilevers from SOI wafers and released them from the BOX using a CHF_3/O_2 plasma. Despite the low nominal silicon etch rate of the process (28 Å/min), the sheet resistance of the resistors located on the cantilevers increased substantially compared with their temperature compensation counterparts located further back on the silicon die (Fig. 4.19).

Changes in piezoresistor electrical properties during wafer processing can be mitigated in two ways. First, the impact of surface damage is inversely proportional to the piezoresistor thickness. Thicker sensors are less sensitive to process variation than their thinner counterparts in general, with the tradeoff being slightly worse performance. The second approach to limiting surface damage is to eliminate the damaging steps from the process. For example, sensors can be released from the SOI BOX using HF vapor rather than RIE to avoid problems with etch selectivity and the deposition of passivation polymer. Surface oxidation is more challenging to control, but atomic layer deposition (ALD) is a promising option for the deposition of thin nitride- or oxide-based surface passivation films at low temperature.

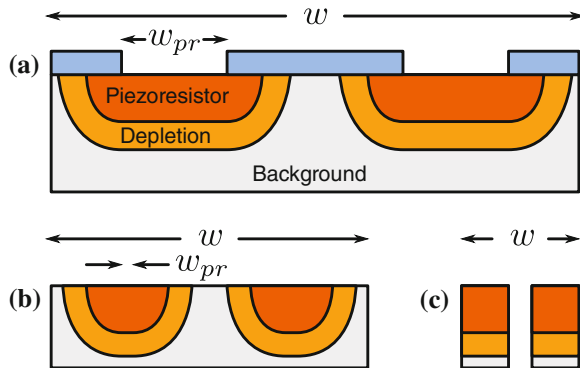


Fig. 4.20 Lateral dopant diffusion effects. In this example, a piezoresistive loop is formed via phosphorus diffusion through an oxide mask. **a** If the piezoresistor dimensions are much larger than the dopant diffusion length then there is negligible error in using the lithographic mask dimensions to model the device. **b** As the piezoresistor dimensions decrease, the effective piezoresistor dimensions can become significantly larger than its nominal dimensions. Additionally, the device width is limited by the size of the depletion regions. **c** The extra material around the piezoresistor can be etched away after doping to control its dimensions and enable further reductions in device size (*Source* Reprinted with permission from [2])

4.9.4 Lateral Dopant Diffusion

Throughout this chapter we have neglected the lateral diffusion of dopants during fabrication. Lateral diffusion results in the actual piezoresistor dimensions not matching the dimensions on the lithographic mask as illustrated in Fig. 4.20. Lateral diffusion becomes a problem as the piezoresistor dimensions approach the dopant diffusion length (Fig. 4.20b). A larger than intended piezoresistor results in a lower sheet resistance, more carriers in the piezoresistor and a greater risk of the depletion regions coming into contact than expected.

As an example, consider a phosphorus predeposition process that yields a phosphorus saturated layer that is 50 nm thick where most of the electrical current is conducted, a junction depth of 300 nm and depletion regions that are 1 μm wide. For simplicity we will assume that the lateral and vertical dopant diffusion lengths are equal [307]. In reality, the lateral diffusion length can be significantly greater than expected due to oxidation enhanced diffusion and surface defects. For example, a four-fold greater lateral diffusivity than expected has been reported [402].

If each leg of the piezoresistor were 30 μm across then the error from lateral diffusion in calculating the piezoresistor resistance would be negligible ($2 \times 50 \text{ nm} / 30 \mu\text{m} = 0.3\%$). Note that most of the electrical current is conducted in the saturated layer of a diffused resistor, hence we use 50 nm rather than 300 nm as the critical dimension in calculating the effect on resistance. If the device dimensions were reduced to a nominal piezoresistor width of 1 μm then there would be significant error between the nominal and effective piezoresistor width ($2 \times 50 \text{ nm} / 1 \mu\text{m} = 10\%$).

Furthermore, the minimum spacing between the two legs of the piezoresistor would be roughly $5\text{ }\mu\text{m}$ to allow a $2.4\text{ }\mu\text{m}$ gap between the two depletion regions that extend $1.3\text{ }\mu\text{m}$ from each lithographic edge of the resistor. This is a particularly important issue for designing sub-micron piezoresistive sensors.

Even if the depletion regions that surround each leg of the piezoresistor do not come into contact (punchthrough), electrical current leaks across the reverse biased p-n junctions. If the piezoresistor is designed with a high impedance (e.g. $>10\text{ k}\Omega$) then the junction leakage can appreciably affect the piezoresistor electrical properties. The current that leaks from the piezoresistor to the substrate ground (or between the piezoresistor legs if the substrate is left floating) will reduce the sensor sensitivity, while carrier generation and recombination can increase the piezoresistor noise [403].

These issues can be eliminated by etching away the material that surrounds the piezoresistor (Fig. 4.20c). For example, Harjee observed a four-fold reduction in piezoresistor 1/f noise when the gap between two piezoresistor legs was etched away [215]. The etch step both defines the lateral dimensions of the piezoresistor and mitigates the current leakage and noise issues with the gap between the piezoresistor legs. For applications that require a continuous structure (e.g. pressure sensors) the gap could be refilled with a dielectric.

4.9.5 Excess Electrical Resistance

Excess electrical resistance degrades piezoresistive sensor by decreasing sensitivity and increasing noise (Sect. 3.2.1). The two main sources of excess resistance are usually interconnects and contact resistance, and both can be minimized through careful design.

Interconnects should be as thick, wide and as short as possible while having a much higher electrical conductivity than the piezoresistor. Aluminum serves this purpose quite well, with a resistivity on the order of $3\text{ }\mu\Omega\text{-cm}$ in contrast with a minimum resistivity on the order of $1100\text{ }\mu\Omega\text{-cm}$ for single crystal silicon doped to 10^{20} cm^{-3} with phosphorus. For example, a $1\text{ }\mu\text{m}$ thick, $30\text{ }\mu\text{m}$ wide and 5 mm long Al interconnect ($30\text{ m}\Omega/\square$) adds a series resistance of just $5\text{ }\Omega$.

When different materials are used for the interconnects and piezoresistors, their interface adds contact resistance to the circuit. The modeling and optimization of electrical contacts is a complex subject and we recommend Ref. [404] as a good introduction. The optimal contact has a thin enough depletion region at the interface so that electrons can tunnel across the barrier without appreciably increasing the resistance.

This goal is best achieved with degenerately doped silicon and a metal that presents a low barrier height. For example, the contact resistivity of Al (0.7 eV barrier height [406]) to n-type Si doped to 10^{20} cm^{-3} is ideally less than $1\text{ }\mu\Omega\text{-cm}^2$ (Fig. 4.21). The contact resistivity is calculated as a function of the contact barrier height and dopant concentration from the model presented in Ref. [405]. A superior alternative to Al for many fabrication processes is Ti (particularly when silicides are not an option),

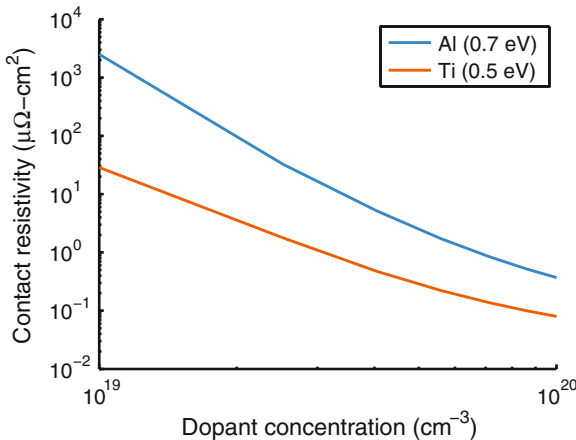


Fig. 4.21 Contact resistivity as a function of n-type dopant concentration for Ti and Al metallization. The contact resistivity is calculated following Ref. [406]. In theory, both Ti and Al metallization can achieve a contact resistivity of less than $1 \mu\Omega \cdot \text{cm}^2$ for a dopant concentration of 10^{20} cm^{-3} (Source Reprinted with permission from [2])

which has a smaller barrier height (0.5 eV) and doubles as a contact diffusion barrier [407, 408].

Note that the contact resistivity decreases three orders of magnitude if the dopant concentration at the piezoresistor surface is increased from 10^{19} to 10^{20} cm^{-3} . If the piezoresistor is lightly doped then it is important to add a second doping step to the fabrication process to minimize the contact resistivity and sheet resistance of the silicon underneath the contacts.

The contact resistance depends on both the resistivity of the contact and its dimensions. In a simple zero-dimensional model, the contact resistance could be calculated from

$$R_{\text{contact}} = \frac{\rho_{\text{contact}}}{w_{\text{contact}} l_{\text{contact}}} \quad (4.57)$$

where w_{contact} and l_{contact} are the width and length of the contact (current flows in the direction of the contact length) while ρ_{contact} is the contact resistivity.

However, the zero-dimensional contact model can dramatically underestimate the contact resistance if the contact is long and narrow or the interconnect and piezoresistor have similar resistivities. A better model is the one-dimensional transmission line. Following Ref. [409], the contact resistance can be calculated as

$$R_{\text{contact}} = \frac{\sqrt{R_s \rho_{\text{contact}}}}{w_{\text{contact}}} \coth \left(l_{\text{contact}} \sqrt{\frac{R_s}{\rho_{\text{contact}}}} \right) \quad (4.58)$$

where R_s is the sheet resistance of the underlying silicon.

To summarize this section, in designing a force probe one should use metal rather than silicon interconnects, maximize the area of the contacts, select an appropriate contact resistance model and dope the contacts as highly as possible.

4.10 Summary

The most commonly used approaches to piezoresistor fabrication were discussed in this chapter: predeposition, ion implantation and epitaxy. Each technique forms a piezoresistor by selectively introducing dopant atoms into the silicon crystal lattice in combination with lithographic patterning. Accurate models were developed in each case to predict the resulting dopant concentration profile from a set of fabrication process parameters. Single crystal silicon was emphasized because it yields higher performance and better repeatability than polycrystalline silicon (discussed in Sect. 4.6).

Predeposition, also known as diffusion, was modeled for the case of phosphorus doping via POCl_3 using an analytical model developed by Tsai [330]. Arsenic and boron predeposition are less commonly used due to practical fabrication issues and were not modeled. A typical phosphorus diffusion concentration profile was compared with the Tsai model in Fig. 4.6. Parameters for the Tsai model that we derived experimentally were presented in Table 4.3.

Ion implantation of boron, phosphorus or arsenic atoms was modeled numerically using TSUPREM-4™. The sensitivity factor (β^*) was decomposed into two separate factors (β_1^* and β_2^*) for compatibility with this lookup-based approach. Tables for the sensitivity factor (β_1^* and β_2^*), sheet resistance (R_s), effective carrier density per unit area (N_z^{eff}) and junction depth (t_j) are presented in Appendix B. Our open source piezoresistor design optimization software (Appendix C) includes the lookup tables in binary format (.mat) as well as the Python and MATLAB® scripts used to generate the tables.

Epitaxy is perhaps the most complex option for fabrication but it yields the simplest dopant concentration profiles. (Sect. 4.5). Concentration profiles vary relatively little between dopant species except when the diffusion length is comparable to the junction depth. The electrical and piezoresistive properties of epitaxial profiles can be calculated from

$$\beta^* = P(1 - t_{\text{pr}}/t) \quad (4.27)$$

$$\overline{P} = P \quad (4.28)$$

$$R_s = \rho/t_{\text{pr}} \quad (4.29)$$

$$N_z^{\text{eff}} = N_{\text{epi}} t_{\text{pr}} \quad (4.30)$$

A temperature- and concentration-dependent model for the resistivity of single crystal silicon was presented in Sect. 4.7. Experimental techniques for measuring the dopant concentration and resistivity profiles, critical for developing any piezoresistor fabrication process, were discussed in Sect. 4.8. We closed this chapter by discussing practical issues with piezoresistor fabrication: wafer selection, dopant-induced lattice strain, surface damage, lateral dopant diffusion and contact resistance.

Chapter 5

Temperature Effects

Silicon piezoresistors are exceptionally sensitive to temperature. Fluctuations in temperature affect both the sensor output (via the resistance) and sensitivity (via the piezoresistance factor). Without any temperature compensation the temperature-induced signal during typical operation can be larger than the intended sensor output.

This characteristic makes silicon thermistors an attractive option for temperature sensing. For example, a thermistor-based temperature-to-digital converter with a resolution of 0.1 mK in a 5 Hz bandwidth was recently demonstrated, a 20-fold improvement over diode-based sensors [410]. Temperature compensation is the art of eliminating this strong temperature sensitivity, which can arise from changes in the ambient temperature, changes in the thermal conductance between the sensor and the ambient, or changes in the Joule heating power of the sensor.

There are two common strategies for temperature compensation: passive and active compensation. Passive compensation combines two or four nominally identical piezoresistors in a Wheatstone bridge configuration. If the piezoresistors are thermally coupled (e.g., fabricated on the same die) then temperature changes generate a common mode signal that can be rejected using an instrumentation amplifier. This approach compensates for resistance but not sensitivity changes with temperature [275]. Active compensation combines the passive approach with a temperature sensor and compensation circuit (Sect. 2.3.1) to cancel both resistance sensitivity changes over temperature. Active compensation is used in most commercial products where a high level of accuracy and/or trimming is required.

The first systematic study of piezoresistance in silicon as a function of temperature was performed by Kurtz in 1962 [411]. Kurtz presented measurements of piezoresistive coefficients (π), resistivity (ρ), temperature coefficient of sensitivity (TCS), temperature coefficient of resistance (TCR) and strain nonlinearity as functions of dopant concentration and temperature. Tufte and Stelzer subsequently presented detailed measurements of these parameters for diffused layers over a wide range of dopant concentrations (10^{18} – 10^{21} atoms cm $^{-3}$) and temperatures (−90 to 100 °C) [202]. They also showed that the piezoresistive coefficient was relatively insensitive to the diffusion depth for a diffused layer. Later in 1963, Kerr and Milnes showed that

the surface dopant concentration could be used as an adequate proxy for the average effective concentration in modeling the piezoresistivity of piezoresistors formed through diffusion/predeposition [214].

Kurtz was the first to clearly highlight the advantages of using higher doping levels for piezoresistors. The temperature coefficient of sensitivity decreases with increasing surface concentration. This trend is desirable, except that increasing surface concentration sacrifices the sensitivity of the piezoresistors. However, the temperature coefficient of sensitivity rolls off faster than sensitivity with concentration. Other parameters that decrease with dopant concentration are strain and temperature sensitivity nonlinearities and the temperature coefficient of resistance. Some piezoresistive pressure sensor manufacturers, such as Kulite Semiconductor Products, Merit Sensors, and GE NovaSensor manufacture high concentration piezoresistors, taking advantage of this reduced temperature sensitivity. Ultimately, some temperature sensitivity is inevitable in silicon strain sensors and must be compensated using a combination of passive and active compensation circuitry.

5.1 Temperature Coefficient of Sensitivity

The Kanda and Richter models that we have presented for calculating the piezoresistance factor and electrical resistivity are temperature dependent, and can be used to predict the temperature-dependent properties of piezoresistors. The temperature coefficient of sensitivity (TCS) can be calculated from the temperature dependent piezoresistance factor models as

$$\text{TCS}(N, T) = \frac{1}{P(N, T)} \frac{\partial P(N, T)}{\partial T}. \quad (5.1)$$

Experimental TCS data from Refs. [67, 202, 207] are plotted in Fig. 5.1. The measured magnitude of the TCS decreases from 3,000 ppm/K below 10^{18} cm^{-3} to less than 500 ppm/K at 10^{21} cm^{-3} . Note that the TCS is a strong function of temperature in addition to concentration. As a conservative estimate of the variation in sensitivity over operating temperature, 500 ppm/K would result in a 6% change in strain sensitivity between -40 and $+85^\circ\text{C}$.

The experimental results fall between the Kanda and Richter piezoresistance factor models. Utilizing the Richter model, our general recommendation for modeling the piezoresistance factor, will result in an average error on the order of 30%. Considering the improvements in experimental and numerical techniques in characterizing dopant concentration profiles over the past 30–50 years (when the experimental data were collected), it is quite possible that one of the theoretical models is more accurate than currently indicated.

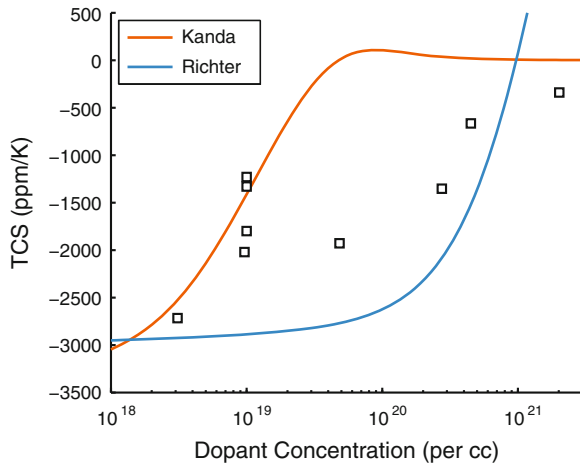


Fig. 5.1 Comparison between experimental and theoretical temperature coefficient of sensitivity (TCS) results at 300 K as a function of dopant concentration. The magnitude of the TCS decreases from approximately $-3,000 \text{ ppm/K}$ at low concentration to less than -500 ppm/K above 10^{21} cm^{-3} . The experimental results fall between the Kanda and Richter models; using either model will result in average error on the order of 30 %. Experimental data is taken from Refs. [67, 202, 207] (Source Adapted with permission from [2])

5.2 Temperature Coefficient of Resistance

The temperature coefficient of resistance (TCR) can be calculated from (4.34) as

$$\alpha = \frac{1}{R} \frac{\partial R}{\partial T} \quad (5.2)$$

$$\approx \frac{1}{\rho} \frac{\partial \rho}{\partial T} \quad (5.3)$$

where α has units of $1/\text{K}$ and is commonly expressed as ppm/K . The TCR decreases sharply as the dopant concentration is increased until it reaches a minimum near $3 \times 10^{18} \text{ cm}^{-3}$ and begins increasing again (Fig. 5.2).

The model accurately predicts the TCR of lightly doped material but has serious deficiencies above 10^{18} cm^{-3} . This is particularly problematic because high doping levels are optimal for most piezoresistor applications. The limitations of analytical theories in predicting TCR for degenerately doped silicon are well known and research is ongoing [412]. We have measured the TCR of silicon doped to 10^{20} cm^{-3} and $5 \times 10^{20} \text{ cm}^{-3}$ with phosphorus via POCl_3 predeposition as 1,300 and 1,700 ppm/K , respectively, in good agreement with the theory [2, 97, 134].

An additional complication with TCR modeling is that temperature changes are transduced into resistance changes both electrically and mechanically. A mismatch in thermal expansion coefficients between the piezoresistive device and the

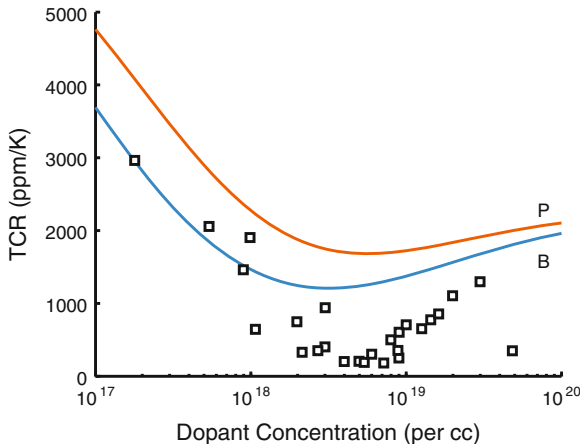


Fig. 5.2 Comparison between experimental and theoretical temperature coefficient of resistance (TCR) results at 300 K for boron (B) and phosphorus (P) doping. Experimental data from p-type silicon resistors are plotted for comparison [412, 413]. The TCR reaches a minimum near $5 \times 10^{18} \text{ cm}^{-3}$ before increasing again slightly. Experimentally measured TCR data is substantially lower than predicted by theory, and research is ongoing [412] (Source Reprinted with permission from [2])

mounting surface can potentially generate temperature-dependent strain and resistance changes. Silicon has a particularly small coefficient of thermal expansion (CTE) of about 3 ppm/K compared with most metals (e.g., 23 ppm/K for aluminum) at room temperature. The use of a low modulus die attach material, such as room temperature vulcanization silicone, can reduce the transmission of shear strain between the sensor and its surroundings.

5.3 Piezoresistor Self-Heating

Self-heating is an inherent byproduct of piezoresistor operation. There are three notable design issues with Joule heating in piezoresistors. First, performance degrades as the piezoresistor temperature increases due to a smaller piezoresistance factor and larger Johnson, amplifier and thermomechanical noise. Second, the maximum sensor temperature is constrained in many applications. Third, in applications where the temperature is not constrained, the maximum power dissipation might be constrained. Most consumer application are power constrained (e.g., altimeter or accelerometer in a smartphone). Additionally, applications at cryogenic temperatures typically require power dissipation on the order of several microwatts.

In this section we will discuss heat transfer models for piezoresistive sensors. Using these models, we will be able to calculate the temperature distribution of a sensor during operation and optimize designs with respect to temperature and power

dissipation constraints. First, we will provide a brief example of heat transfer in a piezoresistive sensor. Next, we will describe the thermal conductivity of common sensor materials, including variation in the thermal conductivity of silicon with film thickness and dopant concentration. Finally, we will develop models to analytically and numerically calculate the temperature distribution within a sensor and compare the results with experimental data.

5.3.1 A Qualitative Example

A balanced Wheatstone bridge with bridge bias of V_{bridge} dissipates electrical power (W) equal to $V_{\text{bridge}}^2/4R$ in each resistor. The heat is conducted away from the piezoresistor via conduction through the sensor structure and convection into the surrounding air or liquid. Electromagnetic radiation is typically small, on the order of a few percent even at temperatures as high as 600 °C [134, 414].

Joule heating induces a temperature rise in the sensor structure. The magnitude of the self-heating effect depends on the sensor geometry, the thermal conductivity of the materials used, and the thermal properties of any surrounding fluid. Figure 5.3a illustrates a cross-section through a pressure sensor and the approximate steady-state

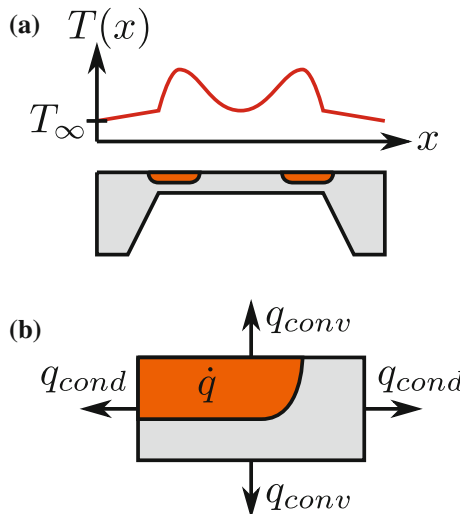


Fig. 5.3 Self-heating during piezoresistor operation. **a** Piezoresistors embedded in a diaphragm dissipate power, which is transferred away to the edge of the device and into its surroundings. Temperature variation with position is qualitatively plotted. The temperature rise is substantially higher in the diaphragm than the rest of the device due to its reduced thickness. **b** The heat generated in the piezoresistor (\dot{q}) is conducted away via conduction through the device and convection directly into the surrounding fluid (Source Reprinted with permission from [2])

temperature distribution. Power is dissipated in the two piezoresistors located at the edges of the diaphragm. The heat is conducted away from the piezoresistors via conduction to the rim of the sensor and via convection directly to the fluid on either side of the diaphragm (Fig. 5.3b).

The temperature reaches a peak near the center of each piezoresistor and decreases toward the center of the diaphragm and the edge of the device. The temperature decay towards the center is due to convection; if the device were operated in vacuum then the temperature would remain approximately constant across the diaphragm. The sharp reduction in the slope of the temperature at the edge of the diaphragm is due to the sudden increase in cross-sectional area available for heat conduction.

The most direct way to decrease self-heating is to simply reduce the power dissipation. However, we'll see in the next section (Sect. 5.4) that decreasing the power dissipation leads to worse sensor resolution. Alternatively, the sensor design can be modified for increased heat transfer efficiency. From a heat transfer standpoint we want to use thick films and high thermal conductivity materials in the device, but from a mechanics standpoint we want to use thin films without any excess layers for thermal management. The tradeoff between power dissipation, the resulting temperature increase, and piezoresistor performance is relatively complex and we will develop the building blocks in this section.

5.3.2 Thermal Conductivity of Typical Materials

Thermal conductivity (k) varies widely between the materials commonly used in piezoresistive sensors (Table 5.1). Metals, with the exception of Ti, conduct heat more than two orders of magnitude better than dielectrics. Silicon is a fairly good conductor of heat, although polysilicon is much less so due to phonon scattering at grain boundaries.

Table 5.1 Thermal conductivities of materials commonly used in piezoresistive silicon sensors

Material	k (W/m-K)
Al	200
Cu	400
Ti	22
Si	142–148
Si (poly)	10–50
SiO ₂	1.4
Si ₃ N ₄	30
Parylene	0.08

The data correspond to bulk samples near room temperature and are compiled from Refs. [415, 416]. Thermal conductivity is reduced by phonon scattering at film boundaries, grain boundaries, and with dopant atoms.

The data in Table 5.1 should only be used as an approximate guide due to large variations in thermal conductivity with film processing details. Thermal conductivity varies with film morphology and thickness due to phonon scattering at film and grain boundaries. It also varies substantially in doped silicon due to phonon scattering with ionized dopants. Finally, it varies with temperature for all materials, and generally reaches a maximum at fairly low temperatures (30–100 K) due to insufficient thermal energy and increasing phonon-phonon scattering at low and high temperatures, respectively. Despite these limitations, we will use the data in Table 5.1 for all of the materials except for silicon, which we will model in more detail. The thermal conductivity of Al is taken from Ref. [415] while the other film properties are taken from the reference literature [416]. We refer the reader to the literature for more detailed models of particular materials and to Kittel for a more general introduction to solid state physics [193].

The thermal conductivity of silicon has been studied extensively for its importance to the IC industry. While the properties of polycrystalline materials vary enormously with processing history, the reproducibility of single crystal silicon makes it amenable to precise characterization. The thermal conductivity of single crystal silicon depends on three factors: film thickness, temperature, and dopant concentration.

We will use two models for the thermal conductivity of silicon. The first is derived from the data that Asheghi et al. measured for lightly doped SOI device layers in 1997 [417]. They measured thermal conductivity as a function of film thickness, holding the temperature and dopant concentration constant. We performed a simple first-order fit to their room temperature (300 K) data, yielding

$$k = k_{\text{bulk}} \frac{t}{t + t_0} \quad (5.4)$$

where t is the characteristic length (e.g., thickness), $t_0 = 120 \text{ nm}$ from fitting to the data in [417], and $k_{\text{bulk}} \approx 142 \text{ W/m-K}$ for bulk silicon at room temperature. For most devices the film thickness is the smallest dimension and is the dominant source of phonon-boundary scattering, but the smallest dimension of the structure should always be used in (5.4). Although this simplified model does not account for variation in thermal conductivity with temperature and dopant concentration, thickness is the most important source of thermal conductivity variation for most piezoresistive devices operating near room temperature.

The second model we will use was developed by Liu et al. in 2006, and includes temperature dependent phonon-impurity and phonon-boundary scattering [418]. Impurity scattering is calculated from the dopant concentration profile, calculated using the models in Chap. 4. The model in Ref. [418] is fairly long and would introduce an excessive amount of new terminology, so we will simply present the model results here and refer the reader to the original paper and our MATLAB® implementation (Appendix C).

Figure 5.4 compares the bulk thermal conductivity of silicon at 300 K, the simplified model based upon Asheghi et al. [417] and the expanded model based upon Liu et al. [418] for a layer of single crystal silicon doped to 10^{19} cm^{-3} with

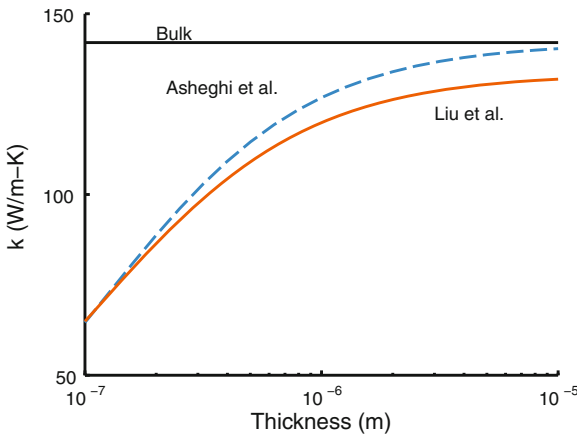


Fig. 5.4 Silicon thermal conductivity as a function of film thickness. The simplified model in (5.4) is based upon work by Ashegh et al. [417] and does not account for dopant concentration or temperature effects. The expanded model developed by Liu et al. [418] accounts for both concentration and temperature effects and is calculated assuming operation at 300 K with a phosphorus dopant concentration of 10^{19} cm^{-3} . The two models match well for thin films where thickness effects dominate (Source Reprinted with permission from [2])

phosphorus. The thermal conductivity decreases noticeably for thin films: 100 nm and 1 μm thick films have 53 and 14 % lower thermal conductivities than bulk samples. The simplified and expanded models agree to within 5 % for films thinner than μm . The simplified model adapted from Ashegh et al. does not account for dopant concentration or temperature effects, so is only accurate when devices are operated near room temperature, the piezoresistor is relatively thin, and the background dopant concentration is low.

Variation in thermal conductivity with dopant concentration and temperature using the model from Liu et al. is presented in Fig. 5.5. A 1 μm thick layer of single crystal silicon is used for both plots, but in the variable temperature case the phosphorus concentration is fixed at 10^{19} cm^{-3} while in the variable concentration case the temperature is fixed at 300 K.

Temperature is a strong influence on thermal conductivity. If the temperature increases from 300 to 400 K, either by self-heating or a high ambient temperature, the thermal conductivity of the silicon drops by 30 %. The decrease in thermal conductivity with temperature acts as a source of positive-feedback and exacerbates self-heating effects. This particularly significant for piezoresistors that are biased with a current source because the positive TCR of silicon (Sect. 5.2) introduces another positive feedback loop, as discussed in [6].

Dopant concentration has a weaker effect on thermal conductivity at room temperature, and the thermal conductivity does not drop noticeably until the dopant concentration reaches 10^{19} cm^{-3} . Considering that the piezoresistor is relatively thin in most devices (<30 % of the sensor thickness) and that the background dopant

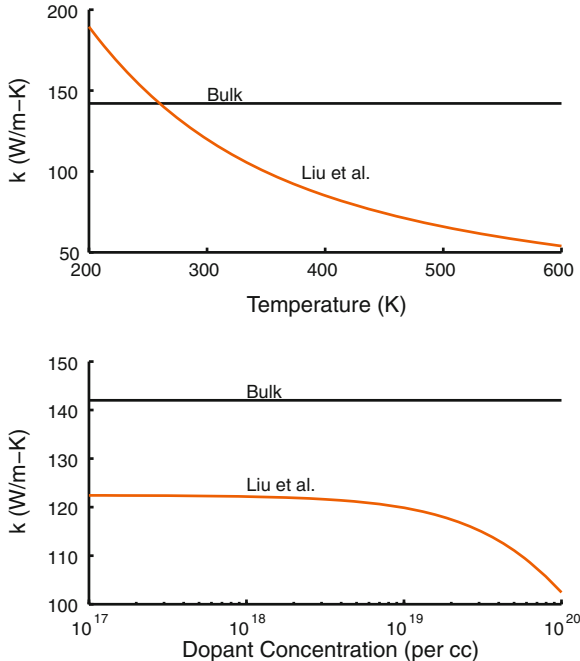


Fig. 5.5 Silicon thermal conductivity as functions of temperature (*top*) and dopant concentration (*bottom*). A $1\text{ }\mu\text{m}$ thick layer of single crystal silicon is used for both plots, but in the variable temperature case the phosphorus concentration is fixed at 10^{19} cm^{-3} while in the variable concentration case the temperature is fixed at 300 K. The thermal conductivity is a much stronger function of temperature than dopant concentration in most applications (*Source* Reprinted with permission from [2])

concentration is far lower than 10^{19} cm^{-3} , heat transfer is relatively insensitive to the piezoresistor dopant concentration. Accordingly, the simplified model (5.4) is accurate for most sensors operating near room temperature.

5.3.3 Heat Transfer Fundamentals

Temperature gradients develop as heat generation (\dot{q}) equilibrates with conductive and convective heat transfer. Conductive heat flux, $q_{\text{cond}} = -k \nabla T$, is proportional to the material's thermal conductivity and the temperature gradient through the material. Convective heat flux, $q_{\text{conv}} = h_{\text{eff}}(T - T_{\infty})$, is proportional to the effective convection coefficient (h_{eff}) and the temperature difference between the device and surrounding fluid (T_{∞}).

The temperature profile, $T(x)$, can be calculated from the steady-state heat equation, $\dot{q} = q_{\text{conv}} + \nabla q_{\text{cond}}$ [419]. For a one-dimensional problem, the result reduces

to

$$\dot{q}'(x) = h_{\text{eff}}(x)P(x)[T(x) - T_{\infty}] - \frac{\partial}{\partial x} \left[A(x)k(x)\frac{\partial T(x)}{\partial x} \right] \quad (5.5)$$

where \dot{q}' is the heat generation per unit length and P is the area per unit length available for convection (e.g., cantilever beam perimeter). If the cross-sectional area, perimeter, convective coefficient and thermal conductivity do not change appreciably with position then the result simplifies to

$$\dot{q}'(x) = h_{\text{eff}} P [T(x) - T_{\infty}] - Ak \frac{\partial^2 T(x)}{\partial x^2}. \quad (5.6)$$

We will solve for the temperature profile in one-dimension using the finite-difference method and in higher dimensions using finite element analysis.

The temperature-dependent power dissipation per unit length is

$$\dot{q}'(x) = I^2 R_s(x)/w_{\text{pr}} \quad (5.7)$$

where I is the current flow, $R_s(x)$ is the position-dependent sheet resistance and w_{pr} is the piezoresistor width. In the case of a cantilever beam where a loop is formed, the power dissipation per unit length is doubled. The sheet resistance as a function of temperature can be experimentally measured or calculated as in Sects. 4.7 and 5.2. When the temperature increase is small, the sheet resistance remains approximately constant along the piezoresistor length and the power dissipation per unit length simplifies to $\dot{q}' = W/l_{\text{pr}}$.

One-dimensional heat transfer models are sufficient when the temperature gradient within a device cross-section is small. In other words, if thermal conduction within the device is faster than the conduction at its interfaces, then the system can be modeled one-dimensionally. The Biot number can be calculated to determine if a one-dimensional model can be used

$$\text{Bi} = \frac{h_{\text{eff}} L_c}{k} \quad (5.8)$$

where L_c is the characteristic length of the system, commonly defined as its volume to surface area ratio. The Biot number is exceedingly small for most MEMS sensors, allowing them to be modeled as one-dimensional systems; $\text{Bi} < 10^{-5}$ for typical piezoresistive cantilevers [420]. A Biot number of less than 10^{-1} indicates that the residual error of a lumped thermal model will be less than 5 % [421].

5.3.4 Convective Heat Transfer

Although we refer to heat transfer through the ambient fluid (e.g., air or water) as convection, buoyancy driven convection is negligible due to the small Rayleigh number of most microscale devices. The Rayleigh number for free convection at a heated wall can be calculated from

$$\text{Ra} = \frac{g\beta}{\nu\alpha}(T_s - T_\infty)L_c^3 \quad (5.9)$$

where g is the acceleration due to gravity, β , ν and α are the thermal expansion coefficient, kinematic viscosity and thermal diffusivity of the fluid, T_s and T_∞ are the temperatures of the heated surface and ambient, and L_c is the characteristic length of the system. The Rayleigh number is small for most microsystems due to the strong dependence on length; we calculated $\text{Ra} = 0.1$ for the piezoresistive cantilevers that we will discuss shortly. The critical Rayleigh number for free convection, above which buoyancy driven convection is significant, depends on the fluid but is on the order of 1,000 typically.

Although free convection does not take place, conduction through the fluid can be modeled using an effective convection coefficient for ease of boundary condition handling during analytical, numerical or FEA modeling. The convection coefficient can be calculated using one of two methods. The most direct method is to calculate it from the measured thermal conductance as

$$h_{\text{eff}} = \frac{G'_f}{P} \quad (5.10)$$

where G'_f is the thermal conductance from the device to the fluid per unit length and P is the surface area per unit length exposed to the fluid [420]. A second, less direct approach to calculating h_{eff} was presented by Hu et al. in 2008 [421],

$$h_{\text{eff}} = \frac{k_f S}{A} \quad (5.11)$$

where k_f is the thermal conductivity of the surrounding fluid, S is the heat conduction shape factor [419], and A is the total area exposed to the fluid. A major challenge with the second approach is calculating an appropriate shape factor. However, it does provide two important results: h_{eff} increases when the sensor is brought near a solid surface due to an increase in S [422], and, h_{eff} scales roughly linearly with the thermal conductivity of the surrounding fluid.

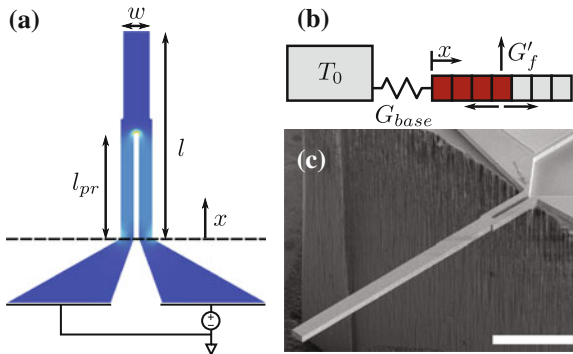


Fig. 5.6 **a** The cantilever geometry and simulated power dissipation density, **b** one-dimensional finite differences model used to calculate the temperature profile, and **c** scanning electron micrograph of a typical cantilever used here (Source Reprinted with permission from [134]. ©2011 American Institute of Physics)

5.3.5 Example Experimental and Modeling Results

The heat transfer and thermal conductivity models we have discussed in this section were used to investigate heat transfer in piezoresistive cantilevers [134]. We were interested in developing an accurate heat transfer model to enable the design of temperature- rather than power-constrained piezoresistive sensors. Until that point in time, most piezoresistor design optimization work either ignored Joule heating or set a power dissipation budget that was decoupled from the device design.

However, most applications are limited by temperature increase rather than power dissipation. The power dissipation is related to the temperature rise by the thermal resistance between the piezoresistor and ambient environment. Assuming that the cantilever cross-section scales as $[L]^2$ and the piezoresistor length as $[L]$, then the conductive thermal resistance from the piezoresistor to the silicon die scales as $[L]^{-1}$. Similarly, the thermal resistance due to heat transfer through the ambient fluid scales with the exposed surface area as $[L]^{-2}$. Clearly, power dissipation needs to scale with cantilever dimensions to maintain a constant temperature rise during operation.

Figure 5.6 shows the cantilever geometry, heat transfer model and a fabricated device. The overall length, width and thickness of the cantilever are l , w and t , respectively. The piezoresistor extends length l_{pr} from the base, encompasses the full cantilever width, and has a narrow slit to form a resistive loop. During operation, the resistor is electrically biased and Joule heating power W is distributed along its length.

The cantilevers were fabricated from silicon-on-insulator (SOI) wafers [132]. Briefly, the wafers were phosphorus doped at 800°C via POCl_3 predeposition. Subsequently the piezoresistor and cantilever were patterned and etched, aluminum was sputtered and patterned for electrical contacts, and the cantilever was released using deep reactive ion etching. The dopant concentration profile was measured using

Table 5.2 Summary of the cantilever designs used to investigate heat transfer in piezoresistive cantilevers [134]

	Design A	Design B
l (μm)	890	124
w (μm)	10	10
t (μm)	2	0.34
l_{pr} (μm)	212	32
k of Si at 300 K (W/m-K)	128.2	98.9
G'_f (mW/m-K)	32.8 ± 3.3	43.4 ± 2.7
h_{eff} (W/m ² -K)	1366 ± 139	2098 ± 131
G_{base} ($\mu\text{W/K}$)	41.9 ± 16.3	17.7 ± 8.4
Λ (μm)	287.1 ± 20.7	104.6 ± 25.0

Calculated and experimentally determined parameters are presented in the bottom half of the table
Experimental parameter uncertainty is presented as $\mu \pm \sigma$

spreading resistance analysis and the electrically active surface concentration was $2 \times 10^{20} \text{ cm}^{-3}$ (Fig. 4.6).

We focused on two cantilever designs whose dimensions are summarized in Table 5.2. The piezoresistor constitutes 90 and 59 % of the total resistance for designs A and B respectively. The piezoresistor self-heating depends primarily on the power dissipated in the released cantilever, so all of the power dissipation levels we will quote refer to the power dissipated in the cantilever itself. The excess resistance was measured using the transfer length method and is primarily due to the silicon interconnect resistance (Sect. 4.9.5).

We calculated the temperature profile, $T(x)$, from (5.6) assuming an isothermal boundary condition at the silicon die (T_0) and adiabatic conditions at the cantilever tip ($\partial T / \partial x = 0$). The thermal conductance between the cantilever and die, G_{base} , is finite. We calculated $k(x)$ using Ref. [418]. The temperature-dependent power dissipation per unit length (5.7) was used to calculate the temperature profile. The temperature dependence of the thermal conductivity, sheet resistance and power dissipation introduce nonlinearity into the problem and iterative numerical methods are required to find the steady-state solution.

There are two unknown parameters in the model (h_{eff} and G_{base}), so we measured the temperature profile of the cantilever and fit the model to the data. To fit the data, we allowed h_{eff} (or equivalently, G'_f) and G_{base} to vary while using the calculated values of k and \dot{q}' to minimize the sum of the squared relative temperature residuals.

There are three common temperature calibration techniques for piezoresistive silicon sensors: Raman thermometry, TCR thermometry and IR thermometry. All three temperature measurement techniques require calibration, whether it is the Raman shift with respect to temperature, the resistor TCR, or the emissivity of the device.

We used Raman thermometry to measure the temperature at discrete locations along the length of the cantilever as in Refs. [423, 424]. The cantilever was biased to induce self-heating and the temperature was measured from the wavelength shift of

the Stokes peak [425]. The laser wavelength, power, and spot diameter were 488 nm, 45 μW and 1 μm , respectively.

We also used a second method to estimate the average piezoresistor temperature: TCR thermometry. For this method, we calibrated the piezoresistor TCR using a temperature controlled oven (Thermotron S-1.2) and small bias power ($< 1 \mu\text{W}$), allowing the average piezoresistor temperature to be calculated from subsequent current-voltage measurements. Due to the high doping level of our diffusion-formed piezoresistors ($\approx 1.2 \times 10^{20} \text{ cm}^{-3}$), the TCR was only $1372 \pm 171 \text{ ppm/K}$ ($\mu \pm \sigma$, $N = 4$ devices) and was linear over the range of temperatures investigated. While the uncertainty of TCR-based measurements is usually higher than Raman-based measurements, the former is relatively quick and easy to perform once the calibration is complete and does not require any specialized optics.

A third method, infrared microscopy, is often used to measure the temperature optically. However, silicon is relatively transparent to infrared light and not enough light reflected off of our thin devices (340 and 2,000 nm thick) to enable accurate measurements. Raman thermometry uses a shorter wavelength of light (e.g., 488 nm) that interacts more readily with silicon.

Figure 5.7 plots the experimental and predicted temperature profiles for designs A and B operating in air. The temperature reaches a maximum approximately $\frac{2}{3}l_{\text{pr}}$ from the cantilever base and then decreases exponentially beyond it. The exponential decay can be described with a thermal healing length [426]

$$\Lambda = \sqrt{\frac{kA}{h_{\text{eff}}P}}. \quad (5.12)$$

While h_{eff} is insensitive to power dissipation, G_{base} and Λ vary considerably because they depend on k , which changes with temperature. The measured effective convection coefficients (Table 5.2) are comparable to recent simulation results (1,000–2,000 $\text{W/m}^2\text{-K}$) [414].

The cantilever tip temperature increases linearly with power dissipation by 2.5 and 36.7 K/mW for designs A and B in air, respectively. The thermal conductance from the piezoresistor to the cantilever base varies less than 20% between the designs. The 15-fold difference in $\partial T_{\text{tip}}/\partial W$ is primarily due to the difference in distance between the piezoresistor and cantilever tip between the designs (2.4 Λ vs. 0.9 Λ). In cantilever designs that are constrained by tip temperature, a shorter piezoresistor is favored during design optimization so that the distance from the piezoresistor to the tip is as large as possible.

The thermal conductivity of water is approximately 25 times greater than that of air. Based upon (5.11), we would expect a corresponding increase in h_{eff} in water. We measured the piezoresistor temperature during operation in air and water using TCR thermometry, and the results are presented in Fig. 5.8. The h_{eff} we measured in water was approximately 59 $\text{kW/m}^2\text{-K}$, or, about 28 times larger than the value in air. In designing piezoresistive cantilevers we assumed h_{eff} of 2 and 50 $\text{kW/m}^2\text{-K}$ in air and water, respectively [2, 97].

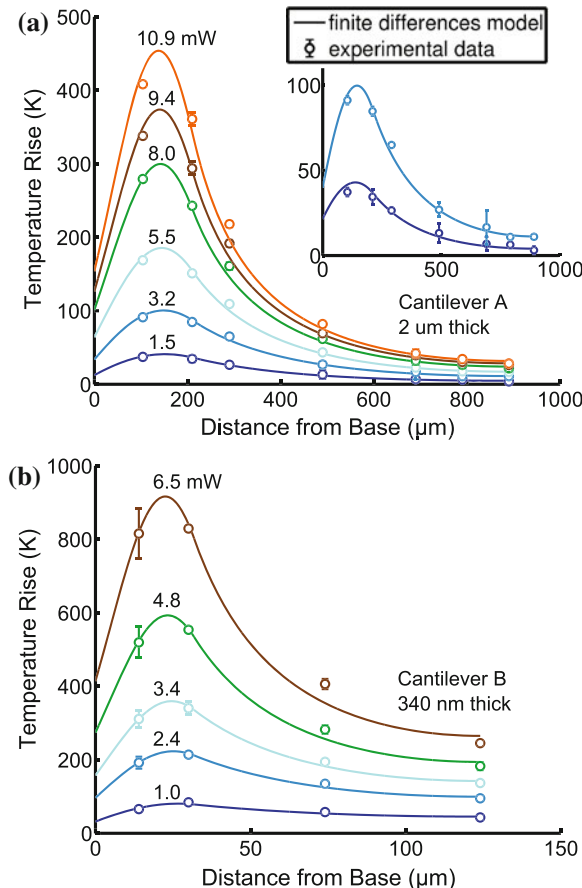


Fig. 5.7 a – b Comparison between Raman thermometry results and the finite differences model over a range of power dissipations in air. Error bars represent the standard deviation and are smaller than some of the symbols. The average model residual for both cantilever designs is 2 %. (inset) Detail of the 1.5 and 3.2 mW data for design A (Source Reprinted with permission from [134]. ©2011 American Institute of Physics)

Increased heat transfer into the fluid enables greater piezoresistor power dissipation for the same temperature rise in the sensor. As we will discuss in the next section, greater power dissipation corresponds to better sensor performance. For example, the force resolution that we measured in air was 76 % worse than in water for the same average piezoresistor temperature increase. The 28-fold increase in h_{eff} corresponds to a fivefold decrease in the thermal healing length, so the temperature beyond the piezoresistor decays far more quickly in water than in air. If the sensor force resolution is compared between air and water for the same tip temperature then the difference is even greater; for 500 μW of power dissipation (force resolution of 2.6 pN in air vs 2.9 pN in water), the predicted tip temperature change was 20 K in

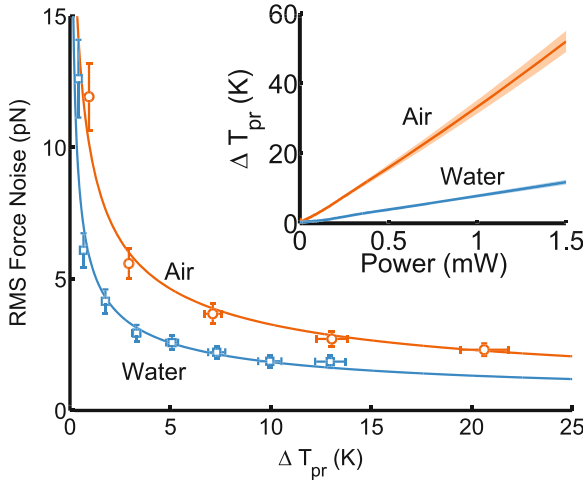


Fig. 5.8 Experimental force resolution in a 10 Hz to 10 kHz bandwidth for a piezoresistive cantilever (design B in Table 5.2) in air and water. The force noise in air is 76 % greater than in water for the same average piezoresistor temperature increase. (inset) Average piezoresistor temperature as a function of total power dissipation calculated from current-voltage curves in air and water. The piezoresistor TCR was calibrated in a temperature controlled oven to infer the piezoresistor temperature during experiments. Error bars represent the standard deviation (*Source* Reprinted with permission from [134]. ©2011 American Institute of Physics)

air and only 50 mK in water, a 400-fold reduction. The thermal advantage of water is slightly offset by water's increased density and viscosity which reduce the cantilever resonant frequency and yield a flatter frequency response [2, 97, 312].

5.3.6 Analytical Temperature Approximations

The results presented in Fig. 5.7 suggest that a fairly simple approach could be used to approximate the maximum and tip temperatures in a piezoresistive cantilever. If we can approximate the maximum temperature in the device and calculate an appropriate thermal healing length, then the temperature at any other location can be quickly calculated.

For a piezoresistive cantilever, the thermal conductance from the piezoresistor to the cantilever base, neglecting conduction to the surrounding fluid, is

$$G_{pr} \approx \frac{2wtk}{l_{pr}}. \quad (5.13)$$

If we assume that the majority of the heat is conducted to the base of the cantilever and not directly into the fluid then

$$T_{\max} \approx W \frac{G_{\text{base}} + G_{\text{pr}}}{G_{\text{base}} G_{\text{pr}}}.$$
 (5.14)

In an ideally designed and fabricated device, $G_{\text{base}} \rightarrow \infty$ and $T_{\max} \rightarrow W/G_{\text{pr}}$. In reality G_{base} will always be finite, although it can be maximized by ensuring a good thermal contact between the thin sensor region and thicker inactive region of the device.

The temperature at the tip of the device can then be calculated from

$$T_{\text{tip}} \approx T_{\max} \exp \left[\frac{-(l - 2l_{\text{pr}}/3)}{\Lambda} \right]$$
 (5.15)

where l is the overall length of the cantilever, $2l_{\text{pr}}/3$ is the approximate distance from the base of the cantilever to where the maximum temperature occurs and Λ is the thermal healing length.

Figure 5.9 compares the approximate tip temperature calculated from (5.15) and the experimental data. The agreement between the simplified model and experimental data is excellent (residual error <10 %) and can be used to speed up initial design work.

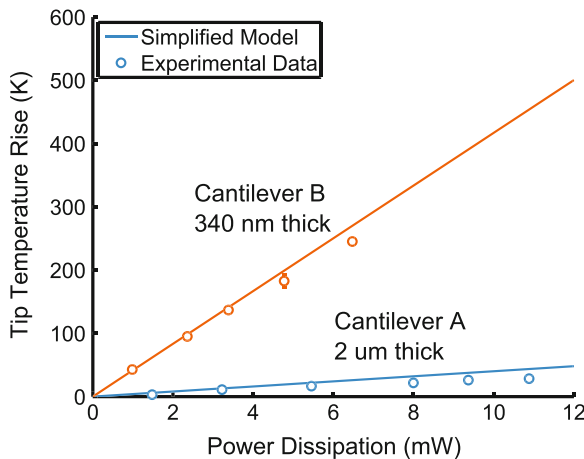


Fig. 5.9 Comparison between the measured and calculated tip temperature as a function of power dissipation. The tip temperature was calculated from (5.15) using the experimentally measured parameters in Table 5.2. The residual error between the simplified model and experimental data is <10 % (Source Reprinted with permission from [2])

5.4 Power Dissipation and Sensor Resolution

Piezoresistor power dissipation affects device performance in a number of ways. Consider the force resolution of a piezoresistive cantilever (3.85). We ignore thermomechanical and amplifier noise for the sake of simplicity because they do not limit measurement resolution in most applications. Then the minimum detectable force (MDF) is

$$\text{MDF} = \frac{\sqrt{V_J^2 + V_H^2}}{S_{\text{FV}}}. \quad (5.16)$$

which we expand following (3.78) and (3.83) to obtain

$$\text{MDF} = \frac{\sqrt{4k_b T_{\text{pr}} R (f_{\max} - f_{\min}) + \alpha V_{\text{bridge}}^2 \ln(f_{\max}/f_{\min})/2N_{\text{eff}}}}{3V_{\text{bridge}}(l - l_{\text{pr}}/2)\pi_1^{\text{ref}} \gamma \phi \beta^*/2wt^2} \quad (5.17)$$

where we emphasize that T_{pr} is the average piezoresistor temperature. Rewriting the resolution in terms of power dissipation rather than bridge bias by using the fact that $W = V_{\text{bridge}}^2/4R$ yields

$$\text{MDF} = \frac{\sqrt{k_b T_{\text{pr}} (f_{\max} - f_{\min})/W + \alpha \ln(f_{\max}/f_{\min})/2N_{\text{eff}}}}{3(l - l_{\text{pr}}/2)\pi_1^{\text{ref}} \gamma \phi \beta^*/2wt^2}. \quad (5.18)$$

The only term in (5.18) that depends on the power dissipation is Johnson noise. Increasing the power dissipation without changing any other design parameters, by increasing the bridge bias for example, will reduce the MDF as $1/\sqrt{W}$. Several earlier design optimization studies have made this observation [127, 131, 133], but is more power dissipation always good?

One important simplification in (5.18) is that self-induced Joule heating is ignored; piezoresistor temperature is independent of power dissipation. But we know that a higher piezoresistor temperature corresponds to increased Johnson noise and decreased sensitivity. We can simplify (5.18) by defining constants

$$c_1 = k_b(f_{\max} - f_{\min}) \quad (5.19)$$

$$c_2 = \alpha \ln(f_{\max}/f_{\min})/2N_{\text{eff}} \quad (5.20)$$

$$c_3 = 3(l - l_{\text{pr}}/2)\pi_1^{\text{ref}} \gamma \phi \beta^*/2wt^2 \quad (5.21)$$

to obtain

$$\text{MDF} = \frac{\sqrt{c_1 T_{\text{pr}}/W + c_2}}{c_3}. \quad (5.22)$$

Table 5.3 Typical model parameters for our power dissipation analysis

Parameter	Units	Description	Typical Value
c_1	-	Hooge noise	10^{-12}
c_2	J/K	Johnson noise	5.5×10^{-18}
c_3	V/N·V	Sensitivity	10^5
c_4	W/K	Thermal conductance	2×10^{-6}
c_5	1/K	TCS	-1.2×10^{-3}
T_0	K	Ambient temperature	300

The temperature coefficient of resistance for the resistor isn't explicitly included in (5.22) here because the problem is formulated in terms of W ; the problem can be formulated in terms of V_{bridge} to explicitly include the TCR.

However, force resolution depends on piezoresistor temperature. As the piezoresistor temperature increases, the Johnson noise increases while the piezoresistance factor decreases. We can add thermal coupling to the model with these two refinements:

$$T_{\text{pr}} = T_0 + W/c_4 \quad (5.23)$$

$$S_{\text{FV}} = c_3 V_{\text{bridge}} (1 + c_5 T_{\text{pr}}) \quad (5.24)$$

where c_4 is the thermal conductance from the piezoresistor to the ambient, which is fixed at temperature T_0 . For our particular example of a piezoresistive cantilever, considering only thermal conduction along the length of the cantilever, the thermal conduction coefficient is approximately

$$c_4 = 2wtk/l_{\text{pr}}. \quad (5.25)$$

The final coefficient, c_5 , is the temperature coefficient of sensitivity (TCS) and accounts for the reduction in piezoresistance factor with increasing temperature. We assume a TCS of -1,300 ppm/K (Fig. 5.1), representative of a piezoresistor doped to about 10^{19} cm^{-3} [67].

Substituting these new parameters into (5.22) yields

$$\text{MDF} = \frac{\sqrt{c_2 + c_1/c_4 + c_1 T_0/W}}{c_3(1 + c_5 T_0 + c_5 W/c_4)}. \quad (5.26)$$

Figure 5.10a plots the force resolution calculated as a function of power dissipation using the parameters in Table 5.3. The variation in force resolution with power dissipation is not monotonic and higher power dissipation is not always desirable. For low powers, when T_{pr} is close to T_0 , the force resolution improves as $1/\sqrt{W}$ and a minimum is reached at 2.58 mW, corresponding to $T_{\text{pr}} = 436 \text{ K}$ and $F_{\min} = 2 \text{ pN}$.

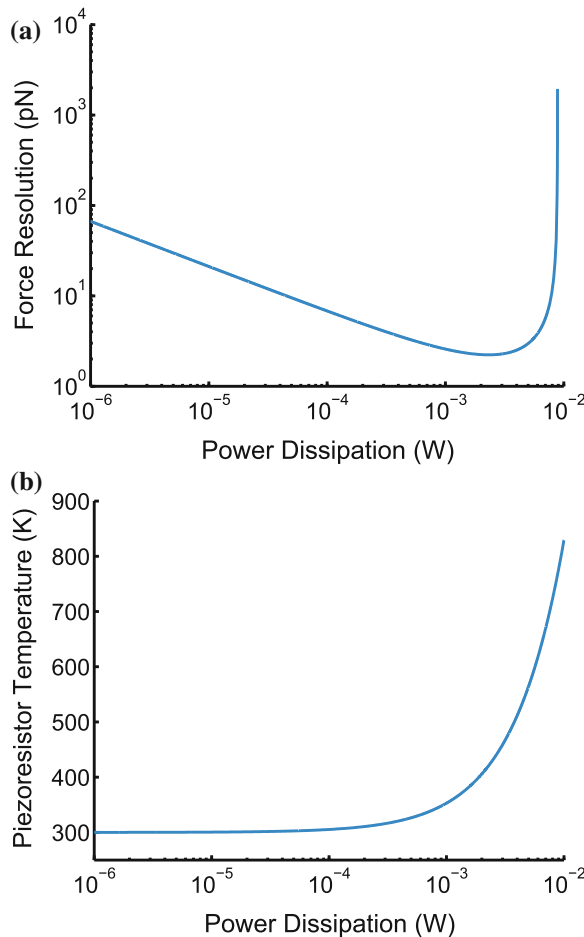


Fig. 5.10 Simplified numerical model results for the (a) minimum detectable force and (b) average piezoresistor temperature as a function of power dissipation. Assuming that neither the power dissipation nor the piezoresistor temperature are constrained by any application requirements, the optimal force resolution of 2 pN corresponds to a power dissipation of 2.58 mW and average temperature of 436 K. Force/displacement resolution improves monotonically as $1/\sqrt{W}$ from 1 μ W to 1 mW until flattening and abruptly degrading due to the increasing piezoresistor temperature (Source Reprinted with permission from [2])

But above a critical power dissipation the temperature begins to take off (Fig. 5.10b). The transition begins when $W \approx c_4 T_0/2$ and the transition rate with respect to power depends on the magnitudes of $c_4 (\partial T_{pr}/\partial W)$ and $c_5 (\partial S_{FV}/\partial T_{pr})$.

This relatively simple model captures the behavior of more complete piezoresistive sensor performance models that include thermomechanical noise, amplifier noise, and more accurate temperature modeling. Ideally, the power dissipation would be chosen to reach the minimum of (5.26). However in applications where the

maximum temperature needs to be limited to avoid damaging the sample, design optimization strives to get as close as possible to the curve minimum without exceeding the temperature constraint.

One aspect of power dissipation that has not been addressed here is the potential for increased low frequency noise at high operating temperatures. Park et al. compared the noise of piezoresistive cantilevers with unreleased piezoresistors at high power dissipation levels [133]. The low frequency noise of the cantilevers increased sharply at high power dissipation whereas the unreleased piezoresistors were unaffected. One plausible explanation for the results is that low frequency changes in air flow significantly modulated the temperature of the piezoresistive cantilevers due to their high operating temperature and high surface area. The effect of power dissipation on low frequency noise is only qualitative at this point in time, but care should be taken when operating piezoresistive sensors in air at temperatures far above (e.g., $> 100^{\circ}\text{C}$) their surroundings.

In summary, there are two regimes for $\partial\text{MDF}/\partial W$. When the cantilever is operated near ambient temperature, performance improves with power as $1/\sqrt{W}$. However, if the piezoresistor temperature gets too far above the ambient then performance rapidly degrades. The power dissipation at which this transition occurs depends on the ambient temperature. If the ambient temperature is low (e.g., 300 mK in a helium cryostat) then the optimal power dissipation will be far smaller than if the same sensor were operated at room temperature.

This analysis bridges the gap between previous studies that indicated higher piezoresistor power dissipation was always favorable [127, 131, 133] and the deleterious performance at high power dissipation levels that researchers have observed [138]. Regardless of the cantilever operating regime, increasing the thermal conductance from the piezoresistive sensor (e.g., operating in a higher thermal conductivity fluid) leads to better performance unless power dissipation is tightly constrained.

5.5 Summary

This chapter addressed a variety of temperature-related effects. As the temperature increases, the sensitivity of a piezoresistor decreases ($\text{TCS} < 0$) while its electrical resistance increases ($\text{TCR} > 0$). These effects lead to a degradation in performance with increasing temperature.

However, the magnitude of both the TCS and TCR vary with dopant concentration. The TCS and TCR of degenerately doped piezoresistors (e.g., 10^{20} cm^{-3}) are 5–10x smaller than their lightly doped counterparts, which is one of the many benefits of high dopant concentrations.

Joule heating is an unavoidable side effect of piezoresistor operation. The temperature increase due to Joule heating can be significant without careful design; experimental temperatures of up to 900°C are presented in Fig. 5.7. Piezoresistors that are biased with a constant current source are prone to thermal runaway due to the increase in electrical resistivity and decrease in thermal resistivity with temperature.

The thermal conductivities of commonly used materials were discussed in Sect. 5.3.2. Two models for the thermal conductivity of single crystal silicon were presented: the simplified model of Asheghi et al. [417] and the expanded model of Liu et al. [418]. The expanded model accounts for variation in thermal conductivity with dopant concentration, temperature and dimensions.

Heat transfer in piezoresistive sensors is typically dominated by solid-state conduction and convection, with radiation playing a role above 600°C. A one-dimensional model of heat transfer was applied to a piezoresistive cantilever to illustrate thermal modeling. Self-heating in a piezoresistive cantilever was experimentally studied using Raman- and TCR-thermometry and model parameters were extracted. We also noted that piezoresistor performance improves with operation in a high thermal conductivity environment (e.g., water vs air) assuming that the piezoresistor power dissipation is chosen to satisfy a maximum temperature constraint.

This chapter closed by discussing the relationship between power dissipation (i.e., Joule heating) and measurement resolution. As an example we discussed the force resolution of a piezoresistive cantilever beam. Excluding amplifier and thermomechanical noise, the broadband force resolution can be written as

$$\text{MDF} = \frac{\sqrt{k_b T_{\text{pr}} (f_{\max} - f_{\min}) / W + \alpha \ln(f_{\max}/f_{\min}) / 2N_{\text{eff}}}}{3(l - l_{\text{pr}}/2)\pi_1^{\text{ref}} \gamma \phi \beta^*/2wt^2}. \quad (5.18)$$

Increasing the power dissipation (W) leads to a reduction in the effective contribution of Johnson noise (Figs. 2.17 and 3.7). From (5.18) it would appear that measurement resolution improves as $1/\sqrt{W}$ until the sensor is 1/f noise limited.

However, resolution sharply degrades once Joule heating increases the piezoresistor temperature significantly above that of its surroundings (Fig. 5.10). As discussed in the last chapter, high temperature is detrimental to all piezoresistive sensors because it leads to a reduction in sensitivity and an increase in noise.

Figure 5.10 also illustrates that low power sensors (e.g., μW power dissipation and μA bias currents) are possible with only a modest degradation in resolution.

Chapter 6

Design Optimization

The design of a typical piezoresistive sensor is specified by at least a dozen separate parameters, such as bias voltage and piezoresistor length. Design optimization is the process of selecting the single most optimal design from this enormous parameter space by employing models to predict device performance for each unique combination of design parameters. Piezoresistor design is complicated by the large number of design parameters and degree of nonlinear coupling between the parameters, design constraints and overall performance. This chapter will summarize the basic design tradeoffs and present numerical optimization as a robust approach to designing optimized piezoresistive sensors.

Consider one of the most important design parameters, the peak dopant concentration of the piezoresistor. Increasing the dopant concentration reduces the noise of the piezoresistor (Sect. 3.1) but also decreases its strain sensitivity (Sects. 2.2.2 and 3.2). Increasing the dopant concentration also has secondary effects that don't directly impact resolution but are important for most applications. Increased dopant concentrations yield reduced temperature coefficients of sensitivity and resistance (Sects. 5.1 and 5.2) but increased power dissipation and self-heating (Sect. 5.3). Table 6.1 summarizes the effect of individual parameter changes on several of the most important measures of sensor performance.

The tight coupling between the design parameters in Table 6.1 makes piezoresistor design non-trivial. Design is further complicated because piezoresistors are simultaneously mechanical, thermal and electronic devices, so multiple interconnected models are required to accurately predict device performance. A final challenge is that designs typically need to be constrained in some way, either in the maximum spring constant for a contact mode scanning probe or the maximum temperature rise of a catheter pressure sensor.

A good general rule of thumb for piezoresistive sensor design is that the two largest noise sources should be balanced in amplitude. Harley first demonstrated

We would like to thank Nahid Harjee and Sung-Jin Park for extensive discussions on design optimization and their contributions to the concepts presented in this chapter.

this effect in 2000 while optimizing the design of epitaxial piezoresistive cantilevers (Fig. 6.1) [127, 301]. We reached the same conclusion in 2009 while optimizing the design of diffused piezoresistors operating in liquid [131].

Balancing noise sources in a piezoresistor leads to optimal performance because the two dominant sources, Johnson and Hooge noise, are uncorrelated (Sect. 3.1). A geometric interpretation of the problem is that for two orthogonal vectors (Johnson and Hooge noise in this case) the ratio of their vector sum to the sum of their individual lengths is minimized when they are equal in magnitude.

We will use a cantilever beam intended for force sensing as an example. Consider the case where the $1/f$ noise is significantly larger than the Johnson noise. We'll assume that the integrated $1/f$ noise is 10 mV RMS, the Johnson noise is 1 mV RMS and the force sensitivity is 1 V/nN. The overall noise is 10.04 mV RMS, giving a force noise floor of 10 pN RMS.

From Table 6.1 we see that increasing the length of the piezoresistor (l_{pr}) will increase the $1/f$ noise (V_H), decrease the Johnson noise (V_J) and increase the force sensitivity (S_{FV}). From Chap. 3 we know that increasing the piezoresistor length by ninefold will decrease the $1/f$ noise threefold (to 3.3 mV RMS), increase the Johnson noise threefold (to 3 mV RMS) and increase the force sensitivity by roughly ninefold (to 9 V/nN) assuming that the cantilever remains much longer than the piezoresistor. Using these new numbers, the overall noise is 4.46 mV RMS and the force noise floor

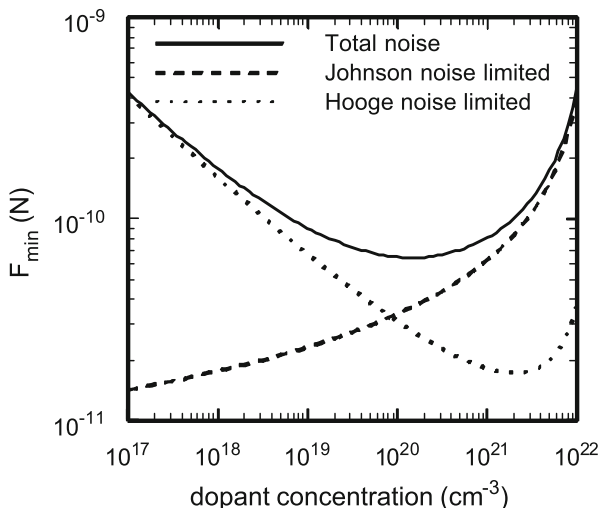


Fig. 6.1 Piezoresistor optimization and noise source balancing. Harley analytically optimized the design of epitaxial piezoresistive cantilevers operating on a fixed power budget (2.5 mW). At each concentration the dimensions of the piezoresistor are optimized to minimize the integrated force noise. Optimal performance is obtained at approximately 10^{20} cm^{-3} when the magnitude of the Johnson and Hooge noise sources are comparable (Source Reprinted with permission from [301] courtesy of Jonah Harley)

Table 6.1 Design matrix showing the effect of design parameter changes on sensor performance

	S_{XV} (V/m)	S_{FV} (V/N)	V_H (V/ \sqrt{Hz})	V_J (V/ \sqrt{Hz})	W (W)	ΔT_{max} (K)	f_0 (Hz)	k (N/m)
l (m)	↓	↑	-	-	-	-	↓	↓
w (m)	-	↓	-	-	-	↓	-	↑
t (m)	↑	↓	-	-	-	↓	↑	↑
l_{pr} (m)	↑	↑	↓	↑	↓	-	-	-
w_{pr} (m)	-	-	↓	↓	↑	↑	-	-
V_{bridge} (V)	↑	↑	↑	-	↑	↑	-	-
N_{epi} (cm $^{-3}$)	↓	↓	↓	↓	↑	↑	-	-
t_{pr} (m)	↓	↓	↓	↓	↑	↑	-	-
T_{diff} ($^{\circ}$ C)	↓	↓	↓	↓	↑	↑	-	-
t_{diff} (min)	↓	↓	↓	↓	↑	↑	-	-
$N_{implant}$ (cm $^{-2}$)	↓	↓	↓	↓	↑	↑	-	-
$E_{implant}$ (keV)	↓	↓	-	-	-	-	-	-
\sqrt{Dt} (m)	↓	↓	↓	↓	↑	↑	-	-

As the indicated design parameter increases (while the other parameters are held constant), the observed parameters *increase* (↑), *decrease* (↓), or *do not change substantially* (-). The observed parameters are the displacement sensitivity (S_{XV}), force sensitivity (S_{FV}), 1/f noise (V_H), Johnson noise (V_J), power dissipation (W), maximum temperature increase (ΔT_{max}), resonant frequency (f_0) and spring constant (k). Design parameters common to all fabrication methods are described first, followed by predeposition-, ion implantation-, and epitaxy-specific parameters. l , w , and t are the overall sensor length, width and thickness, l_{pr} and w_{pr} are the piezoresistor length and width, and V_{bridge} is the bridge bias voltage. In the case of epitaxy, N_{epi} and t_{pr} are the dopant concentration and piezoresistor thickness. In the predeposition/diffusion case, T_{diff} and t_{diff} are the predeposition temperature and time. In the case of ion implantation $N_{implant}$ and $E_{implant}$ are the ion implantation dose and energy while \sqrt{Dt} is the diffusion length of the post-implantation anneal

has decreased to 0.4 pN RMS, a 25-fold improvement. Hopefully this brief example highlights the general principle of balancing noise sources.

6.1 Optimization Fundamentals

Design optimization refers to selecting the best available design from a set of alternatives given a complex set of fabrication and operating constraints. There are three important concepts in design optimization: optimality, parameters, and constraints.

Optimality can be defined in a variety of ways depending on the application. A force sensor for scientific research might be optimized to minimize the force noise irrespective of cost or other constraints, while a commercial pressure sensor might aim to minimize the die area while meeting minimum performance requirements [427]. The first step in design optimization then is to define a goal that can be

minimized or maximized. The goal should be a smooth and continuous function that can be computed from the design parameters that define the sensor.

Design parameters define the size and shape of the piezoresistive sensor. Examples include the overall sensor dimensions, piezoresistor dimensions, ion implantation dose or bridge bias voltage. The size of the design parameter set should be minimized while completely and uniquely defining the device design; in other words, the design parameter set should span the device design space but remain full rank. As the size of the design parameter set increases, the complexity and computational cost of design optimization increases. Accordingly the size of the design parameter set should be minimized; 5–20 parameters is typical. As in the case of the optimization goal function, the design parameters should be smooth and continuous to simplify the optimization process. Both analytical and numerical techniques rely on computing the gradient of the goal function with respect to the design parameters, and while discontinuous goals or parameters can be used if absolutely necessary, they generally add unnecessary complexity and can often be rewritten using constraints.

Constraints define the range of design parameter values that are physically realizable. Constraints come in two varieties: parameter constraints and computed constraints. Parameter constraints apply directly to the design parameters; minimum and maximum dimensions for the piezoresistor or Wheatstone bridge bias voltage. Parameter constraints simply limit the range of realizable design parameters. However, combinations of the design parameters are often important. For example, the sensor stiffness depends on all of the sensor dimensions, so cannot be written as simple bounds on each of the parameters, which is unfortunate because simple bounds (or box constraints) are far simpler to handle in numerical optimization [428]. Computed constraints can be nonlinear and can be either inequality or equality constraints. While some design parameters are flexible and can be modified during the design process (e.g. dopant concentration), others are constrained to predetermined values (e.g. measurement bandwidth, contact via size); parameters that are constrained to a single value can either be excluded from the design parameter set or constrained with the lower and upper bounds set to the desired value.

Device designs can be optimized either analytically or numerically. Both approaches strive to find the combination of design parameters that achieve optimal performance while respecting design constraints. Both methods operate by finding a combination of design parameters where the gradient of the optimization goal, $\nabla f(\mathbf{x})$, approaches zero and the Hessian, $\nabla^2 f(\mathbf{x})$, is either positive or negative depending on whether a minimum or maximum value of the performance function is desirable. In this syntax, $f(\mathbf{x})$ may be the minimum detectable force (MDF) while the vector \mathbf{x} defines the device design parameters. In analytical methods we symbolically manipulate the device design equations to find parameter combinations where $\nabla f(\mathbf{x}) \rightarrow 0$, while in numerical methods we utilize a computer to help us in the task.

6.2 Analytical Optimization

The analytical optimization of piezoresistive devices has been reported numerous times with varying degrees of model complexity [82,126–128]. As an example of analytical optimization, consider the force resolution of a piezoresistive cantilever. Beginning from (5.17), which neglects piezoresistor self-heating, amplifier noise, and thermomechanical noise, the MDF can be written as

$$\text{MDF} = \frac{\sqrt{4k_b T_{\text{pr}} R(f_{\max} - f_{\min}) + \alpha V_{\text{bridge}}^2 \ln(f_{\max}/f_{\min})/2N_{\text{eff}}}}{3V_{\text{bridge}}(l - l_{\text{pr}}/2)\pi_1^{\text{ref}} \gamma \phi \beta^*/2wt^2}. \quad (6.1)$$

In the case of an epitaxial device, we can make the following simplifications

$$R \approx 4l_{\text{pr}}/q\mu nwt_{\text{pr}} \quad (6.2)$$

$$N_{\text{eff}} \approx N_{\text{epi}} l_{\text{pr}} w t_{\text{pr}} \quad (6.3)$$

$$\beta^* \approx P(1 - t_{\text{pr}}/t) \quad (4.27)$$

$$P \approx \log_{10}(1.53 \times 10^{22}/N_{\text{epi}})^{0.2} \quad (2.26)$$

where β^* for epitaxial piezoresistors was derived earlier and we are using Harley's empirical fit for the piezoresistance factor. We also assume that $w \approx 2w_{\text{pr}}$, $\gamma \approx 1$ and $\phi \approx 1$ for simplicity here although γ and ϕ can both be significantly smaller than unity in real designs.

After making these substitutions, the final expression for the MDF is

$$\text{MDF} = \frac{2wt^2 \sqrt{\frac{16k_b T_{\text{pr}} l_{\text{pr}} (f_{\max} - f_{\min})}{q\mu N_{\text{epi}} w t_{\text{pr}}} + \frac{\alpha V_{\text{bridge}}^2 \ln(f_{\max}/f_{\min})}{2N_{\text{epi}} l_{\text{pr}} w t_{\text{pr}}}}}{3V_{\text{bridge}} \left(l - \frac{l_{\text{pr}}}{2}\right) \pi_1^{\text{ref}} \log_{10} \left(\frac{1.53 \times 10^{22}}{N_{\text{epi}}}\right)^{0.2} \left(1 - \frac{t_{\text{pr}}}{t}\right)}. \quad (6.4)$$

In order to analytically optimize the device design the next step would be to calculate the gradient of the MDF with respect to the design parameters. This is by no means a simple task, although the process can be simplified by recognizing certain parameters that should be as large or as small as possible. We refer the reader to Harley et al [127] for a complete design optimization of epitaxial piezoresistive cantilevers for constant power dissipation operation.

The fundamental problem with analytical optimization is one of complexity. Even (6.4), while unwieldy, is a simplified device model that neglects Joule heating, amplifier and thermomechanical noise, and all forms of design constraints. Probably most importantly, the approach does not extend to diffused or ion implanted piezoresistors, where simple expressions for R , β^* and N_{eff} are not available. Other aspects

of device design, such as dynamics when operating in liquid, can not be included in this approach either. Fortunately, numerical optimization methods do not suffer from these limitations and can be implemented in a very user friendly fashion.

6.3 Numerical Optimization

Numerical optimization evaluates the goal function and its gradients numerically in order to automatically find the design optimum. Consider $f(\mathbf{x})$ and an initial set of design parameters, $\mathbf{x} = (x_1, x_2, \dots, x_n)$. Starting from this initial design, we can calculate the gradient, $\nabla f(\mathbf{x}) = (\partial f / \partial x_1, \partial f / \partial x_2, \dots, \partial f / \partial x_n)$, with respect to the design parameters. We can then decrease $f(\mathbf{x})$ by moving along the directions where $\partial f / \partial x_i < 0$. By taking a step in the direction where the gradient is most negative, recalculating the gradient and iterating, we will eventually find a point where $\nabla f(\mathbf{x}) \rightarrow 0$. The gradient can be zero at minima, maxima, and saddle points, so the Hessian, $\nabla^2 f(\mathbf{x})$, is used to determine the nature of the inflection point. The search direction, step length and constraint handling technique varies between optimization methods.

Numerical optimizers can either calculate the gradient at each iteration or use a provided value. Allowing the optimizer to calculate the gradient numerically is slower but allows more complex models to be used and is necessary for piezoresistors fabricated by either predeposition or ion implantation. The numerical optimizer estimates the gradient and Hessian by calculating the change in $f(\mathbf{x})$ for small changes in \mathbf{x} . The optimizer will need to calculate $f(\mathbf{x})$ up to $2n$ times for each step where n is the number of design parameters. Thus our emphasis on calculation speed in the selection of device models (e.g. ion implantation modeling in Sect. 4.4).

Although optimization is conceptually straightforward, there are numerous practical difficulties ranging from large scale and non-convex problems to stochastic and multi-objective problems. For example, optimization problems are convex if $\nabla^2 f(\mathbf{x}) > 0$ for all \mathbf{x} [429]. If the problem is non-convex then multiple minima will exist (Fig. 6.2). Piezoresistor design is non-convex [131], so piezoresistive sensor optimization techniques will occasionally find local minima that are not the global minimum.

Although the problem is not strictly convex, the global optimum can reliably be found by starting from many random initial guesses until multiple iterations converge to within a small tolerance. Typical optimizer operation is illustrated in Fig. 6.3. Three piezoresistive cantilever designs are randomly seeded to start the process. The initial designs are randomly generated assuming a uniform probability density function for each parameter between its upper and lower bounds. At each iteration, the optimizer evaluates the gradient and Hessian matrices and chooses a step direction that would improve the design performance (e.g. minimizing the MDF). The MDF generally decreases every iteration, unless the optimizer runs into a constraint, in which case it may need to briefly increase the MDF. All three initial designs reach the same result

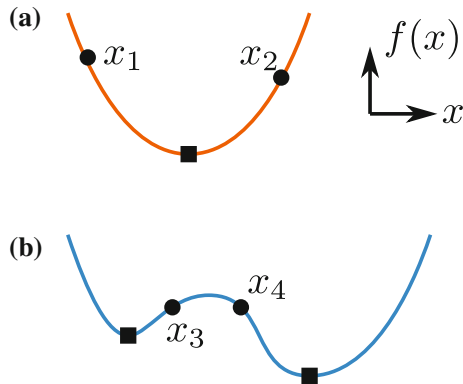


Fig. 6.2 Examples of **a** convex and **b** non-convex optimization problems. In **a**, a single global optimum exists and the same result will be obtained whether x_1 or x_2 is used as the optimization starting point. However, piezoresistive optimization is not usually a convex problem, and many local optima exist. In **b**, the optimizer will return different results depending on whether it starts from x_3 or x_4 . The solution to this problem is seeding the optimizer with several randomly generated starting points (*Source* Reprinted with permission from [2])

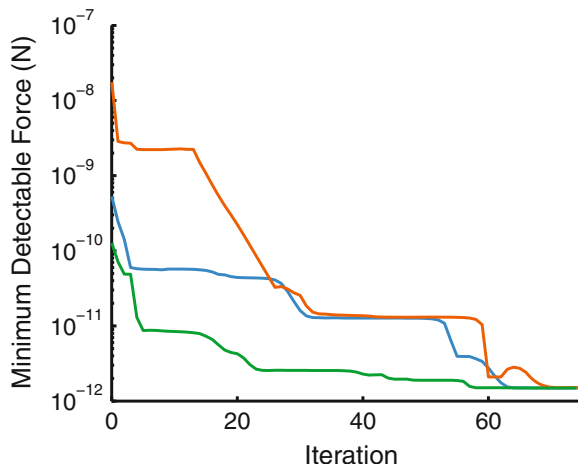


Fig. 6.3 Numerical optimizer operation. Several sensor designs are randomly generated and optimized until each converges. The non-convex nature of the problem is handled by optimizing randomly generated designs until several of them converge to the same solution (*Source* Reprinted with permission from [2])

and the performance improves up to four orders of magnitude compared with the initial, randomly generated designs.

The statistics of the numerical optimizer are presented in Fig. 6.4. The optimizer finds the global optimum 99.3 % of the time in the case of an epitaxial piezoresistive cantilever. The other 0.7 % of the time it finds a local optimum which is slightly

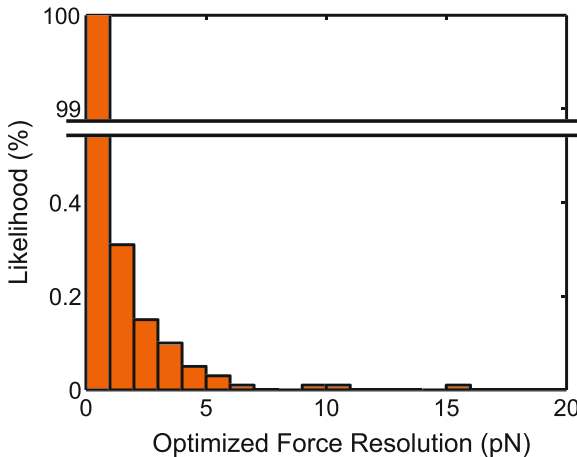


Fig. 6.4 Numerical optimizer convergence statistics. The global optimum is found 99.3 % of the time in the case of an epitaxial piezoresistor. Running the optimizer with randomly generated designs until three of them converge to the same result ensures that the global optimum is missed less than once every million runs (*Source* Reprinted with permission from [2])

inferior to the global optimum. By running the optimizer with randomly generated designs until several of them converge to the same result the global optimum can reliably be found. For example, if the optimizer misses the global optimum 0.7 % of the time, waiting until three optimization runs converge to the same result ensures that the global optimum is missed less than once every million runs.

We won't go into numerical design optimization much further than this, instead relying on widely available optimizer implementations, but we refer the reader to Nocedal and Wright [430] for a comprehensive treatment of numerical optimization. We typically use the sequential quadratic programming (SQP) or interior-point method with the gradient approximated by finite-differences and Quasi-Newton Hessian updates as implemented by `fmincon` in the MATLAB® Optimization Toolbox™. Completely open source alternatives are available as well (e.g. SciPy). Optimizing a single design can take anywhere from 30 s to 10 min depending on the model complexity and CPU speed.

Numerical optimization has been used by several other piezoresistor research groups. Researchers at Bosch have presented several numerical optimization techniques for piezoresistive accelerometers [427, 431]. The Bosch researchers used gradient-based optimization algorithms to find local optima while they used genetic algorithms to aid in finding the global optimum. We use gradient-based methods, but rather than using genetic algorithms, we generate randomized seed designs in order to find the global optimum. Their 2010 paper [427] addresses some of the practical issues with numerical optimization that we did not have room to discuss in our 2009 paper [131]. Most notably, they discuss parameter scaling in detail. In brief, the wide variation in design parameter scale (e.g. $t_{pr} = 10^{-7}$ m while $n = 10^{20}$ cm $^{-3}$) makes

it difficult for the optimizer to choose an appropriate step size for gradient evaluation. To address this issue, we scale the design parameters to be on the order of 1 at every step of the process where the optimizer chooses the direction and distance to step the design parameters.

Our optimizer and piezoresistive sensor modeling implementation (entitled piezoD) is open source and freely available online. Directions for downloading and contributing to piezoD are available in the Preface and Appendix C. Generation of the TSUPREM-4™ lookup table, required for numerically optimizing the design of ion implanted piezoresistors, is also discussed in Appendix C and the table generation code is similarly open source and freely available online.

6.4 Example: Fabrication Process Selection

Several methods for doping piezoresistive sensors have been presented throughout this book. However we have not compared their relative strengths and weaknesses in detail yet. In this section we will utilize design optimization to provide approximate guidelines and design rules for selecting a doping method for a given application.

There are three important issues in selecting a doping method: the optimal dopant concentration to target, the dopant species to use and the fabrication process. We will consider each in turn and focus on the design of a cantilever-based force sensor as a representative test case. Cantilevers, like pressure and surface stress sensors, benefit from being as thin and compliant as possible, resulting in similar design issues.

6.4.1 Problem Definition

Before designing a device, the application and design constraints should be clearly defined. We will describe the conditions used in this section before defining them mathematically.

We will optimize the cantilever dimensions, fabrication process and operating conditions to minimize the force noise (i.e. $V_{\text{noise}}/S_{\text{FV}}$) between 1 mHz and 1 kHz while maintaining a resonant frequency of at least 2 kHz. No constraint will be placed on the cantilever spring constant or power dissipation, but we will limit the maximum temperature increase of the cantilever to 10 K. For this problem we will assume that the cantilever is operating in vacuum at 300 K.

The Wheatstone bridge bias voltage will be constrained to a maximum value of 10 V and we will assume that the readout circuit is temperature compensated with an identical cantilever beam that is not mechanically loaded during measurements. The thickness of the cantilever will vary throughout this optimization example, although we will always constrain the cantilever width to be at least three times the cantilever thickness to ensure that the cantilever is much stiffer in-plane than out-of-plane.

We can write the optimization problem more explicitly as

$$\text{minimize } \text{MDF}(\mathbf{x}) = V_{\text{noise}}(\mathbf{x}) / S_{\text{FV}}(\mathbf{x})$$

where

$$(\text{epitaxy}) \quad \mathbf{x} = (l, w, t, l_{\text{pr}}, V_{\text{bridge}}, t_{\text{pr}}, N_{\text{epi}})$$

$$(\text{diffusion}) \quad \mathbf{x} = (l, w, t, l_{\text{pr}}, V_{\text{bridge}}, t_{\text{diff}}, T_{\text{diff}})$$

$$(\text{implant}) \quad \mathbf{x} = (l, w, t, l_{\text{pr}}, V_{\text{bridge}}, N_{\text{implant}}, E_{\text{implant}}, t_{\text{anneal}}, T_{\text{anneal}})$$

$$\text{subject to } f_{\text{min}} = 1 \text{ mHz}$$

$$f_{\text{max}} = 1 \text{ kHz}$$

$$f_0 \geq 2 \text{ kHz}$$

$$T_{\text{max}} \leq 10 \text{ K}$$

$$V_{\text{bridge}} \leq 10 \text{ V}$$

$$w \geq 3t$$

The design parameters (also known as state variables) that define the cantilever vary with fabrication and, beyond the explicitly stated constraints, need to be limited to physically realistic values. For example, the piezoresistor length needs to be constrained to $0 \leq l_{\text{pr}} \leq l$. We typically implement this constraint by using l_{pr}/l as a state variable rather than l_{pr} and enforcing $0 \leq l_{\text{pr}}/l \leq 1$. Alternatively, one can use l_{pr} as a state variable and update the constraint bounds every iteration based upon changes to l .

A hierarchy of equations are required to calculate the cantilever performance and ensure that our design constraints are respected. We start from our definition of the minimum detectable force,

$$\text{MDF} = \frac{V_{\text{noise}}}{S_{\text{FV}}}. \quad (3.85)$$

We previously defined the voltage noise and force sensitivity as

$$V_{\text{noise}} = \left[(f_{\text{max}} - f_{\text{min}}) \left(4k_{\text{b}}TR + A_{\text{VJ}}^2 + 2A_{\text{IJ}}^2 \left(\frac{R}{2} \right)^2 + S_{\text{FV}}^2 \frac{4k_{\text{c}}k_{\text{b}}T}{\omega_0 Q} \right) + \ln \left(\frac{f_{\text{max}}}{f_{\text{min}}} \right) \left(V_{\text{bridge}}^2 \frac{\alpha}{2N_{\text{eff}}} + A_{\text{VF}}^2 + 2A_{\text{IF}}^2 \left(\frac{R}{2} \right)^2 \right) \right]^{1/2} \quad (3.78)$$

$$S_{\text{FV}} = \frac{V_{\text{bridge}}}{4} \frac{6(l - l_{\text{pr}}/2)}{wt^2} \pi_1^{\text{ref}} \gamma \beta^* \phi. \quad (3.83)$$

Although the cantilever is defined by just seven to nine state variables (depending on the fabrication process), a much larger number of equations are required to fully model the cantilever behavior. We will discuss each of the new parameters in the

V_{noise} and S_{FV} equations in turn. The first three parameters appear several times and are either parameters that we have previously defined (f_{\min} , f_{\max}) or physical constants (k_b).

The next two parameters are T and R which contribute to the Johnson noise term. We assume that the measurement circuit consists of a Wheatstone bridge and instrumentation amplifier. The Johnson noise of the circuit is defined by the resistances seen by the amplifier inputs (R) and their average temperatures (T). Two of the resistors in the circuit are silicon resistors while the other two are macroscale resistors, preferably wirewound, as discussed in Sect. 3.1.6.

The electrical resistance of the piezoresistor is calculated from

$$R = 2R_s l_{\text{pr}} / \gamma w_{\text{pr}} + R_{\text{excess}} \quad (6.5)$$

where w_{pr} is the width of each piezoresistor leg and R_s is the sheet resistance. We will assume that the piezoresistor occupies the entire cantilever width (i.e. $w_{\text{pr}} = w/2$) as discussed in Sect. 4.9.4. The sheet resistance depends on the fabrication process parameters and can be calculated following Sect. 4.7 as

$$R_s = \frac{1}{\int_0^{l_{\text{pr}}} \sigma(z) dz} \quad (4.39)$$

where σ is the electrical conductivity. In the case of ion implantation we calculate R_s through linear interpolation using the lookup tables in Appendix B. We will take R_{excess} as 200Ω to model the excess resistance from contacts and interconnects (Sect. 4.9.5).

The resistance factor, γ , was discussed in Sect. 3.2.1 and is calculated as

$$\gamma = \frac{R_{\text{pr}}}{R} = \left(1 + \frac{R_{\text{excess}} w_{\text{pr}}}{R_s l_{\text{pr}}} \right)^{-1}. \quad (3.37)$$

The maximum cantilever temperature is calculated in this problem using the analytical approximation introduced in Sect. 5.3.6 with $h_{\text{eff}} \approx 0$ due to the surrounding vacuum. The degree of thermal modeling complexity can be easily selected in our piezoresistor optimization code, ranging from the analytical approximation to finite differences with temperature-dependent thermal conductivity and electrical resistivity. For applications near ambient relatively simple models can be employed with error on the order of a few percent.

The impact of piezoresistor self-heating on Johnson noise, thermomechanical noise and sensitivity can be safely neglected because the maximum cantilever temperature is constrained to just 10 K above ambient. Thus, we can assume that $T = 300 \text{ K}$ while introducing a maximum error of just 0.8 %. In the more general case we would calculate the average piezoresistor temperature (T_{pr}) via finite differences as discussed in Sect. 5.3 and then calculate the weighted average of the resistor temperatures (T).

The next two parameters in the expression for V_{noise} are A_{VJ} and A_{IJ} , two of the coefficients that we use to model amplifier noise (Sect. 3.1.4). We presented amplifier noise coefficients for popular instrumentation amplifiers in Table 3.2. For this optimization problem we assume that the Wheatstone bridge output is amplified with an INA103 instrumentation amplifier.

The fourth term in V_{noise} , which accounts for thermomechanical noise, introduces three new parameters: k_c , ω_0 and Q . The spring constant is calculated from Euler-Bernoulli beam theory as

$$k_c = \frac{Ewt^3}{4l^3}. \quad (6.6)$$

The elastic modulus (E) varies with crystallographic orientation [200]. For n-type doping we orient the cantilever and piezoresistor in the $<100>$ direction to maximize the magnitude of the longitudinal piezoresistive coefficient (π_l) following Table 2.2, yielding an elastic modulus of 130 GPa. Similarly, for p-type doping we choose the $<110>$ direction yielding an elastic modulus of 169 GPa.

Given that we are operating in vacuum, the resonant frequency of the first cantilever eigenmode is straightforward to calculate as

$$\omega_0 \approx \frac{t}{l^2} \sqrt{\frac{E}{\rho}}. \quad (6.7)$$

The quality factor is limited by the parallel combination of air damping, anchor loss and thermoelastic dissipation (TED). Air damping is negligible given that the cantilever is operating in a perfect vacuum. Based upon the low resonant frequency of the cantilever (2 kHz), the quality factor will be limited by TED rather than anchor loss [432]. Although the TED quality factor will vary with cantilever dimensions, we assume a quality factor of 5,000 [432] for simplicity because Johnson, Hooge and amplifier noise will all be significantly greater than thermomechanical noise in this case.

In the case of air or water operation, the quality factor and resonant frequency can be calculated following Sader and co-workers in Refs. [312] and [433] as

$$Q = \frac{2\rho t/3\pi\rho_f w + \text{real}(\Gamma)}{\text{imag}(\Gamma)} \quad (6.8)$$

and

$$\frac{f_d}{f_0} = \left(1 + \frac{\pi\rho_f w}{4\rho t}\right)^{-0.5} \quad (6.9)$$

where f_d and f_0 are the damped and undamped frequencies of the first eigenmode, ρ_f is the fluid density and Γ is the hydrodynamic function, calculated from lookup tables in Ref. [312]. Both the mechanical and thermal implications of operation in air and water are incorporated into our optimization code (Appendix C) and we

have experimentally validated the damped quality factor and resonant frequency predictions in Refs. [2] and [97].

The Hooge factor, α , depends on the piezoresistor fabrication method. We assume a value of 10^{-5} for epitaxial and diffused piezoresistors (Sect. 3.1.3). In the case of ion implantation, α is calculated from the post-implantation anneal following (3.20), (3.2.1) and Table 3.1.

The effective number of carriers, N_{eff} , is calculated from the dopant concentration profile. In the case of epitaxy, where we can approximate the dopant concentration as constant with respect to depth, the effective number of carriers can be calculated as $N_{\text{eff}} = 2w_{\text{pr}}l_{\text{pr}}N_{\text{epi}}t_{\text{pr}}$. If the dopant concentration varies substantially over the depth of the piezoresistor (diffusion and ion implantation) then the number of carriers is calculated as

$$N_{\text{eff}} = 2w_{\text{pr}}l_{\text{pr}} \frac{\left(\int_0^{t_{\text{j}}} n \mu dz \right)^2}{\int_0^{t_{\text{j}}} n \mu^2 dz}. \quad (3.19)$$

The maximum piezoresistive coefficient, π_l^{ref} , depends on the dopant type and crystallographic orientation of the piezoresistor and is taken from Table 2.2. For p- and n-type piezoresistors the reference coefficients assuming optimal orientation are $71.8 \times 10^{-11} \text{ Pa}^{-1}$ and $-102 \times 10^{-11} \text{ Pa}^{-1}$, respectively.

The sensitivity factor, β^* , was discussed at length in Sect. 3.2.2 and is calculated as

$$\beta^* = \frac{2}{t} \frac{\int_{-t/2}^{t/2} P \mu n z dz}{\int_{-t/2}^{t/2} \mu n dz}. \quad (3.62)$$

Although it can be simplified in the case of epitaxial fabrication according to (4.27). In the case of ion implantation the lookup tables are used once again.

The last term of the force resolution equations, ϕ , accounts for the transverse current flow at the end of the piezoresistive loop and was discussed in Sect. (3.2.3). We calculate it as

$$\phi = \frac{2l_{\text{pr}}w_{\text{loop}}/w_{\text{pr}}w_{\text{gap}} + (\pi_t/\pi_l)(l - l_{\text{pr}} - w_{\text{loop}}/2)/(l - l_{\text{pr}}/2)}{1 + 2l_{\text{pr}}w_{\text{loop}}/w_{\text{pr}}w_{\text{gap}}} \quad (3.76)$$

where π_t/π_l is equal to $-1/2$ and -1 for p-type and n-type doping, respectively. In both cases we assume that the transverse loop width (w_{loop}) and the gap between the piezoresistor legs (w_{gap}) are equal to $2w_{\text{pr}}$.

We have finished discussing each of the terms used to calculate the force resolution of a piezoresistive cantilever. The remainder of this section will focus on the results obtained by numerically optimizing cantilever designs for each combination of fabrication process and dopant species. The results will allow us to draw broad conclusions about the limits and relative performance of each fabrication method. The conclusions will apply to any cantilever-type piezoresistive sensor that undergoes bending during operation (e.g. accelerometer, pressure sensor, surface stress-based chemical sensor, flexural resonators). In the case of a piezoresistive strain gauge,

a simple modification to the sensitivity equation following (3.6.5) would enable numerical optimization and a similar analysis.

6.4.2 Dopant Concentration

What is the optimal piezoresistor dopant concentration? Assuming that the piezoresistor is formed via epitaxy and doped with boron, we can constraint the dopant concentration to a particular value and then optimize the rest of the cantilever design. Figure 6.5 presents the predicted force resolution of cantilever designs optimized for particular dopant concentrations.

The optimal dopant concentration varies slightly with thickness but is on the order of 10^{20} cm^{-3} and 10^{19} cm^{-3} for 1 and $10 \mu\text{m}$ thick sensors, respectively. In general, high dopant concentrations yield the best sensor performance because the piezoresistance factor rolls off more slowly than the reduction in electrical noise (Johnson and Hooge) with increasing dopant concentration.

More specifically, as the dopant concentration increases the piezoresistor can be made thinner for the same electrical noise (i.e. electrical resistance and number of carriers). The benefit of a piezoresistor thickness reduction depends on the device thickness. As discussed in Sect. 3.2.2, sensor sensitivity is proportional to the sensitivity factor (β^*).

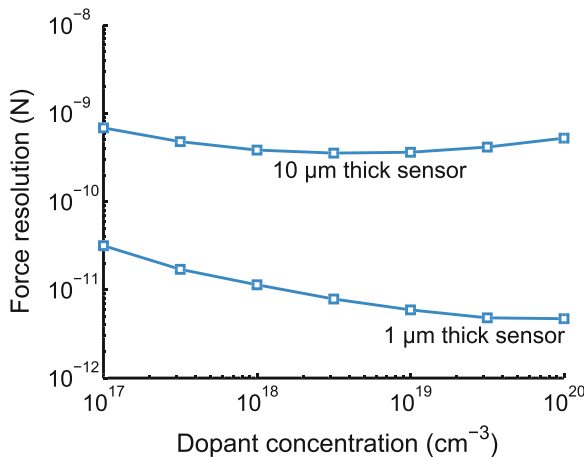


Fig. 6.5 Variation in the optimal dopant concentration with sensor thickness. For each data point, the thickness and dopant concentration of the boron-doped epitaxial piezoresistive cantilever are fixed and the rest of the design parameters are numerically optimized for force resolution. As the sensor thickness decreases, the optimal dopant concentration increases due to a tradeoff between the mechanical, thermal and electrical design considerations discussed in the text. Degenerately doped silicon ($10^{19}\text{--}10^{21} \text{ cm}^{-3}$) is ideal for nearly all applications

Two factors determine the sensitivity factor: the relative piezoresistor thickness and the dopant concentration. As the piezoresistor thickness with respect to the cantilever thickness increases the sensitivity factor decreases due to the reduced mechanical stress away from the sensor surface for a given load. Similarly, as the dopant concentration increases the sensitivity factor decreases due to a reduction in the piezoresistance factor. In order to balance these two factors, thin devices favor slightly higher dopant concentrations than their thicker counterparts.

Degenerately doped silicon ($>10^{18} \text{ cm}^{-3}$) is ideal for nearly all situations, both for resolution optimization and to minimize temperature effects (Sects. 5.1 and 5.2). Designers often focus on maximizing the sensor sensitivity (i.e. gauge factor), but one of the main themes of this chapter has been to instead focus on sensor resolution, which favors more highly doped piezoresistors.

6.4.3 Dopant Type

Next, what dopant species should be utilized? Fig. 6.6 compares the force resolution of optimized n-type (phosphorus) and p-type (boron) epitaxial cantilever designs. At each data point, the cantilever thickness is fixed and the rest of the design is optimized. In contrast with the previous figure, the piezoresistor concentration is allowed to vary freely. Boron doping yields approximately 18 % greater RMS force noise than

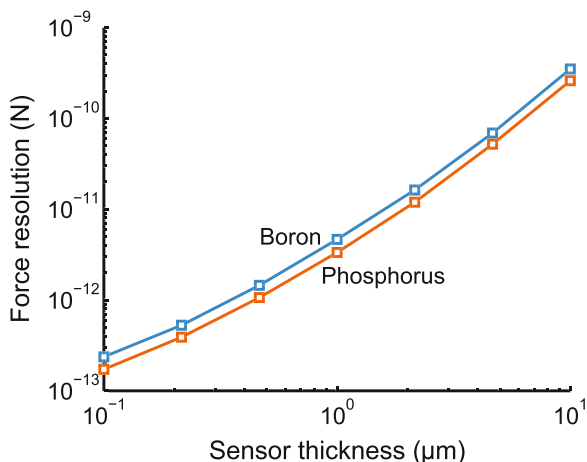


Fig. 6.6 Comparison between n-type (phosphorus) and p-type (boron) doping. For each data point, the thickness is fixed and the rest of the design parameters are optimized to minimize the integrated RMS force noise in the measurement bandwidth. Boron doping yields approximately 18 % greater RMS force noise than phosphorus doping for any given combination of thickness and resonant frequency due to the differences between their longitudinal piezoresistive coefficients and elastic moduli

phosphorus doping for any given combination of thickness and resonant frequency. The reason for this difference is that the longitudinal piezoresistive coefficient for n-type doping is 30 % greater than for p-type doping, but the lower elastic modulus (130 GPa vs. 169 GPa) means that an n-type piezoresistive cantilever beam must be 12 % shorter than a p-type counterpart for any given combination of thickness and resonant frequency.

Note that the force resolution in Fig. 6.6 scales as approximately $t^{3/2}$, although (3.83) suggests that the force resolution should scale as t^2 . The slower than expected scaling is due to the fact that the maximum temperature of the device was constrained. As the thickness of the cantilever decreases the thermal resistance between the cantilever and the silicon die increases linearly (due to the accompanying reductions in cantilever width and piezoresistor length). The increased thermal resistance necessitates a linear reduction in the power dissipation. The resolution of a piezoresistive sensor scales as $1/\sqrt{W}$ (Sect. 5.4), so the overall resolution ends up scaling as approximately $t^{3/2}$ rather than t^2 .

For displacement sensors, n- and p-type piezoresistors yield comparable performance. Recall from (3.83) and (3.84) that the displacement sensitivity of piezoresistive sensors depend linearly on elastic modulus while force sensitivity does not. The changes in elastic modulus and longitudinal piezoresistive coefficient approximately cancel each other, and sensors intended for displacement sensing can obtain nearly identical performance from n- or p-type piezoresistors.

Cantilever sensors are uniaxially loaded in most applications and transverse stress can safely be neglected if the cantilever is sufficiently narrow and long. However, transverse mechanical loading plays a role in both surface stress and pressure sensors. As discussed earlier in this chapter, the magnitude of the transverse piezoresistive coefficient is about half the longitudinal coefficient for n-type piezoresistors ($\pi_t \approx -\pi_{t/2}$) while the two effects are comparable in magnitude for p-type piezoresistors ($\pi_t \approx -\pi_l$).

Pressure sensors can be arranged into a full Wheatstone bridge configuration with two piezoresistors loaded longitudinally and two loaded transversely. The large transverse piezoresistive effect in p-type silicon is utilized in nearly all pressure sensors, and the 30 % reduction in π_L in going from n-type to p-type doping is more than offset by the 100 % increase in π_t . In contrast, surface stress sensors often mechanically load a single piezoresistor in both the longitudinal and transverse directions. The transverse piezoresistive effect actually decreases the sensor output, and so n-type doping is often preferred.

6.4.4 Fabrication Method

Finally, how should the piezoresistor be fabricated? Fig. 6.7 compares the predicted optimal force resolution of epitaxial, diffused and ion implanted piezoresistors as a function of thickness for phosphorus doping. The diffused and epitaxial piezoresistors yield nearly identical performance for cantilevers ranging from 100 nm to 10 μm

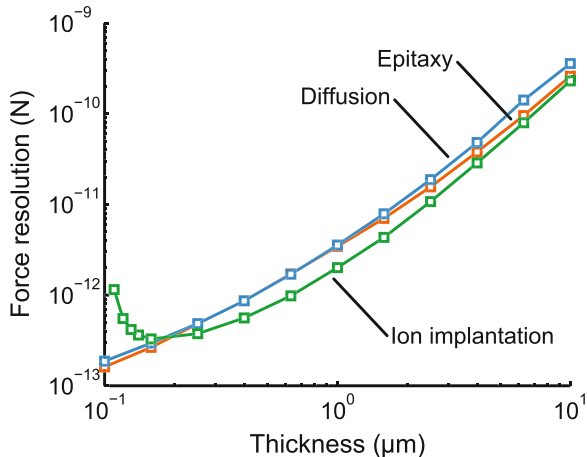


Fig. 6.7 Comparison between the force resolution of phosphorus-doped piezoresistive cantilevers fabricated via diffusion, epitaxy or ion implantation. As in the previous plots, the cantilever thickness is fixed and the remaining design parameters are optimized to minimize the RMS force noise. Diffusion and epitaxy yield nearly identical force resolution for cantilevers ranging from 10 nm to 10 μm thick. Ion implantation yields slightly better performance for micron-scale sensors due to the reduction in 1/f noise possible through post-implantation annealing (no additional annealing is assumed for the epitaxial or diffused piezoresistors in this example)

thick. Epitaxial performance is slightly better for thick sensors due to the ability to target a slightly lower dopant concentration, as discussed in the previous section. The optimal piezoresistor concentration, which varies with cantilever thickness (Fig. 6.5), is adjusted via the diffusion temperature or the epitaxial growth temperature and dopant flow rate.

Ion implantation yields slightly better performance for cantilevers thicker than 200–300 nm. The performance advantage of ion implantation is based upon the smaller Hooge factors reported to date for ion implanted piezoresistors compared with epitaxial and diffused piezoresistors (Sect. 3.1.3). There is simply no data on the 1/f noise effects of annealing epitaxial or diffused piezoresistors to date, and this issue deserves further investigation. The results in Fig. 6.7 assume that an inert anneal is performed after the ion implantation in order to prevent oxidation enhanced diffusion [3]. For passivation, an LPCVD or PECVD oxide could be deposited at low temperature (e.g. 400 °C) afterwards. The other ion implantation design parameters (energy, dose, anneal time and anneal temperature) are optimized at each data point.

The main limitation of ion implantation is in the fabrication of sensors less than 1 μm thick. Figure 6.8 compares the force resolution of ion implanted cantilevers doped with either boron, phosphorus or arsenic. The performance of boron doping degrades sharply for sensors thinner than 400 nm due to dopant diffusion, while phosphorus and arsenic can be used to fabricate sensors as thin as 100–200 nm. The short projected range and low diffusivity of arsenic makes it ideally suited for the fabrication of sub-micron piezoresistive sensors as discussed in Sect. 4.4.

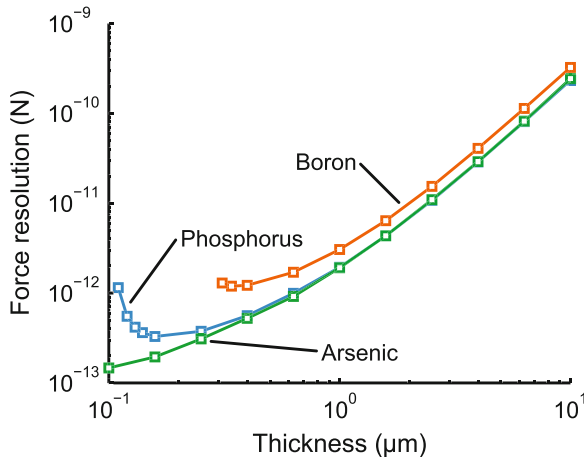


Fig. 6.8 Comparison between the force resolution of ion implanted cantilevers doped with boron, phosphorus or arsenic. The performance of boron doping degrades sharply for sensors thinner than 400 nm due to dopant diffusion, while phosphorus and arsenic can be used to fabricate sensors as thin as 100–200 nm. The short projected range and low diffusivity of arsenic makes it ideally suited for the fabrication of sub-micron piezoresistive sensors

The shallowest ion implanted piezoresistor process described in this book consists of a 20 keV implantation energy, $2 \times 10^{14} \text{ cm}^{-2}$ dose and an inert anneal at 900°C for 15 min. Ion implantation is not capable of fabricating sensors thinner than a certain critical thickness. Beyond this critical thickness the sensor resolution remains constant or even degrades. The critical sensor thickness varies from roughly 500 nm for boron to 300 nm for phosphorus and 100 nm for arsenic. Newer ion implantation techniques (e.g. plasma-immersion ion implantation or multiple implantation steps) could enable shallower ion implanted piezoresistors [349, 351].

Sensor performance degrades for thinner sensors due to a reduction in the sensitivity factor (β^*). Figure 6.9 presents the sensitivity factor for sensors of varying thickness for a single ion implantation process (20 keV, $2 \times 10^{14} \text{ cm}^{-2}$, inert anneal at 900°C and 15 min). For 10 μm thick sensors the sensitivity factor is determined by the maximum dopant concentration of the piezoresistor. The higher diffusivity of boron yields a slightly lower concentration and higher sensitivity factor for thick sensors. As the sensor thickness decreases, the sensitivity factor is determined by dopant diffusion.

The junction depths for the illustrated ion implantation process are 580, 280 and 150 nm for boron, phosphorus and arsenic doping (Tables B.10, B.11 and B.12). The piezoresistor resolution begins to degrade once the gradient of the sensitivity factor with respect to thickness becomes sufficiently negative. Figures 6.7, 6.8 and 6.9 show that ion implantation is well suited for piezoresistive sensors greater than 1 μm thick. While phosphorus and arsenic ion implantation can stretch to sensors that are 100–300 nm thick, epitaxy and diffusion are better suited for thin sensors.

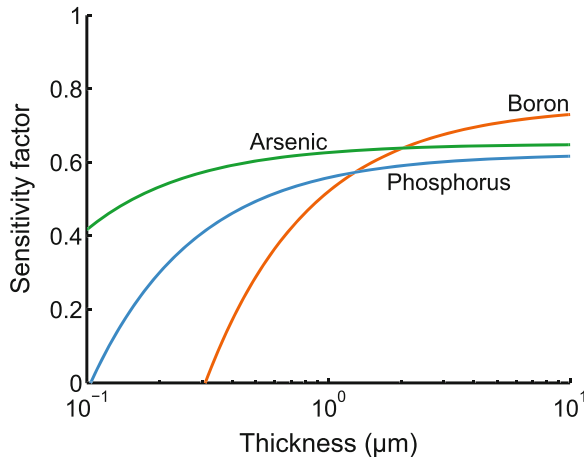


Fig. 6.9 Ion implanted sensor thickness limits. The sensitivity factor (β^*) is calculated as a function of sensor thickness for the shallowest ion implantation process presented in this book (20 keV, $2 \times 10^{14} \text{ cm}^{-2}$ with an inert anneal at 900°C for 15 min). The sensitivity factor degrades for thin sensors due to the finite projected range of the implanted ions and their diffusion during the anneal

This section has illustrated that diffusion, epitaxy and ion implantation can yield comparable performance over a wide range of sensor dimensions if the designs are well optimized. In most cases, the doping method can thus be selected for practical rather than performance considerations.

6.5 Final Thoughts on Design

The difference in performance between “good” and “bad” designs can be up to several orders of magnitude. Bad designs can result from using an overly simplistic model (e.g. assuming $\beta^* = 1$ for simplicity) or misapplying the design rules that were established for a different problem (e.g. assuming that $t_{j/t} = 1/3$ is optimal for all piezoresistive cantilevers) as has often happened with Harley’s seminal paper on piezoresistor design [127]. Tools that enable robust piezoresistor design are available (Appendix C) and simply need to be applied.

Although this chapter has focused on cantilever beams, the results and methods can be generalized to any variety of piezoresistive devices. The piezoresistor optimization toolbox that we developed and applied throughout this chapter can be readily adapted to other sensor form factors. Accurate sensitivity models for other piezoresistive sensors are available in the literature; for example, see Lin et al. for pressure sensor working equations [434]. In our own design work, we adapted the code to optimize the design of cantilever sensors based upon polysilicon, metal gauges and piezoelectric films.

The electrical, mechanical and thermal models for one-dimensional piezoresistive sensors are particularly well suited for numerical optimization because most of the sub-problems can be solved analytically (i.e. quickly). As problem complexity increases, numerical modeling become increasingly necessary and numerical design optimization can become slow. However, two-dimensional problems with simple boundary conditions are tractable using the same numerical optimization approach described here. For example, researchers at Bosch [427, 431] and the University of Florida [435, 436] have developed similar numerical design techniques for piezoresistive accelerometers and piezoelectric microphones, respectively, although neither project has released their code as open source.

Many problems, but not all, can be simplified for fast and efficient gradient-based numerical optimization. Certain two- and three-dimensional problems are difficult to parameterize and lend themselves to topological optimization [437–439]. For more complex problems, numerical design optimization can be integrated with commercial FEA software packages. For example, MATLAB® and COMSOL® (COMSOL AB, Stockholm, Sweden) are particularly straightforward to integrate [440]. As the design space and numerical complexity increases, e.g. three-dimensional geometry that can not be simplified or hundreds of design parameters, then conventional gradient-based optimization becomes inefficient. Gradient-free alternatives such as the Nelder-Mead and Monte Carlo methods are efficient alternatives in these cases.

6.6 Summary

This chapter was the culmination of the five preceding chapters. Design optimization relies on the numerous models presented in this book, ranging from Joule heating to the piezoresistance factor to 1/f noise.

We began this chapter by discussing the qualitative relationships between design parameters (e.g. V_{bridge}) and sensor characteristics (e.g. ΔT_{\max}). An important aspect of piezoresistive sensor design is the tight coupling between design parameters, which leads to a complex relationship between a single parameter and overall sensor performance.

An important rule of thumb for piezoresistor design is that the two largest uncorrelated noise sources (typically Johnson and 1/f noise) should have similar magnitudes. A simple example illustrating this principle was discussed in the chapter introduction.

After defining several fundamental concepts in design (optimality, design parameters and constraints) we moved on to design optimization. We began by discussing analytical design optimization and quickly arrived at an expression for the force resolution of a piezoresistive cantilever,

$$\text{MDF} = \frac{2wt^2 \sqrt{\frac{16k_b T_{\text{pr}} l_{\text{pr}} (f_{\max} - f_{\min})}{q\mu N_{\text{epi}} wt_{\text{pr}}} + \frac{\alpha V_{\text{bridge}}^2 \ln(f_{\max}/f_{\min})}{2N_{\text{epi}} l_{\text{pr}} wt_{\text{pr}}}}}{3V_{\text{bridge}} \left(l - \frac{l_{\text{pr}}}{2}\right) \pi_1^{\text{ref}} \log_{10} \left(\frac{1.53 \times 10^{22}}{N_{\text{epi}}}\right)^{0.2} \left(1 - \frac{t_{\text{pr}}}{t}\right)}. \quad (6.4)$$

Although this expression is unwieldly, it neglects two noise sources (amplifier and thermomechanical), does not model Joule heating, and does not explicitly enforce important constraints such as minimum dimensions and maximum temperatures. The fundamental problem with analytical design optimization is its inability to handle complex and interconnected models.

Numerical design optimization is perfectly suited for the complexity of piezoresistors. A numerical optimizer begins from a starting set of design parameters and iteratively searches for the local optimum (e.g. minimum RMS force noise) by modifying the design parameters within a set of linear and nonlinear constraints. Piezoresistor design is not a convex optimization problem, meaning many local optima exist depending on the starting point of the search. In practice, generating several random starting points is sufficient to find the global optimum.

We applied numerical design optimization to several general piezoresistor design problems as an example. First, we demonstrated that a dopant concentration ranging from 10^{19} to 10^{20} cm^{-3} is optimal for most piezoresistive sensors. The core mechanism behind this result is that the piezoresistance factor rolls off more slowly than $1/f$ noise with increasing concentration.

Second, we compared the performance limits of p- and n-type epitaxial piezoresistors. We found that n-type doping is preferred for force and pressure sensors while similar displacement resolution can be obtained with p- and n-type doping.

Third, we compared fabrication methods (diffusion, ion implantation and epitaxy) with phosphorus doping and found that their performance envelopes are remarkably similar except for the case of 100–200 nm thick sensors where ion implantation performance degrades.

Finally, we compared the ion implantation of boron, phosphorus and arsenic. For thick sensors ($>5 \mu\text{m}$ thick) there is relatively little difference between the dopant species. For sub-micron sensors we found that arsenic yields better performance than phosphorus or boron due to its higher mass and lower diffusivity.

In closing, we discussed how to generalize the methods and results in this book to sensor geometries beyond the canonical cantilever beam. We also discussed approaches for integrating finite element analysis with numerical optimization for the design of more complex mechanical structures.

We emphasize that all of the results in this chapter were generated using piezoD, an open source tool that we developed for piezoresistor modeling and design (Appendix C). All of the models from the preceding chapters are implemented in the tool. Additional functionality that was not described here, such as piezoelectric sensor and actuator modeling, is also available in piezoD.

Chapter 7

Alternative Materials and Transduction Methods

Piezoresistive silicon sensors are widely used but they face competition in every sensor application from alternative materials and transduction techniques. New materials allow piezoresistive sensors to operate in places where they otherwise could not, while alternative transduction methods provide different tradeoffs in sensor performance, power dissipation and size. In this chapter we will explore the strengths and weaknesses of the most common alternatives to silicon piezoresistors.

7.1 Alternative Piezoresistive Materials

Most piezoresistive microsystems utilize single crystal silicon. However, with advances in materials science and processing, newer materials are currently being developed for MEMS and microsystems. These materials have advantages over silicon in some applications (e.g. higher melting temperature, higher/lower modulus of elasticity, or higher piezoresistive coefficients). In this section, we review four alternatives to silicon: silicon carbide, diamond, carbon nanostructures, and metal strain gauges.

7.1.1 Silicon Carbide

Silicon carbide (SiC) has superior material properties to silicon in a number of respects. It has a higher elastic modulus (424 GPa), higher sublimation temperature

Portions of this chapter were adapted from an earlier review of piezoresistance [1]. We would also like to thank A. Alvin Barlian, Nahid Harjee, Joseph R. Mallon Jr., Sung-Jin Park, Woo-Tae Park and Ali J. Rastegar for extensive and productive discussions and their contributions to the concepts presented in this chapter.

(1800 °C), higher thermal conductivity (500 W/m-K) and superior chemical inertness [441]. These differences make SiC particularly attractive for sensing in adverse environments, such as pressure sensors within turbines, engines and petroleum wells [442]. The high elastic modulus of SiC also makes it useful for resonators at the GHZ-scale [87].

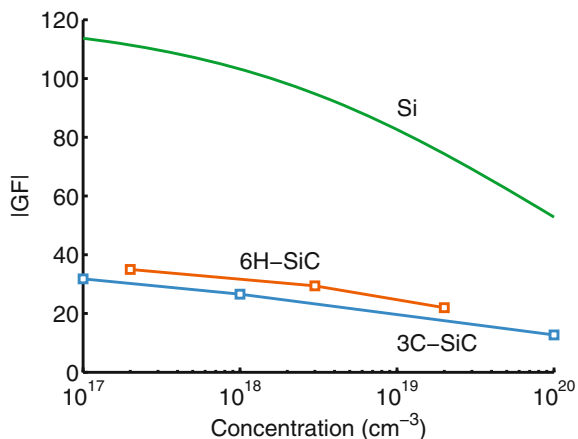
SiC can be deposited on silicon substrates in monocrystalline, polycrystalline and amorphous forms [443]. Poly-SiC can be deposited at moderately high temperatures (800–1000 °C) using LPCVD and PECVD processes. Patterning is performed using fluorine-based etch chemistry, which has poor selectivity with respect to Si_3N_4 and SiO_2 . Alternative masking materials such as aluminum, nickel, and aluminum nitride have been used with some success. Aluminum nitride is a particularly promising option, enabling high etch selectivity without metal contamination problems [444]. Doping can be performed using the same methods as silicon: diffusion, ion implantation, and in-situ doping during film deposition.

In addition to its superior mechanical properties, single crystal SiC also has a wider band gap (2.39–3.33 eV) compared to that of single crystal silicon (1.12 eV) [441]. This reduces the impact of thermal carrier generation on junction leakage currents and sensitivity at any particular temperature. Werner and Fahrner summarized the maximum operating temperatures and band gaps for several semiconductor materials [442]. SiC has several advantages over other wide-bandgap materials (e.g. diamond and GaAs) including substrate cost, processing complexity and the ability to grow stable native oxides [441]. Nevertheless, obtaining a high-quality oxide with low interface state and oxide trap densities has proven challenging because of the carbon on the surface, as well as off-axis epitaxial layers which have rough surface morphologies [445].

SiC has about 200 known polytypes with varying physical properties. A complete review of SiC crystal structures and polytypes is available elsewhere [450]. The most common types are 6H-SiC, 4H-SiC, and 3C-SiC. Polytypes 6H-SiC and 4H-SiC have a hexagonal crystal structure (α -SiC), while 3C-SiC has a cubic crystal structure (β -SiC). In one of the earliest systematic studies in the piezoresistivity of β -SiC, Shor et al. measured the longitudinal and transverse gauge factors as a function of temperature for two different doping levels [446]. Ziermann et al. reported the first piezoresistive pressure sensor using single crystal β -SiC n-type piezoresistors on SOI substrates [448]. Studies performed on the piezoresistivity of α -SiC have shown negative gauge factors as large as –35 for longitudinal and –20 for transverse gauge factors [447, 451]. Werner published summary of the piezoresistive properties of various SiC polytypes in 1999 [449]. The longitudinal gauge factor for α - and β -SiC are compared with single crystal silicon in Fig. 7.1. The gauge factor of Si is roughly three times larger than both SiC polytypes at all dopant concentrations.

In contrast with its single crystal counterpart, polycrystalline SiC exhibits positive gauge factors of smaller magnitude. Strass et al. provided a summary of the gauge factor of polycrystalline SiC as a function of temperature and doping [452]. At room temperature, the gauge factor is around 6 for undoped and 2–5 for doped polycrystalline SiC. The shift from negative to positive values was explained by the greater influence of grain boundaries in polycrystalline wide-bandgap materials

Fig. 7.1 Magnitude of the longitudinal gauge factor for single crystal silicon, 6H-SiC and 3C-SiC at room temperature vs. dopant concentration. The silicon gauge factor is calculated for p-type silicon using Richter's model (Sect. 2.2.2). The SiC experimental data are taken from Refs. [446–449]



compared to polysilicon. As one would expect based upon silicon, the piezoresistive properties of poly-SiC depend on temperature, crystal orientation and dopant type.

Piezoresistance of polycrystalline β -SiC fibers has also been studied [453]. SiC fibers have been used for continuous reinforcement of high-temperature structural composites for their oxidation resistance. With a gauge factor of 5 in 14 μm diameter β -SiC fibers under tension, the fibers are also useful for monitoring the strain in these composite structures.

Additionally, theoretical investigations of the piezoresistivity in the cubic 3C-SiC and hexagonal n-type 6H-SiC, based on electron transfer and the mobility shift mechanism, have been performed [454, 455]. In the hexagonal 6H-SiC, the anisotropic part of the piezoresistance tensor vanishes in the (0001) plane and only the isotropic part remains. As a consequence, longitudinal, transverse, and shear gauge factors and properties are isotropic in the (0001) plane.

Several SiC-based piezoresistive MEMS devices have been developed to withstand harsh operating environments, such as high impact/acceleration (40,000 g) [456] and high temperatures (200–500 °C) [457–459]. Complete reviews of SiC-based MEMS and NEMS, especially for harsh environment applications, are available elsewhere [442, 443, 449, 460–462].

7.1.2 Diamond

Diamond is another attractive material option for elevated temperatures and harsh environments [449, 463]. Like SiC, diamond is superior to silicon with respect to its mechanical, thermal and chemical properties; it has higher physical hardness, elastic modulus and tensile yield strength, greater chemical inertness, and higher thermal conductivity. For example, the elastic modulus of CVD diamond has been

experimentally measured as approximately 1 TPa, nearly an order of magnitude higher than silicon and factor of two higher than SiC [464]. The high hardness and wear resistance of diamond makes it particularly attractive for the fabrication of scanning probes, and sharp diamond tips have been integrated with microheaters for wear resistant nanomanufacturing [465].

Diamond is typically deposited in polycrystalline form via hot-wire CVD although single-crystal deposition techniques have also been developed [466, 467]. Patterning can be performed through oxygen plasma etchback using an inorganic mask such as SiO_2 [465]. Doping can be performed using the same methods as silicon: diffusion, ion implantation, and in-situ doping during film deposition.

Werner et al. summarized both longitudinal and transverse piezoresistive coefficients reported by various research groups before 1998 [463]. The gauge factors of single crystal and poly-crystalline diamond are typically in the ranges of 2000–3800 and 10–100, respectively [469]. Polycrystalline diamond has a higher gauge factor compared with SiC, but like the other piezoresistive properties, these values depend greatly on the doping concentration and temperature. The gauge factor of all polycrystalline semiconductors is strongly dependent on the grain size and distribution of orientations, as shown in Fig. 7.2 for polycrystalline diamond. Reducing the diamond powder seeding density before growth results in larger grains and higher piezoresistive coefficients.

The relatively low GF of polycrystalline diamond is usually attributed to its polycrystalline structure. A study of intra- and inter-grain conduction in large-grain CVD diamond showed the intra-grain resistivities are lower than those of grain boundaries

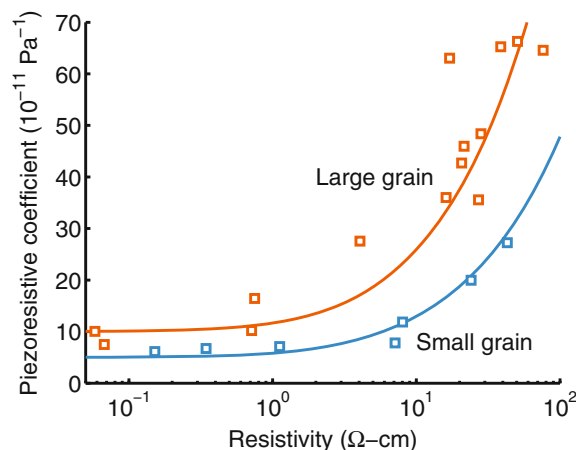


Fig. 7.2 Gauge factor as a function of resistivity for polycrystalline diamond films with large ($0.8 \mu\text{m}$) and small ($0.3 \mu\text{m}$) average grain sizes. Grain size was controlled by adjusting the density of diamond powder seeds on the silicon wafer before film growth in an MPCVD chamber. Gauge factor is proportional to grain size and inversely proportional to dopant concentration (Source Redrawn from [468]. © 2006 Elsevier)

[469]. The intra-grain GF over 4000 for a large grain (50–80 μm) polycrystalline diamond is the largest piezoresistive effect reported for any material. However, the GF deteriorates when grain boundaries are included in the conductance path, with a GF of 133 when the conductance path includes eight grain-boundaries.

Yamamoto and Tsutsumoto suggested two methods to improve the GF of polycrystalline diamond films [466]. The first was to decrease the ratio of carbon to hydrogen when depositing boron-doped diamond films. Decreasing the ratio of C–O/H from 5.5 to 2.2 %, increased the GF from 3 to 30. In this case, the quality of diamond was improved by decreasing the C–O/H ratio and the GF increased as the diamond quality was improved and the grain size became larger. A second method varied boron doping time and the boron-doped layer thickness. Varying doping time from 3 to 10 min (corresponding to layer thickness of 0.1–0.33 μm) increased the GF from 0 to 50.

Note that the gauge factor of silicon is on the order of 10–100 depending on the dopant concentration and temperature. In contrast, the gauge factor of single crystal diamond is one to two orders of magnitude larger. Recall that the gauge factor is calculated from

$$\text{GF} = \frac{\Delta R/R}{\varepsilon}. \quad (7.1)$$

Based upon the constitutive relationship between stress and strain ($\sigma = E\varepsilon$) and the fundamental piezoresistive equation ($\Delta R/R = \pi\sigma$) we see that the gauge factor scales according to

$$\text{GF} = \pi E. \quad (7.2)$$

These novel materials have much higher gauge factors than silicon because their elastic moduli are roughly an order of magnitude larger although their piezoresistive coefficients are comparable in magnitude or smaller depending on the dopant concentration and orientation.

7.1.3 Nanotubes and Nanowires

Carbon nanotubes (CNTs) are graphene sheets rolled-up into cylinders with diameters as small as one nanometer and lengths of up to several centimeters [471–473]. This form of carbon was first reported by Iijima in 1991 [474]. Mechanically, nanotubes are among the strongest and most resilient materials known in nature. The elastic modulus of CNTs is on the order of 1 TPa, like diamond, with a tensile strength nearly two orders of magnitude greater than steel [475].

Electronically, CNTs can be metallic, semiconducting or small-gap semiconducting [471]. Qian et al. reviewed theoretical predictions and experimental techniques that are widely used for visualization, manipulation, and measurements of mechanical properties of CNTs [476]. Most experiments use an AFM tip to deflect a CNT suspended over a trench and several experiments have measured electromechanical properties of CNTs [477–479]. Hierold reviewed the material properties and piezoresistive sensor applications for single-walled carbon nanotubes in 2007 [480].

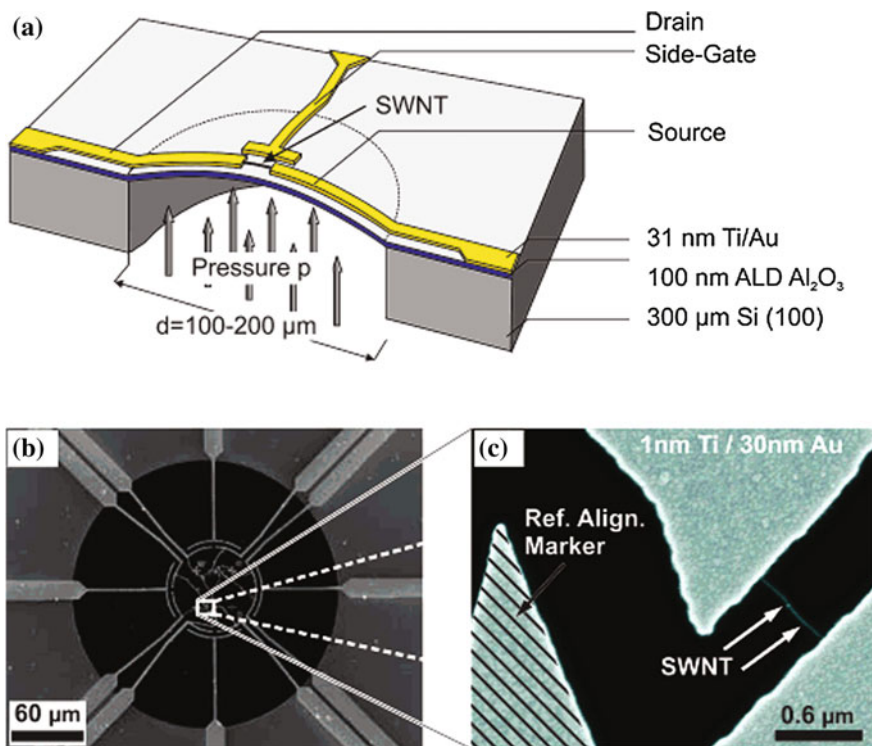


Fig. 7.3 Example of a carbon nanotube-based pressure sensor. **a** Schematic of the single-walled nanotube (SWNT) on a 100 nm thick alumina membrane. A side gate is used to modulate the electrical properties of the SWNT. **b, c** Scanning electron micrographs of a fabricated device (*Source* Reprinted with permission from [470]. ©2006 American Chemical Society)

Piezoresistance in CNTs is attributed to energy band shifts and is observed as a shift in nonlinear CNT I-V curves. Grow et al. reported measurements of the electromechanical response of CNTs adhered to pressurized membranes in 2005 [481]. Single-tube CNTs were adhered to a silicon nitride membrane by van der Waals interactions. The pressure resolution of the sensor was on the order of 1 psi with CNT gauge factors of 400 and 850 for semiconducting and small-gap semiconducting tubes, respectively. Stampfer et al. reported a metallic SWNT-based pressure sensor the following year, shown in Fig. 7.3, with an effective gauge factor of 210 [470].

The integration of CNTs with polymer films and flexible substrates is particularly promising. Chiamori et al. [483] mixed single-wall nanotubes (SWNTs) into SU-8, a negative photoresist, and investigated the properties of the SU-8/SWNT nanocomposite. They measured a gauge factor of 2–4 for a 1–5 % composite and an effective elastic modulus of 500 MPa for the 1 % composite.

Nanowires are electrically conducting wires, in which quantum transport effects are important. As the width of the wire is reduced to Fermi wavelength scale, the

conductance between the electrodes connected by the nanowire is quantized in steps of $2q^2/h$ (where q is the single electron charge and h is Planck's constant) and conductance is no longer dependent on the length of the wire [484].

Nanowires can be synthesized from a wide variety of materials, each possessing unique electromechanical properties. Example nanowire materials include gallium nitride (GaN), zinc oxide (ZnO), tantalum oxide (Ta_2O_5), copper, and gold [484–489]. Nanoindentation is typically used to determine the mechanical properties of nanowires, although several groups have developed MEMS-based experimental test beds for determining the electrical and mechanical properties of nanowires simultaneously [486, 489, 490].

To date, relatively few reports on the development of piezoresistive silicon nanowire-based sensors are available [491]. However, p-type nanowires have been studied for sensor applications [492, 493]. Toriyama et al. fabricated silicon nanowires from SIMOX wafers and used electron beam lithography and reactive ion etching to fabricate piezoresistive test structures [492]. Both the longitudinal and transverse piezoresistive coefficients were found to depend on the cross-sectional area of the nanowires. The longitudinal coefficient of the nanowires increased (up to 60%) while the transverse coefficient decreased as the size of the nanowire was reduced (Fig. 7.4). The longitudinal enhancement behavior was explained qualitatively using one-dimensional conduction theory while the reduction in the transverse coefficient was due to reduced stress transmission from the substrate to the nanowire. The maximum longitudinal value of $48 \times 10^{-11} \text{ Pa}^{-1}$ at a surface concentration of $5 \times 10^{19} \text{ cm}^{-3}$ is comparable to single crystal silicon. Dao et al. incorporated these p-type silicon nanowires as piezoresistive elements in a miniaturized 3-degrees-of-freedom (3-DOF) accelerometer [494]. Roukes and Tang patented strain sensors

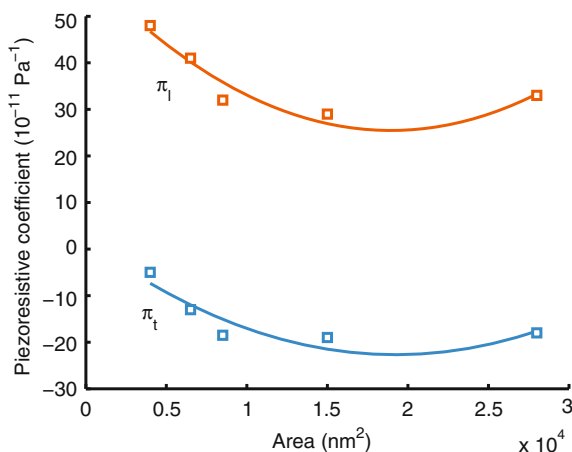


Fig. 7.4 Relation between cross-sectional area and the magnitude of the longitudinal and transverse piezoresistive coefficients of boron-doped silicon nanowires (Source Redrawn with permission from [482]. ©2003 Elsevier)

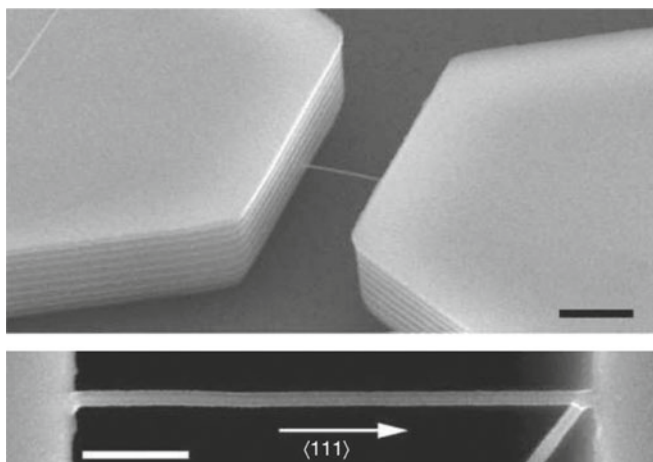


Fig. 7.5 Silicon nanowire example. *Top* Scanning electron micrograph of a silicon nanowire grown and anchored onto a (110) silicon substrate. The sidewall scallops are from the DRIE process used to fabricate the trench. Scale bar represents $2\text{ }\mu\text{m}$. *Bottom* Morphology of a bridged nanowire oriented in the $<111>$ direction. Scale bar represents 500 nm (*Source* Reprinted with permission from [496]. ©2006 Macmillan Publishers Ltd)

based on cantilever-embedded nanowire-piezoresistor wires and ultra-high density free-standing nanowire arrays [495]. Note that the noise characteristics of bulk silicon crystal silicon piezoresistors are well understood while significant work remains to be done on nanowire noise.

He and Yang reported on very large piezoresistance effect (commonly referred to as “giant piezoresistance”) in p-type silicon nanowires, particularly in the $\langle 111 \rangle$ direction [496]. The measured piezoresistance values were a function of the nanowire diameters and resistivities, with the largest value of $-3550 \times 10^{-11}\text{ Pa}^{-1}$ in the longitudinal direction. Silicon nanowires in the $\langle 111 \rangle$ direction, with diameters of 50–350 nm and resistivities of $0.003\text{--}10\text{ }\Omega\text{-cm}$, were grown and anchored to a silicon substrate (from SOI wafers) to form a bridge structure (Fig. 7.5) and uniaxial stress was applied to the nanowires using a four-point bending setup.

Cao et al. explained the giant piezoresistance phenomenon in $\langle 111 \rangle$ silicon nanowires based on a first-principles density-functional analysis [497]. Their model and calculations captured all the main features of the experimental results by He and Yang. Following the experimental results from He and Yang, Reck et al. combined electron beam lithography and lift-off to fabricate silicon test chips and study the piezoresistive properties of crystalline and polycrystalline nanowires as a function of stress and temperature [498]. The magnitude of the piezoresistive effect in monocrystalline and polycrystalline nanowires was 633 and 34 % larger than the size of the effect in bulk silicon, respectively. They also found that the piezoresistive effect greatly increases as the nanowire diameter decreases, consistent with the results from He and Yang [496].

7.1.4 Metals

Metals, while far from a new material option, are the final alternative material that we will discuss. Metal strain gauges have recently been used in a variety of nanomechanical systems, such as UHF resonators [87]. Metal strain gauges are straightforward to model, and the piezoresistor optimization code (Appendix C) already includes a metal strain gauge subclass. In this section we will discuss the tradeoffs between silicon and metal strain gauges and why metal is the preferred option for certain applications.

Although metal gauge factors are substantially smaller than the highest gauge factors achievable by silicon, this is not a particularly useful metric. As we have seen, optimized piezoresistive sensors typically use dopant concentrations ranging from 10^{19} to 10^{21} cm^{-3} in order to balance strain sensitivity with noise sources and minimize variation in performance with temperature. We can calculate the gauge factor of a piezoresistor as a function of dopant concentration from

$$\text{GF}(N) = P(N)\pi_1^{\text{ref}} E + (1 + 2\nu). \quad (7.3)$$

where the piezoresistance factor, P , varies with dopant concentration. The Poisson's ratio of silicon, ν , is 0.07 or 0.28 in the $<110>$ or $<100>$ directions, respectively [196]. Variation in the elastic modulus, E , with dopant concentration is small and can be neglected for most sensor designs excluding resonators [200].

The longitudinal gauge factor of a p-type piezoresistor oriented in the $<110>$ direction is compared with the gauge factors of Al, Au, Cu and Ti as functions of

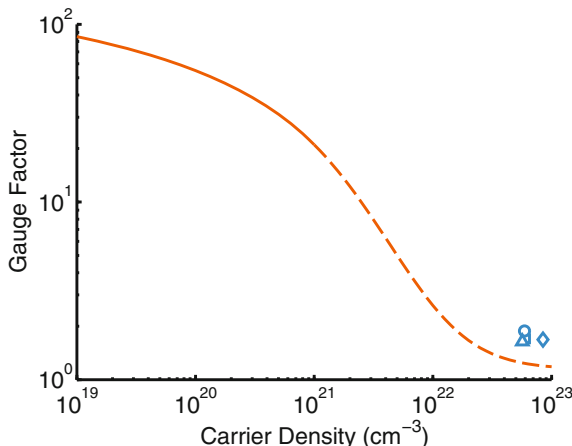


Fig. 7.6 Gauge factors of p-type single crystal silicon and several metals as functions of carrier concentration. Silicon data are extrapolated (dashed line) to physically unrealizable concentrations ($3 \times 10^{20} \text{ cm}^{-3}$ is the solid solubility limit of boron at 1100°C) for the sake of comparison. Four metals are plotted for comparison: Al (square), Au (circle), Cu (diamond) and Ti (triangle)

carrier concentration in Fig. 7.6. The concentrations of free carriers in the metals are assumed to be equal to the concentration of atoms for simplicity.

We see that the gauge factor of silicon at 10^{20} cm^{-3} (approximately 55) is substantially larger than that of the metals (1.6–1.9). However, extrapolating to higher concentrations, we see that the gauge factor of silicon would be lower than all of the metals at comparable carrier concentrations. The smaller gauge factor of silicon is due to its lower Poisson's ratio (0.07 vs. 0.32–0.44). However, such high dopant concentrations are not possible in practice. The solid solubility limit of boron at 1100°C is approximately $3 \times 10^{20} \text{ cm}^{-3}$ and the density of silicon atoms in the crystal lattice is $5 \times 10^{22} \text{ cm}^{-3}$.

This analysis suggests that metal strain gauges can have more carriers than silicon for the same gauge factor and hence lower 1/f noise. However, single crystal silicon has a substantially smaller Hooge factor (10^{-7} – 10^{-5}) compared with polycrystalline metals and semiconductors ($\approx 10^{-3}$) (Sect. 3.1.3). Accordingly, a typical piezoresistor and metal film of the same dimensions would actually exhibit similar 1/f noise levels, and silicon's 30-fold gauge factor advantage would translate to better sensor performance. Thus, 1/f noise is not a compelling reason to use a metal rather than silicon strain gauge for devices of comparable size. However, certain applications have additional requirements that favor metal strain gauges.

Impedance matching can be a challenge in interfacing piezoresistive devices with high frequency measurement systems. Designing a silicon piezoresistor with an impedance of 50Ω and nanoscale dimensions while maintaining a high β^* value can be nearly impossible. For applications limited by impedance matching

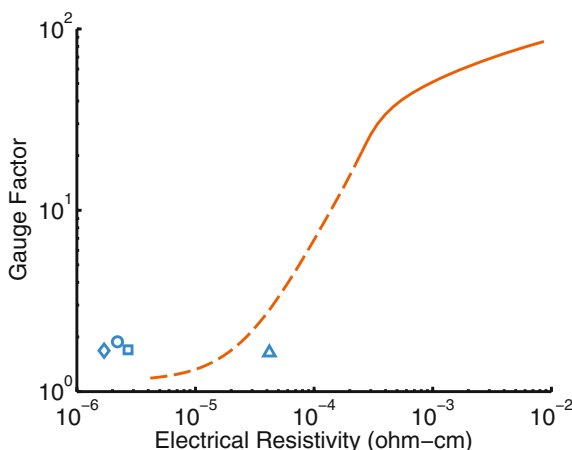


Fig. 7.7 Gauge factors of p-type single crystal silicon and several metals as functions of resistivity. Silicon data are extrapolated (dashed line) to physically unrealizable concentrations ($3 \times 10^{20} \text{ cm}^{-3}$ is the solid solubility limit of boron at 1100°C) for the sake of comparison. Four metals are plotted for comparison: Al (square), Au (circle), Cu (diamond) and Ti (triangle). The lowest physically realizable silicon resistivity ($\approx 10^{-4} \Omega\text{-cm}$) is nearly two orders of magnitude greater than that of Al, Au and Cu

a better metric for comparing silicon and metal strain gauges is gauge factor as a function of resistivity (Fig. 7.7). The lowest physically realizable silicon resistivity ($\approx 10^{-4} \Omega\text{-cm}$) is nearly two orders of magnitude greater than that of Al, Au and Cu.

With such a large difference in minimum resistivity, metal strain gauges are often a better choice for applications driven by impedance matching. A secondary benefit of using a metal strain gauge in this case is that it can be deposited onto a mechanical element with superior mechanical and thermal properties to silicon (e.g. SiC or diamond) enabling superior performance in all respects. Note that 1/f noise in both silicon piezoresistors and metal strain gauges can be largely neglected in the design of resonators but will degrade close to carrier phase noise when the loop is closed to form an oscillator.

7.2 Alternative Transduction Mechanisms

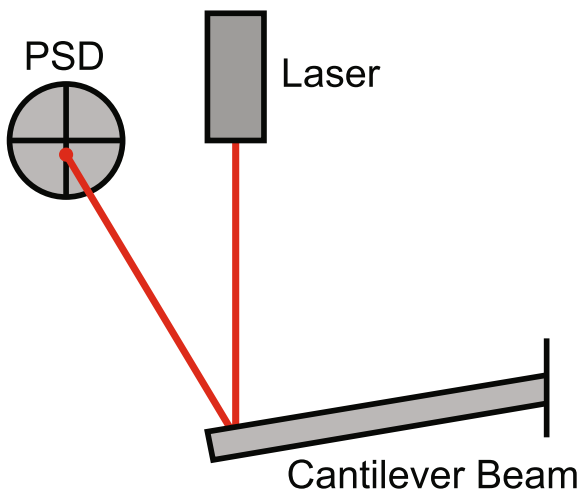
There are numerous techniques for transducing mechanical loads into an electrical signal besides the piezoresistive effect. The most common microscale transduction techniques are optical, piezoelectric, capacitive and the pseudo-Hall and piezojunction effects. We will briefly discuss the measurement resolution, dynamic range and bandwidth of each approach. We refer interested readers to Kenny's force transduction review for an additional perspective [499].

7.2.1 Optical

Deflections can be measured optically using either interferometry or the optical lever technique. Both approaches are discussed extensively by Solgaard [500], and we will briefly summarize the strengths and weaknesses of optical sensing here. For simplicity we will focus on measuring the deflection of a cantilever beam via the optical lever principle (Fig. 7.8).

The resolution of optical detection is fundamentally limited by thermomechanical noise. The impact of other optical and electronic noise sources, such as laser noise, shot noise and amplifier noise, can be reduced nearly indefinitely by increasing the distance from the cantilever beam to the position sensitive detector (PSD). In contrast, piezoresistor noise includes Johnson, Hooge and amplifier noise on top of thermomechanical noise. While increasing the displacement sensitivity of the piezoresistive cantilever can drive the noise equivalent deflection of these additional noise sources below the thermomechanical noise floor, changing the mechanics of the piezoresistive cantilever affects other aspects of the sensor operation. For example, the displacement sensitivity of a piezoresistive cantilever can be increased by reducing its length and increasing its thickness but the accompanying increase in spring constant (Table 6.1) can make the cantilever unusable for certain applications.

Fig. 7.8 Optical transduction example. A laser beam is reflected off of the back of a mechanical structure (e.g. a cantilever beam) and onto a position sensitive detector (PSD). The laser spot is centered onto the PSD using a mirror (not shown). Movement of the mechanical structure leads to changes in the PSD output current, which is converted to a voltage using a transimpedance amplifier (Source Reprinted with permission from [2])



Thus, optical detection has superior resolution to piezoresistive detection except when thermomechanical noise exceeds Johnson, Hooge and amplifier noise. Performance of the two approaches becomes comparable when resolution is not critical or when high damping leads to increased thermomechanical noise (e.g. operation in liquid). The long-term stability of both transduction techniques is generally limited by temperature variation, due to the TCR and TCS of piezoresistors and relative movements between the optically-sensed cantilever and the PSD.

The dynamic range and bandwidth of optically- and piezoresistively-sensed cantilever beams is typically comparable. Due to their nearly identical form factor, very similar spring constants and resonant frequencies can be achieved. One exception might be the case of very thin, narrow cantilever beams, where optical transduction can require the addition of a reflective paddle, slightly increasing its mass [2, 501]. Dynamic range in piezoresistive cantilevers is typically limited by the ratio of the instrumentation amplifier supply rails to the noise floor of the system [133]. Piezoresistive and Wheatstone bridge nonlinearity are generally small, and due to their repeatable nature can be compensated through calibration. Dynamic range in optical levers is limited by the size of the PSD and the amplifier supply rails, so is similarly difficult to define [500]. The dynamic range is not typically limited by the yield strength of silicon in either case.

Optical transduction is used widely in atomic force microscopy. One major benefit of optical transduction in this situation is that the scanning probe is extremely simple; no electrical connections are required and all of the detection circuitry is integrated into the microscope itself. This enables the production of AFM cantilevers with the lowest possible cost and their simple replacement whenever they are damaged or contaminated. In contrast, piezoresistive sensors require electrical connections, leading to a higher cost during assembly and making them less desirable in applications where they must be replaced often. The main downsides of optical detection

are the relatively high cost of the measurement system (laser, PSD and electronics), the relatively large volume of the overall system and the need for mechanical alignment to center the reflected laser onto the PSD. These limitations make capacitive, piezoelectric or piezoresistive transduction the preferred options for high volume, MEMS-based products.

7.2.2 Capacitive

Capacitive sensors measure deflections from changes in electrical capacitance. The capacitance between two parallel plate electrodes is proportional to their overlap area and inversely proportional to their separation distance. A deflection can be coupled to a capacitance change using either interdigitated electrodes or parallel plates. Capacitance is inversely proportional to electrical impedance, so deflections can be inferred from impedance changes.

Two examples of the parallel plate arrangement are shown in Fig. 7.9. In Fig. 7.9a, the middle electrode deflects to the right in response to a load. The deflection increases the capacitance between the middle and top electrode while decreasing the capacitance between the middle and bottom electrode. Biasing the top and bottom electrodes 180° out of phase, an AC-bridge is formed and the voltage amplitude at the middle electrode is proportional to the deflection. Similarly in Fig. 7.9b, a cantilever beam is used as the middle electrode and stationary electrodes above and below it are used to form a differential pair of capacitors.

As in the case of piezoresistive sensing, differential measurements are typically used in order to reject common-mode parasitic capacitance changes. There are numerous capacitive readout circuit architectures, including the differential AC-bridge shown in Fig. 7.9c. Another approach for AC coupled measurements (e.g. microphones) is to DC bias the capacitor, as shown in Fig. 7.9d [502]. Other readout circuit architectures are presented and compared in Ref. [503].

In contrast with piezoresistive sensing, capacitors do not contribute noise to the measurement system. Noise is limited by amplifier noise, any additional resistors in the system, and thermomechanical noise. The capacitance of the sensor is usually less than 1 pF, and parasitic capacitances are a major factor in determining measuring resolution. Parasitic capacitances play the same role in capacitive sensing as parasitic resistances in piezoresistive sensing (Sect. 3.2.1). While parasitic resistances can be minimized easily, capacitive parasitics are unavoidable and can be large compared with the capacitance changes being measured, making monolithic or hybrid integration with signal conditioning circuitry far more important.

The displacement resolution of capacitive sensors can reach the thermomechanical noise floor by either reducing the amplifier noise or increasing the displacement sensitivity by increasing the size or number of transduction capacitors. As in the case of piezoresistive cantilevers, force resolution can be improved by reducing the spring constant of the system. For example, the ADXL202 can measure forces of less than 1 pN in a 1 Hz bandwidth [499]. However, increasing the electrode

size adds mass to the system, leading to a direct tradeoff between resolution and bandwidth. In applications that are primarily driven by measurement bandwidth and resolution concerns, one of the first goals should be minimizing the excess mass in the system. Hence, nanoscale piezoresistive cantilever beams are well suited for the high bandwidth measurement of atomic scale forces as discussed at length in Sect. 1.3 of Ref. [2].

Capacitive transduction is the dominant technique in the commercial MEMS market, with products ranging from accelerometers and gyroscopes to microphones and micromirrors. Capacitive sensing has several advantages over piezoresistive sensing. First, capacitive transduction does not have any inherent $1/f$ noise and much lower temperature sensitivity, making it far better suited for long-term measurements. Second, capacitive transduction can be used for both sensing and actuation, enabling sensor self-testing and applications such as gyroscopes, resonators, and micromirrors. Third, multi-axis sensors are straightforward to fabricate with capacitive sensing. Multi-axis piezoresistive, piezoelectric and optical sensors are less

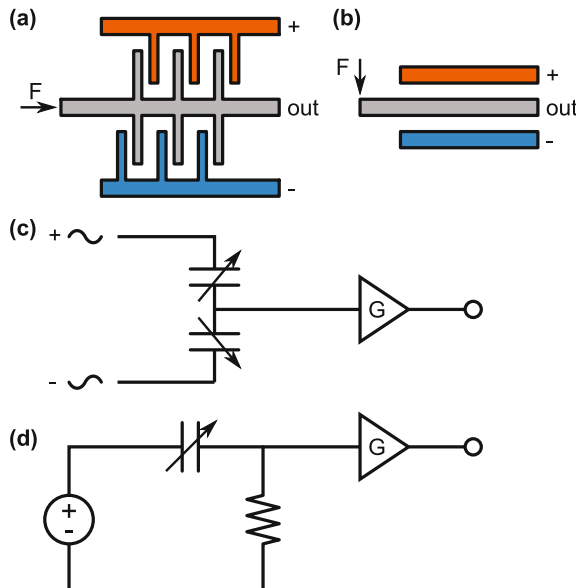


Fig. 7.9 Capacitive transduction overview. **a** Deflection of the middle electrode is coupled to an increase in capacitance between the *middle* and *top* electrode and a decrease in the capacitance between the *middle* and *bottom* electrode. The *top* and *bottom* electrodes are stationary while the middle electrode is mounted on a set of flexures and the deflection to the right is determined by $x = F/k$. **b** Similarly, a force to a cantilever beam can be transduced from the capacitance change between it and a pair of stationary electrodes located above and below it. **c** An AC-bridge is often used to transduce a differential capacitance change into an output signal. The amplifier output is demodulated and measured to calculate deflections and loads. **d** For AC coupled measurements (e.g. microphones), the movable capacitor can be DC biased so that the voltage across a load resistor is proportional to the rate of capacitance change (Source Reprinted with permission from [2])

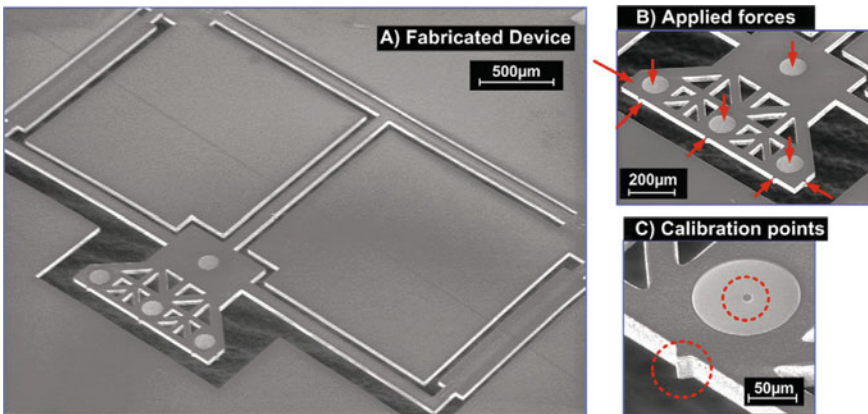


Fig. 7.10 Example of a six-axis piezoresistive force sensor. The active portion of the sensor is $3\text{ mm} \times 1.5\text{ mm} \times 30\text{ }\mu\text{m}$ and has a measurement bandwidth of 4.5 kHz . The sensor integrates 24 piezoresistors, with 8 used for temperature compensation. The force and torque resolution of the sensor are $20\text{ }\mu\text{N}$ and $10\text{ nN}\cdot\text{m}$ in a 1 Hz bandwidth, respectively (*Source* Reprinted with permission from [504]. ©2012 Elsevier)

common although there are many notable examples, such as the 6-axis force sensor presented in Fig. 7.10 [504]. Fourth, capacitive sensors dissipate very little power in most applications due to their high impedance (with the notable exception of GHz-scale resonators). Finally, capacitive sensors can be simpler to fabricate and integrate with CMOS processes in many circumstances, e.g. the post-CMOS process [505]. Capacitive sensors are insensitive to thermal budget, so can also be fabricated prior to CMOS and encapsulated at the wafer-scale using an epitaxial polysilicon layer deposited at high temperature (Fig. 7.11) which enables the fabrication of stable timing references with aging performance better than quartz [163, 164].

That said, there are a number of disadvantages to capacitive transduction and we would argue that several of the advantages are smaller than usually thought. First, capacitive parasitics and feedthrough are less of an issue for piezoresistive sensors due to their relatively low electrical impedance. This allows the amplifier to be located far from the sensor with almost no performance degradation. Second, piezoresistive sensors and thermal actuators can be designed for an arbitrary supply voltage with no change in performance in most cases, while capacitive transducers typically operate at relatively high voltages (e.g. $>10\text{ V}$). Third, while multi-axis piezoresistive sensors are not as common as their capacitive counterparts, they can be fabrication through sidewall ion implantation or diffusion [89, 102, 506]. Fourth, regarding power dissipation, we have demonstrated that piezoresistive sensors can be optimized for microwatt-scale power dissipation while maintaining a high level of performance (Sect. 5.4). Fifth, capacitive transduction requires a narrow, high aspect ratio gap which can be challenging to fabricate and is sensitive to defects, moisture and thin-film damping.

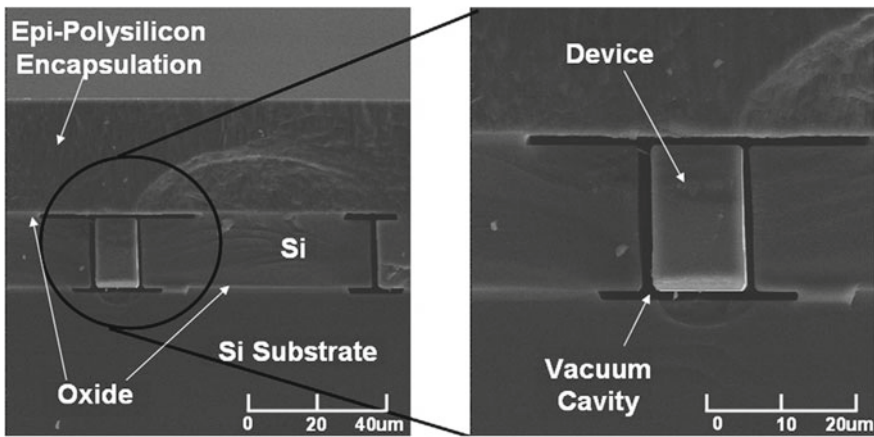


Fig. 7.11 SEM cross-sections of a capacitive resonator fabricated by the epi-seal encapsulation process. The polysilicon cap layer creates a hermetically sealed enclosure. The $25\text{ }\mu\text{m}$ thick encapsulation layer is deposited at 950°C in an epitaxial reactor, enabling a high deposition rate and providing a clean, low pressure (11 mTorr) environment for resonator operation (Source Reprinted with permission from [164]. ©2007 Elsevier)

Finally, regarding integrated actuation capability, thermal actuators can be easily cofabricated with piezoresistive sensors. While capacitive actuation is limited in frequency only by device mechanics, thermal actuation is usually limited by the heater dynamics. Fortunately, the heater time constant scales with device size and benefits from device scaling. Examples of high frequency actuation include scanning probes operating at 600 kHz and resonators operating at 60 MHz [167, 507]. Rahafrooz et al. modeled thermally actuated piezoresistive resonators operating up to 1 GHz with motional impedances of $1\text{ k}\Omega$ for several microwatts of heater power [167]. At low frequency, thermal actuation was integrated with piezoresistive detection for device self-testing in 1992 by NovaSensor and continues to be used [508, 509].

7.2.3 Piezoelectric

Whereas optical and capacitive sensors measure deflection directly, piezoelectric sensors (like piezoresistors) respond to stress. Mechanical stress induces charge polarization within piezoelectric materials (Fig. 7.12). Conversely, the application of an external electric field induces stress, enabling piezoelectric films to operate as both sensors and actuators. Piezoelectric sensors, like capacitive sensors, can be efficiently actuated at high-speed [95] and used for simultaneous actuation and sensing [510–512]. Advantages of on-chip actuation include the ability to scale to large sensor arrays [513] and high frequency feedback control [514].

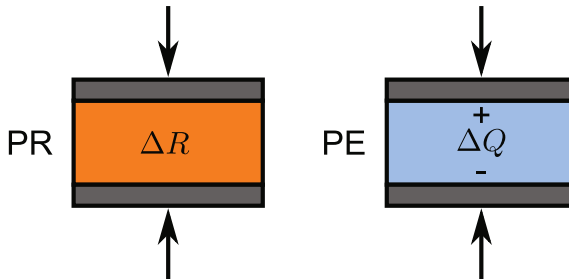


Fig. 7.12 Mechanical stress induces a resistance change in piezoresistive (PR) materials and charge polarization in piezoelectric (PE) materials. This contrasts sharply with capacitive and optical sensing, which both transduce deflection into an electrical signal. Sensors that transduce stress can maintain performance that is relatively independent of sensor size (in contrast with sensors that transduce deflection), making them attractive for high frequency and nanoscale sensors (*Source* Reprinted with permission from [2])

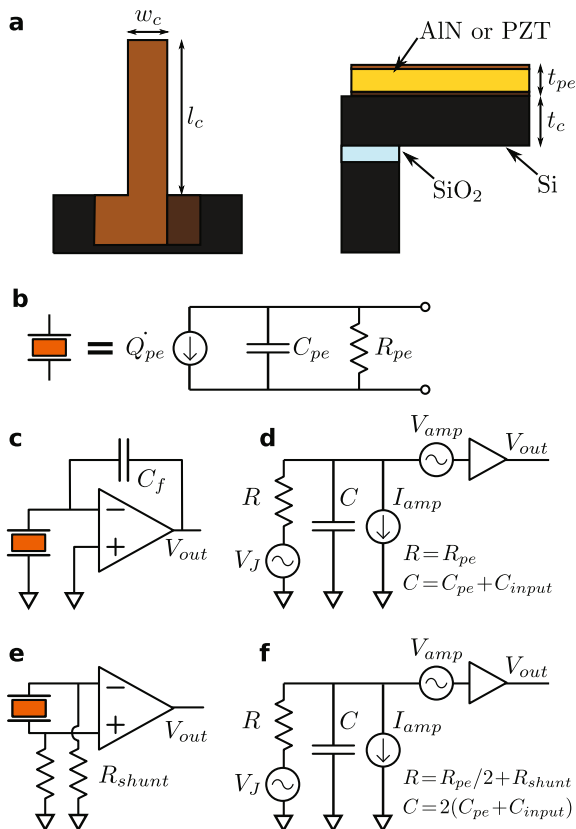
Piezoresistive and piezoelectric transduction have many similarities: they do not require optics, work for a wide variety of samples and measurement conditions, and their fabrication processes are well suited for forming cantilever structures for out-of-plane operation. A piezoelectric film transduces stress into a polarization charge proportional to the appropriate piezoelectric coefficient, usually d_{33} or d_{31} . We wrote an in-depth 2010 paper comparing the resolution of piezoresistive and piezoelectric scanning probes, and will discuss the noise and sensitivity models as well as some of the results here [515].

We will provide a brief overview of the fabrication and operation of piezoelectric films, but recommend reviews by Tadigadapa and Trolier-McKinstry [516, 517]. Piezoelectric films are typically deposited by sputtering or sol-gel deposition. The most widely used piezoelectric materials in MEMS are ZnO, AlN, PVDF, PZT. New PZT-related relaxor ferroelectrics, such as PMN-PT, are under active development and yield improved material properties [518]. AlN in particular is used widely, and variation in its film properties with deposition conditions has been studied extensively [519–522]. Piezoelectric materials behave electrically as dielectrics, and need to be deposited between conductive electrodes in order to collect charge or apply an electric field, either in a sandwich or interdigitated electrode configuration. Typical material properties for AlN and PZT are summarized in Table 7.1.

Although we won't present the entire noise and sensitivity analysis for piezoelectric sensors as in Ref. [515], we'll briefly summarize the circuit models one could use before discussing the typical resolution of piezoelectric sensors. A piezoelectric cantilever and its equivalent circuit model are shown in Fig. 7.13a, b. The piezoelectric film can be modeled as a charge generation source in parallel with a capacitor and resistor. The capacitance and resistance of the film are set by its geometry and material properties.

Piezoelectric sensors can be operated in charge- or voltage- sensing modes. In the charge-sensing configuration (Fig. 7.13c, d), the piezoelectric film is connected

Fig. 7.13 Example of the **a** structure and **b** circuit model for a piezoelectric cantilever. The film can be represented as a stress-dependent charge generator (Q_{pe}) in parallel with its resistance (R_{pe}) and capacitance (C_{pe}). **c** The charge on the piezoelectric sensor can be integrated to generate an output voltage; **d** the equivalent noise circuit is shown. **e** Alternatively, the voltage across the piezoelectric film can be directly amplified, with shunt resistors added to limit the common mode voltage induced by the amplifier bias current; **f** the equivalent noise circuit is shown (Source Reprinted with permission from [515]. ©2010 IOP)



to the inverting terminal of an op-amp. Negative feedback draws current across the feedback capacitor (C_f) in order to maintain a virtual ground. The additional charge required to cancel the piezoelectric charge is measured at the output of the operational amplifier, where $V_{out} = Q/C_f$. A switch in parallel with C_f can be used to reset the amplifier output to zero. Charge-sensing has two benefits. First, both terminals of the piezoelectric are at the same potential so the only leakage current is from

Table 7.1 Typical material properties for two popular piezoelectric materials, aluminum nitride (AlN) and lead zirconate titanate (PZT)

Material	E (GPa)	ρ (kg/m ³)	d_{31} (pm/V)	ϵ_r	ρ ($\Omega\text{-cm}$)
AlN	396 ± 40	3260	2.2 ± 0.5	10.2 ± 0.5	10^{12}
PZT	55 ± 20	7550	70 ± 30	900 ± 300	10^8

Material properties are dependent on film thickness and other processing conditions. Higher piezoelectric coefficient films such as epitaxial PZT ($d_{31} = 130$ pm/V) and PMN-PT ($d_{31} = 235$ pm/V) have been demonstrated but are not widely available [518, 523]. AlN data are from Refs. [517, 521, 524–529] while PZT data are from Refs. [514, 523, 526, 530–536]

the amplifier input bias current. Leakage current reduces low frequency sensitivity, hence the common and mostly incorrect assumption that piezoelectric sensors can only be used at high frequencies. The second benefit of charge-sensing is that V_{out} is relatively insensitive to parasitic input capacitances if C_f is large so the amplifier can be located far away from the sensor.

In the voltage-sensing configuration (Fig. 7.13e, f), the piezoelectric sensor is connected directly to the terminals of a differential amplifier. Polarization of the piezoelectric film induces an output of $V_{\text{out}} = Q/C$ assuming an amplifier gain of 1. The capacitance, C , in this case is the total capacitance from the amplifier terminals and to ground. The first downside of voltage-sensing is that charge slowly leaks across the piezoelectric film, reducing low frequency sensitivity. Second, parasitic capacitances (e.g. amplifier inputs, device layout and cables) directly reduce the sensitivity of the sensor. In contrast with the charge-sensing case where the amplifier can be located relatively far from the sensor, the voltage-sensing piezoelectrics benefit enormously from monolithic or hybrid integration.

Noise and sensitivity analysis can be performed using the circuit schematics in Fig. 7.13 and complete derivations can be found in Ref. [515] for piezoelectric cantilevers. The first choice that the designer needs to make when using piezoelectric sensors is whether to operate the sensor in charge- or voltage-sensing mode. Figure 7.14 compares the resolution of AlN in the two operating modes as a function of measurement bandwidth. If the material has a low piezoelectric coefficients and relative permittivity (e.g. AlN, ZnO) then it is best to operate the sensor in voltage-mode.

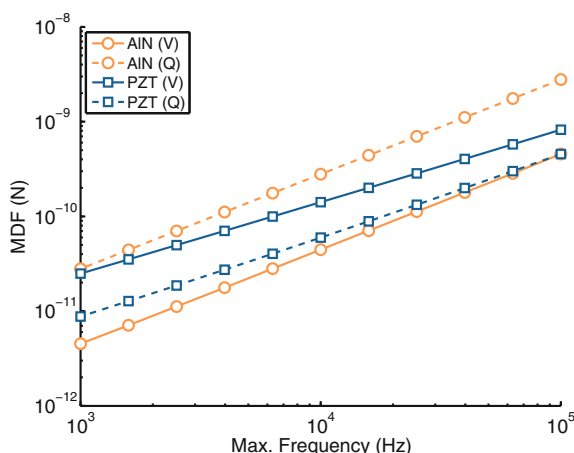


Fig. 7.14 A comparison between the optimal force resolution of AlN and PZT piezoelectric cantilevers using charge sensing or voltage sensing circuits. For each value of f_{max} the cantilever is optimized for force resolution. Charge measurement is preferred for PZT while voltage readout is preferred for AlN due to differences in their piezoelectric coefficients and permittivity. Piezoelectric cantilevers and modeled and numerically optimized using a branch of our piezoresistor optimization code (Appendix C) (Source Reprinted with permission from [515]. ©2010 IOP)

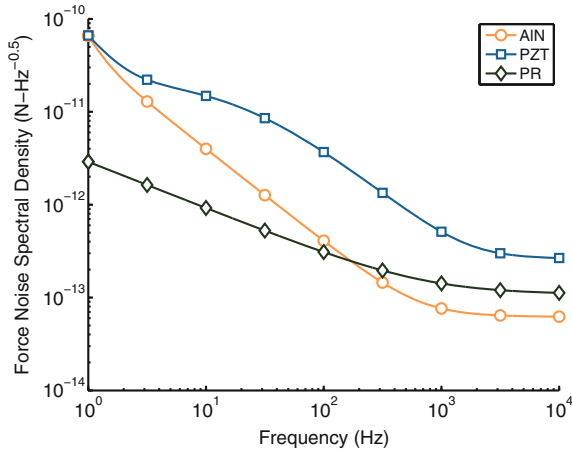


Fig. 7.15 A comparison of the force noise spectral density between 1 μm thick AlN, PZT and piezoresistive cantilevers optimized for a measurement bandwidth of 1 Hz–10 kHz ($f_0 = 20\text{ kHz}$). The power dissipation of the piezoresistive cantilever is 1 mW while the passively operated piezoelectric cantilevers do not actively dissipate any power. The thermomechanical force noise spectral density for the cantilevers is roughly $10\text{ fN}\cdot\text{Hz}^{-0.5}$ (Source Reprinted with permission from [515]. ©2010 IOP)

Conversely, ferroelectrics such as PZT operate best in charge-sensing mode due to their high piezoelectric coefficients and relative permittivity.

Figure 7.15 compares typical noise spectra for piezoresistive and piezoelectric sensors. The noise is calculated for the AlN and PZT films in voltage- and charge-sensing modes, respectively. Both types of piezoelectric sensors exhibit $1/f^2$ noise in contrast with the $1/f$ noise of the piezoresistor. The low frequency noise in both the AlN and PZT cases is generated by the Johnson noise of the film which is low-pass filtered by the film capacitance. The corner frequency of the Johnson noise is inversely proportional to the permittivity and resistivity of the piezoelectric film.

The integrated displacement noise of the three cantilever varieties is compared in Fig. 7.16 as a function of cantilever stiffness. The piezoresistor performance is plotted for power dissipations of 1 μW and 1 mW to show the strong performance dependence on power dissipation (see Sect. 5.4). The resolution of the AlN cantilever is about a factor of two better than the PZT cantilever, and can be better or worse than the piezoresistive cantilever depending on its power dissipation.

In comparing the resolution of piezoelectric and piezoresistive cantilevers the most important parameter is the power dissipation of the piezoresistor. Depending on the available power dissipation and temperature constraints piezoresistors can either perform better or worse than piezoelectric sensors. Another important parameter in comparing piezoresistive and piezoelectric sensors is the minimum sensor thickness. As the sensor becomes thinner, the piezoresistor and piezoelectric must also become thinner in order to maximize β^* and optimize the location of the neutral axis. While several groups and companies have developed the deposition of ultra-thin

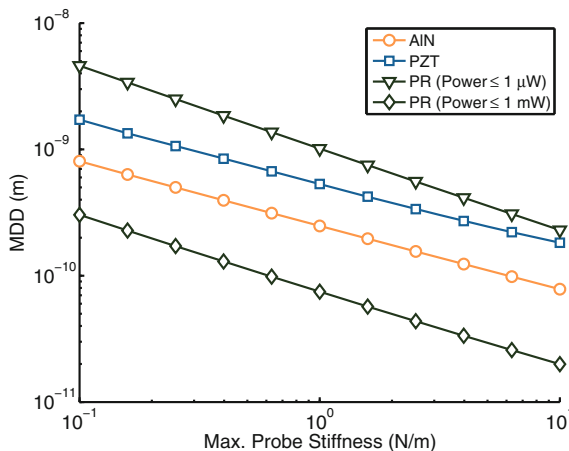


Fig. 7.16 Minimum detectable displacement for optimized cantilever designs with varying maximum stiffness. A measurement bandwidth of 1 Hz–10 kHz is used in the calculations ($f_0 \geq 20$ kHz). All four cantilever types are capable of sub-nm resolution for the given constraints, and are capable of sub-Å resolution for smaller measurement bandwidths (Source Reprinted with permission from [515]. ©2010 IOP)

(<100 nm) AlN films [537], the piezoelectric coefficients decrease as film thickness is reduced [98].

Piezoelectric sensors can be designed with comparable measurement bandwidth and dynamic range to piezoresistive sensors. The fact that both respond to stress rather than deflection leads to similar design geometries (e.g. bilayer cantilevers and diaphragms). Both can be made quite small, making them suitable for nanomechanical systems and ultra high frequency resonators [123, 538].

Piezoelectrics have several strengths with respect to piezoresistors. First, piezoelectrics are usually the preferred option in devices that require simultaneous actuation and sensing (e.g. gyroscopes and resonators). While thermally actuated piezoresistive resonators have been demonstrated [154, 155], piezoelectrics are far more widely used, notably in film bulk acoustic resonators (FBARs) [168, 169]. Second, piezoelectric sensors do not continuously dissipate power (although piezoelectric actuators do, presenting a capacitive load). While piezoresistors can be designed for ultra-low power dissipation, piezoelectrics are unbeatable in this regard. Finally, piezoelectric films are processed at low temperatures (typically <300 °C) so can readily be integrated post-CMOS.

The primary weakness of piezoelectric transduction is the technical challenge of film deposition. Reproducibly depositing a low stress film with high piezoelectric coefficients at low cost is notoriously difficult and was a major barrier that the first commercial FBARs managed to overcome [168]. In comparison with silicon doping processes, which can be performed at any silicon foundry at low cost, the number of AlN, ZnO or PZT foundry services can be counted on one hand as of 2012. A secondary weakness of piezoelectric films is their general lack of compatibility

with front-end CMOS processes due to the advantages of depositing the film on a metal electrode rather than doped silicon such as piezoelectric coefficient magnitude, etch selectivity, series electrical resistance.

7.2.4 Pseudo-Hall and Piezojunction Effects

This book has focused on the conventional piezoresistive effect, but the stress sensitivity of silicon can also be exploited using the pseudo-Hall and piezojunction effects. While investigating the noise and sensitivity of each effect is beyond the scope of this book, we will introduce them and refer the reader to additional reference material.

The pseudo-Hall effect is based on the shear piezoresistive effect (π_{44}), whereby the induced shear stress distorts the potential distribution in a piezoresistive plane. Motorola Semiconductor (now Freescale Semiconductor) used this configuration in a pressure sensor in the 1970s [539] and has continued producing this type of pressure sensor. Doelle et al. and Gieschke et al. reported geometry-based design rules and novel applications for the pseudo-Hall effect piezoresistive plates and developed piezo-FETs based upon the pseudo-Hall effect [48, 184]. Gieschke et al. developed a compact, highly integrated piezo-FET device using the pseudo-Hall effect [540]. Doelle et al. also optimized the geometry of pseudo-Hall piezo-FETs in order to maximize their stress sensitivity [541]. The design of pseudo-Hall devices can be optimized and modeled using the same methodology that we have used for the conventional piezoresistive effect. Their sensitivity can be calculated from the piezoresistance factor and β^* while most of their noise sources (Johnson, thermo-mechanical, amplifier) can be calculated with no model changes. Their 1/f noise is less straightforward to calculate due to the increased importance of surface effects and large variations in current density.

The piezojunction effect is defined as the change in the saturation current of a BJT or a p-n junction due to mechanical stress [542]. The main advantage over conventional piezoresistors lies in reduced power consumption but this trades off with size and circuit complexity [543]. The piezojunction effect is also important to understanding sources of unwanted offset in integrated circuits and sensors [267, 544–546]. We recommend Fruett and Meijer’s 2002 book on the piezojunction effect for an in-depth discussion of the piezojunction effect [547].

Piezoresistive sensors have also been designed to sense resistance changes in the channel of a MOSFET rather than a discrete resistor [263, 548, 549]. MOSFET-based piezoresistive sensors should not be confused with the piezojunction effect because no junctions are utilized for sensing. MOSFET sensors are operated in the saturation regime and the resistance of the channel is being modulated. However, MOSFET-based sensors yield similar benefits to piezojunction sensors. Both are inherently integrated with a transistor. One advantage of MOSFET devices over piezojunction devices is that the latter is limited to using the lateral PNP transistor in a CMOS process or switching to a BiCMOS process.

The primary advantage of using a FET channel to sense stress rather than a discrete resistor is simpler scaling to large arrays of devices. For example, Hafizovic et al. fabricated a 12×1 array of MOSFET-based piezoresistive cantilevers with thermal actuators and integrated with amplifiers, ADCs and DACS on a single chip [260]. All input and output with the chip was digital, and they even integrated square-root circuits onto the chip to linearize the voltage-response of the thermal actuators. One possible issue to keep in mind when integrating transistors onto thin piezoresistive sensors is the added mass, increased stiffness and film stress from the additional metal and dielectric layers. The same noise and sensitivity models that we developed for discrete piezoresistors can be applied to MOSFET-based piezoresistive sensors although, as in the case of piezojunction sensors, surface effects will play a much larger role in $1/f$ noise.

7.3 Summary

In the final chapter of this book we discussed alternative piezoresistive materials and transduction techniques.

We discussed four novel piezoresistive materials with various strengths and weaknesses: silicon carbide, diamond, nanostructures and metals. Silicon carbide and diamond piezoresistors exceed silicon in their temperature and chemical stability. However, deposition and micropatterning is less straightforward for both materials. Both materials are most commonly deposited as polycrystalline rather than single crystal films, which reduces the magnitude of their piezoresistive effects.

Carbon nanotubes and silicon nanowires were discussed next. CNTs can be integrated into polymer films for large area and flexible sensing structures. However, handling, sorting and patterning individual CNTs has proven nontrivial to date. Silicon nanowires with diameters on the order of 100 nm have been reported with piezoresistive coefficients ranging from 60 to 600 % larger than bulk single crystal silicon. Given our understanding of $1/f$ noise in conventional silicon piezoresistors, it is likely that silicon nanowires will have high $1/f$ noise due to their small volume which will limit their utility for certain applications (e.g. long-term chemical sensing).

Metal strain gauges, although far from a novel material, have found new applications in nanomechanical resonators. Their high electrical conductivity and modest gauge factor makes them well suited for impedance matched nanoscale resonators. Many metals have a gauge factor that is 30–50x smaller than highly doped silicon (e.g. 10^{20} cm^{-3}) but an electrical resistivity that is two to three orders of magnitude smaller.

We closed this chapter and the book by discussing the most common alternatives to piezoresistive sensing: optical, capacitive and piezoelectric transduction in addition to two lesser known techniques, the pseudo-Hall and piezojunction effects. For each technique, we compared the sources of noise, fundamental sensing limits, power dissipation and the quirks of each transduction technique.

The overarching conclusion was that the optimal transduction technique for a particular application depends on the measurement type, fabrication capabilities, cost constraints and other applications specifics. The performance envelope of a sensing mechanism depends in part on the model accuracy and thoroughness of the design process. We hope that this book improves the effectiveness of your next design, and even if it does not use a silicon piezoresistor, that it allows you to more quantitatively compare it with the alternatives.

Appendix A

Glossary of Mathematical Symbols

This Appendix summarizes the mathematical symbols that are used throughout the book. Several symbols have multiple meanings; for example, α is used to represent the temperature coefficient of resistance, the coefficient of thermal expansion, and the Hooge factor. We have tried to separate these overloaded symbols in the text and make their meaning clear whenever they are used. Symbols that are only used once or twice (e.g. the Tsai model for phosphorus predeposition) are not included in the table for succinctness.

Table A.1 Glossary of mathematical symbols

Symbol	Units	Description
α	-	Hooge factor
α	ppm/K	Coefficient of thermal expansion
α	ppm/K	Temperature coefficient of resistance
β^*	-	Sensitivity factor
β_1^*	-	Sensitivity factor (piezoresistance factor effect)
β_2^*	-	Sensitivity factor (depth effect)
ϵ	F/m	Electrical permittivity
ϵ	-	Mechanical strain
η	Pa-s	Fluid viscosity
γ	-	Resistance factor
Λ	m	Thermal healing length
μ	cm ² /V-sec	Carrier mobility
ω	rad/s	Angular frequency
π	1/Pa	Piezoresistive coefficient
π^{ref}	1/Pa	Piezoresistive coefficient at 300 K and 10 ¹⁷ cm ⁻³
π_l	1/Pa	Longitudinal piezoresistive coefficient
π_t	1/Pa	Transverse piezoresistive coefficient
ϕ	-	Transverse loading factor
ρ	$\Omega\text{-m}$	Electrical resistivity
ρ	kg/m ³	Density
ρ_f	kg/m ³	Fluid density
σ	Pa	Mechanical stress
σ	S/m	Electrical conductivity
A	m ²	Cross-sectional or film area
A_{VJ}	V/ $\sqrt{\text{Hz}}$	Amplifier Johnson voltage noise coefficient
A_{VF}	V	Amplifier 1/f voltage noise coefficient
A_{IJ}	A/ $\sqrt{\text{Hz}}$	Amplifier Johnson current noise coefficient
A_{IF}	A	Amplifier 1/f current noise coefficient
b	kg/s	Drag coefficient
C	1/m	Curvature
C	Pa	Elastic stiffness tensor
C	F	Electrical capacitance
D	m ² /s	Diffusivity
d_{31}	pm/V	Transverse piezoelectric coefficient
E	Pa	Elastic modulus
E_F	eV	Fermi energy level
E_g	eV	Bandgap energy
F_{TMN}	N/ $\sqrt{\text{Hz}}$	Thermomechanical force noise
f_{-3dB}	Hz	-3 dB frequency
f_0	Hz	Undamped first resonant mode frequency
f_d	Hz	Damped first resonant mode frequency
f_{min}	Hz	Minimum measurement frequency
f_{max}	Hz	Maximum measurement frequency
G	-	Amplifier gain
G	W/K	Thermal conductance

(continued)

Table A.1 (continued)

Symbol	Units	Description
G'_f	W/m-K	Structure-fluid thermal conductance per unit length
h_{eff}	W/m ² -K	Effective convection coefficient
h	J-sec	Planck's constant
I	m ⁴	Second moment of area
I	A	Electrical current
J	A/m ²	Electrical current density
k	W/m-K	Thermal conductivity
k	N/m	Spring constant
k_b	J/K	Boltzmann's constant
l	m	Sensor length
l_{pr}	m	Piezoresistor length
m	kg	Mass
m_{eff}	kg	Effective mass
MDD	m	Minimum detectable displacement
MDF	N	Minimum detectable force
N	cm ⁻³	Dopant concentration
N_A	cm ⁻³	Acceptor dopant concentration
N_B	cm ⁻³	Background dopant concentration
N_D	cm ⁻³	Donor dopant concentration
N_{epi}	cm ⁻³	Epitaxial layer dopant concentration
n	cm ⁻³	Carrier density
n_i	cm ⁻³	Intrinsic carrier density
N_{pr}	-	Number of piezoresistors in the Wheatstone bridge
N_{eff}	-	Effective number of carriers
N_{total}	-	Total number of carriers
N_z^{eff}	μm ⁻²	Effective carrier density per unit area
N_z^{total}	μm ⁻²	Total carrier density per unit area
P	m	Perimeter
P	-	Piezoresistance factor
\bar{P}	-	Average piezoresistance factor
q	C	Single electron charge
Q	C	Electrical polarization charge
Q	-	Quality factor
R	Ω	Total electrical resistance
R	K/W	Thermal resistance
$R_{contact}$	Ω	Contact resistance
R_{excess}	Ω	Excess electrical resistance
R_{pr}	Ω	Piezoresistor electrical resistance
R_s	Ω/□	Sheet resistance
S	1/Pa	Elastic compliance tensor
S_{XV}	V/m	Displacement sensitivity
S_{FV}	V/N	Force sensitivity
S_A	V ² /Hz	Amplifier noise power spectral density
S_H	V ² /Hz	Hooge (1/f) noise power spectral density

(continued)

Table A.1 (continued)

Symbol	Units	Description
S_J	V ² /Hz	Johnson noise power spectral density
S_{TMN}	V ² /Hz	Thermomechanical noise power spectral density
T	K	Temperature
T_∞	K	Ambient temperature
T_{pr}	K	Average piezoresistor temperature
T_n	-	Temperature normalized to 300 K
t	s	Time
t	m	Sensor thickness
t_j	m	Junction depth
t_{pr}	m	Epitaxial piezoresistor thickness
V_{bias}	V	Resistor bias voltage
V_{bridge}	V	Bridge bias voltage
V_A	V/ $\sqrt{\text{Hz}}$	Amplifier noise spectral density
V_H	V/ $\sqrt{\text{Hz}}$	Hooge (1/f) noise spectral density
V_J	V/ $\sqrt{\text{Hz}}$	Johnson noise spectral density
V_{noise}	V/ $\sqrt{\text{Hz}}$	Overall noise spectral density
V_{TMN}	V/ $\sqrt{\text{Hz}}$	Thermomechanical noise spectral density
w	m	Sensor width
w_{pr}	m	Piezoresistor width
W	W	Electrical power dissipation
z_n	m	Neutral axis

Appendix B

Ion Implantation Lookup Tables

The following lookup tables can be used to calculate the sensitivity factor (β_1^* and β_2^*), effective density of carriers per unit area (N_z^{eff}), sheet resistance (R_s) and junction depth (t_j) for boron, phosphorus and arsenic ion implantation processes.

Park presented the first version of these lookup tables in 2010 [133, 295]. The following tables generalize the results to multiple dopant types and include tables for additional parameters (N_z^{eff} , R_s and t_j). The TSUPREM-4™ templates and combination of Python and MATLAB® scripts used to generate the tables are part of our open source piezoresistor design code (Appendix C).

In all of the tables, the first number corresponds to a process with only an inert anneal while the second number (in parentheses) corresponds to a process with a 1,500 Å wet passivation oxide grown immediately before the N₂ anneal. The wet passivation oxide was grown at the indicated process temperature for 66, 15, or 5 minutes at 900, 1,000, or 1,100 °C, respectively. Junction depths are calculated assuming a background resistivity of 10 Ω-cm.

Table B.1 Look-up table for β_1^* (-) and β_2^* (μm) for boron ion implantation

		Time (min)										
		15	30	45	60	75	90	105	120			
		β_1^* β_2^*										
20	900	0.75 (0.82)	0.12 (0.18)	0.75 (0.82)	0.12 (0.18)	0.75 (0.82)	0.12 (0.18)	0.75 (0.82)	0.12 (0.18)	0.75 (0.82)	0.12 (0.19)	0.75 (0.82)
	1,000	0.73 (0.83)	0.12 (0.23)	0.73 (0.84)	0.13 (0.24)	0.74 (0.84)	0.14 (0.24)	0.74 (0.84)	0.14 (0.25)	0.74 (0.84)	0.15 (0.25)	0.74 (0.84)
	1,100	0.76 (0.85)	0.22 (0.37)	0.77 (0.86)	0.26 (0.40)	0.78 (0.86)	0.29 (0.42)	0.78 (0.86)	0.33 (0.45)	0.79 (0.47)	0.36 (0.86)	0.79 (0.49)
	900	0.77 (0.80)	0.22 (0.26)	0.77 (0.80)	0.22 (0.26)	0.77 (0.80)	0.22 (0.26)	0.77 (0.80)	0.22 (0.26)	0.77 (0.80)	0.22 (0.26)	0.77 (0.80)
	1,000	0.76 (0.81)	0.22 (0.30)	0.76 (0.81)	0.22 (0.30)	0.76 (0.81)	0.23 (0.30)	0.76 (0.82)	0.23 (0.31)	0.76 (0.82)	0.23 (0.31)	0.76 (0.82)
	1,100	0.77 (0.83)	0.28 (0.42)	0.78 (0.84)	0.31 (0.44)	0.78 (0.84)	0.34 (0.47)	0.78 (0.84)	0.37 (0.49)	0.79 (0.84)	0.40 (0.51)	0.79 (0.85)
	900	0.77 (0.80)	0.28 (0.31)	0.77 (0.80)	0.28 (0.31)	0.77 (0.80)	0.28 (0.31)	0.77 (0.80)	0.28 (0.31)	0.77 (0.80)	0.28 (0.31)	0.77 (0.80)
	1,000	0.77 (0.81)	0.28 (0.34)	0.77 (0.81)	0.28 (0.34)	0.77 (0.81)	0.29 (0.35)	0.77 (0.81)	0.29 (0.35)	0.77 (0.81)	0.29 (0.36)	0.77 (0.81)
	1,100	0.78 (0.83)	0.33 (0.45)	0.79 (0.83)	0.36 (0.48)	0.79 (0.83)	0.39 (0.50)	0.79 (0.83)	0.41 (0.52)	0.80 (0.84)	0.44 (0.54)	0.80 (0.84)
	900	0.47 (0.67)	0.05 (0.16)	0.47 (0.68)	0.06 (0.16)	0.48 (0.68)	0.06 (0.16)	0.49 (0.68)	0.07 (0.16)	0.50 (0.68)	0.08 (0.16)	0.52 (0.68)
20	1,000	0.53 (0.66)	0.12 (0.23)	0.54 (0.66)	0.14 (0.24)	0.55 (0.67)	0.16 (0.24)	0.55 (0.67)	0.17 (0.25)	0.56 (0.67)	0.18 (0.26)	0.56 (0.67)
	1,100	0.58 (0.69)	0.25 (0.38)	0.59 (0.69)	0.29 (0.40)	0.60 (0.70)	0.33 (0.43)	0.61 (0.70)	0.36 (0.45)	0.62 (0.71)	0.40 (0.48)	0.62 (0.71)
	900	0.55 (0.65)	0.17 (0.25)	0.55 (0.65)	0.17 (0.25)	0.56 (0.65)	0.17 (0.25)	0.56 (0.65)	0.18 (0.26)	0.56 (0.65)	0.18 (0.26)	0.57 (0.65)
	1,000	0.53 (0.69)	0.17 (0.25)	0.54 (0.65)	0.17 (0.25)	0.55 (0.65)	0.17 (0.25)	0.56 (0.65)	0.18 (0.26)	0.57 (0.65)	0.18 (0.26)	0.57 (0.65)

(continued)

Table B.1 (continued)

Dose (cm ⁻²)	Energy (keV)	Temp. (°C)	Time (min)													
			15	30	45	60	75	90	105	120	β_1^*	β_2^*	β_1^*	β_2^*		
2×10^{15}	50	1,000	0.57 (0.65)	0.19 (0.29)	0.57 (0.66)	0.20 (0.30)	0.57 (0.66)	0.21 (0.30)	0.57 (0.66)	0.21 (0.31)	0.58 (0.66)	0.22 (0.31)	0.58 (0.66)	0.23 (0.31)	0.58 (0.67)	
		1,100	0.59 (0.68)	0.27 (0.40)	0.60 (0.68)	0.31 (0.43)	0.61 (0.69)	0.35 (0.46)	0.62 (0.69)	0.38 (0.48)	0.62 (0.69)	0.41 (0.50)	0.63 (0.50)	0.44 (0.50)	0.63 (0.54)	0.46 (0.70)
		900	0.60 (0.65)	0.27 (0.34)	0.60 (0.65)	0.27 (0.34)	0.60 (0.65)	0.27 (0.65)	0.60 (0.34)	0.27 (0.65)	0.60 (0.34)	0.27 (0.66)	0.60 (0.66)	0.27 (0.34)	0.58 (0.66)	0.24 (0.34)
	80	1,000	0.59 (0.66)	0.26 (0.35)	0.59 (0.66)	0.27 (0.36)	0.59 (0.66)	0.27 (0.36)	0.60 (0.66)	0.28 (0.66)	0.60 (0.37)	0.28 (0.66)	0.60 (0.37)	0.29 (0.66)	0.60 (0.38)	0.30 (0.66)
		1,100	0.60 (0.67)	0.32 (0.45)	0.61 (0.68)	0.35 (0.47)	0.62 (0.68)	0.38 (0.50)	0.62 (0.59)	0.41 (0.52)	0.63 (0.69)	0.41 (0.54)	0.63 (0.69)	0.44 (0.56)	0.63 (0.69)	0.46 (0.57)
		900	0.48 (0.51)	0.09 (0.12)	0.48 (0.51)	0.10 (0.12)	0.48 (0.50)	0.10 (0.12)	0.48 (0.50)	0.10 (0.13)	0.48 (0.50)	0.11 (0.13)	0.48 (0.51)	0.11 (0.13)	0.48 (0.51)	0.12 (0.51)
2×10^{16}	50	1,000	0.42 (0.45)	0.14 (0.20)	0.41 (0.46)	0.17 (0.21)	0.41 (0.46)	0.19 (0.23)	0.41 (0.47)	0.21 (0.25)	0.41 (0.47)	0.22 (0.26)	0.41 (0.47)	0.24 (0.27)	0.41 (0.48)	0.27 (0.48)
		1,100	0.38 (0.45)	0.30 (0.39)	0.40 (0.48)	0.37 (0.44)	0.41 (0.49)	0.43 (0.49)	0.42 (0.47)	0.48 (0.49)	0.43 (0.51)	0.52 (0.54)	0.43 (0.54)	0.52 (0.56)	0.44 (0.56)	0.45 (0.59)
		900	0.48 (0.50)	0.17 (0.18)	0.48 (0.50)	0.18 (0.18)										
	80	1,000	0.40 (0.42)	0.17 (0.20)	0.40 (0.42)	0.18 (0.22)	0.40 (0.23)	0.20 (0.42)	0.40 (0.42)	0.22 (0.25)	0.40 (0.42)	0.24 (0.26)	0.40 (0.42)	0.25 (0.28)	0.40 (0.42)	0.27 (0.42)
		1,100	0.38 (0.45)	0.32 (0.41)	0.40 (0.46)	0.39 (0.45)	0.41 (0.47)	0.45 (0.49)	0.42 (0.47)	0.49 (0.53)	0.43 (0.53)	0.53 (0.56)	0.43 (0.48)	0.53 (0.59)	0.44 (0.59)	0.45 (0.62)
		900	0.49 (0.50)	0.26 (0.27)	0.48 (0.50)	0.26 (0.28)	0.48 (0.51)	0.26 (0.28)	0.48 (0.51)	0.26 (0.28)	0.48 (0.51)	0.26 (0.28)	0.48 (0.50)	0.26 (0.28)	0.48 (0.50)	0.26 (0.28)

Table B.2 Look-up table for β_1^* (-) and β_2^* (μm) for phosphorus ion implantation

		Dose (cm^{-2}) Energy (keV) Temp. (°C)										Time (min)					
		15		30		45		60		75		90		105		120	
		β_1^*	β_2^*	β_1^*	β_2^*	β_1^*	β_2^*	β_1^*	β_2^*	β_1^*	β_2^*	β_1^*	β_2^*	β_1^*	β_2^*	β_1^*	β_2^*
20	900	0.62 (0.80)	0.03 (0.09)	0.63 (0.80)	0.03 (0.09)	0.63 (0.80)	0.04 (0.09)	0.64 (0.80)	0.04 (0.09)	0.64 (0.80)	0.04 (0.09)	0.64 (0.80)	0.04 (0.09)	0.64 (0.80)	0.04 (0.09)	0.65 (0.80)	0.04 (0.09)
	1,000	0.68 (0.86)	0.07 (0.16)	0.70 (0.87)	0.08 (0.17)	0.71 (0.87)	0.09 (0.17)	0.71 (0.87)	0.10 (0.18)	0.72 (0.87)	0.11 (0.18)	0.73 (0.87)	0.12 (0.19)	0.73 (0.87)	0.13 (0.19)	0.73 (0.87)	0.13 (0.19)
	1,100	0.76 (0.91)	0.20 (0.32)	0.78 (0.91)	0.25 (0.35)	0.78 (0.91)	0.29 (0.37)	0.79 (0.92)	0.32 (0.40)	0.80 (0.92)	0.36 (0.42)	0.80 (0.92)	0.39 (0.44)	0.81 (0.92)	0.41 (0.46)	0.81 (0.92)	0.44 (0.48)
	900	0.65 (0.73)	0.06 (0.10)	0.65 (0.73)	0.06 (0.10)	0.65 (0.73)	0.06 (0.10)	0.65 (0.73)	0.06 (0.10)	0.65 (0.73)	0.06 (0.10)	0.65 (0.73)	0.06 (0.10)	0.65 (0.73)	0.07 (0.10)	0.65 (0.73)	0.07 (0.10)
	1,000	0.68 (0.78)	0.08 (0.17)	0.68 (0.78)	0.09 (0.18)	0.69 (0.79)	0.10 (0.18)	0.70 (0.79)	0.11 (0.19)	0.70 (0.79)	0.12 (0.19)	0.71 (0.79)	0.13 (0.20)	0.71 (0.79)	0.13 (0.20)	0.72 (0.79)	0.14 (0.21)
	1,100	0.74 (0.85)	0.20 (0.35)	0.76 (0.85)	0.25 (0.38)	0.77 (0.85)	0.29 (0.40)	0.77 (0.86)	0.33 (0.43)	0.78 (0.86)	0.36 (0.45)	0.78 (0.86)	0.39 (0.45)	0.79 (0.86)	0.41 (0.47)	0.79 (0.86)	0.44 (0.52)
2×10^{14}	900	0.69 (0.73)	0.10 (0.12)	0.69 (0.73)	0.10 (0.12)	0.69 (0.73)	0.10 (0.12)	0.69 (0.73)	0.10 (0.12)	0.69 (0.73)	0.10 (0.12)	0.69 (0.73)	0.10 (0.12)	0.69 (0.73)	0.10 (0.12)	0.69 (0.73)	0.10 (0.12)
	1,000	0.70 (0.76)	0.11 (0.19)	0.71 (0.77)	0.12 (0.19)	0.71 (0.77)	0.13 (0.20)	0.71 (0.77)	0.13 (0.20)	0.72 (0.77)	0.14 (0.20)	0.72 (0.77)	0.15 (0.21)	0.72 (0.77)	0.15 (0.21)	0.73 (0.77)	0.16 (0.22)
	1,100	0.75 (0.82)	0.22 (0.36)	0.76 (0.83)	0.26 (0.39)	0.77 (0.83)	0.30 (0.41)	0.78 (0.83)	0.33 (0.44)	0.78 (0.84)	0.37 (0.46)	0.79 (0.84)	0.39 (0.48)	0.79 (0.84)	0.42 (0.51)	0.79 (0.84)	0.45 (0.53)
	900	0.49 (0.64)	0.09 (0.09)	0.49 (0.65)	0.09 (0.09)	0.50 (0.65)	0.09 (0.09)	0.50 (0.65)	0.10 (0.09)	0.50 (0.65)	0.10 (0.09)	0.50 (0.65)	0.10 (0.09)	0.51 (0.65)	0.10 (0.09)	0.51 (0.65)	0.10 (0.09)
	1,000	0.51 (0.74)	0.10 (0.16)	0.52 (0.74)	0.11 (0.17)	0.53 (0.74)	0.12 (0.17)	0.53 (0.74)	0.12 (0.18)	0.54 (0.74)	0.13 (0.18)	0.54 (0.74)	0.13 (0.18)	0.55 (0.75)	0.14 (0.19)	0.55 (0.75)	0.15 (0.20)
	1,100	0.58 (0.82)	0.20 (0.34)	0.59 (0.82)	0.24 (0.37)	0.61 (0.83)	0.28 (0.40)	0.62 (0.83)	0.31 (0.43)	0.62 (0.83)	0.34 (0.45)	0.63 (0.84)	0.37 (0.48)	0.64 (0.84)	0.40 (0.50)	0.64 (0.84)	0.42 (0.52)
20	900	0.41 (0.57)	0.05 (0.12)	0.43 (0.57)	0.06 (0.12)	0.44 (0.57)	0.07 (0.12)	0.45 (0.57)	0.08 (0.12)	0.46 (0.57)	0.08 (0.13)	0.46 (0.57)	0.08 (0.13)	0.47 (0.57)	0.09 (0.13)	0.47 (0.57)	0.09 (0.13)
	1,000	0.49 (0.64)	0.09 (0.09)	0.49 (0.65)	0.09 (0.09)	0.50 (0.65)	0.09 (0.09)	0.50 (0.65)	0.10 (0.09)	0.50 (0.65)	0.10 (0.09)	0.50 (0.65)	0.10 (0.09)	0.51 (0.65)	0.10 (0.09)	0.51 (0.65)	0.10 (0.09)

(continued)

Table B.2 (continued)

		Dose (cm^{-2}) Energy (keV) Temp. ($^{\circ}\text{C}$)										Time (min)											
		15					30					45		60		75		90		105		120	
		β_1^*	β_2^*	β_1^*	β_2^*	β_1^*	β_2^*	β_1^*	β_2^*	β_1^*	β_2^*	β_1^*	β_2^*	β_1^*	β_2^*	β_1^*	β_2^*	β_1^*	β_2^*	β_1^*	β_2^*		
2 × 10 ¹⁵	50	0.47	0.09	0.49	0.10	0.50	0.11	0.50	0.12	0.51	0.13	0.51	0.14	0.52	0.14	0.52	0.14	0.52	0.14	0.52	0.15		
		(0.59)	(0.14)	(0.59)	(0.15)	(0.60)	(0.15)	(0.60)	(0.16)	(0.60)	(0.16)	(0.61)	(0.17)	(0.61)	(0.18)	(0.61)	(0.18)	(0.61)	(0.18)	(0.61)	(0.18)		
		0.55	0.20	0.57	0.24	0.58	0.28	0.59	0.31	0.60	0.34	0.61	0.37	0.61	0.39	0.62	0.42	0.42	0.42	0.42	0.42		
		(0.71)	(0.34)	(0.72)	(0.37)	(0.72)	(0.39)	(0.73)	(0.42)	(0.73)	(0.44)	(0.73)	(0.47)	(0.74)	(0.49)	(0.74)	(0.49)	(0.74)	(0.49)	(0.74)	(0.51)		
		0.42	0.05	0.42	0.05	0.42	0.06	0.42	0.06	0.43	0.06	0.43	0.06	0.44	0.06	0.44	0.06	0.44	0.06	0.44	0.07		
		(0.55)	(0.13)	(0.55)	(0.13)	(0.55)	(0.13)	(0.55)	(0.13)	(0.55)	(0.13)	(0.55)	(0.13)	(0.56)	(0.13)	(0.56)	(0.13)	(0.56)	(0.13)	(0.56)	(0.13)		
80	1,000	0.47	0.09	0.49	0.10	0.50	0.11	0.50	0.12	0.51	0.13	0.52	0.13	0.52	0.14	0.53	0.15	0.53	0.15	0.53	0.15		
		(0.56)	(0.14)	(0.56)	(0.15)	(0.57)	(0.15)	(0.57)	(0.16)	(0.57)	(0.16)	(0.58)	(0.17)	(0.58)	(0.17)	(0.58)	(0.17)	(0.58)	(0.17)	(0.58)	(0.18)		
		0.55	0.20	0.57	0.24	0.58	0.28	0.59	0.31	0.60	0.34	0.61	0.37	0.61	0.39	0.62	0.42	0.42	0.42	0.42	0.42		
		(0.67)	(0.33)	(0.68)	(0.36)	(0.68)	(0.38)	(0.69)	(0.41)	(0.69)	(0.43)	(0.70)	(0.46)	(0.70)	(0.48)	(0.70)	(0.50)	(0.50)	(0.50)	(0.50)	(0.50)		
		0.49	0.53	0.49	0.54	0.49	0.55	0.49	0.55	0.49	0.56	0.48	0.56	0.48	0.56	0.48	0.56	0.48	0.56	0.48	0.56		
		(0.53)	(0.28)	(0.53)	(0.28)	(0.53)	(0.28)	(0.53)	(0.28)	(0.53)	(0.28)	(0.53)	(0.29)	(0.54)	(0.29)	(0.54)	(0.29)	(0.54)	(0.29)	(0.54)	(0.29)		
20	1,000	0.39	0.35	0.39	0.35	0.40	0.36	0.40	0.36	0.40	0.36	0.40	0.36	0.40	0.37	0.40	0.37	0.41	0.37	0.41	0.37		
		(0.49)	(0.15)	(0.49)	(0.15)	(0.49)	(0.16)	(0.50)	(0.16)	(0.50)	(0.17)	(0.50)	(0.18)	(0.51)	(0.18)	(0.51)	(0.18)	(0.51)	(0.19)	(0.51)	(0.19)		
		0.41	0.36	0.41	0.38	0.42	0.41	0.43	0.43	0.43	0.45	0.44	0.44	0.47	0.44	0.49	0.45	0.51	0.51	0.51	0.51		
		(0.59)	(0.30)	(0.60)	(0.33)	(0.61)	(0.36)	(0.62)	(0.39)	(0.62)	(0.41)	(0.63)	(0.43)	(0.63)	(0.46)	(0.63)	(0.46)	(0.63)	(0.48)	(0.63)	(0.48)		
		0.38	0.15	0.39	0.17	0.39	0.18	0.39	0.19	0.40	0.20	0.40	0.21	0.40	0.22	0.40	0.22	0.40	0.23	0.40	0.23		
		(0.48)	(0.59)	(0.48)	(0.59)	(0.49)	(0.59)	(0.49)	(0.60)	(0.49)	(0.59)	(0.49)	(0.59)	(0.49)	(0.59)	(0.49)	(0.59)	(0.49)	(0.59)	(0.49)	(0.60)		
2 × 10 ¹⁶	50	0.33	0.22	0.33	0.22	0.33	0.22	0.33	0.23	0.34	0.24	0.34	0.24	0.34	0.24	0.35	0.25	0.35	0.26	0.35	0.26		
		(0.39)	(0.25)	(0.39)	(0.26)	(0.39)	(0.26)	(0.39)	(0.27)	(0.40)	(0.27)	(0.40)	(0.28)	(0.40)	(0.28)	(0.40)	(0.28)	(0.40)	(0.28)	(0.40)	(0.28)		
		0.35	0.26	0.36	0.30	0.38	0.34	0.38	0.37	0.39	0.40	0.40	0.42	0.40	0.45	0.41	0.47	0.41	0.47	0.41	0.47		
		(0.46)	(0.27)	(0.47)	(0.30)	(0.48)	(0.33)	(0.49)	(0.36)	(0.49)	(0.38)	(0.50)	(0.41)	(0.50)	(0.43)	(0.51)	(0.45)	(0.45)	(0.45)	(0.45)	(0.45)		
		0.30	0.08	0.31	0.09	0.32	0.11	0.33	0.12	0.34	0.13	0.34	0.14	0.35	0.15	0.35	0.16	0.35	0.16	0.35	0.16		
		(0.47)	(0.59)	(0.47)	(0.60)	(0.47)	(0.60)	(0.47)	(0.60)	(0.47)	(0.61)	(0.47)	(0.61)	(0.47)	(0.61)	(0.47)	(0.61)	(0.47)	(0.61)	(0.47)	(0.61)		
80	1,000	0.31	0.17	0.31	0.18	0.32	0.19	0.32	0.19	0.33	0.20	0.33	0.21	0.33	0.22	0.34	0.23	0.34	0.23	0.34	0.23		
		(0.37)	(0.25)	(0.37)	(0.26)	(0.38)	(0.26)	(0.38)	(0.27)	(0.38)	(0.27)	(0.38)	(0.27)	(0.38)	(0.28)	(0.38)	(0.28)	(0.39)	(0.28)	(0.39)	(0.29)		
		0.35	0.25	0.36	0.29	0.38	0.33	0.39	0.36	0.39	0.39	0.40	0.41	0.41	0.44	0.41	0.44	0.41	0.46	0.41	0.46		
	1,000	(0.43)	(0.27)	(0.45)	(0.30)	(0.46)	(0.33)	(0.46)	(0.36)	(0.47)	(0.39)	(0.48)	(0.41)	(0.48)	(0.43)	(0.49)	(0.45)	(0.45)	(0.45)	(0.45)	(0.45)		

Table B.3 Look-up table for β_1^* (-) and β_2^* (μm) for arsenic ion implantation

		Time (min)																					
		15					30					45					60						
		Dose (cm^{-2})		Energy (keV)		Temp. (°C)		β_1^*	β_2^*														
20	900	0.65	0.01	0.66	0.01	0.66	0.01	0.66	0.01	0.67	0.01	0.67	0.01	0.67	0.01	0.67	0.02	0.68	0.02	0.68	0.02		
	(0.84)	(0.01)	(0.84)	(0.01)	(0.84)	(0.01)	(0.84)	(0.01)	(0.84)	(0.01)	(0.85)	(0.01)	(0.85)	(0.01)	(0.85)	(0.01)	(0.85)	(0.01)	(0.85)	(0.01)	(0.85)	(0.01)	
	1,000	0.71	0.03	0.73	0.03	0.74	0.03	0.74	0.04	0.75	0.04	0.75	0.04	0.75	0.04	0.75	0.04	0.76	0.05	0.76	0.05	0.76	0.05
	1,100	0.79	0.08	0.80	0.09	0.81	0.11	0.82	0.12	0.82	0.13	0.83	0.14	0.83	0.15	0.83	0.15	0.83	0.16	0.83	0.16	0.83	0.16
	900	0.53	0.02	0.54	0.02	0.54	0.02	0.54	0.02	0.55	0.02	0.55	0.02	0.55	0.02	0.55	0.02	0.55	0.02	0.56	0.02	0.56	0.02
	(0.69)	(0.02)	(0.69)	(0.02)	(0.69)	(0.02)	(0.69)	(0.02)	(0.69)	(0.02)	(0.69)	(0.02)	(0.69)	(0.02)	(0.69)	(0.02)	(0.69)	(0.02)	(0.70)	(0.02)	(0.70)	(0.02)	
	1,000	0.59	0.03	0.60	0.04	0.61	0.04	0.62	0.04	0.62	0.05	0.63	0.05	0.63	0.05	0.63	0.05	0.63	0.05	0.63	0.05	0.63	0.06
	1,100	0.66	0.08	0.68	0.10	0.69	0.11	0.70	0.13	0.71	0.14	0.71	0.15	0.71	0.16	0.72	0.16	0.72	0.17	0.72	0.17	0.72	0.17
	900	0.59	0.04	0.59	0.03	0.59	0.04	0.59	0.04	0.59	0.04	0.59	0.04	0.59	0.04	0.59	0.04	0.59	0.04	0.59	0.04	0.59	0.04
	(0.65)	(0.03)	(0.65)	(0.03)	(0.65)	(0.03)	(0.65)	(0.03)	(0.65)	(0.03)	(0.65)	(0.03)	(0.65)	(0.03)	(0.65)	(0.03)	(0.66)	(0.03)	(0.66)	(0.03)	(0.66)	(0.03)	
80	900	0.61	0.04	0.62	0.05	0.62	0.05	0.63	0.05	0.63	0.05	0.64	0.06	0.64	0.06	0.64	0.06	0.64	0.06	0.64	0.06	0.64	0.06
	1,000	(0.68)	(0.04)	(0.68)	(0.04)	(0.69)	(0.05)	(0.70)	(0.05)	(0.70)	(0.05)	(0.70)	(0.05)	(0.70)	(0.05)	(0.70)	(0.05)	(0.71)	(0.05)	(0.71)	(0.05)	(0.71)	(0.06)
	1,100	0.67	0.08	0.68	0.10	0.70	0.12	0.70	0.13	0.71	0.14	0.72	0.15	0.72	0.16	0.72	0.17	0.72	0.17	0.72	0.17	0.72	0.17
	900	0.45	0.01	0.46	0.01	0.46	0.01	0.47	0.02	0.48	0.02	0.48	0.02	0.48	0.02	0.48	0.02	0.49	0.02	0.49	0.02	0.49	0.02
	(0.70)	(0.01)	(0.71)	(0.01)	(0.71)	(0.01)	(0.71)	(0.01)	(0.72)	(0.01)	(0.72)	(0.01)	(0.72)	(0.01)	(0.72)	(0.01)	(0.72)	(0.02)	(0.72)	(0.02)	(0.73)	(0.02)	
	1,000	0.54	0.03	0.55	0.04	0.56	0.04	0.57	0.05	0.57	0.05	0.58	0.05	0.58	0.05	0.58	0.05	0.59	0.06	0.59	0.06	0.59	0.06
	1,100	(0.80)	(0.03)	(0.81)	(0.03)	(0.82)	(0.03)	(0.82)	(0.04)	(0.82)	(0.04)	(0.83)	(0.04)	(0.83)	(0.04)	(0.83)	(0.04)	(0.83)	(0.04)	(0.83)	(0.04)	(0.83)	(0.05)
20	900	0.36	0.02	0.36	0.02	0.36	0.02	0.36	0.02	0.36	0.02	0.36	0.02	0.36	0.02	0.36	0.02	0.37	0.02	0.37	0.02	0.37	0.02
	(0.49)	(0.01)	(0.50)	(0.01)	(0.50)	(0.02)	(0.51)	(0.02)	(0.51)	(0.02)	(0.52)	(0.02)	(0.52)	(0.02)	(0.52)	(0.02)	(0.52)	(0.02)	(0.52)	(0.02)	(0.52)	(0.02)	

(continued)

Table B.3 (continued)

Dose (cm ⁻²)		Energy (keV)		Temp. (°C)		Time (min)														
		β_1^*	β_2^*	β_1^*	β_2^*	15	30	45	60	75	90	105	120	β_1^*	β_2^*	β_1^*	β_2^*	β_1^*	β_2^*	
2 × 10 ¹⁵	50	1,000	0.39 (0.56)	0.04 (0.03)	0.40 (0.57)	0.04 (0.04)	0.41 (0.58)	0.05 (0.04)	0.42 (0.59)	0.06 (0.05)	0.43 (0.60)	0.06 (0.05)	0.44 (0.60)	0.06 (0.05)	0.44 (0.61)	0.07 (0.06)	0.45 (0.61)	0.07 (0.06)	0.45 (0.61)	0.07 (0.06)
	1,000	0.48 (0.67)	0.10 (0.09)	0.49 (0.68)	0.12 (0.11)	0.51 (0.69)	0.14 (0.12)	0.52 (0.70)	0.15 (0.71)	0.52 (0.71)	0.16 (0.71)	0.53 (0.71)	0.17 (0.71)	0.54 (0.72)	0.19 (0.16)	0.54 (0.72)	0.20 (0.17)	0.54 (0.72)	0.20 (0.18)	
	900	0.37 (0.44)	0.02 (0.02)	0.37 (0.44)	0.02 (0.02)	0.37 (0.45)	0.02 (0.02)	0.37 (0.45)	0.02 (0.02)	0.37 (0.46)	0.02 (0.02)									
	1,000	0.40 (0.50)	0.04 (0.04)	0.41 (0.51)	0.05 (0.04)	0.42 (0.52)	0.05 (0.05)	0.43 (0.53)	0.06 (0.05)	0.44 (0.54)	0.06 (0.06)	0.44 (0.54)	0.06 (0.06)	0.44 (0.54)	0.07 (0.06)	0.45 (0.55)	0.07 (0.06)	0.45 (0.55)	0.07 (0.06)	
	1,100	0.48 (0.61)	0.10 (0.10)	0.50 (0.63)	0.12 (0.11)	0.51 (0.64)	0.14 (0.13)	0.52 (0.64)	0.15 (0.14)	0.53 (0.65)	0.16 (0.15)	0.53 (0.66)	0.17 (0.16)	0.54 (0.66)	0.19 (0.16)	0.54 (0.66)	0.19 (0.17)	0.54 (0.66)	0.20 (0.18)	
	900	0.33 (0.50)	0.02 (0.01)	0.33 (0.51)	0.02 (0.01)	0.34 (0.52)	0.02 (0.01)	0.34 (0.53)	0.02 (0.01)	0.34 (0.53)	0.02 (0.02)	0.34 (0.54)	0.02 (0.02)	0.34 (0.54)	0.02 (0.02)	0.34 (0.54)	0.02 (0.02)	0.34 (0.54)	0.02 (0.02)	
2 × 10 ¹⁶	20	1,000	0.35 (0.62)	0.04 (0.03)	0.37 (0.63)	0.05 (0.03)	0.37 (0.64)	0.05 (0.04)	0.38 (0.65)	0.06 (0.04)	0.39 (0.65)	0.06 (0.04)	0.39 (0.66)	0.07 (0.05)	0.40 (0.66)	0.07 (0.05)	0.40 (0.66)	0.07 (0.05)	0.40 (0.67)	0.08 (0.05)
	1,000	0.43 (0.73)	0.10 (0.09)	0.45 (0.74)	0.10 (0.10)	0.46 (0.75)	0.14 (0.12)	0.47 (0.76)	0.16 (0.13)	0.48 (0.76)	0.17 (0.14)	0.49 (0.77)	0.19 (0.15)	0.49 (0.77)	0.20 (0.16)	0.49 (0.78)	0.20 (0.17)	0.50 (0.78)	0.21 (0.17)	
	900	0.27 (0.31)	0.02 (0.02)	0.28 (0.32)	0.02 (0.02)	0.28 (0.32)	0.02 (0.02)	0.28 (0.33)	0.03 (0.02)	0.29 (0.33)	0.03 (0.02)	0.29 (0.33)	0.03 (0.02)	0.29 (0.33)	0.03 (0.03)	0.29 (0.33)	0.03 (0.03)	0.29 (0.33)	0.03 (0.03)	
	1,000	0.28 (0.35)	0.04 (0.04)	0.29 (0.35)	0.05 (0.05)	0.29 (0.36)	0.06 (0.06)	0.29 (0.37)	0.06 (0.06)	0.29 (0.37)	0.07 (0.07)	0.30 (0.38)	0.07 (0.07)	0.30 (0.38)	0.08 (0.08)	0.30 (0.39)	0.08 (0.08)	0.30 (0.39)	0.08 (0.08)	
	1,100	0.31 (0.47)	0.12 (0.12)	0.32 (0.48)	0.15 (0.14)	0.33 (0.49)	0.17 (0.15)	0.34 (0.50)	0.19 (0.17)	0.34 (0.50)	0.21 (0.18)	0.34 (0.51)	0.21 (0.19)	0.35 (0.51)	0.23 (0.19)	0.35 (0.52)	0.24 (0.20)	0.36 (0.52)	0.25 (0.21)	
	900	0.28 (0.29)	0.02 (0.03)	0.28 (0.30)	0.02 (0.03)	0.28 (0.31)	0.02 (0.03)	0.28 (0.31)	0.03 (0.03)											
80	50	1,000	0.28 (0.32)	0.04 (0.05)	0.29 (0.33)	0.05 (0.05)	0.29 (0.33)	0.06 (0.06)	0.29 (0.34)	0.06 (0.06)	0.30 (0.34)	0.07 (0.07)	0.30 (0.35)	0.07 (0.07)	0.30 (0.35)	0.08 (0.08)	0.30 (0.35)	0.08 (0.08)	0.30 (0.35)	
	1,000	0.31 (0.42)	0.12 (0.13)	0.32 (0.43)	0.15 (0.15)	0.33 (0.44)	0.17 (0.16)	0.34 (0.45)	0.19 (0.18)	0.34 (0.45)	0.21 (0.19)	0.35 (0.46)	0.21 (0.20)	0.35 (0.46)	0.23 (0.21)	0.36 (0.47)	0.24 (0.22)	0.36 (0.47)	0.25 (0.23)	
	900	0.28 (0.28)	0.02 (0.03)	0.28 (0.30)	0.02 (0.03)	0.28 (0.31)	0.02 (0.03)	0.28 (0.31)	0.03 (0.03)											
	1,000	0.31 (0.42)	0.12 (0.13)	0.32 (0.43)	0.15 (0.15)	0.33 (0.44)	0.17 (0.16)	0.34 (0.45)	0.19 (0.18)	0.34 (0.45)	0.21 (0.19)	0.35 (0.46)	0.21 (0.20)	0.35 (0.52)	0.23 (0.20)	0.36 (0.52)	0.24 (0.21)	0.36 (0.47)	0.25 (0.23)	

Table B.4 Look-up table for R_s (Ω/\square) for boron ion implantation

Dose (cm ⁻²)	Energy (keV)	Temp. (°C)	Time (min)					
			15	30	45	60	75	90
20	900	5.94e2 (8.49e2)	5.85e2 (8.50e2)	5.78e2 (8.51e2)	5.72e2 (8.52e2)	5.66e2 (8.53e2)	5.61e2 (8.53e2)	5.57e2 (8.53e2)
	1,000	4.67e2 (7.72e2)	4.47e2 (7.67e2)	4.32e2 (7.63e2)	4.21e2 (7.59e2)	4.10e2 (7.55e2)	4.01e2 (7.52e2)	3.93e2 (7.48e2)
	1,100	3.39e2 (6.02e2)	3.15e2 (5.87e2)	2.98e2 (5.73e2)	2.86e2 (5.62e2)	2.77e2 (5.51e2)	2.68e2 (5.42e2)	2.62e2 (5.34e2)
50	900	3.68e2 (4.69e2)	3.67e2 (4.69e2)	3.67e2 (4.69e2)	3.67e2 (4.70e2)	3.66e2 (4.70e2)	3.66e2 (4.70e2)	3.65e2 (4.71e2)
	1,000	3.48e2 (4.66e2)	3.44e2 (4.65e2)	3.40e2 (4.64e2)	3.36e2 (4.63e2)	3.33e2 (4.61e2)	3.30e2 (4.60e2)	3.27e2 (4.59e2)
	1,100	3.03e2 (4.17e2)	2.89e2 (4.08e2)	2.79e2 (4.00e2)	2.70e2 (3.93e2)	2.63e2 (3.87e2)	2.57e2 (3.82e2)	2.52e2 (3.77e2)
80	900	3.10e2 (3.75e2)	3.10e2 (3.76e2)	3.10e2 (3.76e2)	3.11e2 (3.76e2)	3.11e2 (3.76e2)	3.11e2 (3.76e2)	3.11e2 (3.76e2)
	1,000	3.05e2 (3.78e2)	3.04e2 (3.78e2)	3.02e2 (3.77e2)	3.00e2 (3.76e2)	2.98e2 (3.76e2)	2.97e2 (3.75e2)	2.96e2 (3.74e2)
	1,100	2.81e2 (3.53e2)	2.71e2 (3.47e2)	2.64e2 (3.41e2)	2.58e2 (3.36e2)	2.52e2 (3.31e2)	2.47e2 (3.27e2)	2.43e2 (3.23e2)
20	900	9.80e1 (2.20e2)	9.21e1 (2.20e2)	8.93e1 (2.20e2)	8.79e1 (2.21e2)	8.83e1 (2.21e2)	8.81e1 (2.21e2)	8.74e1 (2.22e2)
	1,000	6.83e1 (1.30e2)	6.53e1 (1.30e2)	6.32e1 (1.29e2)	6.17e1 (1.28e2)	6.05e1 (1.27e2)	5.96e1 (1.27e2)	5.87e1 (1.26e2)
	1,100	5.50e1 (1.00e2)	5.27e1 (9.80e1)	5.11e1 (9.60e1)	5.00e1 (9.43e1)	4.90e1 (9.27e1)	4.82e1 (9.13e1)	4.75e1 (9.00e1)
900	6.61e1 (1.04e2)	6.62e1 (1.05e2)	6.64e1 (1.05e2)	6.66e1 (1.05e2)	6.68e1 (1.05e2)	6.69e1 (1.05e2)	6.70e1 (1.05e2)	6.70e1 (1.06e2)

(continued)

Table B.4 (continued)

Dose (cm ⁻²)	Energy (keV)	Temp. (°C)	Time (min)							
			15	30	45	60	75	90	105	120
2 × 10 ¹⁵	50	1,000	6.22e1 (9.71e1)	6.09e1 (9.70e1)	5.99e1 (9.68e1)	5.91e1 (9.66e1)	5.85e1 (9.63e1)	5.79e1 (9.61e1)	5.74e1 (9.58e1)	5.69e1 (9.55e1)
	1,100	5.45e1 (8.40e1)	5.26e1 (8.23e1)	5.13e1 (8.09e1)	5.02e1 (7.96e1)	4.93e1 (7.85e1)	4.85e1 (7.74e1)	4.78e1 (7.65e1)	4.72e1 (7.56e1)	4.72e1 (7.56e1)
	900	6.02e1 (8.10e1)	6.01e1 (8.11e1)	6.00e1 (8.12e1)	5.99e1 (8.13e1)	5.98e1 (8.14e1)	5.97e1 (8.15e1)	5.97e1 (8.16e1)	5.96e1 (8.17e1)	5.96e1 (8.17e1)
	80	1,000	5.66e1 (7.96e1)	5.60e1 (7.97e1)	5.54e1 (7.97e1)	5.49e1 (7.96e1)	5.45e1 (7.95e1)	5.42e1 (7.95e1)	5.39e1 (7.93e1)	5.36e1 (7.92e1)
	1,100	5.19e1 (7.37e1)	5.07e1 (7.26e1)	4.97e1 (7.17e1)	4.88e1 (7.07e1)	4.81e1 (6.99e1)	4.74e1 (6.91e1)	4.74e1 (6.84e1)	4.68e1 (6.77e1)	4.63e1 (6.77e1)
	900	6.09e1 (5.90e1)	5.74e1 (5.70e1)	5.47e1 (5.52e1)	5.25e1 (5.35e1)	5.06e1 (5.20e1)	4.89e1 (5.10e1)	4.74e1 (5.03e1)	4.60e1 (4.94e1)	4.60e1 (4.94e1)
20	1,000	2.14e1 (2.12e1)	1.81e1 (2.04e1)	1.60e1 (1.98e1)	1.45e1 (1.93e1)	1.34e1 (1.90e1)	1.25e1 (1.87e1)	1.17e1 (1.87e1)	1.13e1 (1.83e1)	1.13e1 (1.83e1)
	1,100	7.40e0 (1.24e1)	7.00e0 (1.22e1)	6.88e0 (1.20e1)	6.79e0 (1.18e1)	6.72e0 (1.17e1)	6.66e0 (1.16e1)	6.61e0 (1.15e1)	6.57e0 (1.14e1)	6.57e0 (1.14e1)
	900	3.59e1 (3.84e1)	3.49e1 (3.79e1)	3.41e1 (3.75e1)	3.34e1 (3.71e1)	3.28e1 (3.67e1)	3.22e1 (3.62e1)	3.16e1 (3.56e1)	3.11e1 (3.55e1)	3.11e1 (3.55e1)
	50	1,000	1.62e1 (1.53e1)	1.44e1 (1.40e1)	1.31e1 (1.30e1)	1.21e1 (1.22e1)	1.14e1 (1.15e1)	1.08e1 (1.09e1)	1.03e1 (1.05e1)	9.81e0 (1.02e1)
2 × 10 ¹⁶	1,100	6.87e0 (1.03e1)	6.70e0 (1.01e1)	6.59e0 (9.91e0)	6.51e0 (9.78e0)	6.44e0 (9.68e0)	6.39e0 (9.59e0)	6.34e0 (9.51e0)	6.30e0 (9.45e0)	6.22e0 (9.45e0)
	900	2.43e1 (2.64e1)	2.38e1 (2.68e1)	2.34e1 (2.69e1)	2.30e1 (2.68e1)	2.27e1 (2.67e1)	2.25e1 (2.66e1)	2.23e1 (2.65e1)	2.21e1 (2.63e1)	2.21e1 (2.63e1)
	80	1,000	1.29e1 (1.31e1)	1.17e1 (1.20e1)	1.09e1 (1.12e1)	1.03e1 (1.06e1)	9.77e0 (1.01e1)	9.32e0 (9.73e0)	8.94e0 (9.35e0)	8.64e0 (9.12e0)
1,100	6.73e0 (9.46e0)	6.59e0 (9.30e0)	6.49e0 (9.17e0)	6.41e0 (9.07e0)	6.35e0 (8.98e0)	6.30e0 (8.90e0)	6.26e0 (8.83e0)	6.22e0 (8.77e0)	6.22e0 (8.77e0)	6.22e0 (8.77e0)

Table B.5 Look-up table for R_s (Ω/\square) for phosphorus ion implantation

Dose (cm^{-2})	Energy (keV)	Temp. ($^{\circ}\text{C}$)	Time (min)						
			15	30	45	60	75	90	
20	900	3.99e2 (7.10e2)	3.88e2 (7.05e2)	3.80e2 (7.01e2)	3.75e2 (6.98e2)	3.70e2 (6.95e2)	3.66e2 (6.92e2)	3.63e2 (6.90e2)	3.59e2 (6.88e2)
	1,000	3.20e2 (8.53e2)	3.04e2 (8.41e2)	2.92e2 (8.30e2)	2.83e2 (8.20e2)	2.75e2 (8.11e2)	2.68e2 (8.02e2)	2.63e2 (7.94e2)	2.58e2 (7.86e2)
	1,100	2.24e2 (9.15e2)	2.07e2 (8.90e2)	1.95e2 (8.68e2)	1.87e2 (8.51e2)	1.80e2 (8.36e2)	1.74e2 (8.23e2)	1.70e2 (8.12e2)	1.66e2 (8.02e2)
	900	2.74e2 (3.29e2)	2.67e2 (3.28e2)	2.63e2 (3.26e2)	2.61e2 (3.25e2)	2.60e2 (3.24e2)	2.58e2 (3.24e2)	2.57e2 (3.24e2)	2.56e2 (3.22e2)
	1,000	2.40e2 (3.12e2)	2.32e2 (3.09e2)	2.26e2 (3.05e2)	2.21e2 (3.02e2)	2.16e2 (2.99e2)	2.12e2 (2.96e2)	2.08e2 (2.94e2)	2.05e2 (2.91e2)
	1,100	1.81e2 (3.16e2)	1.69e2 (3.05e2)	1.60e2 (2.96e2)	1.53e2 (2.89e2)	1.48e2 (2.83e2)	1.43e2 (2.77e2)	1.40e2 (2.72e2)	1.37e2 (2.67e2)
2 \times 10 ¹⁴	900	2.44e2 (2.76e2)	2.39e2 (2.75e2)	2.37e2 (2.74e2)	2.36e2 (2.74e2)	2.36e2 (2.73e2)	2.35e2 (2.72e2)	2.35e2 (2.72e2)	2.34e2 (2.71e2)
	1,000	2.26e2 (2.49e2)	2.22e2 (2.46e2)	2.18e2 (2.44e2)	2.14e2 (2.41e2)	2.10e2 (2.39e2)	2.07e2 (2.37e2)	2.04e2 (2.35e2)	2.02e2 (2.34e2)
	1,100	1.82e2 (2.37e2)	1.70e2 (2.29e2)	1.61e2 (2.23e2)	1.55e2 (2.17e2)	1.50e2 (2.12e2)	1.46e2 (2.08e2)	1.42e2 (2.05e2)	1.39e2 (2.01e2)
	900	5.14e1 (1.74e2)	4.95e1 (1.73e2)	4.86e1 (1.72e2)	4.81e1 (1.72e2)	4.78e1 (1.71e2)	4.75e1 (1.71e2)	4.73e1 (1.71e2)	4.71e1 (1.70e2)
	1,000	4.74e1 (2.16e2)	4.67e1 (2.14e2)	4.62e1 (2.11e2)	4.56e1 (2.09e2)	4.52e1 (2.07e2)	4.48e1 (2.05e2)	4.44e1 (2.03e2)	4.41e1 (2.01e2)
	1,100	4.20e1 (2.33e2)	4.03e1 (2.25e2)	3.91e1 (2.19e2)	3.81e1 (2.13e2)	3.73e1 (2.08e2)	3.67e1 (2.04e2)	3.61e1 (2.00e2)	3.56e1 (1.96e2)
900	4.59e1 (6.61e1)	4.28e1 (6.60e1)	4.11e1 (6.58e1)	4.00e1 (6.57e1)	3.93e1 (6.56e1)	3.88e1 (6.55e1)	3.84e1 (6.54e1)	3.81e1 (6.53e1)	(continued)
	900	4.59e1 (6.61e1)	4.28e1 (6.60e1)	4.11e1 (6.58e1)	4.00e1 (6.57e1)	3.93e1 (6.56e1)	3.88e1 (6.55e1)	3.84e1 (6.54e1)	

Table B.5 (continued)

Dose (cm ⁻²)	Energy (keV)	Temp. (°C)	Time (min)							
			15	30	45	60	75	90	105	120
2 × 10 ¹⁵	50	1,000	3.79e1 (6.63e1)	3.72e1 (6.57e1)	3.67e1 (6.51e1)	3.63e1 (6.46e1)	3.59e1 (6.41e1)	3.56e1 (6.36e1)	3.53e1 (6.32e1)	3.50e1 (6.28e1)
		1,100	3.34e1 (8.17e1)	3.22e1 (7.95e1)	3.13e1 (7.77e1)	3.06e1 (7.61e1)	3.00e1 (7.46e1)	2.95e1 (7.34e1)	2.91e1 (7.22e1)	2.87e1 (7.11e1)
		900	4.60e1 (5.34e1)	4.40e1 (5.32e1)	4.31e1 (5.31e1)	4.25e1 (5.29e1)	4.21e1 (5.28e1)	4.17e1 (5.28e1)	4.14e1 (5.27e1)	4.11e1 (5.26e1)
	80	1,000	3.91e1 (5.05e1)	3.84e1 (5.01e1)	3.79e1 (4.97e1)	3.74e1 (4.93e1)	3.70e1 (4.90e1)	3.67e1 (4.87e1)	3.64e1 (4.84e1)	3.61e1 (4.81e1)
		1,100	3.44e1 (5.94e1)	3.31e1 (5.79e1)	3.22e1 (5.67e1)	3.14e1 (5.56e1)	3.09e1 (5.47e1)	3.03e1 (5.38e1)	2.99e1 (5.31e1)	2.95e1 (5.24e1)
		900	9.97e0 (2.20e1)	9.66e0 (2.19e1)	9.39e0 (2.18e1)	9.14e0 (2.18e1)	8.91e0 (2.18e1)	8.70e0 (2.18e1)	8.51e0 (2.18e1)	8.32e0 (2.17e1)
20	50	1,000	5.95e0 (2.58e1)	5.83e0 (2.56e1)	5.75e0 (2.55e1)	5.70e0 (2.53e1)	5.65e0 (2.52e1)	5.62e0 (2.51e1)	5.59e0 (2.50e1)	5.57e0 (2.49e1)
		1,100	5.54e0 (3.22e1)	5.46e0 (3.15e1)	5.40e0 (3.10e1)	5.35e0 (3.05e1)	5.31e0 (3.01e1)	5.28e0 (2.97e1)	5.25e0 (2.94e1)	5.22e0 (2.90e1)
		900	1.62e1 (7.76e0)	1.49e1 (7.70e0)	1.40e1 (7.64e0)	1.32e1 (7.60e0)	1.26e1 (7.57e0)	1.20e1 (7.54e0)	1.15e1 (7.52e0)	1.10e1 (7.50e0)
	80	1,000	5.61e0 (6.93e0)	5.27e0 (6.87e0)	5.09e0 (6.82e0)	4.97e0 (6.78e0)	4.89e0 (6.75e0)	4.82e0 (6.71e0)	4.76e0 (6.68e0)	4.72e0 (6.67e0)
		1,100	4.62e0 (1.10e1)	4.48e0 (1.08e1)	4.40e0 (1.06e1)	4.34e0 (1.05e1)	4.28e0 (1.04e1)	4.24e0 (1.03e1)	4.21e0 (1.02e1)	4.17e0 (1.01e1)
		900	1.60e1 (6.58e0)	1.45e1 (6.55e0)	1.36e1 (6.50e0)	1.29e1 (6.46e0)	1.24e1 (6.40e0)	1.19e1 (6.35e0)	1.15e1 (6.31e0)	1.12e1 (6.28e0)
1,100	1,000	6.55e0 (6.14e0)	5.81e0 (6.06e0)	5.50e0 (6.00e0)	5.31e0 (5.96e0)	5.19e0 (5.92e0)	5.10e0 (5.89e0)	5.03e0 (5.86e0)	4.97e0 (5.83e0)	4.97e0 (5.83e0)
	1,100	4.78e0 (8.95e0)	4.64e0 (8.80e0)	4.55e0 (8.68e0)	4.48e0 (8.57e0)	4.42e0 (8.49e0)	4.38e0 (8.41e0)	4.34e0 (8.35e0)	4.31e0 (8.28e0)	4.31e0 (8.28e0)

Table B.6 Look-up table for $R_s(\Omega/\square)$ for arsenic ion implantation

Dose (cm ⁻²)	Energy (keV)	Temp. (°C)	Time (min)						
			15	30	45	60	75	90	105
20	900	1.58e3 (1.04e4)	1.53e3 (9.95e3)	1.50e3 (9.58e3)	1.47e3 (9.28e3)	1.45e3 (9.03e3)	1.43e3 (8.81e3)	1.42e3 (8.62e3)	1.40e3 (8.46e3)
	1,000	1.20e3 (9.61e3)	1.13e3 (9.06e3)	1.08e3 (8.68e3)	1.04e3 (8.41e3)	1.01e3 (8.19e3)	9.84e2 (8.02e3)	9.61e2 (7.86e3)	9.41e2 (7.72e3)
	1,100	7.83e2 (7.13e3)	7.17e2 (6.87e3)	6.74e2 (6.69e3)	6.42e2 (6.56e3)	6.18e2 (6.47e3)	5.98e2 (6.39e3)	5.81e2 (6.33e3)	5.67e2 (6.28e3)
	900	3.68e2 (1.43e3)	3.55e2 (1.39e3)	3.48e2 (1.36e3)	3.44e2 (1.33e3)	3.41e2 (1.31e3)	3.38e2 (1.29e3)	3.35e2 (1.27e3)	3.33e2 (1.26e3)
	1,000	3.05e2 (1.02e3)	2.95e2 (9.81e2)	2.88e2 (9.50e2)	2.82e2 (9.24e2)	2.77e2 (9.03e2)	2.73e2 (8.84e2)	2.69e2 (8.68e2)	2.66e2 (8.53e2)
	1,100	2.40e2 (8.29e2)	2.26e2 (7.75e2)	2.16e2 (7.35e2)	2.08e2 (7.05e2)	2.02e2 (6.81e2)	1.97e2 (6.61e2)	1.92e2 (6.44e2)	1.89e2 (6.29e2)
50	900	3.31e2 (8.71e2)	3.21e2 (8.46e2)	3.17e2 (8.29e2)	3.15e2 (8.18e2)	3.14e2 (8.10e2)	3.13e2 (8.04e2)	3.12e2 (7.98e2)	3.11e2 (7.93e2)
	1,000	2.96e2 (5.85e2)	2.89e2 (5.68e2)	2.84e2 (5.55e2)	2.79e2 (5.43e2)	2.75e2 (5.34e2)	2.72e2 (5.23e2)	2.69e2 (5.17e2)	2.66e2 (5.10e2)
	1,100	2.42e2 (4.90e2)	2.29e2 (4.62e2)	2.19e2 (4.40e2)	2.11e2 (4.24e2)	2.05e2 (4.11e2)	2.00e2 (3.99e2)	1.96e2 (3.89e2)	1.92e2 (3.81e2)
	900	2.69e2 (2.28e3)	2.54e2 (2.21e3)	2.44e2 (2.16e3)	2.37e2 (2.12e3)	2.32e2 (2.09e3)	2.29e2 (2.06e3)	2.26e2 (2.04e3)	2.23e2 (2.02e3)
	1,000	2.00e2 (2.57e3)	1.93e2 (2.42e3)	1.88e2 (2.30e3)	1.84e2 (2.22e3)	1.82e2 (2.15e3)	1.79e2 (2.09e3)	1.77e2 (2.04e3)	1.75e2 (2.00e3)
	1,100	1.90e2 (1.91e3)	1.52e2 (1.78e3)	1.46e2 (1.69e3)	1.41e2 (1.63e3)	1.38e2 (1.58e3)	1.35e2 (1.53e3)	1.32e2 (1.50e3)	1.30e2 (1.47e3)
20	900	1.03e2 (3.29e2)	9.49e1 (3.22e2)	8.92e1 (3.16e2)	8.47e1 (3.12e2)	8.10e1 (3.08e2)	7.79e1 (3.05e2)	7.54e1 (3.02e2)	7.31e1 (3.00e2)
	1,000	2.00e2 (2.57e3)	1.93e2 (2.42e3)	1.88e2 (2.30e3)	1.84e2 (2.22e3)	1.82e2 (2.15e3)	1.79e2 (2.09e3)	1.77e2 (2.04e3)	1.75e2 (2.00e3)

Table B.6 (continued)

Dose (cm ⁻²)	Energy (keV)	Temp. (°C)	Time (min)						
			15	30	45	60	75	90	105
2×10^{15}	50	1,000	5.12e1 (2.36e2)	4.80e1 (2.30e2)	4.61e1 (2.25e2)	4.47e1 (2.21e2)	4.38e1 (2.18e2)	4.20e1 (2.14e2)	4.23e1 (2.12e2)
		1,100	3.89e1 (2.19e2)	3.74e1 (2.09e2)	3.64e1 (2.01e2)	3.57e1 (1.95e2)	3.51e1 (1.89e2)	3.46e1 (1.85e2)	3.42e1 (1.81e2)
		900	8.80e1 (1.87e2)	8.24e1 (1.81e2)	7.87e1 (1.76e2)	7.59e1 (1.72e2)	7.36e1 (1.69e2)	7.15e1 (1.66e2)	6.98e1 (1.64e2)
	80	1,000	5.17e1 (1.24e2)	4.88e1 (1.21e2)	4.71e1 (1.19e2)	4.58e1 (1.17e2)	4.49e1 (1.15e2)	4.41e1 (1.14e2)	4.35e1 (1.13e2)
		1,100	4.01e1 (1.26e2)	3.85e1 (1.21e2)	3.75e1 (1.18e2)	3.68e1 (1.15e2)	3.62e1 (1.12e2)	3.57e1 (1.10e2)	3.52e1 (1.08e2)
		900	7.37e1 (4.35e2)	7.06e1 (4.24e2)	6.77e1 (4.15e2)	6.51e1 (4.08e2)	6.28e1 (4.03e2)	6.07e1 (3.98e2)	5.88e1 (3.94e2)
20	50	1,000	3.78e1 (4.47e2)	3.44e1 (4.32e2)	3.24e1 (4.19e2)	3.10e1 (4.09e2)	3.00e1 (4.01e2)	2.92e1 (3.93e2)	2.86e1 (3.89e2)
		1,100	2.53e1 (3.92e2)	2.42e1 (3.69e2)	2.35e1 (3.52e2)	2.30e1 (3.39e2)	2.26e1 (3.28e2)	2.23e1 (3.19e2)	2.20e1 (3.12e2)
		900	4.00e1 (5.45e1)	3.92e1 (5.36e1)	3.82e1 (5.24e1)	3.72e1 (5.11e1)	3.62e1 (4.98e1)	3.53e1 (4.87e1)	3.45e1 (4.77e1)
	2×10^{16}	1,000	2.18e1 (3.14e1)	1.90e1 (2.90e1)	1.71e1 (2.73e1)	1.58e1 (2.62e1)	1.48e1 (2.53e1)	1.40e1 (2.46e1)	1.33e1 (2.40e1)
		1,100	9.03e0 (2.98e1)	7.90e0 (2.89e1)	7.24e0 (2.83e1)	6.82e0 (2.78e1)	6.50e0 (2.74e1)	6.27e0 (2.70e1)	6.08e0 (2.67e1)
		900	4.43e1 (4.05e1)	4.20e1 (4.04e1)	4.02e1 (3.98e1)	3.88e1 (3.91e1)	3.75e1 (3.84e1)	3.64e1 (3.77e1)	3.54e1 (3.64e1)
80	1,000	2.17e1 (2.56e1)	1.89e1 (2.33e1)	1.71e1 (2.16e1)	1.58e1 (2.05e1)	1.48e1 (1.95e1)	1.40e1 (1.88e1)	1.33e1 (1.82e1)	1.28e1 (1.77e1)
	1,100	9.09e0 (1.85e1)	7.96e0 (1.78e1)	7.33e0 (1.73e1)	6.90e0 (1.70e1)	6.59e0 (1.67e1)	6.35e0 (1.65e1)	6.16e0 (1.63e1)	6.01e0 (1.61e1)

Table B.7 Look-up table for N_z^{eff} (μm^{-2}) for boron ion implantation

Dose (cm^{-2})	Energy (keV)	Temp. (°C)	Time (min)						
			15	30	45	60	75	90	105
20	900	8.87e5 (4.44e5)	9.05e5 (4.43e5)	9.20e5 (4.41e5)	9.33e5 (4.40e5)	9.45e5 (4.39e5)	9.56e5 (4.38e5)	9.65e5 (4.37e5)	9.74e5 (4.36e5)
	1,000	1.22e6 (4.49e5)	1.27e6 (4.47e5)	1.31e6 (4.46e5)	1.33e6 (4.44e5)	1.36e6 (4.42e5)	1.38e6 (4.41e5)	1.39e6 (4.40e5)	1.41e6 (4.39e5)
	1,100	1.53e6 (5.06e5)	1.57e6 (5.08e5)	1.60e6 (5.11e5)	1.62e6 (5.14e5)	1.63e6 (5.17e5)	1.65e6 (5.20e5)	1.66e6 (5.22e5)	1.66e6 (5.24e5)
	900	1.37e6 (9.01e5)	1.37e6 (8.99e5)	1.37e6 (8.98e5)	1.37e6 (8.96e5)	1.37e6 (8.95e5)	1.37e6 (8.93e5)	1.37e6 (8.91e5)	1.37e6 (8.90e5)
	1,000	1.48e6 (8.49e5)	1.49e6 (8.45e5)	1.50e6 (8.41e5)	1.51e6 (8.38e5)	1.52e6 (8.36e5)	1.52e6 (8.33e5)	1.53e6 (8.30e5)	1.53e6 (8.28e5)
	1,100	1.60e6 (8.26e5)	1.62e6 (8.30e5)	1.64e6 (8.31e5)	1.65e6 (8.34e5)	1.66e6 (8.35e5)	1.67e6 (8.35e5)	1.68e6 (8.41e5)	1.69e6 (8.43e5)
2 × 10 ¹⁴	900	1.58e6 (1.15e6)	1.58e6 (1.14e6)	1.57e6 (1.14e6)	1.57e6 (1.14e6)	1.57e6 (1.14e6)	1.57e6 (1.14e6)	1.57e6 (1.14e6)	1.57e6 (1.14e6)
	1,000	1.62e6 (1.08e6)	1.62e6 (1.08e6)	1.62e6 (1.07e6)	1.62e6 (1.07e6)	1.63e6 (1.07e6)	1.63e6 (1.07e6)	1.63e6 (1.06e6)	1.63e6 (1.06e6)
	1,100	1.67e6 (1.02e6)	1.68e6 (1.02e6)	1.68e6 (1.02e6)	1.69e6 (1.02e6)	1.69e6 (1.03e6)	1.70e6 (1.03e6)	1.71e6 (1.03e6)	1.71e6 (1.03e6)
	900	1.08e7 (3.39e6)	1.16e7 (3.28e6)	1.20e7 (3.36e6)	1.21e7 (3.35e6)	1.19e7 (3.33e6)	1.19e7 (3.32e6)	1.19e7 (3.31e6)	1.19e7 (3.29e6)
	1,000	1.54e7 (6.00e6)	1.59e7 (5.98e6)	1.62e7 (5.95e6)	1.64e7 (5.93e6)	1.65e7 (5.92e6)	1.67e7 (5.91e6)	1.68e7 (5.91e6)	1.69e7 (5.90e6)
	1,100	1.73e7 (6.97e6)	1.75e7 (6.98e6)	1.76e7 (6.99e6)	1.76e7 (7.00e6)	1.77e7 (7.02e6)	1.77e7 (7.04e6)	1.77e7 (7.06e6)	1.77e7 (7.07e6)
900	1.39e7 (7.38e6)	1.38e7 (7.36e6)	1.38e7 (7.33e6)	1.37e7 (7.31e6)	1.36e7 (7.29e6)	1.36e7 (7.27e6)	1.36e7 (7.25e6)	1.36e7 (7.23e6)	1.36e7 (7.23e6)

(continued)

Table B.7 (continued)

Dose (cm ⁻²)	Energy (keV)	Temp. (°C)	Time (min)						
			15	30	45	60	75	90	105
2 × 10 ¹⁵	50	1,000	1.50e7 (8.02e6)	1.53e7 (8.00e6)	1.56e7 (7.98e6)	1.58e7 (7.96e6)	1.59e7 (7.95e6)	1.61e7 (7.94e6)	1.62e7 (7.94e6)
		1,100	1.69e7 (8.65e6)	1.71e7 (8.66e6)	1.72e7 (8.67e6)	1.73e7 (8.69e6)	1.73e7 (8.70e6)	1.73e7 (8.71e6)	1.74e7 (8.72e6)
		900	1.42e7 (9.41e6)	1.43e7 (9.39e6)	1.43e7 (9.37e6)	1.43e7 (9.35e6)	1.43e7 (9.33e6)	1.43e7 (9.31e6)	1.44e7 (9.27e6)
	80	1,000	1.56e7 (9.64e6)	1.58e7 (9.60e6)	1.60e7 (9.57e6)	1.61e7 (9.55e6)	1.62e7 (9.53e6)	1.63e7 (9.52e6)	1.64e7 (9.50e6)
		1,100	1.69e7 (9.90e6)	1.71e7 (9.91e6)	1.73e7 (9.92e6)	1.73e7 (9.93e6)	1.74e7 (9.93e6)	1.75e7 (9.93e6)	1.75e7 (9.93e6)
		900	1.71e7 (1.74e7)	1.83e7 (1.81e7)	1.93e7 (1.88e7)	2.03e7 (1.94e7)	2.11e7 (2.00e7)	2.19e7 (2.04e7)	2.27e7 (2.10e7)
20	50	1,000	5.59e7 (5.45e7)	6.65e7 (5.64e7)	7.53e7 (5.78e7)	8.31e7 (5.90e7)	9.02e7 (5.98e7)	9.67e7 (6.05e7)	1.03e8 (6.10e7)
		1,100	1.70e8 (9.26e7)	1.76e8 (9.34e7)	1.77e8 (9.39e7)	1.78e8 (9.43e7)	1.78e8 (9.46e7)	1.78e8 (9.49e7)	1.79e8 (9.51e7)
		900	2.86e7 (2.63e7)	2.97e7 (2.67e7)	3.05e7 (2.70e7)	3.12e7 (2.74e7)	3.19e7 (2.78e7)	3.26e7 (2.82e7)	3.33e7 (2.85e7)
	80	1,000	7.42e7 (7.79e7)	8.44e7 (8.54e7)	9.30e7 (9.24e7)	1.00e8 (9.84e7)	1.07e8 (1.04e8)	1.13e8 (1.10e8)	1.19e8 (1.15e8)
		1,100	1.83e8 (1.14e8)	1.84e8 (1.15e8)	1.85e8 (1.16e8)	1.86e8 (1.17e8)	1.86e8 (1.17e8)	1.86e8 (1.17e8)	1.87e8 (1.18e8)
		900	4.19e7 (3.77e7)	4.30e7 (3.71e7)	4.39e7 (3.69e7)	4.47e7 (3.70e7)	4.54e7 (3.72e7)	4.59e7 (3.74e7)	4.65e7 (3.76e7)
2 × 10 ¹⁶	50	1,000	9.19e7 (8.97e7)	1.02e8 (9.86e7)	1.10e8 (1.06e8)	1.17e8 (1.14e8)	1.24e8 (1.19e8)	1.31e8 (1.24e8)	1.36e8 (1.29e8)
	1,100	1.86e8 (1.24e8)	1.87e8 (1.25e8)	1.88e8 (1.26e8)	1.88e8 (1.27e8)	1.89e8 (1.27e8)	1.89e8 (1.27e8)	1.89e8 (1.28e8)	1.89e8 (1.28e8)

Table B.8 Look-up table for N_z^{eff} (μm^{-2}) for phosphorus ion implantation

Dose (cm ⁻²)	Energy (keV)	Temp. (°C)	Time (min)					
			15	30	45	60	75	90
20	900	1.11e6 (3.01e5)	1.14e6 (3.04e5)	1.16e6 (3.07e5)	1.18e6 (3.08e5)	1.19e6 (3.09e5)	1.20e6 (3.10e5)	1.21e6 (3.11e5)
	1,000	1.25e6 (1.63e5)	1.26e6 (1.64e5)	1.26e6 (1.65e5)	1.26e6 (1.65e5)	1.26e6 (1.66e5)	1.25e6 (1.66e5)	1.26e6 (1.67e5)
	1,100	1.25e6 (1.02e5)	1.25e6 (1.02e5)	1.26e6 (1.02e5)	1.26e6 (1.03e5)	1.26e6 (1.03e5)	1.27e6 (1.03e5)	1.27e6 (1.03e5)
	900	1.40e6 (9.41e5)	1.45e6 (9.40e5)	1.48e6 (9.50e5)	1.50e6 (9.53e5)	1.51e6 (9.55e5)	1.52e6 (9.58e5)	1.53e6 (9.60e5)
	1,000	1.63e6 (7.84e5)	1.66e6 (7.8e5)	1.68e6 (7.90e5)	1.69e6 (7.91e5)	1.70e6 (7.93e5)	1.71e6 (7.95e5)	1.71e6 (7.97e5)
	1,100	1.71e6 (5.14e5)	1.71e6 (5.17e5)	1.72e6 (5.20e5)	1.72e6 (5.23e5)	1.72e6 (5.25e5)	1.73e6 (5.27e5)	1.73e6 (5.29e5)
50	900	1.42e6 (1.11e6)	1.46e6 (1.11e6)	1.48e6 (1.12e6)	1.49e6 (1.12e6)	1.49e6 (1.12e6)	1.50e6 (1.12e6)	1.50e6 (1.13e6)
	1,000	1.55e6 (1.08e6)	1.57e6 (1.09e6)	1.59e6 (1.09e6)	1.60e6 (1.09e6)	1.61e6 (1.09e6)	1.62e6 (1.10e6)	1.63e6 (1.10e6)
	1,100	1.65e6 (8.07e5)	1.66e6 (8.11e5)	1.66e6 (8.15e5)	1.66e6 (8.19e5)	1.67e6 (8.22e5)	1.67e6 (8.24e5)	1.68e6 (8.26e5)
	900	1.24e7 (2.52e6)	1.28e7 (2.53e6)	1.31e7 (2.54e6)	1.32e7 (2.55e6)	1.32e7 (2.55e6)	1.32e7 (2.56e6)	1.33e7 (2.56e6)
	1,000	1.37e7 (1.45e6)	1.38e7 (1.45e6)	1.38e7 (1.46e6)	1.39e7 (1.46e6)	1.39e7 (1.46e6)	1.39e7 (1.47e6)	1.39e7 (1.47e6)
	1,100	1.38e7 (8.44e5)	1.37e7 (8.49e5)	1.36e7 (8.54e5)	1.35e7 (8.57e5)	1.35e7 (8.60e5)	1.34e7 (8.64e5)	1.33e7 (8.67e5)
20	900	1.63e7 (8.26e6)	1.72e7 (8.28e6)	1.76e7 (8.29e6)	1.78e7 (8.30e6)	1.79e7 (8.31e6)	1.80e7 (8.32e6)	1.81e7 (8.33e6)

(continued)

Table B.8 (continued)

Dose (cm ⁻²)	Energy (keV)	Temp. (°C)	Time (min)						
			15	30	45	60	75	90	105
2×10^{15}	50	1,000	1.89e7 (8.34e6)	1.89e7 (8.34e6)	1.89e7 (8.34e6)	1.89e7 (8.33e6)	1.89e7 (8.33e6)	1.89e7 (8.32e6)	1.89e7 (8.32e6)
	1,100	1.87e7 (4.40e6)	1.85e7 (4.40e6)	1.83e7 (4.40e6)	1.82e7 (4.40e6)	1.82e7 (4.40e6)	1.82e7 (4.40e6)	1.80e7 (4.41e6)	1.80e7 (4.41e6)
	900	1.52e7 (1.07e7)	1.61e7 (1.07e7)	1.65e7 (1.08e7)	1.67e7 (1.08e7)	1.69e7 (1.08e7)	1.70e7 (1.08e7)	1.71e7 (1.08e7)	1.71e7 (1.08e7)
	80	1,000	1.79e7 (1.19e7)	1.80e7 (1.19e7)	1.81e7 (1.19e7)	1.81e7 (1.19e7)	1.82e7 (1.19e7)	1.82e7 (1.19e7)	1.82e7 (1.19e7)
	1,100	1.80e7 (7.10e6)	1.78e7 (7.10e6)	1.77e7 (7.08e6)	1.76e7 (7.08e6)	1.75e7 (7.07e6)	1.75e7 (7.07e6)	1.74e7 (7.07e6)	1.73e7 (7.06e6)
	900	6.33e7 (2.64e7)	6.49e7 (2.65e7)	6.68e7 (2.66e7)	6.88e7 (2.66e7)	7.09e7 (2.66e7)	7.30e7 (2.66e7)	7.51e7 (2.66e7)	7.73e7 (2.67e7)
20	1,000	1.32e8 (2.71e7)	1.34e8 (2.71e7)	1.35e8 (2.71e7)	1.36e8 (2.72e7)	1.37e8 (2.72e7)	1.37e8 (2.72e7)	1.38e8 (2.72e7)	1.38e8 (2.72e7)
	1,100	1.41e8 (1.71e7)	1.42e8 (1.70e7)	1.42e8 (1.69e7)	1.43e8 (1.69e7)	1.43e8 (1.69e7)	1.43e8 (1.69e7)	1.44e8 (1.69e7)	1.44e8 (1.69e7)
	900	4.87e7 (8.78e7)	5.30e7 (8.87e7)	5.64e7 (8.93e7)	5.95e7 (9.00e7)	6.25e7 (9.00e7)	6.54e7 (9.09e7)	6.82e7 (9.12e7)	7.09e7 (9.14e7)
	50	1,000	1.71e8 (1.18e8)	1.8e8 (1.19e8)	1.85e8 (1.19e8)	1.88e8 (1.19e8)	1.89e8 (1.20e8)	1.90e8 (1.20e8)	1.91e8 (1.20e8)
2×10^{16}	1,100	1.97e8 (6.90e7)	1.98e8 (6.88e7)	1.98e8 (6.86e7)	1.98e8 (6.84e7)	1.98e8 (6.84e7)	1.98e8 (6.83e7)	1.98e8 (6.83e7)	1.98e8 (6.83e7)
	900	6.27e7	6.80e7	7.15e7	7.35e7	7.50e7	7.64e7	7.81e7	7.91e7
	80	1,000	1.10e8 (1.38e8)	1.11e8 (1.39e8)	1.12e8 (1.39e8)	1.13e8 (1.40e8)	1.14e8 (1.40e8)	1.15e8 (1.41e8)	1.17e8 (1.41e8)
1,100	1,92e8 (8.81e7)	1.92e8 (8.78e7)	1.92e8 (8.76e7)	1.92e8 (8.74e7)	1.92e8 (8.72e7)	1.91e8 (8.72e7)	1.91e8 (8.70e7)	1.91e8 (8.68e7)	1.91e8 (8.67e7)

Table B.9 Look-up table for N_z^{eff} (μm^{-2}) for arsenic ion implantation

Dose (cm ⁻²)	Energy (keV)	Temp. (°C)	Time (min)					
			15	30	45	60	75	90
20	900	2.30e5 (1.38e4)	2.45e5 (1.46e4)	2.52e5 (1.52e4)	2.57e5 (1.57e4)	2.61e5 (1.62e4)	2.65e5 (1.65e4)	2.68e5 (1.69e4)
	1,000	2.90e5 (1.03e4)	2.94e5 (1.06e4)	2.96e5 (1.08e4)	2.98e5 (1.09e4)	2.99e5 (1.10e4)	3.01e5 (1.11e4)	3.02e5 (1.11e4)
	1,100	3.09e5 (1.00e4)	3.12e5 (1.00e4)	3.14e5 (1.00e4)	3.16e5 (9.98e3)	3.17e5 (9.96e3)	3.18e5 (9.93e3)	3.19e5 (9.91e3)
	900	1.36e6 (2.09e5)	1.44e6 (2.19e5)	1.48e6 (2.27e5)	1.51e6 (2.34e5)	1.53e6 (2.40e5)	1.55e6 (2.45e5)	1.56e6 (2.50e5)
	1,000	1.75e6 (2.93e5)	1.81e6 (3.05e5)	1.84e6 (3.13e5)	1.87e6 (3.19e5)	1.88e6 (3.23e5)	1.90e6 (3.27e5)	1.91e6 (3.30e5)
	1,100	1.90e6 (2.51e5)	1.89e6 (2.55e5)	1.88e6 (2.57e5)	1.87e6 (2.59e5)	1.87e6 (2.60e5)	1.87e6 (2.61e5)	1.86e6 (2.62e5)
50	900	1.30e6 (3.48e5)	1.36e6 (3.66e5)	1.39e6 (3.78e5)	1.40e6 (3.87e5)	1.41e6 (3.93e5)	1.42e6 (3.98e5)	1.43e6 (4.02e5)
	1,000	1.54e6 (5.92e5)	1.59e6 (6.13e5)	1.62e6 (6.28e5)	1.65e6 (6.40e5)	1.67e6 (6.50e5)	1.69e6 (6.59e5)	1.71e6 (6.66e5)
	1,100	1.78e6 (5.64e5)	1.80e6 (5.74e5)	1.80e6 (5.80e5)	1.81e6 (5.84e5)	1.80e6 (5.86e5)	1.81e6 (5.89e5)	1.80e6 (5.91e5)
	900	2.82e6 (1.44e5)	3.01e6 (1.50e5)	3.12e6 (1.53e5)	3.21e6 (1.55e5)	3.27e6 (1.57e5)	3.31e6 (1.58e5)	3.34e6 (1.60e5)
	1,000	3.52e6 (8.07e4)	3.55e6 (8.37e4)	3.55e6 (8.57e4)	3.54e6 (8.70e4)	3.54e6 (8.80e4)	3.53e6 (8.87e4)	3.52e6 (8.93e4)
	1,100	3.41e6 (6.74e4)	3.37e6 (6.82e4)	3.35e6 (6.87e4)	3.33e6 (6.90e4)	3.32e6 (6.94e4)	3.30e6 (6.96e4)	3.29e6 (6.97e4)
20	900	8.69e6 (2.13e6)	9.60e6 (2.18e6)	1.04e7 (2.21e6)	1.10e7 (2.24e6)	1.16e7 (2.26e6)	1.22e7 (2.27e6)	1.26e7 (2.29e6)
	1,000	3.52e6 (8.07e4)	3.55e6 (8.37e4)	3.55e6 (8.57e4)	3.54e6 (8.70e4)	3.54e6 (8.80e4)	3.53e6 (8.87e4)	3.51e6 (8.93e4)

(continued)

Table B.9 (continued)

Dose (cm ⁻²)	Energy (keV)	Temp. (°C)	Time (min)							
			15	30	45	60	75	90	105	120
2 × 10 ¹⁵	50	1,000	1.87e7 (2.67e6)	1.96e7 (2.70e6)	2.01e7 (2.71e6)	2.04e7 (2.72e6)	2.06e7 (2.72e6)	2.07e7 (2.72e6)	2.08e7 (2.72e6)	2.09e7 (2.72e6)
	1,100	2.11e7	2.10e7 (2.01e6)	2.10e7 (2.01e6)	2.09e7 (2.01e6)	2.09e7 (2.01e6)	2.09e7 (2.00e6)	2.08e7 (2.00e6)	2.08e7 (2.00e6)	2.07e7 (2.00e6)
	900	9.54e6	1.04e7 (4.01e6)	1.11e7 (4.15e6)	1.16e7 (4.26e6)	1.20e7 (4.36e6)	1.25e7 (4.45e6)	1.28e7 (4.52e6)	1.28e7 (4.58e6)	1.32e7 (4.63e6)
	80	1,000	1.76e7 (5.85e6)	1.85e7 (5.93e6)	1.90e7 (5.97e6)	1.93e7 (6.00e6)	1.95e7 (6.03e6)	1.97e7 (6.05e6)	1.98e7 (6.06e6)	1.99e7 (6.06e6)
	1,100	2.02e7 (4.38e6)	2.02e7 (4.36e6)	2.02e7 (4.35e6)	2.01e7 (4.33e6)	2.01e7 (4.32e6)	2.01e7 (4.30e6)	2.00e7 (4.30e6)	1.99e7 (4.28e6)	1.99e7 (4.28e6)
	900	1.53e7	1.58e7 (1.73e6)	1.64e7 (1.75e6)	1.70e7 (1.76e6)	1.76e7 (1.77e6)	1.82e7 (1.77e6)	1.87e7 (1.78e6)	1.92e7 (1.78e6)	1.92e7 (1.78e6)
20	1,000	2.83e7 (1.21e6)	3.02e7 (1.21e6)	3.14e7 (1.21e6)	3.22e7 (1.20e6)	3.28e7 (1.20e6)	3.32e7 (1.20e6)	3.37e7 (1.20e6)	3.40e7 (1.20e6)	3.40e7 (1.20e6)
	1,100	3.55e7 (8.46e5)	3.58e7 (8.50e5)	3.59e7 (8.51e5)	3.60e7 (8.53e5)	3.60e7 (8.54e5)	3.60e7 (8.55e5)	3.59e7 (8.55e5)	3.59e7 (8.55e5)	3.59e7 (8.55e5)
	900	3.27e7 (2.18e7)	3.26e7 (2.16e7)	3.32e7 (2.20e7)	3.41e7 (2.24e7)	3.50e7 (2.29e7)	3.59e7 (2.34e7)	3.68e7 (2.38e7)	3.68e7 (2.38e7)	3.76e7 (2.43e7)
	1,000	6.14e7 (3.48e7)	7.00e7 (3.68e7)	7.69e7 (3.84e7)	8.24e7 (3.94e7)	8.73e7 (4.03e7)	9.16e7 (4.09e7)	9.51e7 (4.15e7)	9.86e7 (4.19e7)	9.79e7 (4.19e7)
	1,100	1.34e8 (2.81e7)	1.47e8 (2.81e7)	1.57e8 (2.81e7)	1.63e8 (2.81e7)	1.68e8 (2.81e7)	1.72e8 (2.80e7)	1.76e8 (2.80e7)	1.79e8 (2.80e7)	1.79e8 (2.79e7)
	900	2.61e7	2.79e7	2.93e7	3.07e7	3.19e7	3.30e7	3.40e7	3.50e7	3.50e7
80	1,000	3.03e7 (4.51e7)	2.95e7 (4.90e7)	2.96e7 (5.20e7)	3.00e7 (5.44e7)	3.00e7 (5.63e7)	3.11e7 (5.79e7)	3.16e7 (5.93e7)	3.22e7 (6.04e7)	3.22e7 (6.04e7)
	1,100	1.32e8 (5.00e7)	1.46e8 (5.06e7)	1.54e8 (5.09e7)	1.61e8 (5.12e7)	1.66e8 (5.13e7)	1.70e8 (5.14e7)	1.73e8 (5.14e7)	1.75e8 (5.15e7)	1.75e8 (5.15e7)

Table B.10 Look-up table for t_f (μm) for boron ion implantation

Dose (cm^{-2})	Energy (keV)	Temp. ($^{\circ}\text{C}$)	Time (min)						
			15	30	45	60	75	90	105
2×10^{14}	900	0.58(0.74)	0.59(0.74)	0.59(0.74)	0.60(0.75)	0.60(0.75)	0.61(0.75)	0.61(0.75)	0.61(0.75)
	1,000	0.66(0.94)	0.70(0.96)	0.74(0.99)	0.77(1.01)	0.80(1.03)	0.83(1.05)	0.86(1.07)	0.89(1.09)
	1,100	1.10(1.57)	1.29(1.69)	1.46(1.80)	1.60(1.90)	1.73(2.00)	1.86(2.08)	1.97(2.17)	2.07(2.25)
	900	0.99(1.08)	0.99(1.08)	1.00(1.08)	1.00(1.08)	1.00(1.09)	1.00(1.09)	1.00(1.09)	1.01(1.09)
	1,000	1.01(1.22)	1.04(1.24)	1.06(1.26)	1.09(1.28)	1.12(1.30)	1.14(1.31)	1.16(1.33)	1.19(1.35)
	1,100	1.37(1.78)	1.53(1.89)	1.67(2.00)	1.80(2.10)	1.92(2.19)	2.03(2.28)	2.13(2.37)	2.23(2.45)
80	900	1.21(1.28)	1.21(1.29)	1.21(1.29)	1.22(1.29)	1.22(1.29)	1.22(1.29)	1.22(1.29)	1.22(1.29)
	1,000	1.20(1.39)	1.23(1.41)	1.25(1.43)	1.27(1.45)	1.30(1.46)	1.32(1.48)	1.34(1.50)	1.36(1.51)
	1,100	1.52(1.92)	1.68(2.03)	1.82(2.13)	1.94(2.23)	2.06(2.32)	2.16(2.41)	2.26(2.49)	2.36(2.57)
	900	0.61(0.75)	0.62(0.75)	0.64(0.76)	0.66(0.76)	0.68(0.76)	0.70(0.76)	0.71(0.77)	0.73(0.77)
	1,000	0.80(1.09)	0.88(1.12)	0.96(1.16)	1.02(1.19)	1.08(1.22)	1.14(1.25)	1.19(1.28)	1.24(1.31)
	1,100	1.45(1.92)	1.70(2.07)	1.92(2.21)	2.10(2.34)	2.27(2.46)	2.42(2.58)	2.56(2.68)	2.69(2.79)
2×10^{15}	900	1.46(1.51)	1.46(1.51)	1.47(1.51)	1.47(1.51)	1.48(1.52)	1.48(1.52)	1.49(1.52)	1.49(1.52)
	1,000	1.45(1.58)	1.49(1.60)	1.52(1.62)	1.55(1.64)	1.58(1.66)	1.60(1.67)	1.63(1.69)	1.65(1.71)
	1,100	1.77(2.13)	1.94(2.26)	2.10(2.39)	2.24(2.51)	2.39(2.62)	2.52(2.73)	2.65(2.84)	2.77(2.94)
	900	1.92(1.95)	1.92(1.95)	1.92(1.95)	1.93(1.95)	1.93(1.95)	1.93(1.95)	1.94(1.95)	1.94(1.96)
	1,000	1.84(1.95)	1.87(1.96)	1.89(1.98)	1.92(2.00)	1.94(2.01)	1.96(2.03)	1.99(2.05)	2.01(2.06)
	1,100	2.10(2.41)	2.25(2.53)	2.39(2.64)	2.52(2.75)	2.63(2.86)	2.75(2.96)	2.86(3.05)	2.96(3.14)
20	900	1.06(1.16)	1.09(1.17)	1.11(1.19)	1.13(1.21)	1.14(1.22)	1.16(1.24)	1.18(1.25)	1.20(1.27)
	1,000	1.34(1.59)	1.52(1.69)	1.70(1.77)	1.86(1.85)	2.01(1.92)	2.15(1.98)	2.28(2.04)	2.40(2.10)
	1,100	2.66(2.67)	3.05(2.92)	3.35(3.14)	3.61(3.34)	3.84(3.52)	4.06(3.68)	4.25(3.84)	4.43(3.98)
	900	1.83(1.86)	1.84(1.86)	1.85(1.87)	1.87(1.88)	1.88(1.88)	1.89(1.89)	1.90(1.90)	1.92(1.90)
	1,000	1.94(2.04)	2.03(2.13)	2.11(2.21)	2.20(2.30)	2.28(2.39)	2.37(2.49)	2.47(2.60)	2.58(2.69)
	1,100	2.78(2.85)	3.14(3.11)	3.44(3.34)	3.70(3.54)	3.94(3.73)	4.15(3.90)	4.35(4.06)	4.53(4.21)
2×10^{16}	900	2.77(2.76)	2.78(2.76)	2.79(2.77)	2.80(2.77)	2.81(2.77)	2.82(2.78)	2.83(2.78)	2.83(2.78)
	1,000	2.68(2.72)	2.76(2.79)	2.83(2.86)	2.89(2.92)	2.96(2.98)	3.02(3.04)	3.08(3.10)	3.14(3.15)
	1,100	3.10(3.14)	3.33(3.32)	3.57(3.52)	3.80(3.70)	4.03(3.88)	4.23(4.05)	4.42(4.20)	4.60(4.36)

Table B.11 Look-up table for t_f (μm) for phosphorus ion implantation

Dose (cm^{-2})	Energy (keV)	Temp. ($^{\circ}\text{C}$)	Time (min)						
			15	30	45	60	75	90	105
2×10^{14}	900	0.28(0.45)	0.29(0.45)	0.29(0.45)	0.30(0.46)	0.30(0.46)	0.30(0.46)	0.30(0.46)	0.31(0.46)
	1,000	0.38(0.67)	0.43(0.68)	0.47(0.70)	0.51(0.72)	0.55(0.73)	0.59(0.75)	0.62(0.76)	0.65(0.78)
	1,100	0.93(1.17)	1.12(1.26)	1.29(1.33)	1.43(1.41)	1.55(1.48)	1.67(1.54)	1.77(1.61)	1.88(1.67)
	900	0.50(0.58)	0.51(0.58)	0.51(0.58)	0.51(0.58)	0.51(0.59)	0.52(0.59)	0.52(0.59)	0.52(0.59)
	1,000	0.55(0.82)	0.58(0.84)	0.60(0.86)	0.63(0.88)	0.66(0.90)	0.68(0.91)	0.71(0.93)	0.73(0.95)
	1,100	0.99(1.42)	1.18(1.52)	1.34(1.62)	1.48(1.71)	1.61(1.79)	1.73(1.87)	1.84(1.95)	1.94(2.02)
80	900	0.66(0.71)	0.66(0.71)	0.66(0.71)	0.67(0.71)	0.67(0.71)	0.67(0.71)	0.67(0.72)	0.67(0.72)
	1,000	0.69(0.91)	0.71(0.93)	0.73(0.94)	0.75(0.96)	0.77(0.98)	0.79(0.99)	0.81(1.01)	0.83(1.02)
	1,100	1.05(1.52)	1.22(1.62)	1.38(1.72)	1.51(1.81)	1.64(1.90)	1.75(1.98)	1.86(2.06)	1.96(2.14)
	900	0.88(0.58)	0.90(0.59)	0.92(0.59)	0.93(0.59)	0.94(0.59)	0.95(0.60)	0.96(0.60)	0.96(0.60)
	1,000	0.84(0.82)	0.87(0.84)	0.90(0.86)	0.93(0.88)	0.96(0.90)	0.99(0.92)	1.02(0.94)	1.04(0.96)
	1,100	1.27(1.48)	1.49(1.59)	1.68(1.69)	1.84(1.78)	1.99(1.87)	2.13(1.96)	2.25(2.04)	2.37(2.12)
20	900	0.69(0.96)	0.73(0.97)	0.77(0.97)	0.81(0.97)	0.84(0.97)	0.86(0.98)	0.88(0.98)	0.90(0.98)
	1,000	0.76(0.91)	0.80(0.94)	0.85(0.97)	0.89(0.99)	0.93(1.02)	0.97(1.04)	1.00(1.07)	1.04(1.09)
	1,100	1.29(1.73)	1.52(1.85)	1.72(1.97)	1.90(2.08)	2.05(2.18)	2.19(2.28)	2.32(2.37)	2.44(2.46)
	900	0.82(1.07)	0.82(1.08)	0.83(1.08)	0.84(1.09)	0.84(1.09)	0.85(1.09)	0.86(1.09)	0.87(1.10)
	1,000	0.87(0.98)	0.89(1.01)	0.91(1.03)	0.94(1.06)	0.97(1.08)	0.99(1.11)	1.02(1.13)	1.05(1.16)
	1,100	1.29(1.80)	1.52(1.93)	1.72(2.05)	1.89(2.16)	2.04(2.27)	2.18(2.37)	2.31(2.47)	2.43(2.56)
2×10^{15}	900	4.98(2.53)	4.98(2.54)	4.98(2.54)	4.98(2.55)	4.98(2.55)	4.98(2.56)	4.98(2.56)	4.98(2.56)
	1,000	4.61(1.19)	4.59(1.22)	4.60(1.24)	4.61(1.27)	4.63(1.30)	4.65(1.32)	4.66(1.35)	4.68(1.37)
	1,100	4.15(1.89)	4.24(2.04)	4.32(2.17)	4.40(2.30)	4.49(2.42)	4.58(2.54)	4.69(2.64)	4.85(2.75)
	900	2.09(4.23)	2.20(4.22)	2.31(4.24)	2.42(4.22)	2.52(4.19)	2.62(4.19)	2.71(4.19)	2.80(4.20)
	1,000	2.95(2.94)	2.93(2.95)	2.94(2.97)	2.97(2.99)	2.99(3.00)	3.01(3.01)	3.03(3.03)	3.05(3.04)
	1,100	2.59(2.03)	2.74(2.23)	2.90(2.41)	3.08(2.58)	3.24(2.73)	3.41(2.88)	3.56(3.01)	3.71(3.13)
20	900	1.27(4.19)	1.42(4.19)	1.56(4.21)	1.69(4.21)	1.81(4.22)	1.93(4.22)	2.03(4.20)	2.13(4.19)
	1,000	2.21(3.09)	2.31(3.11)	2.35(3.12)	2.39(3.14)	2.43(3.15)	2.46(3.17)	2.49(3.18)	2.52(3.20)
	1,100	2.21(2.09)	2.47(2.31)	2.72(2.50)	2.94(2.67)	3.13(2.83)	3.31(2.98)	3.48(3.12)	3.64(3.25)

Table B.12 Look-up table for t_f (μm) for arsenic ion implantation

Dose (cm^{-2})	Energy (keV)	Temp. ($^{\circ}\text{C}$)	Time (min)						
			15	30	45	60	75	90	105
2×10^{14}	900	0.15(0.10)	0.16(0.10)	0.16(0.10)	0.16(0.10)	0.16(0.10)	0.16(0.10)	0.16(0.10)	0.16(0.10)
	1,000	0.16(0.12)	0.17(0.13)	0.18(0.14)	0.19(0.14)	0.20(0.15)	0.21(0.15)	0.22(0.16)	0.23(0.17)
	1,100	0.34(0.27)	0.41(0.30)	0.46(0.34)	0.51(0.37)	0.56(0.39)	0.60(0.42)	0.64(0.44)	0.67(0.46)
	900	0.35(0.25)	0.35(0.25)	0.35(0.25)	0.35(0.25)	0.35(0.25)	0.35(0.25)	0.35(0.25)	0.35(0.25)
	1,000	0.35(0.29)	0.35(0.29)	0.36(0.29)	0.36(0.30)	0.36(0.30)	0.36(0.30)	0.37(0.30)	0.37(0.31)
	1,100	0.43(0.40)	0.51(0.45)	0.57(0.50)	0.63(0.55)	0.68(0.58)	0.73(0.62)	0.77(0.65)	0.81(0.69)
80	900	0.51(0.41)	0.51(0.41)	0.51(0.41)	0.51(0.41)	0.51(0.41)	0.51(0.41)	0.51(0.41)	0.51(0.41)
	1,000	0.52(0.44)	0.52(0.44)	0.52(0.45)	0.52(0.45)	0.52(0.45)	0.52(0.45)	0.53(0.45)	0.53(0.45)
	1,100	0.55(0.51)	0.58(0.54)	0.62(0.58)	0.66(0.62)	0.71(0.66)	0.75(0.69)	0.79(0.73)	0.83(0.76)
	900	0.19(0.11)	0.19(0.11)	0.19(0.11)	0.19(0.11)	0.19(0.11)	0.19(0.11)	0.19(0.11)	0.19(0.11)
	1,000	0.20(0.15)	0.22(0.16)	0.24(0.17)	0.26(0.18)	0.27(0.18)	0.29(0.19)	0.30(0.20)	0.31(0.21)
	1,100	0.44(0.33)	0.53(0.38)	0.60(0.43)	0.67(0.47)	0.72(0.50)	0.77(0.53)	0.82(0.56)	0.86(0.59)
2×10^{15}	900	0.39(0.23)	0.39(0.23)	0.39(0.23)	0.39(0.23)	0.39(0.23)	0.39(0.23)	0.39(0.23)	0.39(0.23)
	1,000	0.39(0.31)	0.40(0.31)	0.40(0.31)	0.40(0.31)	0.41(0.32)	0.42(0.32)	0.44(0.32)	0.45(0.33)
	1,100	0.61(0.49)	0.72(0.56)	0.81(0.62)	0.89(0.67)	0.96(0.72)	1.02(0.76)	1.08(0.80)	1.13(0.84)
	900	0.55(0.38)	0.55(0.38)	0.55(0.38)	0.55(0.38)	0.55(0.38)	0.55(0.38)	0.55(0.38)	0.55(0.38)
	1,000	0.55(0.44)	0.55(0.44)	0.55(0.45)	0.55(0.45)	0.55(0.45)	0.56(0.45)	0.56(0.45)	0.56(0.46)
	1,100	0.63(0.57)	0.73(0.63)	0.82(0.69)	0.90(0.75)	0.96(0.80)	1.02(0.85)	1.08(0.89)	1.13(0.93)
20	900	0.20(0.08)	0.20(0.09)	0.20(0.09)	0.20(0.09)	0.20(0.10)	0.20(0.10)	0.20(0.10)	0.21(0.11)
	1,000	0.29(0.17)	0.33(0.19)	0.37(0.20)	0.40(0.22)	0.43(0.23)	0.45(0.24)	0.48(0.25)	0.50(0.26)
	1,100	0.67(0.43)	0.80(0.50)	0.90(0.55)	0.99(0.60)	1.07(0.65)	1.13(0.69)	1.20(0.73)	1.26(0.77)
	900	0.46(0.29)	0.46(0.29)	0.46(0.29)	0.46(0.29)	0.46(0.29)	0.46(0.29)	0.46(0.29)	0.46(0.29)
50	1,000	0.47(0.35)	0.47(0.38)	0.48(0.41)	0.51(0.44)	0.55(0.48)	0.59(0.50)	0.63(0.53)	0.66(0.55)
	1,100	0.92(0.74)	1.11(0.84)	1.27(0.93)	1.40(1.00)	1.51(1.07)	1.61(1.13)	1.71(1.18)	1.79(1.24)
	900	0.65(0.48)	0.65(0.48)	0.65(0.48)	0.65(0.48)	0.65(0.48)	0.65(0.48)	0.65(0.48)	0.65(0.48)
80	1,000	0.65(0.53)	0.66(0.53)	0.66(0.54)	0.66(0.55)	0.66(0.57)	0.67(0.59)	0.68(0.61)	0.69(0.63)
	1,100	0.94(0.85)	1.12(0.96)	1.26(1.05)	1.39(1.14)	1.51(1.21)	1.61(1.28)	1.70(1.34)	1.79(1.40)

Appendix C

Code

The numerical optimization and modeling code relies upon a combination of MATLAB® and Python classes. All of the code is open source and can be found online at <http://microsystems.stanford.edu/piezod> or <http://github.com/jcdoll/PiezoD>. Although we considered reproducing it here, at the time of writing it would add roughly 100 pages to the length of this book without much practical benefit. Instead, in this appendix we want to simply highlight the overall structure of the code and ensure that it is perfectly clear where it can be accessed.

C.1 Ion Implantation Lookup Table Generation

Ion implantation and annealing is a complex process. We precomputed lookup tables using TSUPREM-4™ (see Appendix B) in order to speed up the numerical design optimization of ion implanted piezoresistors by several orders of magnitude. The lookup tables were generated by a set of MATLAB® and Python scripts that automatically run the TSUPREM-4™ simulations and compile the results.

A control script (`simulationControl.py`) manages the simulation and substitutes appropriate parameter values into a template (`simulation.template`) before running the simulation from the command line. Performing all 1296 simulations (3 dopants, 3 energies, 3 doses, 3 temperatures, 8 times, and 2 anneal conditions) takes about 12 h on the Stanford computing cluster where TSUPREM-4™ is installed. The simulations generated 2,592 output text files containing the dopant concentration before and after the anneal.

These text files are postprocessed (`postProcessTables.m`) using several helper files (`calculateProfileProperties.m`, `richterModel.m` and `resistivity.m`) in order to generate a .mat file that can be used for design optimization. The output .mat file, including the raw post-anneal dopant concentration profiles, is about 4 MB in size. The lookup tables are used during numerical design optimization to calculate β_1^* , β_2^* , R_s , N_z^{eff} , t_j and $n(z)$ (the complete concentration profile) through linear interpolation.

C.2 Optimization and Modeling Code

Numerical modeling and optimization is used heavily throughout this book. The code has been open source since its original development in 2009. The code is written in object oriented MATLAB® and requires at least MATLAB® R2008a with the optimization toolbox. Cantilevers based upon silicon piezoresistors (diffusion, epitaxy, ion implantation and polysilicon), metal strain gauges and piezoelectric films are supported in both end loaded and surface stress loaded configurations. The thermal and multilayered beam models are integrated into the code for both sensor and actuator design.

The code consists of an abstract base class (`cantilever.m`) that is inherited by several cantilever subclasses (e.g. `cantileverDiffusion.m`). The user instantiates a subclass based upon the type of cantilever that they are designing. Each subclass has several additional instantiation parameters on top of the base class parameters (e.g. diffusion temperature and time), implements anything that is specific to the particular cantilever type (e.g. calculating the dopant concentration profile) and overrides several of the optimization functions so that everything fits together nicely. The cantilever base class includes all of the thermal modeling, noise and sensitivity functions and can model the effect of an actuator at the base of the sensor (i.e. the force probes presented in [2, 97, 98]). The code supports the optimization of the actuator, but the actuator design is typically straightforward enough that it is simpler to just test several possible actuator designs.

The optimization is a straightforward application of `fmincon` within MATLAB®. The code supports arbitrary optimization constraints that are passed in as parameters to the optimization routine (see `sampleCode.m`) and additional nonlinear constraints can be added to the cantilever base class. Depending on the speed of your computer and the degree of complexity in the optimization (which can be controlled using flags, e.g. whether to account for variation in the thermal conductivity with temperature) an optimized cantilever design can be generated in as little as 30s.

Subclasses of `cantilever.m` include diffused (`cantileverDiffusion.m`), epitaxial (`cantileverEpitaxy.m`) and ion implanted (`cantileverImplantation.m`) single crystal silicon piezoresistive cantilevers. Separate classes (`cantileverPoly.m` and `cantileverPiezoelectric.m`) have been written for the modeling and design optimization of cantilevers based upon polysilicon, metal thin films and piezoelectric films.

References

1. A.A. Barlian, W.-T. Park, J.R. Mallon, A.J. Rastegar, B.L. Pruitt, Review: Semiconductor piezoresistance for microsystems. *Proc. IEEE* **97**(3), 513–552 (2009)
2. J.C. Doll, Advances in high bandwidth nanomechanical force sensors with integrated actuation. Ph.D. dissertation, Stanford University, 2012
3. J.D. Plummer, M.D. Deal, P.B. Griffin, *Silicon VLSI Technology Fundamentals, Practice, and Modeling* (Prentice Hall, New Jersey, 2000)
4. R. Jaeger, *Introduction to Microelectronic Fabrication* (Prentice Hall, New Jersey, 2002)
5. R.F. Pierret, *Semiconductor Device Fundamentals* (Addison Wesley, Reading, 1996)
6. S. Senturia, *Microsystem Design* (Springer, New York, 2000)
7. H.A. Nielsen, *From Locomotives to Strain Gages* (Vantage Press, New York, 1985)
8. C.S. Smith, Piezoresistance effect in germanium and silicon. *Phys. Rev.* **94**(1), 42–49 (1954)
9. J. Bryzek, MEMS: a closer look - part 2: the MEMS industry in Silicon Valley and its impact on sensor technology. *Sensors* **13**(7), 4–8 (1996)
10. J.W. Knutti, Finding markets for microstructures, in *Micromachining and Microfabrication Process Technology IV*, pp. 17–23 (1998)
11. T. Akiyama, S. Gautsch, N.F. de Rooij, U. Staufer, P. Niedermann, L. Howald, D. Müller, A. Tonin, H.R. Hidber, W.T. Pike, M.H. Hecht, Atomic force microscope for planetary applications. *Sens. Actuators A* **91**(3), 321–325 (2001)
12. W. Thomson, On the electro-dynamic qualities of metals: Effects of magnetization on the electric conductivity of nickel and of iron. *Proc. R. Soc. Lond.* **8**, 546–550 (1856)
13. H. Tomlinson, The influence of stress and strain on the action of physical forces. *Philos. Trans. R. Soc. Lond.* **174**, 1–172 (1883)
14. H. Tomlinson, On the increase in resistance to the passage of an electric current produced on wires by stretching. *Proc. R. Soc. Lond.* **25**, 451–453 (1876)
15. P.W. Bridgman, Some properties of single metal crystals. *Proc. Nat. Acad. Sci.* **10**, 411–415 (1924)
16. P.W. Bridgman, General survey of the effects of pressure on the properties of matter. *Proc. Phys. Soc.* **41**, 341–360 (1928)
17. P.W. Bridgman, The effect of homogeneous mechanical stress on the electrical resistance of crystals. *Phys. Rev.* **42**(6), 858–863 (1932)
18. W.E. Williams, On the influence of stress on the electrical conductivity of metals. *Phil. Mag. Ser. 6* **13**(77), 635–643 (1907)
19. H. Rolnick, Tension coefficient of resistance of metals. *Phys. Rev.* **36**(3), 506–512 (1930)
20. M. Allen, The effect of tension on the electrical resistance of single bismuth crystals. *Phys. Rev.* **42**(6), 848–857 (1932)

21. M. Allen, The effect of tension on the electrical resistance of single antimony crystals. *Phys. Rev.* **43**(7), 569–576 (1933)
22. M. Allen, The tension coefficients of resistance of the hexagonal crystals zinc and cadmium. *Phys. Rev.* **49**(3), 248–253 (1936)
23. M. Allen, The effect of tension on the electrical resistance of single tetragonal tin crystals. *Phys. Rev.* **52**(12), 1246–1249 (1937)
24. J.W. Cookson, Theory of the piezo-resistive effect. *Phys. Rev.* **47**(2), 194–195 (1935)
25. F. Pockels, *Pyro- und piezoelektrizitat Elektrizitat und Magnetismus I (Handbuch der Physik vol 4)* (J A Barth, Leipzig, 1905)
26. M. Trainer, Kelvin and piezoelectricity. *Eur. J. Phys.* **24**(5), 535–542 (2003)
27. J. Curie, P. Curie, Developpement, par pression de l'electricite polaire dans les cristaux hemiedres a faces inclinees. *C. R. Acad. Sci.* **91**, 294–295 (1880)
28. W. Voigt, *Lehrbuch der kristallphysik* (B. G. Teubner, Leipzig, 1910)
29. W. Thomson, Elements of a mathematical theory of elasticity. *Proc. R. Soc. Lond.* **8**, 85–87 (1856)
30. L. Kelvin, Note by Lord Kelvin on electric molecules for the explanation of the piezo-electric and pyro-electric properties of crystals. *Phil. Mag. Ser.* **5**, **36**(221), 384 (1893)
31. L. Kelvin, On the theory of pyro-electricity and piezo-electricity of crystals. *Phil. Mag. Ser.* **5**, **36**(222), 453–459 (1893)
32. L. Kelvin, On the piezo-electric property of quartz. *Phil. Mag. Ser.* **5**, **36**(221), 331–342 (1893)
33. D.S. Clark, G. Datwyler, Stress-strain relations under impact loading. *Proc. Am. Soc. Test. Mater.* **38**, 98 (1938)
34. P.K. Stein, 1936—a banner year for strain gages and experimental stress analysis—an historical perspective. *Exp. Tech.* **30**(1), 23–41 (2006)
35. E.E. Simmons, Method and apparatus for making strain gauges. U.S. Patent 2,344,647, 21, 1944
36. E.E. Simmons, Strain gauge. U.S. Patent 2,350,972, 6, 1946
37. J. Bardeen, W. Shockley, Deformation potentials and mobilities in non-polar crystals. *Phys. Rev.* **80**(1), 72–80 (1950)
38. O. Paul, J. Gaspar, P. Ruther, Advanced silicon microstructures, sensors, and systems. *IEEE Trans. Electr. Electron. Eng.* **2**(3), 199–215 (2007)
39. K.D. Wise, Integrated sensors, MEMS, and Microsystems: Reflections on a fantastic voyage. *Sens. Actuators A* **136**(1), 39–50 (2007)
40. W.P. Mason, R.N. Thurston, Use of piezoresistive materials in the measurement of displacement, force, and torque. *J. Acoust. Soc. Am.* **29**(10), 1096–1101 (1957)
41. J.C. Sanchez, W.V. Wright, Recent developments in flexible silicon strain gages, in *Semiconductor and Conventional Strain Gages*, ed. by M. Dean (Academic Press, New York, 1962), pp. 307–345
42. G.R. Higson, Recent advances in strain gauges. *J. Sci. Instrum.* **41**(7), 405–414 (1964)
43. D. Bittle, J. Suhling, R. Beaty, R. Jaeger, R.W. Johnson, Piezoresistive stress sensors for structural analysis of electronic packages. *J. Electron. Packag.* **113**, 203–215 (1991)
44. M. Mayer, J. Schwizer, O. Paul, D. Bolliger, and H. Baltes, In situ ultrasonic stress measurements during ball bonding using integrated piezoresistive microsensors, in *Proceedings of ASME International Intersociety Electronic and Photonic Packaging Conference*, pp. 973–978, 1999
45. J. Schwizer, M. Mayer, D. Bolliger, O. Paul, H. Baltes, Thermosonic ball bonding: Friction model based on integrated microsensor measurements, in *Proceedings of IEEE/CPMT International Electronics Manufacturing Technology, Symposium*, pp. 108–114, 1999
46. J. Richter, A. Hyldgard, K. Birkelund, O. Hansen, and E. V. Thomsen, Realtime 3D stress measurement in curing epoxy packaging, in *Proceedings of Transducers*, pp. 2083–2086, 2007
47. J. Richter, A. Hyldgard, K. Birkelund, M. B. Arnoldus, O. Hansen, and E. V. Thomsen, CMOS-integrated silicon 3D force sensor system for micro component coordinate measurement machines, in *Proceedings of IEEE MEMS*, pp. 69–72, 2007

48. P. Gieschke, J. Richter, J. Joos, P. Ruther, and O. Paul, Four-degree-of-freedom solid state MEMS joystick, in *Proceedings of IEEE MEMS*, pp. 86–89, 2008
49. P. Ruther, M. Wandt, Innovativer miniaturisierter 3D-kraftsensor für koordinatenmesssysteme von mikrokomponenten. *Sens. Magazin* 30–33 (2008)
50. M. Esashi, S. Sugiyama, K. Ikeda, Y.L. Wang, H. Miyashita, Vacuum-sealed silicon micro-machined pressure sensors. *Proc. IEEE* **86**(8), 1627–1639 (1998)
51. F. P. Burns, Piezoresistive semiconductor microphone. U.S. Patent 2,905,771, 22, 1959
52. J.A. Hoerni, Planar silicon diodes and transistors. *IEEE Trans. Electron Devices* **8**(2), 178 (1961)
53. W.G. Pfann, R.N. Thurston, Semiconducting stress transducers utilizing transverse and shear piezoresistance effects. *J. Appl. Phys.* **32**(10), 2008–2019 (1961)
54. O.N. Tufte, D. Long, P.W. Chapman, Silicon diffused-element piezoresistive diaphragms. *J. Appl. Phys.* **33**(11), 3322–3327 (1962)
55. E.R. Peake, A.R. Zias, J.V. Egan, Solid-state digital pressure transducer. *IEEE Trans. Electron Devices* **16**(10), 870–876 (1969)
56. C.K. Stedman, Transducers with substantially linear response characteristics. U.S. Patent 3,341,794, 12, 1967
57. S. Samaun, K. Wise, E. Nielsen, and J. Angell, An IC piezoresistive pressure sensor for biomedical instrumentation, in *Proceedings of IEEE International Solid-State Circuits Conference*, pp. 104–105, 1971
58. L.B. Wilner, A diffused silicon pressure transducer with stress concentrated at transverse gages, in *Proceedings of International Instrumentation, Symposium*, pp. 361–365, 1977
59. L.B. Wilner, Sculptured pressure diaphragm. U.S. Patent, 4,093,933, 6, 1978
60. J.F. Marshall, Fabrication of semiconductor devices utilizing ion implantation. U.S. Patent 4,033,787, 5, 1977
61. A.D. Kurtz, J.R. Mallon, T.A. Nunn, Semiconductor transducers employing flexure frames. U.S. Patent 4,236,137, 25, 1980
62. S.K. Clark, K.D. Wise, Pressure sensitivity in anisotropically etched thin-diaphragm pressure sensors. *IEEE Trans. Electron Devices* **26**(12), 1887–1896 (1979)
63. K.E. Petersen, Silicon as a mechanical material. *Proc. IEEE* **70**(5), 420–457 (1982)
64. W.P. Eaton, J.H. Smith, Micromachined pressure sensors: review and recent developments. *Smart Mater. Struct.* **6**(5), 530 (1997)
65. J.C. Greenwood, Ethylene diamine-catechol-water mixture shows preferential etching of p-n junction. *J. Electrochem. Soc.* **116**(9), 1325–1326 (1969)
66. T.N. Jackson, M.A. Tischler, K.D. Wise, An electrochemical p-n junction etch-stop for the formation of silicon microstructures. *IEEE Electron Device Lett.* **2**(2), 44–45 (1981)
67. S.-C. Kim, K. Wise, Temperature sensitivity in silicon piezoresistive pressure transducers. *IEEE Trans. Electron Devices* **30**(7), 802–810 (1983)
68. B. Kloeck, S.D. Collins, N.F. de Rooij, R.L. Smith, Study of electrochemical etch-stop for high-precision thickness control of silicon membranes. *IEEE Trans. Electron Devices* **36**(4), 663–669 (1989)
69. K. Petersen, P. Barth, J. Poydock, J. Brown, J.J. Mallon, J. Bryzek, Silicon fusion bonding for pressure sensors, in *Proceedings of Solid State Sensors, Actuators, and Microsystems, Workshop*, pp. 144–147, 1988
70. L. Christel, K. Petersen, P. Barth, F. Pourahmadi, J. Mallon, J. Bryzek, Single-crystal silicon pressure sensors with 500x overpressure protection. *Sens. Actuators A* **21**(1–3), 84–88 (1990)
71. J.R. Mallon, F. Pourahmadi, K. Petersen, P. Barth, T. Vermeulen, J. Bryzek, Low-pressure sensors employing bossed diaphragms and precision etch-stopping. *Sens. Actuators A* **21**(1–3), 89–95 (1990)
72. K. Petersen, J. Brown, T. Vermeulen, P. Barth, J. Mallon, J. Bryzek, Ultra-stable, high-temperature pressure sensors using silicon fusion bonding. *Sens. Actuators A* **21**(1–3), 96–101 (1990)
73. F. Pourahmadi, P. Barth, K. Petersen, Modeling of thermal and mechanical stresses in silicon microstructures. *Sens. Actuators A* **23**(1–3), 850–855 (1990)

74. S. Armbruster, F. Schafer, G. Lammel, H. Artmann, C. Schelling, H. Benz, S. Finkbeiner, F. Larmer, P. Ruther, and O. Paul, A novel micromachining process for the fabrication of monocrystalline Si-membranes using porous silicon, in *Proceedings of Transducers*, pp. 246–249, 2003
75. G. Lammel, S. Armbruster, C. Schelling, H. Benz, J. Brasas, M. Illing, R. Gampp, V. Senz, F. Schafer, S. Finkbeiner, Next generation pressure sensors in surface micromachining technology, in *Proceedings of Transducers*, pp. 35–36, 2005
76. G. El-Hak, *The MEMS Handbook* (CRC Press, Boca Raton, 2002)
77. H.L. Chau, K.D. Wise, Scaling limits in batch-fabricated silicon pressure sensors. *IEEE Trans. Electron Devices* **34**(4), 850–858 (1987)
78. R.R. Spencer, B.M. Fleischer, P.W. Barth, J.B. Angell, A theoretical study of transducer noise in piezoresistive and capacitive silicon pressure sensors. *IEEE Trans. Electron Devices* **35**(8), 1289–1298 (1988)
79. Y.C. Sun, Z.B. Gao, L.Q. Tian, Y. Zhang, Modelling of the reverse current and its effects on the thermal drift of the offset voltage for piezoresistive pressure sensors. *Sens. Actuators A* **116**(1), 125–132 (2004)
80. Y. Kanda, A. Yasukawa, Optimum design considerations for silicon piezoresistive pressure sensors. *Sens. Actuators A* **62**(1–3), 539–542 (1997)
81. B. Bae, B.R. Flachsbart, K. Park, M. Shannon, Design optimization of a piezoresistive pressure sensor considering the output signal-to-noise ratio. *J. Micromech. Microeng.* **14**(12), 1597–1607 (2004)
82. S. Bhardwaj, M. Sheplak, T. Nishida, S/N optimization and noise considerations for piezoresistive microphones, in *Proceedings of the International Conference on Noise in Physical Systems and 1/f Fluctuations*, pp. 549–552, 2001
83. M. Tortonese, R. Barrett, C. Quate, Atomic resolution with an atomic force microscope using piezoresistive detection. *Appl. Phys. Lett.* **62**(8), 834–836 (1993)
84. J.A. Harley, T.W. Kenny, High-sensitivity piezoresistive cantilevers under 1000 angstroms thick. *Appl. Phys. Lett.* **75**(2), 289–291 (1999)
85. A. Loui, F.T. Goericke, T.V. Ratto, J. Lee, B.R. Hart, W.P. King, The effect of piezoresistive microcantilever geometry on cantilever sensitivity during surface stress chemical sensing. *Sens. Actuators A* **147**(2), 516–521 (2008)
86. F.T. Goericke, W.P. King, Modeling piezoresistive microcantilever sensor response to surface stress for biochemical sensors. *IEEE Sens.* **8**(7–8), 1404–1410 (2008)
87. M. Li, H.X. Tang, M.L. Roukes, Ultra-sensitive NEMS-based cantilevers for sensing, scanned probe and very high-frequency applications. *Nat. Nano.* **2**(2), 114–120 (2007)
88. M. Li, E.B. Myers, H.X. Tang, S.J. Aldridge, H.C. McCaig, J.J. Whiting, R.J. Simonson, N.S. Lewis, M.L. Roukes, Nanoelectromechanical resonator arrays for ultrafast, gas-phase chromatographic chemical analysis. *Nano Lett.* **10**(10), 3899–3903 (2010)
89. A. Partridge, J.K. Reynolds, B.W. Chui, E.M. Chow, A.M. Fitzgerald, L. Zhang, N.I. Maluf, T.W. Kenny, A high-performance planar piezoresistive accelerometer. *J. Microelectromech. Syst.* **9**(1), 58–66 (2000)
90. W.T. Park, A. Partridge, R.N. Candler, V. Ayanoor-Vitikkate, G. Yama, M. Lutz, T.W. Kenny, Encapsulated submillimeter piezoresistive accelerometers. *J. Microelectromech. Syst.* **15**(3), 507–514 (2006)
91. R.J. Wilfinger, P.H. Bardell, D.S. Chhabra, Resonistor—a frequency selective device utilizing mechanical resonance of a silicon substrate. *IBM J. Res. Dev.* **12**(1), 113–118 (1968)
92. D.E. Fulkerson, A silicon integrated circuit force sensor. *IEEE Trans. Electron Devices* **16**(10), 867–870 (1969)
93. G. Binnig, C. Quate, C. Gerber, Atomic force microscope. *Phys. Rev. Lett.* **56**(9), 930–933 (1986)
94. S.R. Manalis, S.C. Minne, A. Atalar, C.F. Quate, Interdigital cantilevers for atomic force microscopy. *Phys. Rev. Lett.* **69**(25), 3944–3946 (1996)
95. S.C. Minne, S.R. Manalis, C.F. Quate, Parallel atomic force microscopy using cantilevers with integrated piezoresistive sensors and integrated piezoelectric actuators. *Phys. Rev. Lett.* **67**(26), 3918–3920 (1995)

96. G.E. Fantner, W. Schumann, R.J. Barbero, A. Deutschinger, V. Todorov, D.S. Gray, A.M. Belcher, I.W. Rangelow, K. Youcef-Toumi, Use of self-actuating and self-sensing cantilevers for imaging biological samples in fluid. *Nanotechnology* **20**(43), 434003 (2009)
97. J.C. Doll, B.L. Pruitt, High bandwidth piezoresistive force probes with integrated thermal actuation. *J. Micromech. Microeng.* **22**(9), 095012 (2012)
98. J.C. Doll, A.W. Peng, A.J. Ricci, B.L. Pruitt, Faster than the speed of hearing: Nanomechanical force probes enable the electromechanical observation of cochlear hair cells. *Nano Lett.* **12**(12), 6107–6111 (2012)
99. J. Brugger, J. Burger, M. Binggeli, R. Imura, and N. F. de Rooij, Lateral force measurements in a scanning force microscope with piezoresistive sensors, in *Proceedings of Transducers*, pp. 636–639, 1995
100. J. Brugger, M. Despont, C. Rossel, H. Rothuizen, P. Vettiger, M. Willemijn, Microfabricated ultrasensitive piezoresistive cantilevers for torque magnetometry. *Sens. Actuators A* **73**(3), 235–242 (1999)
101. C. Hagleitner, D. Lange, T. Akiyama, A. Tonin, R. Vogt, H. Baltes, On-chip circuitry for a CMOS parallel scanning AFM, in *Proceedings of SPIE*, pp. 240–248, 1999
102. B.W. Chui, T.W. Kenny, H.J. Mamin, B.D. Terris, D. Rugar, Independent detection of vertical and lateral forces with a sidewall-implanted dual-axis piezoresistive cantilever. *Appl. Phys. Lett.* **72**(11), 1388–1390 (1998)
103. H. Jensenius, J. Thayesen, A.A. Rasmussen, L.H. Veje, O. Hansen, A. Boisen, A microcantilever-based alcohol vapor sensor-application and response model. *Appl. Phys. Lett.* **76**(18), 2615–2617 (2000)
104. M. Yang, X. Zhang, K. Vafai, C. Ozkan, High sensitivity piezoresistive cantilever design and optimization for analyte-receptor binding. *J. Micromech. Microeng.* **13**(6), 864–872 (2003)
105. G. Villanueva, F. Perez-Murano, M. Zimmermann, J. Lichtenberg, J. Bausells, Piezoresistive cantilevers in a commercial CMOS technology for intermolecular force detection. *Microelectron. Eng.* **83**(4–9), 1302–1305 (2006)
106. J.L. Arlett, M.R. Paul, J.E. Solomon, M.C. Cross, S.E. Fraser, M.L. Roukes, BioNEMS: Nanomechanical systems for single-molecule biophysics, in *Controlled Nanoscale Motion*, ed. by H. Linke, A. Mansson (Springer, Berlin, 2007), pp. 241–270
107. A. Boisen, J. Thayesen, H. Jensenius, O. Hansen, Environmental sensors based on micromachined cantilevers with integrated read-out. *Ultramicroscopy* **82**(1–4), 11–16 (2000)
108. W. Franks, D. Lange, S. Lee, A. Hierlemann, N. Spencer, H. Baltes, Nanochemical surface analyzer in CMOS technology. *Ultramicroscopy* **91**(1–4), 21–27 (2002)
109. D.R. Baselt, G.U. Lee, K.M. Hansen, L.A. Chrisey, R.J. Colton, A high-sensitivity micromachined biosensor. *Proc. IEEE* **85**(4), 672–680 (1997)
110. B.L. Pruitt, T.W. Kenny, Piezoresistive cantilevers and measurement system for characterizing low force electrical contacts. *Sens. Actuators A* **104**(1), 68–77 (2003)
111. B.L. Pruitt, W.T. Park, T.W. Kenny, Measurement system for low force and small displacement contacts. *J. Microelectromech. Syst.* **13**(2), 220–229 (2004)
112. S.C. Seel, C.V. Thompson, Piezoresistive microcantilevers for in situ stress measurements during thin film deposition. *Rev. Sci. Instrum.* **76**(7), 075103 (2005)
113. Y. Su, A. Evans, A. Brunnenschweiler, G. Ensell, Characterization of a highly sensitive ultra-thin piezoresistive silicon cantilever probe. *J. Micromech. Microeng.* **12**(6), 780–785 (2002)
114. J. Lee, K. Naeli, H. Hunter, J. Berg, T. Wright, C. Courcimault, N. Naik, M. Allen, O. Brand, A. Glezer, W.P. King, Characterization of liquid and gaseous micro- and nanojets using microcantilever sensors. *Sens. Actuators A* **134**(1), 128–139 (2007)
115. B.W. Chui, T.D. Stowe, Y.S. Ju, K.E. Goodson, T.W. Kenny, H.J. Mamin, B.D. Terris, R.P. Ried, D. Rugar, Low-stiffness silicon cantilevers with integrated heaters and piezoresistive sensors for high-density AFM thermomechanical data storage. *J. Microelectromech. Syst.* **7**(1), 69–78 (1998)
116. M. Lutwyche, C. Andreoli, G. Binnig, J. Brugger, U. Drechsler, W. Haberle, H. Rohrer, H. Rothuizen, P. Vettiger, G.Y.C. Quate, 5x5 2D AFM cantilever arrays a first step towards a terabit storage device. *Sens. Actuators A* **73**(1–2), 89–94 (1999)

117. H.J. Mamin, R.P. Ried, B.D. Terris, D. Rugar, High-density data storage based on the atomic force microscope. *Proc. IEEE* **87**(6), 1014–1027 (1999)
118. L. Aeschmann, F. Goericke, J. Polesel-Maris, A. Meister, T. Akiyama, B. Chui, U. Staufer, R. Pugin, H. Heinzelmann, N.F. de Rooij, W.P. King, P. Vettiger, Piezoresistive scanning probe arrays for operation in liquids. *J. Phys: Conf. Ser.* **61**, 6–10 (2007)
119. Y. Liang, S. Ueng, T.W. Kenny, Performance characterization of ultra-thin n-type piezoresistive cantilevers, in *Proceedings of Transducers*, pp. 998–1001, 2001
120. C. Bergaud, E. Cocheteau, L. Bary, R. Plana, B. Belier, Formation of implanted piezoresistors under 100-nm thick for nanoelectromechanical systems, in *Proceedings of IEEE MEMS*, pp. 360–363, 2002
121. J. Arlett, Properties of piezoresistive silicon nano-scale cantilevers with applications to BioNEMS. Ph.D. dissertation, California Institute of Technology, 2011
122. J.L. Arlett, J.R. Maloney, B. Gudlewski, M. Muluneh, M.L. Roukes, Self-sensing micro-and nanocantilevers with attonewton-scale force resolution. *Nano Lett.* **6**(5), 1000–1006 (2006)
123. I. Bargatin, E.B. Myers, J. Arlett, B. Gudlewski, M.L. Roukes, Sensitive detection of nanomechanical motion using piezoresistive signal downmixing. *Appl. Phys. Lett.* **86**(13), 133109 (2005)
124. M.L. Roukes, Nanoelectromechanical systems, in *Proceedings of Solid State Sensors, Actuators, and Microsystems, Workshop*, pp. 1–10, 2000
125. M.L. Roukes, Nanoelectromechanical systems face the future. *Phys. World* **14**(2), 25–31 (2001)
126. O. Hansen, A. Boisen, Noise in piezoresistive atomic force microscopy. *Nanotechnology* **10**(1), 51–60 (1999)
127. J.A. Harley, T.W. Kenny, 1/f noise considerations for the design and process optimization of piezoresistive cantilevers. *J. Microelectromech. Syst.* **9**(2), 226–235 (2000)
128. X.M. Yu, J. Thaysen, O. Hansen, A. Boisen, Optimization of sensitivity and noise in piezoresistive cantilevers. *J. Appl. Phys.* **92**(10), 6296–6301 (2002)
129. P.A. Rasmussen, J. Thaysen, O. Hansen, S.C. Eriksen, A. Boisen, Optimised cantilever biosensor with piezoresistive read-out. *Ultramicroscopy* **97**(1–4), 371–376 (2003)
130. Z.Y. Wang, R.F. Yue, R.X. Zhang, L.T. Liu, Design and optimization of laminated piezoresistive microcantilever sensors. *Sens. Actuators A* **120**(2), 325–336 (2005)
131. J.C. Doll, S.-J. Park, B.L. Pruitt, Design optimization of piezoresistive cantilevers for force sensing in air and water. *J. Appl. Phys.* **106**(6), 064310 (2009)
132. J.C. Doll, B.C. Petzold, P. Ghale, M.B. Goodman, B.L. Pruitt, High frequency force sensing with piezoresistive cantilevers, in *Proceedings of Transducers*, pp. 1928–1931, 2009
133. S.-J. Park, J.C. Doll, A.J. Rastegar, B.L. Pruitt, Piezoresistive cantilever performance—part II: Optimization. *J. Microelectromech. Syst.* **19**(1), 149–161 (2010)
134. J.C. Doll, E.A. Corbin, W.P. King, B.L. Pruitt, Self-heating in piezoresistive cantilevers. *Appl. Phys. Lett.* **98**(22), 223103 (2011)
135. G. Yoshikawa, T. Akiyama, S. Gautsch, P. Vettiger, H. Rohrer, Nanomechanical membrane-type surface stress sensor. *Nano Lett.* **11**(3), 1044–1048 (2011)
136. G.G. Stoney, The tension of metallic films deposited by electrolysis. *Proc. R. Soc. Lond.* **82**(553), 172–175 (1909)
137. C.A. Klein, How accurate are stoney's equation and recent modifications. *J. Appl. Phys.* **88**(9), 5487–5489 (2000)
138. F.T. Goericke, J. Lee, W.P. King, Microcantilever hotplates with temperature-compensated piezoresistive strain sensors. *Sens. Actuators A* **143**(2), 181–190 (2008)
139. N. Yazdi, F. Ayazi, K. Najafi, Micromachined inertial sensors. *Proc. IEEE* **86**(8), 1640–1659 (1998)
140. C. Gravel, A. Brosh, Subminiature solid state accelerometer, in *Proceedings of the International ISA Aerospace Instrumentation, Symposium*, pp. 368–372, 1969
141. L.M. Roylance, A miniature integrated circuit accelerometer for biomedical applications. Ph.D. dissertation, Stanford University, 1978

142. P.W. Barth, F. Pourahmadi, R. Mayer, J. Poydock, K. Petersen, A monolithic silicon accelerometer with integral air damping and overrange protection, in *Proceedings of Solid State Sensors, Actuators, and Microsystems Workshop*, pp. 35–38, 1988
143. W. Riethmüller, W. Benecke, U. Schnakenberg, B. Wagner, A smart accelerometer with on-chip electronics fabricated by a commercial CMOS process. *Sens. Actuators A* **31**(1–3), 121–124 (1992)
144. H. Seidel, U. Fritsch, R. Gottinger, J. Schalk, J. Walter, K. Ambaum, A piezoresistive silicon accelerometer with monolithically integrated CMOS-circuitry, in *Proceedings of Transducers*, pp. 597–600, 1995
145. H.V. Allen, S.C. Terry, D.W. Debruin, Accelerometer systems with self-testable features. *Sens. Actuator* **20**(1–2), 153–161 (1989)
146. H. Chen, M.H. Bao, H.J. Zhu, S.Q. Shen, A piezoresistive accelerometer with a novel vertical beam structure. *Sens. Actuators A* **63**(1), 19–25 (1997)
147. K. Kwon, S. Park, A bulk-micromachined three-axis accelerometer using silicon direct bonding technology and polysilicon layer. *Sens. Actuators A* **66**(1–3), 250–255 (1998)
148. W.-T. Park, K.N. O'Connor, K.-L. Chen, J.R. Mallon, T. Maetani, P. Dalal, R.N. Candler, V. Ayanoor-Vitikkate, J.B. Roberson, S. Puria, T.W. Kenny, Ultraminiature encapsulated accelerometers as a fully implantable sensor for implantable hearing aids. *Biomed. Microdevices* **9**(6), 939–949 (2007)
149. A. Partridge, Lateral piezoresistive accelerometer with epipoly encapsulation. Ph.D. dissertation, Stanford University, 2003
150. J.P. Lynch, A. Partridge, K.H. Law, T.W. Kenny, A.S. Kiremidjian, E. Carryer, Design of piezoresistive MEMS-based accelerometer for integration with wireless sensing unit for structural monitoring. *J. Aerospace Eng.* **16**(3), 108–114 (2003)
151. F. Paoletti, M.A. Gretillat, N.F. de Rooij, A silicon micromachined vibrating gyroscope with piezoresistive detection and electromagnetic excitation, in *Proceedings of IEEE MEMS*, pp. 162–167, 1996
152. R. Voss, K. Bauer, W. Ficker, T. Gleissner, W. Kupke, M. Rose, S. Sassen, J. Schalk, H. Seidel, E. Stenzel, Silicon angular rate sensor for automotive applications with piezoelectric drive and piezoresistive read-out, in *Proceedings of Transducers*, pp. 879–882, 1997
153. F. Gretillat, M.A. Gretillat, N.F. de Rooij, Improved design of a silicon micromachined gyroscope with piezoresistive detection and electromagnetic excitation. *J. Microelectromech. Syst.* **8**(3), 243–250 (1999)
154. A. Rahafrooz, S. Pourkamali, Fabrication and characterization of thermally actuated micro-mechanical resonators for airborne particle mass sensing: I. resonator design and modeling. *J. Micromech. Microeng.* **20**(12), 125018 (2010)
155. A. Hajjam, J.C. Wilson, A. Rahafrooz, S. Pourkamali, Fabrication and characterization of thermally actuated micromechanical resonators for airborne particle mass sensing: II. device fabrication and characterization. *J. Micromech. Microeng.* **20**(12), 125019 (2010)
156. J.R. Mallon, A.J. Rastegar, A.A. Barlian, M.T. Meyer, T.H. Fung, B.L. Pruitt, Low 1/f noise, full bridge, microcantilever with longitudinal and transverse piezoresistors. *Appl. Phys. Lett.* **92**(3), 033508 (2008)
157. J.T.M. van Beek, K.L. Phan, G.J.A.M. Verheijden, G.E.J. Koops, C. van der Avoort, J. van Wingerden, D.E. Badaroglu, J.J.M. Bontemps, R. Puers, A piezo-resistive resonant MEMS amplifier, in *Proceedings of IEEE Electron Devices Meeting*, pp. 1–4, 2008
158. A. Rahafrooz, S. Pourkamali, Fully micromechanical piezo-thermal oscillators, in *Proceedings of IEEE IEDM*, pp. 7.2.1–7.2.4, 2010
159. J.T.M. van Beek, R. Puers, A review of MEMS oscillators for frequency reference and timing applications. *J. Micromech. Microeng.* **22**(1), 013001 (2012)
160. C.M. Lin, T.T. Yen, Y.J. Lai, V.V. Felmetser, M.A. Hopcroft, J.H. Kuypers, A.P. Pisano, Temperature-compensated aluminum nitride lamb wave resonators. *IEEE Trans. Ultrason. Ferroelectr. Freq. Control* **57**(3), 524–532 (2010)
161. J.T.M. van Beek, P.G. Steeneken, B. Giesbers, A 10 mhz piezoresistive MEMS resonator with high Q, in *Proceedings of IEEE International Frequency Control Symposium and Exposition*, pp. 475–480, 2006

162. C. Zuo, J. Van Der Spiegel, G. Piazza, 1.05-ghz CMOS oscillator based on lateral- field-excited piezoelectric AlN contour- mode MEMS resonators. *IEEE Trans. Ultrason. Ferroelectr. Freq. Control* **57**(1), 82–87 (2010)
163. R.N. Candler, W.-T. Park, H. Li, G. Yama, A. Partridge, M. Lutz, T.W. Kenny, Single wafer encapsulation of MEMS devices. *IEEE Trans. Adv. Packag.* **26**(3), 227–232 (2003)
164. B. Kim, R.N. Candler, M.A. Hopcroft, M. Agarwal, W.-T. Park, T.W. Kenny, Frequency stability of wafer-scale film encapsulated silicon based MEMS resonators. *Sens. Actuators A* **136**(1), 125–131 (2007)
165. K.L. Phan, J.T.M. van Beek, G.E.J. Koops, Piezoresistive ring-shaped MEMS resonator, in *Proceedings of Transducers*, pp. 1413–1416, 2009
166. J.J.M. Bontemps, A. Murroni, J.T.M. van Beek, J.A.T.M. van den Homberg, J.J. Koning, G.E. J. Koops, G.J.A.M. Verheijden, J. van Wingerden, K.L. Phan, P. Vermeeren, C. van der Avoort, H.C.W. Beijerinck, P.G.M. Baltus, 56 mhz piezoresistive micromechanical oscillator, in *Proceedings of Transducers*, pp. 1433–1436, 2009
167. A. Rahafrooz, S. Pourkamali, High-frequency thermally actuated electromechanical resonators with piezoresistive readout. *IEEE Trans. Electron Devices* **58**(4), 1205–1214 (2011)
168. R.C. Ruby, P. Merchant, Micromachined thin film bulk acoustic resonators, in *Proceedings of IEEE International Frequency Control Symposium*, pp. 135–138, 1994
169. R.C. Ruby, P. Bradley, Y. Oshmyansky, A. Chien, J.D.I. Larson, Thin film bulk wave acoustic resonators (fbar) for wireless applications. *Proc. IEEE Ultrason. Symp.* **1**, 813–821 (2001)
170. S. Rai, Y. Su, W. Pang, R.C. Ruby, B. Otis, A digitally compensated 1.5 ghz CMOS/FBAR frequency reference. *IEEE Trans. Ultrason. Ferroelectr. Freq. Control* **57**(3), 552–561 (2010)
171. G. Piazza, A.P. Pisano, Two-port stacked contour-mode aluminum nitride piezoelectric micro-mechanical resonators. *Sens. Actuators A* **134**(1), 239–244 (2007)
172. A.M. Malek, S.L. Alper, S. Izumo, Hemodynamic shear stress and its role in atherosclerosis. *Jama-J. Am. Med. Assoc.* **282**(21), 2035–2042 (1999)
173. J.W. Naughton, M. Sheplak, Modern developments in shear-stress measurement. *Prog. Aerosp. Sci.* **38**(6–7), 515–570 (2002)
174. M. Sheplak, L. Cattafesta, T. Nishida, C.B. McGinley, MEMS shear stress sensors: Promise and progress, in *Proceedings of 24th AIAA Aerodynamic Measurement Technology and Ground Testing Conference*, pp. 1–13, 2004
175. K.Y. Ng, J. Shajii, M.A. Schmidt, A liquid shear-stress sensor fabricated using wafer bonding technology, in *Proceedings of Transducers*, pp. 931–934, 1991
176. J. Shajii, K.Y. Ng, M.A. Schmidt, A microfabricated floating-element shear stress sensor using wafer-bonding technology. *J. Microelectromech. Syst.* **1**(2), 89–94 (1992)
177. A.A. Barlian, S.-J. Park, V. Mukundan, B.L. Pruitt, Design and characterization of microfabricated piezoresistive floating element-based shear stress sensors. *Sens. Actuators A* **134**(1), 77–87 (2007)
178. A.A. Barlian, R. Narain, J.T. Li, C.E. Quance, A.C. Ho, V. Mukundan, B.L. Pruitt, Piezoresistive MEMS underwater shear stress sensors, in *Proceedings of IEEE MEMS*, pp. 626–629, 2006
179. Y. Li, T. Nishida, D.P. Arnold, M. Sheplak, Microfabrication of a wall shear stress sensor using side-implanted piezoresistive tethers, in *Proceedings of SPIE*, pp. 1–11, 2007
180. Y. Li, M. Papila, T. Nishida, L. Cattafesta, M. Sheplak, Modeling and optimization of a side-implanted piezoresistive shear stress sensor, in *Proceedings of SPIE*, pp. 1–12, 2006
181. M.C. Hsieh, Y.K. Fang, M.S. Ju, G.S. Chen, J.J. Ho, C.H. Yang, P.M. Wu, G.S. Wu, T.Y.F. Chen, A contact-type piezoresistive micro-shear stress sensor for above-knee prosthesis application. *J. Microelectromech. Syst.* **10**(1), 121–127 (2001)
182. M.S. Bartsch, W. Federle, R.J. Full, T.W. Kenny, A multiaxis force sensor for the study of insect biomechanics. *J. Microelectromech. Syst.* **16**(3), 709–718 (2007)
183. B.J. Kane, M.R. Cutkosky, G.T.A. Kovacs, A traction stress sensor array for use in high-resolution robotic tactile imaging. *J. Microelectromech. Syst.* **9**(4), 425–434 (2000)
184. M. Doelle, C. Peters, P. Ruther, O. Paul, Piezo-FET stress-sensor arrays for wire-bonding characterization. *J. Microelectromech. Syst.* **15**(1), 120–130 (2006)

185. R.C. Jaeger, J.C. Suhling, M.T. Carey, R.W. Johnson, A piezoresistive sensor chip for measurement of stress in electronic packaging, in *Proceedings of Electronic Components and Technology Conference*, pp. 686–692, 1993
186. K. Noda, K. Hoshino, K. Matsumoto, I. Shimoyama, A shear stress sensor for tactile sensing with the piezoresistive cantilever standing in elastic material. *Sens. Actuators A* **127**(2), 295–301 (2006)
187. Z.F. Fan, J. Chen, J. Zou, D. Bullen, C. Liu, F. Delcomyn, Design and fabrication of artificial lateral line flow sensors. *J. Micromech. Microeng.* **12**(5), 655–661 (2002)
188. N. Chen, C. Tucker, J.M. Engel, Y. Yang, S. Pandya, C. Liu, Design and characterization of artificial haircell sensor for flow sensing with ultrahigh velocity and angular sensitivity. *J. Microelectromech. Syst.* **16**(5), 999–1014 (2007)
189. W.A. Brantley, Calculated elastic-constants for stress problems associated with semiconductor devices. *J. Appl. Phys.* **44**(1), 534–535 (1973)
190. D.R. Franca, A. Blouin, All-optical measurement of in-plane and out-of-plane young's modulus and poisson's ratio in silicon wafers by means of vibration modes. *Meas. Sci. Technol.* **15**(5), 859–868 (2004)
191. I.S. Sokolnikoff, *Mathematical Theory of Elasticity* (R.E. Krieger Pub, Malabar, 1983)
192. G.N. Greaves, A.L. Greer, R.S. Lakes, T. Rouxel, Poisson's ratio and modern materials. *Nat. Mater.* **10**(11), 823–837 (2011)
193. C. Kittel, *Introduction to Solid State Physics* (John Wiley & Sons, New York, 2005)
194. J.F. Nye, *Physical Properties of Crystals: Their Representation by Tensors and Matrices* (Oxford University Press, Oxford, 1985)
195. W.C. Young, R. Budynas, *Roark's Formulas for Stress and Strain* (McGraw-Hill, New York, 2002)
196. J.J. Wortman, R.A. Evans, Young's modulus, shear modulus, and poisson's ratio in silicon and germanium. *J. Appl. Phys.* **36**(1), 153–156 (1965)
197. Y. Kanda, A graphical representation of the piezoresistance coefficients in silicon. *Electron Dev.* **29**(1), 64–70 (1982)
198. S. Suthram, J.C. Ziegert, T. Nishida, S.E. Thompson, Piezoresistance coefficients of (100) silicon nMOSFETs measured at low and high channel stress. *IEEE Electr. Device Lett.* **28**(1), 58–61 (2007)
199. T.A. Rost, Transistor design and layout for performance improvement with strain. U.S. Patent 0095,988, 16, 2009
200. M.A. Hopcroft, W.D. Nix, T.W. Kenny, What is the Young's modulus of silicon. *J. Microelectromech. Syst.* **19**(2), 229–238 (2010)
201. J. Richter, Piezoresistivity in microsystems. Ph.D. dissertation, DTU Nanotech, Lyngby, 2008
202. O.N. Tufte, E.L. Stelzer, Piezoresistive properties of silicon diffused layers. *J. Appl. Phys.* **34**(2), 313–318 (1963)
203. E. Lund, T.G. Finstad, Measurement of the temperature dependency of the piezoresistance coefficients in p-type silicon, in *Proceedings of ASME Advances in Electronic Packaging*, pp. 215–218, 1999
204. E. Lund, T.G. Finstad, Design and construction of a four-point bending based set-up for measurement of piezoresistance in semiconductors. *Rev. Sci. Instrum.* **75**(11), 4960–4966 (2004)
205. C.-H. Cho, R.C. Jaeger, J.C. Suhling, Characterization of the temperature dependence of the piezoresistive coefficients of silicon from -150C to +125C. *IEEE Sens.* **8**(8), 1455–1468 (2008)
206. J. Richter, J. Pedersen, M. Brandbyge, E.V. Thomsen, O. Hansen, Piezoresistance in p-type silicon revisited. *J. Appl. Phys.* **104**(2), 023715 (2008)
207. A.D. Kurtz, C. Gravel, Semiconductor transducers using transverse and shear piezoresistance, in *Proceedings of ISA*, 1967
208. S.M. Sze, K.K. Ng, *Physics of Semiconductor Devices* (John Wiley & Sons, New York, 2007)
209. M.A. Green, Intrinsic concentration, effective densities of states, and effective mass in silicon. *J. Appl. Phys.* **67**(6), 2944–2954 (1990)

210. N.G. Nilsson, An accurate approximation of the generalized Einstein relation for degenerate semiconductors. *Phys. Status Solidi A* **19**(1), K75–K78 (1973)
211. J.S. Blakemore, Approximations for fermi-dirac integrals, especially the function used to describe electron density in a semiconductor. *Solid-State Electron.* **25**(11), 1067–1076 (1982)
212. O.N. Tufte, E.L. Stelzer, Piezoresistive properties of heavily doped n-type silicon. *Phys. Rev. A* **133**(6A), 1705–1716, 1964
213. W.P. Mason, J.J. Forst, L.M. Tornillo, Recent developments in semiconductor strain transducers, in *Proceedings of The Instrument Society of America*, pp. 110–120, 1962
214. D.R. Kerr, A.G. Milnes, Piezoresistance of diffused layers in cubic semiconductors. *J. Appl. Phys.* **34**(4), 727–731 (1963)
215. N. Harjee, Coaxial-tip piezoresistive cantilever probes for high-resolution scanning gate microscopy. Ph.D. dissertation, Stanford University, 2011
216. F.J. Morin, T.H. Geballe, C. Herring, Temperature dependence of the piezoresistance of high-purity silicon and germanium. *Phys. Rev.* **105**(2), 525–539 (1957)
217. J.M. Chen, N.C. MacDonald, Measuring the nonlinearity of silicon piezoresistance by tensile loading of a submicron diameter fiber using a microinstrument. *Rev. Sci. Instrum.* **75**(1), 276–278 (2004)
218. K. Matsuda, Y. Kanda, K. Yamamura, K. Suzuki, Nonlinearity of piezoresistance effect in p-type and n-type silicon. *Sens. Actuators A* **21**(1–3), 45–48 (1990)
219. K. Matsuda, K. Suzuki, K. Yamamura, Y. Kanda, Nonlinear piezoresistance effects in silicon. *J. Appl. Phys.* **73**(4), 1838–1847 (1993)
220. R.F. Pierret, *Semiconductor Fundamentals: Modular Series on Solid State Devices* (Addison Wesley, Reading, 1983)
221. Y. Sun, S.E. Thompson, T. Nishida, Physics of strain effects in semiconductors and MOSFETs. *J. Appl. Phys.* **101**(10), 104503 (2007)
222. G.E. Kimball, The electronic structure of diamond. *J. Chem. Phys.* **3**(9), 560–564 (1935)
223. J.F. Mullaney, Optical properties and electronic structure of solid silicon. *Phys. Rev.* **66**(11/12), 326–339 (1944)
224. C. Herring, Transport properties of a many-valley semiconductor. *Bell. Syst. Tech. J.* **34**(2), 237–290 (1955)
225. C. Herring, E. Vogt, Transport and deformation-potential theory for many-valley semiconductors with anisotropic scattering. *Phys. Rev.* **101**(3), 944–961 (1956)
226. D. Long, Stress dependence of piezoresistance effect. *J. Appl. Phys.* **32**(10), 2050–2051 (1961)
227. C. Herring, Theory of the thermoelectric power of semiconductors. *Phys. Rev.* **96**(5), 1163–1187 (1954)
228. R.W. Keyes, The effects of elastic deformation on the electrical conductivity of semiconductors, in *Solid State Physics*, vol. 11, eds. by F. Seitz, D. Turnbull (Academic Press, New York, 1960)
229. M. Becker, H.Y. Fan, Optical properties of semiconductors. *Phys. Rev.* **76**(10), 1531–1532 (1949)
230. H.Y. Fan, Temperature dependence of the energy gap in monatomic semiconductors. *Phys. Rev.* **78**(6), 808–809 (1950)
231. B. Abeles, S. Meiboom, Theory of the galvanomagnetic effects in germanium. *Phys. Rev.* **95**(1), 31–37 (1954)
232. M. Shibuya, Magnetoresistance effect in cubic semiconductors with spheroidal energy surfaces. *Phys. Rev.* **95**(6), 1385–1393 (1954)
233. S. Meiboom, B. Abeles, Theory of the galvanomagnetic effects in n-germanium. *Phys. Rev.* **93**(5), 1121–1121 (1954)
234. R.W. Keyes, Explaining strain. *IEEE Circ. Dev.* **18**(5), 36–39 (2002)
235. M.S. Lin, A better understanding of the channel mobility of Si MOSFETs based on the physics of quantized subbands. *IEEE Trans. Electron Devices* **35**(12), 2406–2411 (1988)
236. K. Rim, K. Chan, L. Shi, D. Boyd, J. Ott, N. Klymko, F. Cardone, L. Tai, S. Koester, M. Cobb, D. Canaperi, B. To, E. Duch, I. Babich, R. Carruthers, P. Saunders, G. Walker, Y. Zhang, M. Steen, M. Jeong, Fabrication and mobility characteristics of ultra-thin strained Si directly on insulator (SSDOI) MOSFETs, in *Proceedings of IEEE IEDM*, 2003

237. S. Thompson, G. Sun, K. Wu, J. Lim, T. Nishida, Key differences for process-induced uniaxial vs. substrate-induced biaxial stressed Si and Ge channel MOSFETs, in *Proceedings of IEEE IEDM*, pp. 221–224, 2004
238. E. Wang, P. Matagne, L. Shifren, B. Obradovic, R. Kotlyar, S. Cea, J. He, Z. Ma, R. Nagisetty, S. Tyagi, M. Stettler, M.D. Giles, Quantum mechanical calculation of hole mobility in silicon inversion layers under arbitrary stress, in *Proceedings of IEEE IEDM*, pp. 147–150, 2004
239. Y. Ohmura, Role of the valence-band density-of-states in the piezoresistance of p-type semiconductors Si and Ge. *J. Phys. Soc. Jpn.* **62**(10), 3615–3620 (1993)
240. K. Matsuda, Strain-dependent hole masses and piezoresistive properties of silicon, in *Proceedings of IWCE Workshop on Computational Electronics*, pp. 173–174, 2004
241. M.V. Fischetti, Z. Ren, P.M. Solomon, M. Yang, K. Rim, Six-band k-p calculation of the hole mobility in silicon inversion layers: Dependence on surface orientation, strain, and silicon thickness. *J. Appl. Phys.* **94**(2), 1079–1095 (2003)
242. R. Oberhuber, G. Zandler, P. Vogl, Subband structure and mobility of two-dimensional holes in strained Si/SiGe MOSFETs. *Phys. Rev. B* **58**(15), 9941–9948 (1998)
243. T. Toriyama, S. Sugiyama, Analysis of piezoresistance in p-type silicon for mechanical sensors. *J. Microelectromech. Syst.* **11**(5), 598–604 (2002)
244. G.L. Bir, G.E. Pikus, *Symmetry and Strain-Induced Effects in Semiconductors* (John Wiley & Sons, New York, 1974)
245. W.H. Kleiner, L.M. Roth, Deformation potential in germanium from optical absorption lines for exciton formation. *Phys. Rev. Lett.* **2**(8), 334–336 (1959)
246. G.E. Pikus, G.L. Bir, Cyclotron and paramagnetic resonance in strained crystals. *Phys. Rev. Lett.* **6**(1), 103–105 (1961)
247. J.C. Hensel, G. Feher, Valence band parameters in silicon from cyclotron resonances in crystals subjected to uniaxial stress. *Phys. Rev. Lett.* **5**(7), 307–309 (1960)
248. H. Hasegawa, Theory of cyclotron resonance in strained silicon crystals. *Phys. Rev.* **129**(3), 1029–1040 (1963)
249. J.C. Hensel, G. Feher, Cyclotron resonance experiments in uniaxially stressed silicon—valence band inverse mass parameters and deformation potentials. *Phys. Rev.* **129**(3), 1041–1062 (1963)
250. J.C. Hensel, H. Hasegawa, M. Nakayama, Cyclotron resonance in uniaxially stressed silicon. *Phys. Rev.* **138**(1A), A225–A238 (1965)
251. J.C. Hensel, K. Suzuki, Quantum resonances in valence bands of germanium. *Phys. Rev. B* **9**(10), 4219–4257 (1974)
252. L. Smith, V. Moroz, G. Eneman, P. Verheyen, F. Nouri, L. Washington, M. Jurczak, O. Penzin, D. Pramanik, K.D. Meyer, Exploring the limits of stress-enhanced hole mobility. *IEEE Electron Device Lett.* **26**(9), 652–654 (2005)
253. S.E. Thompson, S. Suthram, Y. Sun, G. Sun, S. Parthasarathy, M. Chu, T. Nishida, Future of strained Si/semiconductors in nanoscale MOSFETs, in *Proceedings of IEEE IEDM*, pp. 1–4, 2006
254. Errors due to wheatstone bridge nonlinearity, TN-507, Vishay Inc, Tech. Rep., 2005
255. B. Konrad, M. Ashauer, Demystifying piezoresistive pressure sensors. *Sens. Magazine* **16**(7), 12–25 (1999)
256. K.F. Anderson, The new current loop: An instrumentation and measurement circuit topology. *IEEE Trans. Instrum. Meas.* **46**(5), 1061–1067 (1997)
257. C. Lu, M. Lemkin, B.E. Boser, A monolithic surface micromachined accelerometer with digital output. *IEEE J. Solid-State Circuits* **30**(12), 1367–1373 (1995)
258. T. Muller, M. Brandl, O. Brand, H. Baltes, An industrial CMOS process family adapted for the fabrication of smart silicon sensors. *Sens. Actuators A* **84**(1–2), 126–133 (2000)
259. A. Bindra, Integrated analog signal-conditioning IC handles harsh environments. *Electron. Des.* **48**, 84–87 (2000)
260. S. Hafizovic, D. Barretino, T. Volden, J. Sedivy, K.U. Kirstein, O. Brand, A. Hierlemann, Single-chip mechatronic microsystem for surface imaging and force response studies. *PNAS* **101**(49), 17011–17015 (2004)

261. A.J. Rastegar, J. Bryzek, A high-performance CMOS processor for piezoresistive sensors. *SenS. Magazine* **14**(10), 82–87 (1997)
262. T. Ishihara, K. Suzuki, S. Suwazono, M. Hirata, H. Tanigawa, CMOS integrated silicon pressure sensor. *IEEE J. Solid-State Circuits* **22**(2), 151–156 (1987)
263. T. Akiyama, U. Staufer, N.F. de Rooij, D. Lange, C. Hagleitner, O. Brand, H. Baltes, A. Tonin, H.R. Hidber, Integrated AFM array probe with MOSFET stress sensor, thermal bimorph actuator and on-chip CMOS electronics. *J. Vac. Sci. Technol. B* **18**(6), 2669–2675 (2000)
264. D. Lange, C. Hagleitner, O. Brand, H. Baltes, CMOS resonant beam gas sensing system with on-chip self excitation, in *Proceedings of IEEE MEMS*, pp. 547–552, 2001
265. T. Volden, M. Zimmermann, D. Lange, O. Brand, H. Baltes, Dynamics of CMOS-based thermally actuated cantilever arrays for force microscopy. *Sens. Actuators A* **115**(2–3), 516–522 (2004)
266. J. Lu, T. Ikehara, Y. Zhang, T. Mihara, T. Itoh, R. Maeda, High-Q and CMOS compatible single crystal silicon cantilever with separated on-chip piezoelectric actuator for ultra-sensitive mass detection, in *Proceedings of IEEE MEMS*, pp. 665–668, 2008
267. F. Fruett, G.C.M. Meijer, The influence of the piezojunction effect at different temperatures on the accuracy of silicon temperature sensors, in *Proceedings of the International Conference on Microelectronics and Packaging*, pp. 153–157, 2000
268. R.C. Jaeger, R. Ramani, J.C. Suhling, Y. Kang, CMOS stress sensor circuits using piezoresistive field-effect transistors (PIFETs), in *Proceedings of VLSI Circuits*, pp. 43–44, 1995
269. J. Bartholomeyczik, S. Brugger, P. Ruther, O. Paul, Multidimensional CMOS in-plane stress sensor. *IEEE Sens.* **5**(5), 872–882 (2005)
270. G. Lin, K.S.J. Pister, K.P. Roos, Standard CMOS piezoresistive sensor to quantify heart cell contractile forces, in *Proceedings of IEEE MEMS*, pp. 150–155, 1996
271. B. Levey, P. Gieschke, M. Doelle, S. Spinner, A. Trautmann, P. Ruther, O. Paul, CMOS-integrated silicon 3D force sensor system for micro component coordinate measurement machines, in *Proceedings of IEEE MEMS*, pp. 611–614, 2007
272. G. Villanueva, J.A. Plaza, J. Montserrat, F. Perez-Murano, J. Bausells, Crystalline silicon cantilevers for piezoresistive detection of biomolecular forces. *Microelectron. Eng.* **85**(5–6), 1120–1123 (2008)
273. H. Baltes, O. Brand, A. Hierlemann, D. Lange, C. Hagleitner, CMOS-MEMS present and future, in *Proceedings of IEEE MEMS*, pp. 459–466, 2002
274. H. Baltes, O. Brand, CMOS-based microsensors and packaging. *Sens. Actuators A* **92**(1–3), 1–9 (2001)
275. B.W. Chui, L. Aeschimann, T. Akiyama, U. Staufer, N.F. de Rooij, J. Lee, F. Goericke, W.P. King, P. Vettiger, Advanced temperature compensation for piezoresistive sensors based on crystallographic orientation. *Rev. Sci. Instrum.* **78**(4), 043706 (2007)
276. P.L.P. Hoa, G. Suchaneck, G. Gerlach, Influence of polycrystalline silicon as electrical shield on reliability and stability of piezoresistive sensors. *Sens. Actuators A* **120**(2), 567–572 (2005)
277. P. Gray, P. Hurst, S. Lewis, R. Meyer, *Analysis and Design of Analog Integrated Circuits* (John Wiley & Sons, New York, 2001)
278. J.B. Johnson, Thermal agitation of electricity in conductors. *Phys. Rev.* **32**(1), 97 (1928)
279. H. Nyquist, Thermal agitation of electric charge in conductors. *Phys. Rev.* **32**(1), 110–113 (1928)
280. M.S. Keshner, 1/f noise. *Proc. IEEE* **70**(3), 212–218 (1982)
281. R.F. Voss, J. Clarke, Flicker (1/f) noise—equilibrium temperature and resistance fluctuations. *Phys. Rev. B* **13**(2), 556–573 (1976)
282. F.N. Hooge, L.K.J. Vandamme, Lattice scattering causes 1/f noise. *Phys. Lett. A* **66**(4), 315–316 (1978)
283. P. Dutta, P.M. Horn, Low-frequency fluctuations in solids—1/f noise. *Rev. Mod. Phys.* **53**(3), 497–516 (1981)
284. D.M. Fleetwood, N. Giordano, Resistivity dependence of 1/f noise in metal films. *Phys. Rev. B* **27**(2), 667–671 (1983)

285. A. van der Ziel, Unified presentation of 1/f noise in electron devices: fundamental 1/f noise sources. *Proc. IEEE* **76**(3), 233–258 (1988)
286. L.K.J. Vandamme, G. Trefan, 1/f noise in homogeneous and inhomogeneous media. *IEE Proc. Circuits Devices Syst.* **149**(1), 3–12 (2002)
287. L.K.J. Vandamme, Bulk and surface 1/f noise. *IEEE Trans. Electron Devices* **36**(5), 987–992 (1989)
288. A.L. McWhorter, *1/f Noise and Related Surface Effects in Germanium* (MIT Lincoln Laboratory, Cambridge, 1955)
289. A.L. McWhorter, *Semiconductor Surface Physics* (University of Pennsylvania Press, Philadelphia, 1957)
290. F.N. Hooge, 1/f noise is no surface effect. *Phys. Lett. A* **29**(3), 139–140 (1969)
291. F.N. Hooge, 1/f noise sources. *Electron Dev.* **41**(11), 1926–1935 (1994)
292. F.N. Hooge, T.G.M. Kleinpenning, L.K.J. Vandamme, Experimental studies on 1/f noise. *Rep. Prog. Phys.* **44**(5), 479–532 (1981)
293. T.G.M. Kleinpenning, A.H. Dekuijper, Relation between variance and sample duration of 1/f noise signals. *J. Appl. Phys.* **63**(1), 43–45 (1988)
294. M. Gel, I. Shimoyma, Force sensing submicrometer thick cantilevers with ultra-thin piezoresistors by rapid thermal diffusion. *J. Micromech. Microeng.* **14**(3), 423–428 (2004)
295. S.-J. Park, J.C. Doll, B.L. Pruitt, Piezoresistive cantilever performance—part I: Analytical model for sensitivity. *J. Microelectromech. Syst.* **19**(1), 149–161 (2010)
296. A.A. Barlian, N. Harjee, V. Mukundan, T.H. Fung, S.-J. Park, B.L. Pruitt, Sidewall epitaxial piezoresistor process for in-plane sensing applications, in *Proceedings of IEEE MEMS*, pp. 331–334, 2008
297. B. Neri, C. Ciofi, V. Dattilo, Noise and fluctuations in submicrometric al-si interconnect lines. *IEEE Trans. Electron Devices* **44**(9), 1454–1459 (1997)
298. E.P. Vandamme, L.K.J. Vandamme, Current crowding and its effect on 1/f noise and third harmonic distortion—a case study for quality assessment of resistors. *Microelectron. Reliab.* **40**(11), 1847–1853 (2000)
299. F.N. Hooge, Discussion of recent experiments on 1/f noise. *Physica* **60**(1), 130–144 (1972)
300. L.K.J. Vandamme, W.V. Bokhoven, Conductance noise investigations with four arbitrarily shaped and placed electrodes. *Appl. Phys. A* **14**(2), 205–215 (1977)
301. J. Harley, Advances in piezoresistive probes for atomic force microscopy. Ph.D. dissertation, Stanford University, 2000
302. R.H.M. Clevers, 1/f noise in ion-implanted resistors between 77 and 300 k. *J. Appl. Phys.* **62**(5), 1877–1881 (1987)
303. L.K.J. Vandamme, S. Oosterhoff, Annealing of ion implanted resistors reduces the 1/f noise. *J. Appl. Phys.* **59**(9), 3169–3174 (1986)
304. L.K.J. Vandamme, Noise as a diagnostic tool for quality and reliability of electronic devices. *IEEE Trans. Electron Devices* **41**(11), 2176–2187 (1994)
305. B.W. Chui, T.D. Stowe, T.W. Kenny, H.J. Mamin, B.D. Terris, Low-stiffness silicon cantilevers for thermal writing and piezoresistive readback. *Appl. Phys. Lett.* **69**, 2767–2769 (1996)
306. B. Bhushan (ed.), *Springer Handbook of Nanotechnology* (Springer, New York, 2007)
307. S.W. Jones, *Diffusion in Silicon* (IC Knowledge LLC, Georgetown, 2008)
308. M.M. Jevtic, Impurity concentration dependence of the 1/f noise parameter in silicon. *Solid-State Electron.* **31**(6), 1049–1052 (1988)
309. A. Armigliato, D. Nobili, M. Servidori, S. Solmi, SiP precipitation within the doped silicon lattice, concomitant with phosphorus predeposition. *J. Appl. Phys.* **47**(12), 5489–5491 (1976)
310. S. Solmi, A. Parisini, R. Angelucci, A. Armigliato, D. Nobili, L. Moro, Dopant and carrier concentration in Si in equilibrium with monoclinic SiP precipitates. *Phys. Rev. B* **53**(12), 7836–7841 (1996)
311. T.B. Gabrielson, Mechanical-thermal noise in micromachined acoustic and vibration sensors. *IEEE Trans. Electron Devices* **40**(5), 903–909 (1993)
312. D.R. Brumley, M. Willcox, J.E. Sader, Oscillation of cylinders of rectangular cross section immersed in fluid. *Phys. Fluids* **22**(5), 052001 (2010)

313. M. Tortonese, Force sensors for scanning probe microscopy. Ph.D. dissertation, Stanford University, 1993
314. O.N. Tufte, D. Long, Recent developments in semiconductor piezoresistive devices. *Solid-State Electron.* **6**(4), 323–338 (1963)
315. V.P. Group, Errors due to transverse sensitivity in strain gauges, TN-509. Vishay Inc, Tech. Rep., 2011
316. C.T. Sah, *Fundamentals of Solid-State Electronics* (World Scientific, London, 1991)
317. R.G. Pires, R.M. Dickstein, S.L. Titcomb, R.L. Anderson, Carrier freezeout in silicon. *Cryogenics* **30**(12), 1064–1068 (1990)
318. A. Volodin, K. Temst, C.V. Haesendonck, Y. Bruynseraeed, Low temperature magnetic force microscopy with enhanced sensitivity based on piezoresistive detection. *Rev. Sci. Instrum.* **71**(12), 4468–4473 (2000)
319. M. Roseman, P. Grutter, Cryogenic magnetic force microscope. *Rev. Sci. Instrum.* **71**(10), 3782–3787 (2000)
320. F.A. Trumbore, Solid solubilities of impurity elements in germanium and silicon. *Bell. Syst. Tech. J.* **39**(1), 205–233 (1960)
321. V.E. Borisenko, S.G. Yudin, Steady-state solubility of substitutional impurities in silicon. *Phys. Status Solidi A* **101**(1), 123–127 (1987)
322. G.L. Vick, K.M. Whittle, Solid solubility and diffusion coefficients of boron in silicon. *J. Electrochem. Soc.* **116**(8), 1142–1144 (1969)
323. J.C. Wolfe, W. Zagozdzon-Wosik, Method and apparatus for doping silicon wafers using a solid dopant source and rapid thermal processing. U.S. Patent 5,550,082, 27, 1996
324. C.S. Yoo, *Semiconductor Manufacturing Technology* (World Scientific, London, 2008)
325. B.H. Justice, R.F. Aycock, Spin-on dopant method. U.S. Patent 4,514,440, 12, 1983
326. S.P. Proctor, M.M. Crain, K.M. Walsh, P+ structural layers for microelectromechanical systems using spin-on dopants. *Sens. Lett.* **2**(3–4), 211–216 (2004)
327. Z.T. Zhu, E. Menard, K. Hurley, R.G. Nuzzo, J.A. Rogers, Spin on dopants for high-performance single-crystal silicon transistors on flexible plastic substrates. *Appl. Phys. Lett.* **86**(13), 133507 (2005)
328. S. Franssila, *Introduction to Microfabrication* (John Wiley & Sons, New York, 2004)
329. S. Solmi, D. Nobili, High concentration diffusivity and clustering of arsenic and phosphorus in silicon. *J. Appl. Phys.* **83**(5), 2484–2490 (1998)
330. J.C.C. Tsai, Shallow phosphorus diffusion profiles in silicon. *Proc. IEEE* **57**(9), 1499–1506 (1969)
331. Y.M. Haddara, B.T. Folmer, M.E. Law, T. Buyuklimanli, Accurate measurements of the intrinsic diffusivities of boron and phosphorus in silicon. *Appl. Phys. Lett.* **77**(13), 1976–1978 (2000)
332. R. Duffy, V.C. Venezia, J. Loo, M.J.P. Hopstaken, M.A. Verheijen, J.G.M. van Berkum, G.C.J. Maas, Y. Tamminga, T. Dao, C. Demeurisse, Low-temperature diffusion of high-concentration phosphorus in silicon, a preferential movement toward the surface. *Appl. Phys. Lett.* **86**(8), 081917 (2005)
333. A.N. Gorban, V.A. Gorodokin, Low-temperature diffusion of phosphorus in silicon. *Russ. Phys. J.* **31**(9), 737–740 (1988)
334. R.B. Fair, J.C.C. Tsai, A quantitative model for the diffusion of phosphorus in silicon and the emitter dip effect. *J. Electrochem. Soc.* **124**(7), 1107–1118 (1977)
335. S.M. Hu, P. Fahey, R.W. Dutton, On models of phosphorus diffusion in silicon. *J. Appl. Phys.* **54**(12), 6912–6922 (1983)
336. C.T. Sah, H. Sello, D.A. Tremere, Diffusion of phosphorus in silicon oxide film. *J. Phys. Chem. Solids* **11**(3–4), 288–298 (1959)
337. M. Ghezzo, D.M. Brown, Diffusivity summary of b, ga, p, as, and sb in sio2. *J. Electrochem. Soc.* **120**(1), 146–148 (1973)
338. R.S. Ohl, Properties of ionic bombarded silicon. *Bell Syst. Tech. J.* **31**(1), 104–121 (1952)
339. W. Shockley, Forming semiconductive devices by ionic bombardment. U.S. Patent 2,787,564, 28, 1954

340. W.D. Cussins, Effects produced by the ionic bombardment of germanium. *P. Phys. Soc. Lond. B* **68**(4), 213–222 (1955)
341. J.W. Mayer, O.J. Marsh, G.A. Shifrin, R. Baron, Ion implantation of silicon: II. electrical evaluation using hall-effect measurements. *Can. J. Phys.* **45**(12), 4073–4089 (1967)
342. J.F. Gibbons, Ion implantation in semiconductors: I. range distribution theory and experiments. *Pr. Inst. Electr. Elect.* **56**(3), 295–319 (1968)
343. L.N. Large, Ion implantation—a new method of doping semiconductors. *Contemp. Phys.* **10**(5), 505–531 (1969)
344. T.E. Seidel, A.U. Macrae, Some properties of ion implanted boron in silicon. *T. Metall Soc. Aime* **245**(3), 491–498 (1969)
345. J.F. Gibbons, Ion implantation in semiconductors: II. damage production and annealing. *Pr. Inst. Electr. Elect.* **60**(9), 1062–1096 (1972)
346. J.W. Mayer, Ion implantation in semiconductors, in *Proceedings of IEEE IEDM*, pp. 3–5, 1973
347. J.A. Davies, Early ion implantation history. *Mater. Chem. Phys.* **46**(2–3), 111–117 (1996)
348. C.B. Yarling, History of industrial and commercial ion implantation 1906–1978. *J. Vac. Sci. Technol. A* **18**(4), 1746–1750 (2000)
349. L. Godet, G.D. Papasouliotis, A. Kontos, T. Miller, V. Singh, Advanced plasma doping technique for usj, in *International Workshop on Junction Technology*, pp. 86–90, 2009
350. H. Chen, F. Sinclair, M. Sugitani, Dose control for use in an ion implanter. U.S. Patent 5,760,409 1998
351. M. Gel, I. Shimoyama, Sub-micron thick high sensitive piezoresistive cantilevers by boron etch stop and argon implantation. *J. Microelectromech. Syst.* **12**(6) (2003)
352. F.N. Schwettmann, Characterization of incomplete activation of high dose boron implants in silicon. *J. Appl. Phys.* **45**(4), 1918–1920 (1974)
353. K. Sakamoto, K. Nishi, F. Ichikawa, S. Ushio, Segregation and transport coefficients of impurities at the si/sio₂ interface. *J. Appl. Phys.* **61**(4), 1553–1555 (1987)
354. B. Joyce, J. Baldrey, Selective epitaxial deposition of silicon. *Nature* **195**(4840), 485–486 (1962)
355. L. Jastrzebski, SOI by CVD: epitaxial lateral overgrowth (ELO) process-review. *J. Cryst. Growth* **63**(3), 493–526 (1983)
356. R. Pagliaro, J. Corboy, L. Jastrzebski, R. Soydan, Uniformly thick selective epitaxial silicon. *J. Electrochem. Soc.* **134**(5), 1235–1238 (1987)
357. B.J. Ginsberg, J. Burghartz, G.B. Bronner, S.R. Mader, Selective epitaxial growth of silicon and some potential applications. *IBM J. Res. Dev.* **34**(6), 816–827 (1990)
358. M.R. Goulding, The selective epitaxial growth of silicon. *J. Phys. IV France* **02**(C2), 745–778 (1991)
359. M. Bartek, P.T.J. Gennissen, P.J. French, P.M. Sarro, R.F. Wolffenbuttel, Study of selective and non-selective deposition of single- and polycrystalline silicon layers in an epitaxial reactor, in *Proceedings of Transducers*, pp. 1403–1406, 1997
360. J. Pak, Micromechanical sensors using merged epitaxial lateral overgrowth of silicon. Ph.D. dissertation, Purdue University, 1993
361. J.L. Regolini, D. Bensahel, E. Scheid, J. Mercier, Selective epitaxial silicon growth in the 650–1100 C range in a reduced pressure chemical vapor deposition reactor using dichlorosilane. *Appl. Phys. Lett.* **54**(7), 658–659 (1989)
362. Y. Onuma, K. Sekiya, Piezoresistive properties of polycrystalline silicon thin-film. *Jpn. J. Appl. Phys.* **11**(1), 20–23 (1972)
363. R.W. Gurtler, R.W. Zwerneemann, Polycrystalline silicon pressure sensor. U.S. Patent 3,858,150, 31, 1974
364. J.Y.W. Seto, The electrical properties of polycrystalline silicon films. *J. Appl. Phys.* **46**, 5247–5254 (1975)
365. J.Y.W. Seto, Piezoresistive properties of polycrystalline silicon. *J. Appl. Phys.* **47**(11), 4780–4783 (1976)

366. N.C.C. Lu, L. Gerzberg, C.Y. Lu, J.D. Meindl, Modeling and optimization of monolithic polycrystalline silicon resistors. *IEEE Trans. Electron Devices* **28**(7), 818–830 (1981)
367. N.C.C. Lu, L. Gerzberg, C.Y. Lu, J.D. Meindl, A new conduction model for polycrystalline silicon films. *Electron Device Lett.* **2**(4), 95–98 (1981)
368. M.M. Mandurah, K.C. Saraswat, T.I. Kamins, A model for conduction in polycrystalline silicon: I. theory. *IEEE Trans. Electron Devices* **28**(10), 1163–1171 (1981)
369. M.M. Mandurah, The physical and electrical properties of polycrystalline-silicon. Ph.D. dissertation, Stanford University, 1981
370. H. Mikoshiba, Stress-sensitive properties of silicon-gate mos devices. *Solid State Electron.* **24**(3), 221–232 (1981)
371. W. Germer, W. Todt, Low-cost pressure force transducer with silicon thin-film strain-gauges. *Sens. Actuator* **4**(2), 183–189 (1983)
372. J.C. Erskine, Polycrystalline silicon-on-metal strain-gauge transducers. *IEEE Trans. Electron Devices* **30**(7), 796–801 (1983)
373. P.J. French, A.G.R. Evans, Piezoresistance in polysilicon. *Electron. Lett.* **20**(24), 999–1000 (1984)
374. P.J. French, A.G.R. Evans, Piezoresistance in polysilicon and its applications to strain-gauges. *Solid State Electron.* **32**(1), 1–10 (1989)
375. M. Madou, *Fundamentals of Microfabrication: The Science of Miniaturization* (Taylor & Francis Group, London, 2002)
376. M. Bao, *Analysis and Design Principles of MEMS Devices* (Elsevier, Amsterdam, 2005)
377. T. Trupke, M.A. Green, P. Wurfel, P.P. Altermatt, A. Wang, J. Zhao, R. Corkish, Temperature dependence of the radiative recombination coefficient of intrinsic crystalline silicon. *J. Appl. Phys.* **94**(8), 4930–4937 (2003)
378. C.D. Thurmond, The standard thermodynamic functions for the formation of electrons and holes in Ge, Si, GaAs, and GaP. *J. Electrochem. Soc.* **122**(8), 1133–1141 (1975)
379. S. Reggiani, M. Valdinoci, L. Colalongo, M. Rudan, G. Baccarani, A.D. Stricker, F. Illien, N. Felber, W. Fichtner, L. Zullino, Electron and hole mobility in silicon at large operating temperatures. I. bulk mobility. *IEEE Trans. Electron Devices* **49**(3), 490–499 (2002)
380. A. Manara, A. Ostidich, G. Pedroli, G. Restelli, Anodic oxidation as sectioning technique for the analysis of impurity concentration profiles in silicon. *Thin Solid Films* **8**(5), 359–375 (1971)
381. P. Gaworzewski, L. Kalman, H. Rausch, M. Trapp, Doping profile techniques for Si epitaxial layers. *J. Radioanal. Nucl. Chem.* **52**, 93–100 (1979)
382. R. Levy, *Microelectronic Materials and Processes* (Springer, New York, 1989)
383. D.K. Schroder, *Semiconductor Material and Device Characterization* (John Wiley & Sons, New York, 2006)
384. H.W. Werner, Quantitative secondary ion mass spectrometry: a review. *Surf. Interface Anal.* **2**(2), 56–74 (1980)
385. P. Williams, Secondary ion mass spectrometry. *Annu. Rev. Mater. Sci.* **15**(1), 517–548 (1985)
386. A. Benninghoven, F.G. Rudenauer, H.W. Werner, *Secondary Ion Mass Spectrometry: Basic Concepts, Instrumental Aspects, Applications and Trends* (John Wiley & Sons, New York, 1987)
387. D.H. Dickey, J.R. Ehrestein, *Spreading Resistance Analysis for Silicon Layers with Nonuniform Resistivity* (National Bureau of Standards, Washington DC, 1979)
388. R.G. Mazur, D.H. Dickey, A spreading resistance technique for resistivity measurements on silicon. *J. Electrochem. Soc.* **113**(3), 255–259 (1966)
389. C.C. Williams, Two-dimensional dopant profiling by scanning capacitance microscopy. *Annu. Rev. Mater. Sci.* **29**(1), 471–504 (1999)
390. J.J. Kopanski, J.F. Marchiando, J.R. Lowney, Scanning capacitance microscopy measurements and modeling: Progress towards dopant profiling of silicon. *J. Vac. Sci. Technol. B* **14**(1), 242–247 (1996)
391. A.K. Henning, T. Hochwitz, J. Slinkman, J. Never, S. Hoffmann, P. Kaszuba, C. Daglian, Two-dimensional surface dopant profiling in silicon using scanning kelvin probe microscopy. *J. Appl. Phys.* **77**(5), 1888–1896 (1995)

392. R. Galloni, A. Sardo, Fully automatic apparatus for the determination of doping profiles in Si by electrical measurements and anodic stripping. *Rev. Sci. Instrum.* **54**(3), 369–373 (1983)
393. A. Gharbi, B. Remaki, A. Halimaoui, D. Bensahel, A. Souifi, p-type silicon doping profiling using electrochemical anodization. *J. Appl. Phys.* **109**(2), 023715 (2011)
394. S.S. Iyer, A.J. Auberton-Herve, *Silicon Wafer Bonding Technology for VLSI and MEMS Applications* (The Institution of Electrical Engineers, London, 2002)
395. A.J. Maria, *SiMOX* (The Institution of Electrical Engineers, London, 2004)
396. A. Nafari, D. Karlen, C. Rusu, K. Svensson, P. Enoksson, Boron impurity at the Si/SiO₂ interface in SOI wafers and consequences for piezoresistive MEMS devices. *J. Micromech. Microeng.* **19**(1), 015034 (2009)
397. T. Iida, T. Itoh, D. Noguchi, Y. Takano, Residual lattice strain in thin silicon-on-insulator bonded wafers: Thermal behavior and formation mechanisms. *J. Appl. Phys.* **87**(2), 675–681 (2000)
398. G. Celotti, D. Nobili, P. Ostoja, Lattice parameter study of silicon uniformly doped with boron and phosphorus. *J. Mater. Sci.* **9**, 821–828 (1974)
399. C.S. Lee, J.H. Lee, C.A. Choi, K. No, D.M. Wee, Effects of phosphorus on stress of multi-stacked polysilicon film and single crystalline silicon. *J. Micromech. Microeng.* **9**(3), 252 (1999)
400. K.G. McQuhae, A.S. Brown, The lattice contraction coefficient of boron and phosphorus in silicon. *Solid-State Electron.* **15**(3), 259–264 (1972)
401. T. Hubbard, J. Wylde, Residual strain and resultant postrelease deflection of surface micro-machined structures. *J. Vac. Sci. Technol. A* **18**(2), 734–737 (2000)
402. A.M. Lin, R.W. Dutton, D.A. Antoniadis, The lateral effect of oxidation on boron diffusion in (100) silicon. *Appl. Phys. Lett.* **35**(10), 799–801 (1979)
403. F.N. Hooge, L. Ren, On generation-recombination noise. *Physica B: Condens. Matter* **191**(34), 220–226 (1993)
404. H.H. Berger, Contact resistance and contact resistivity. *J. Electrochem. Soc.* **119**(4), 507–514 (1972)
405. K.K. Ng, R. Liu, On the calculation of specific contact resistivity on (100) Si. *IEEE Trans. Electron Devices* **37**(6), 1535–1537 (1990)
406. D.K. Schroder, D.L. Meier, Solar cell contact resistance—a review. *IEEE Trans. Electron Devices* **31**(5), 637–647 (1984)
407. C.Y. Ting, M. Wittmer, The use of titanium-based contact barrier layers in silicon technology. *Thin Solid Films* **96**(4), 327–345 (1982)
408. S.P. Murarka, Interactions in metallization systems for integrated circuits. *J. Vac. Sci. Technol. B* **2**(4), 693–706 (1984)
409. N.G. Einspruch, S.S. Cohen, G.S. Gildenblat, *VLSI Metallization* (Academic Press, New York, 1987)
410. M. Perrott, J. Salvia, F. Lee, A. Partridge, S. Mukherjee, C. Arft, J.-T. Kim, N. Arumugam, P. Gupta, S. Tabatabaei, S. Pamarti, H.-C. Lee, F. Assaderaghi, A temperature-to-digital converter for a MEMS-based programmable oscillator with better than 0.5ppm frequency stability, in *Proceedings of IEEE Solid-State Circuits Conference*, pp. 206–208, 2012
411. A.D. Kurtz, Adjusting crystal characteristics to minimize temperature dependency, in *Semiconductor and Conventional Strain Gages*, ed. by M. Dean (Academic Press, New York, 1962)
412. M. Olszacki, C. Maj, M.A. Bahri, J.C. Marrot, A. Boukabache, P. Pons, A. Napieralski, Experimental verification of temperature coefficients of resistance for uniformly doped p-type resistors in SOI. *J. Micromech. Microeng.* **20**(6), 064008 (2010)
413. W.M. Bullis, F.H. Brewer, C.D. Kolstad, L.J. Swartzendruber, Temperature coefficient of resistivity of silicon and germanium near room temperature. *Solid-State Electron.* **11**(7), 639–646 (1968)
414. K.J. Kim, W.P. King, Thermal conduction between a heated microcantilever and a surrounding air environment. *Appl. Therm. Eng.* **29**(8–9), 1631–1641 (2009)

415. M. von Arx, O. Paul, H. Baltes, Process-dependent thin-film thermal conductivities for thermal CMOS MEMS. *J. Microelectromech. Syst.* **9**(1), 136–145 (2000)
416. C. Liu, *Foundations of MEMS* (Pearson Prentice Hall, New Jersey, 2006)
417. M. Asheghi, Y.K. Leung, S.S. Wong, K.E. Goodson, Phonon-boundary scattering in thin silicon layers. *Appl. Phys. Lett.* **71**(13), 1798–1800 (1997)
418. W. Liu, K. Etessam-Yazdani, R. Hussin, M. Asheghi, Modeling and data for thermal conductivity of ultrathin single-crystal SOI layers at high temperature. *IEEE Trans. Electron Devices* **53**(8), 1868–1876 (2006)
419. F.P. Incropera, T.L. Bergman, A.S. Lavine, D.P. DeWitt, *Fundamentals of Heat and Mass Transfer* (John Wiley & Sons, New York, 2011)
420. O. Ozsun, B.E. Alaca, A.D. Yalcinkaya, M. Yilmaz, M. Zervas, Y. Leblebici, On heat transfer at microscale with implications for microactuator design. *J. Micromech. Microeng.* **19**(4), 045020 (2009)
421. X.J. Hu, A. Jain, K.E. Goodson, Investigation of the natural convection boundary condition in microfabricated structures. *Int. J. Therm. Sci.* **47**(7), 820–824 (2008)
422. K. Park, G.L.W. Cross, Z.M. Zhang, W.P. King, Experimental investigation on the heat transfer between a heated microcantilever and a substrate. *J. Heat Transfer* **130**(10), 102401 (2008)
423. J. Lee, T. Beechem, T.L. Wright, B.A. Nelson, S. Graham, W.P. King, Electrical, thermal, and mechanical characterization of silicon microcantilever heaters. *J. Microelectromech. Syst.* **15**(6), 1644–1655 (2006)
424. B.A. Nelson, W.P. King, Temperature calibration of heated silicon atomic force microscope cantilevers. *Sens. Actuators A* **140**(1), 51–59 (2007)
425. M.R. Abel, T.L. Wright, W.P. King, S. Graham, Thermal metrology of silicon microstructures using raman spectroscopy. *IEEE Trans. Compon. Packag. Technol.* **30**(2), 200–208 (2007)
426. K.E. Goodson, M.I. Flik, Effect of microscale thermal conduction on the packing limit of silicon-on-insulator electronic devices. *IEEE Trans. Compon. Hybrids Manuf. Technol.* **15**(5), 715–722 (1992)
427. M. Engesser, A.R. Franke, M. Maute, D.C. Meisel, J.G. Korvink, A robust and flexible optimization technique for efficient shrinking of MEMS accelerometers. *Microsyst. Technol.* **16**(4), 647–654 (2010)
428. C. Zhu, R. Byrd, P. Lu, J. Nocedal, L-BFGS-B: Fortran subroutines for large-scale bound constrained optimization. *ACM Trans. Math. Softw.* **23**(4), 550–560 (1997)
429. S.P. Boyd, L. Vandenberghe, *Convex Optimization* (Cambridge University Press, Cambridge, 2004)
430. J. Nocedal, S.J. Wright, *Numerical Optimization* (Springer, New York, 1999)
431. M. Engesser, A. Franke, M. Maute, D. Meisel, J. Korvink, Miniaturization limits of piezoresistive MEMS accelerometers. *Microsyst. Technol.* **15**, 1835–1844 (2009)
432. K. Naeli, O. Brand, Dimensional considerations in achieving large quality factors for resonant silicon cantilevers in air. *J. Appl. Phys.* **105**(1), 014908 (2009)
433. C.V. Eysden, J. Sader, Frequency response of cantilever beams immersed in viscous fluids with applications to the atomic force microscope: Arbitrary mode order. *J. Appl. Phys.* **101**(4), 044908 (2007)
434. L. Lin, H.-C. Chu, Y.-W. Lu, A simulation program for the sensitivity and linearity of piezoresistive pressure sensors. *J. Microelectromech. Syst.* **8**(4), 514–522 (1999)
435. M.D. Williams, Development of a MEMS piezoelectric microphone for aeroacoustic applications. Ph.D. dissertation, University of Florida, 2011
436. M.D. Williams, B.A. Griffin, T.N. Reagan, J.R. Underbrink, M. Sheplak, An AlN MEMS piezoelectric microphone for aeroacoustic applications. *J. Microelectromech. Syst.* **21**(2), 270–283 (2012)
437. S. Kota, J. Joo, Z. Li, S.M. Rodgers, J. Sniegowski, Design of compliant mechanisms: Applications to MEMS. *Analog Integr. Circ. Sig. Process.* **29**(1–2), 7–15 (2001)
438. L. Yin, G.K. Ananthasuresh, A novel topology design scheme for the multi-physics problems of electro-thermally actuated compliant micromechanisms. *Sens. Actuators A* **97–98**, 599–609 (2002)

439. K. Maute, D.M. Frangopol, Reliability-based design of MEMS mechanisms by topology optimization. *Comput. Struct.* **81**(8–11), 813–824 (2003)
440. J.C. Doll, Biocompatible nanoplasmonic probes for the detection of single biomolecules. Master's thesis, UC Berkeley, 2005
441. O. Kordina, S.E. Saddow, Silicon carbide overview, in *Advances in Silicon Carbide Processing*, eds. by S.E. Saddow, A. Agarwal (Artech House Publishers, Norwood, 2004)
442. M.R. Werner, W.R. Fahrner, Review on materials, microsensors, systems, and devices for high-temperature and harsh-environment applications. *IEEE T. Ind. Electron.* **48**(2), 249–257 (2001)
443. P.M. Sarro, Silicon carbide as a new MEMS technology. *Sens. Actuators A* **82**(1–3), 210–218 (2000)
444. D.G. Senesky, A.P. Pisano, Aluminum nitride as a masking material for the plasma etching of silicon carbide structures, in *Proceedings of IEEE MEMS*, pp. 352–355, 2010
445. J.B. Casady, R.W. Johnson, Status of silicon carbide (sic) as a wide-bandgap semiconductor for high-temperature applications: A review. *Solid-State Electron.* **39**(10), 1409–1422 (1996)
446. J.S. Shor, D. Goldstein, A.D. Kurtz, Characterization of n-type beta-sic as a piezoresistor. *IEEE Trans. Electron Devices* **40**(6), 1093–1099 (1993)
447. J.S. Shor, L. Bemis, A.D. Kurtz, Characterization of monolithic n-type 6h-sic piezoresistive sensing elements. *IEEE Trans. Electron Devices* **41**(5), 661–665 (1994)
448. R. Ziermann, J. von Berg, W. Reichert, E. Obermeier, M. Eickhoff, G. Krotz, A high temperature pressure sensor with beta-SiC piezoresistors on SOI substrates, in *Proceedings of Transducers*, pp. 1411–1414, 1997
449. M. Werner, G. Krotz, H. Moller, M. Eickhoff, P. Gluche, M. Adamschik, C. Johnston, P.R. Chalker, High-temperature sensors based on SiC and diamond technology. *Sens. Update* **5**(1), 141–190 (1999)
450. F. Bechstedt, P. Kackell, A. Zywietz, K. Karch, B. Adolph, K. Tenelsen, J. Furthmuller, Polyytypism and properties of silicon carbide. *Phys. Status Solidi B* **202**(1), 35–62 (1997)
451. R.S. Okojie, A.A. Ned, A.D. Kurtz, W.N. Carr, Characterization of highly doped n- and p-type 6H-SiC piezoresistors. *IEEE Trans. Electron Devices* **45**(4), 785–790 (1998)
452. J. Strass, M. Eickhoff, G. Kroetz, The influence of crystal quality on the piezoresistive effect of beta-SiC between rt and 450c measured by using microstructures, in *Proceedings of Transducers*, pp. 1439–1442, 1997
453. S.K. Wang, D.D.L. Chung, Piezoresistivity in silicon carbide fibers. *J. Electroceram.* **10**(3), 147–152 (2003)
454. T. Toriyama, S. Sugiyama, Analysis of piezoresistance in n-type beta-SiC for high-temperature mechanical sensors. *Appl. Phys. Lett.* **81**(15), 2797–2799 (2002)
455. T. Toriyama, Piezoresistance consideration on n-type 6H-SiC for MEMS-based piezoresistance sensors. *J. Micromech. Microeng.* **14**(11), 1445–1448 (2004)
456. A.R. Atwell, R.S. Okojie, K.T. Kornegay, S.L. Roberson, A. Beliveau, Simulation, fabrication and testing of bulk micromachined 6H-SiC high-g piezoresistive accelerometers. *Sens. Actuators A* **104**(1), 11–18 (2003)
457. M. Eickhoff, H. Moller, G. Kroetz, J.V. Berg, R. Ziermann, A high temperature pressure sensor prepared by selective deposition of cubic silicon carbide on SOI substrates. *Sens. Actuators A* **74**(1–3), 56–59 (1999)
458. R.S. Okojie, A.A. Ned, A.D. Kurtz, Operation of alpha(gh)-sic pressure sensor at 500 degrees c. *Sens. Actuators A* **66**(1–3), 200–204 (1998)
459. C.H. Wu, C.A. Zorman, M. Mehregany, Fabrication and testing of bulk micromachined silicon carbide piezoresistive pressure sensors for high temperature applications. *IEEE Sens.* **6**(2), 316–324 (2006)
460. M. Mehregany, C.A. Zorman, N. Rajan, C.H. Wu, Silicon carbide MEMS for harsh environments. *Proc. IEEE* **86**(8), 1594–1610 (1998)
461. M. Mehregany, C.A. Zorman, SiC MEMS: opportunities and challenges for applications in harsh environments. *Thin Solid Films* **355**, 518–524 (1999)

462. C.A. Zorman, M. Mehregany, Silicon carbide for MEMS and NEMS, in *Proceedings of IEEE Sensors*, pp. 1109–1114, 2002
463. M. Werner, P. Gluche, M. Adamschik, E. Kohn, H.J. Fecht, Review on diamond based piezoresistive sensors, in *Proceedings of IEEE International Symposium on Industrial Electronics*, pp. 147–152, 1998
464. P.D' Evelyn, E. Slutz, E. Williams, Elastic properties of CVD diamond via dynamic resonance measurements, in *Proceedings of Material Research Society, Symposium*, pp. 115–120, 1995
465. P.C. Fletcher, J.R. Felts, Z. Dai, T.D. Jacobs, H. Zeng, W. Lee, P.E. Sheehan, J.A. Carlisle, R.W. Carpick, W.P. King, Wear-resistant diamond nanoprobe tips with integrated silicon heater for tip-based nanomanufacturing. *ACS Nano* **4**(6), 3338–3344 (2010)
466. A. Yamamoto, T. Tsutsumoto, Piezoresistive effect of cvd polycrystalline diamond films. *Diam. Relat. Mater.* **13**(4–8), 863–866 (2004)
467. J. Isberg, J. Hammersberg, E. Johansson, T. Wikström, D.J. Twitchen, A.J. Whitehead, S.E. Coe, G.A. Scarsbrook, High carrier mobility in single-crystal plasma-deposited diamond. *Science* **297**(5587), 1670–1672 (2002)
468. Y. Tang, D.M. Aslam, J. Wang, K.D. Wise, Study of polycrystalline diamond piezoresistive position sensors for application in cochlear implant probe. *Diam. Relat. Mater.* **15**, 199–202 (2006)
469. S. Sahli, D.M. Aslam, Ultra-high sensitivity intra-grain poly-diamond piezoresistors. *Sens. Actuators A* **71**(3), 193–197 (1998)
470. C. Stampfer, T. Helbling, D. Obergfell, B. Schoberle, M.K. Tripp, A. Jungen, S. Roth, V.M. Bright, C. Hierold, Fabrication of single-walled carbon-nanotube-based pressure sensors. *Nano Lett.* **6**(2), 233–237 (2006)
471. H.J. Dai, Carbon nanotubes: opportunities and challenges. *Surf. Sci.* **500**(1–3), 218–241 (2002)
472. A. Maiti, Carbon nanotubes—bandgap engineering with strain. *Nat. Mater.* **2**(7), 440–442 (2003)
473. R.J. Grow, Electromechanical properties and applications of carbon nanotubes, in *Carbon Nanotubes: Properties and Applications*, ed. by M.J. O'Connell (CRC Press, Boca Raton, 2006)
474. S. Iijima, Helical microtubules of graphitic carbon. *Nature* **354**(6348), 56–58 (1991)
475. J.P. Salvetat, A.J. Kulik, J.M. Bonard, G.A.D. Briggs, T. Stockli, K. Metenier, S. Bonnamy, F. Beguin, N.A. Burnham, L. Forro, Elastic modulus of ordered and disordered multiwalled carbon nanotubes. *Adv. Mater.* **11**(2), 161–165 (1999)
476. D. Qian, G. Wagner, W. Liu, M. Yu, R.S. Ruoff, Mechanics of carbon nanotubes. *Appl. Mech. Rev.* **55**(6), 495–533 (2002)
477. J. Cao, Q. Wang, H.J. Dai, Electromechanical properties of metallic, quasimetallic, and semiconducting carbon nanotubes under stretching. *Phys. Rev. Lett.* **90**(15), 157601 (2003)
478. P. Regoliosi, A. Reale, A.D. Carlo, S. Orlanducci, M.L. Terranova, P. Lugli, Piezoresistive behaviour of single wall carbon nanotubes, in *Proceedings of IEEE, Nanotechnology*, pp. 149–151, 2004
479. T.W. Tombler, C.W. Zhou, L. Alexseyev, J. Kong, H.J. Dai, L. Lei, C.S. Jayanthi, M.J. Tang, S.Y. Wu, Reversible electromechanical characteristics of carbon nanotubes under local-probe manipulation. *Nature* **405**(6788), 769–772 (2000)
480. C. Hierold, A. Jungen, C. Stampfer, T. Helbling, Nanoelectromechanical sensors based on carbon nanotubes. *Sens. Actuators A* **136**(1), 51–61 (2007)
481. R.J. Grow, Q. Wang, J. Cao, D.W. Wang, H.J. Dai, Piezoresistance of carbon nanotubes on deformable thin-film membranes. *Appl. Phys. Lett.* **86**(9), 093104 (2005)
482. T. Toriyama, S. Sugiyama, Single crystal silicon piezoresistive nano-wire bridge. *Sens. Actuators A* **108**, 244–249 (2003)
483. H.C. Chiamori, J.W. Brown, E.V. Adhiprakasha, E.T. Hantsoo, J.B. Straalsund, N.A. Melosh, B.L. Pruitt, Suspension of nanoparticles in SU-8: Processing and characterization of nanocomposite polymers. *Microelectron. J.* **39**(2), 228–236 (2008)

484. Y. Kondo, K. Takayanagi, Synthesis and characterization of helical multi-shell gold nanowires. *Science* **289**(5479), 606–608 (2000)
485. S. Bansal, E. Toimil-Molares, A. Saxena, R.R. Tummala, Nanoindentation of single crystal and polycrystalline copper nanowires, in *Proceedings of Electronic Components and Technology Conference*, pp. 71–76, 2005
486. A. Desai, M. Haque, Test bed for mechanical characterization of nanowires. *Proc. Inst. Mech. Eng.* **219**(2), 57–65 (2006)
487. T.H. Fang, W.J. Chang, Nanolithography and nanoindentation of tantalum-oxide nanowires and nanodots using scanning probe microscopy. *Phys. B* **352**(1–4), 190–199 (2004)
488. X.D. Li, P. Nardi, C.W. Baek, J.M. Kim, Y.K. Kim, Direct nanomechanical machining of gold nanowires using a nanoindenter and an atomic force microscope. *J. Micromech. Microeng.* **15**(3), 551–556 (2005)
489. S. Lu, J. Chung, D. Dikin, J. Lee, R.S. Ruoff, An integrated MEMS system for in-situ mechanical testing of nanostructures, in *Proceedings of ASME Integrated Nanosystems*, 2004
490. Y. Zhu, H.D. Espinosa, An electromechanical material testing system for in situ electron microscopy and applications. *Proc. Nat. Acad. Sci.* **102**(41), 14503–14508 (2005)
491. M.W. Shao, Y.Y. Shan, N.B. Wong, S.T. Lee, Silicon nanowire sensors for bioanalytical applications: Glucose and hydrogen peroxide detection. *Adv. Funct. Mater.* **15**(9), 1478–1482 (2005)
492. T. Toriyama, D. Funai, S. Sugiyama, Piezoresistance measurement on single crystal silicon nanowires. *J. Appl. Phys.* **93**(1), 561–565 (2003)
493. T. Toriyama, Y. Tanimoto, S. Sugiyama, Single crystal silicon nano-wire piezoresistors for mechanical sensors. *J. Microelectromech. Syst.* **11**(5), 605–611 (2002)
494. D.V. Dao, T. Toriyama, S. Sugiyama, Noise and frequency analyses of a miniaturized 3-DOF accelerometer utilizing silicon nanowire piezoresistors, in *Proceedings of IEEE Sensors*, pp. 1464–1467, 2004
495. M.L. Roukes, H. Tang, Strain sensors based on nanowire piezoresistor wires and arrays. U.S. Patent 7,302,856, 04, 2007
496. R. He, P. Yang, Giant piezoresistance effect in silicon nanowires. *Nat. Nanotechnol.* **1**(1), 42–46 (2006)
497. J.X. Cao, X.G. Gong, R.Q. Wu, Giant piezoresistance and its origin in Si (111) nanowires: First-principles calculations. *Phys. Rev. B* **75**(23), 233302 (2007)
498. K. Reck, J. Richter, O. Hansen, E.V. Thomsen, Determination of the piezoresistivity of micro-crystalline silicon-germanium and application to a pressure sensor, in *Proceedings of IEEE MEMS*, pp. 717–720, 2008
499. T.W. Kenny, Nanometer-scale force sensing with MEMS devices. *IEEE Sens.* **1**(2), 148–157 (2001)
500. O. Solgaard, *Photonic Microsystems: Micro and Nanotechnology Applied to Optical Devices and Systems* (Springer, New York, 2009)
501. C.L. Degen, M. Poggio, H.J. Mamin, C.T. Rettner, D. Rugar, Nanoscale magnetic resonance imaging. *Proc. Nat. Acad. Sci.* **106**(5), 1313–1317 (2009)
502. P.R. Scheper, A.G.H. van der Donk, W. Olthuis, P. Bergveld, A review of silicon microphones. *Sens. Actuators A* **44**(1), 1–11 (1994)
503. N. Yazdi, H. Kulah, K. Najafi, Precision readout circuits for capacitive microaccelerometers, in *Proceedings of IEEE Sensors*, pp. 28–31, 2004
504. P. Estevez, J.M. Bank, M. Porta, J. Wei, P.M. Sarro, M. Tichem, U. Staufer, 6 DOF force and torque sensor for micro-manipulation applications. *Sens. Actuators A* **186**, 86–93 (2012)
505. H. Xie, L. Erdmann, X. Zhu, K.J. Gabriel, G.K. Fedder, Post-CMOS processing for high-aspect-ratio integrated silicon microstructures. *J. Microelectromech. Syst.* **11**(2), 93–101 (2002)
506. G.C. Hill, D.R. Soto, S.J. Lue, A.M. Peattie, R.J. Full, T.W. Kenny, Investigating the role of orientation angle on gecko setae adhesion using a dual-axis MEMS force sensor. *Proc. Trans.* 2263–2266 (2007)

507. Y. Sarov, T. Ivanov, A. Frank, I. Rangelow, Thermally driven multi-layer actuator for 2D cantilever arrays. *Appl. Phys. A* **102**, 61–68 (2011)
508. F. Pourahmadi, L. Christel, K. Petersen, Silicon accelerometer with new thermal self-test mechanism, in *Proceedings of Solid State Sensors, Actuators, and Microsystems, Workshop*, pp. 122–125, 1992
509. J.A. Plaza, A. Collado, E. Cabruja, J. Esteve, Piezoresistive accelerometers for MCM package. *J. Microelectromech. Syst.* **11**(6), 794–801 (2002)
510. J. Chu, R. Maeda, T. Itoh, T. Suga, Tip-scanning dynamic force microscope using piezoelectric cantilever for full wafer inspection. *Jpn. J. Appl. Phys., Part 1* **38**(12B), 7155–7158 (1999)
511. T. Itoh, C. Lee, T. Suga, Deflection detection and feedback actuation using a self-excited piezoelectric pzt microcantilever for dynamic scanning force microscopy. *Appl. Phys. Lett.* **69**(14), 2036–2038 (1996)
512. P.J. Stephanou, G. Piazza, C.D. White, M.B.J. Wijesundara, Mechanically coupled contour mode piezoelectric aluminum nitride MEMS filters, in *Proceedings of IEEE MEMS*, pp. 906–909, 2006
513. S. Minne, J.D. Adams, G. Yaralioglu, S.R. Manalis, A. Atalar, C.F. Quate, Centimeter scale atomic force microscope imaging and lithography. *Appl. Phys. Lett.* **73**(12), 1742–1744 (1998)
514. C. Lee, T. Itoh, R. Maeda, T. Suga, Characterization of micromachined piezoelectric PZT force sensors for dynamic scanning force microscopy. *Rev. Sci. Instrum.* **68**(5), 2091–2100 (1997)
515. J.C. Doll, B.L. Pruitt, Design of piezoresistive versus piezoelectric contact mode scanning probes. *J. Micromech. Microeng.* **20**(9), 095023 (2010)
516. S. Trolier-McKinstry, P. Muralt, Thin film piezoelectrics for MEMS. *J. Electroceram.* **12**, 7–17 (2004)
517. S. Tadigadapa, K. Mateti, Piezoelectric MEMS sensors: state-of-the-art and perspectives. *Meas. Sci. Technol.* **20**(9), 092001 (2009)
518. S.H. Baek, J. Park, D.M. Kim, V.A. Aksyuk, R.R. Das, S.D. Bu, D.A. Felker, J. Lettieri, V. Vaithyanathan, S.S.N. Bharadwaja, N. Bassiri-Gharb, Y.B. Chen, H.P. Sun, C.M. Folkman, H.W. Jang, D.J. Kreft, S.K. Streiffer, R. Ramesh, X.Q. Pan, S. Trolier-McKinstry, D.G. Schlom, M.S. Rzchowski, R.H. Blick, C.B. Eom, Giant piezoelectricity on Si for hyperactive MEMS. *Science* **334**(6058), 958–961 (2011)
519. J.A. Ruffner, P.G. Clem, B.A. Tuttle, D. Dimos, D.M. Gonzales, Effect of substrate composition on the piezoelectric response of reactively sputtered AlN thin films. *Thin Solid Films* **354**(1–2), 256–261 (1999)
520. J. Lee, J. Jung, M. Lee, J. Park, Effects of bottom electrodes on the orientation of AlN films and the frequency responses of resonators in AlN-based FBARs. *Thin Solid Films* **447–448**, 610–614 (2004)
521. F. Martin, P. Muralt, M.A. Dubois, A. Pezous, Thickness dependence of the properties of highly c-axis textured AlN thin films. *J. Vac. Sci. Technol. A* **22**(2), 361–365 (2004)
522. M. Akiyama, N. Ueno, H. Tateyama, K. Nagao, T. Yamada, Preparation of highly oriented aluminum nitride thin films on molybdenum bottom electrodes using metal interlayers. *J. Mater. Sci.* **40**(5), 1159–1162 (2005)
523. D. Isarakorn, A. Sambri, P. Janphuang, D. Briand, S. Gariglio, J.M. Triscone, F. Guy, J.W. Reiner, C.H. Ahn, N.F. de Rooij, Epitaxial piezoelectric MEMS on silicon. *J. Micromech. Microeng.* **20**(5), 055008 (2010)
524. K. Tsubouchi, N. Mikoshiba, Zero temperature coefficient SAW devices on AlN epitaxial films. *IEEE Trans. Sonics Ultrason.* **32**(5), 634–644 (1985)
525. A.F. Wright, Elastic properties of zinc-blende and wurtzite AlN, GaN, and InN. *J. Appl. Phys.* **82**(6), 2833–2839 (1997)
526. M.-A. Dubois, P. Muralt, Measurement of the effective transverse piezoelectric coefficient e_{31}^{TM} of AlN and PZT thin films. *Sens. Actuators A* **77**(2), 106–112 (1999)
527. K. Tonisch, V. Cimalla, C. Foerster, H. Romanus, O. Ambacher, D. Dontsov, Piezoelectric properties of polycrystalline AlN thin films for MEMS application. *Sens. Actuators A* **132**(2), 658–663 (2006)

528. N. Sinha, G.E. Wabiszewski, R. Mahameed, V.V. Felmetser, S.M. Tanner, R.W. Carpick, G. Piazza, Piezoelectric aluminum nitride nanoelectromechanical actuators. *Appl. Phys. Lett.* **95**(5), 053106 (2009)
529. J.C. Doll, B.C. Petzold, B. Ninan, R. Mullapudi, B.L. Pruitt, Aluminum nitride on titanium for CMOS compatible piezoelectric transducers. *J. Micromech. Microeng.* **20**(2), 025008 (2010)
530. H.D. Chen, K.R. Udayakumar, L.E. Cross, J.J. Bernstein, L.C. Niles, Dielectric, ferroelectric, and piezoelectric properties of lead zirconate titanate thick films on silicon substrates. *J. Appl. Phys.* **77**(7), 3349–3353 (1995)
531. S. Watanabe, T. Fujii, T. Fujii, Effect of poling on piezoelectric properties of lead zirconate titanate thin films formed by sputtering. *Appl. Phys. Lett.* **66**(12), 1481–1483 (1995)
532. P. Muralt, M. Kohli, T. Maeder, A. Kholkin, K. Brooks, N. Setter, R. Luthier, Fabrication and characterization of PZT thin-film vibrators for micromotors. *Sens. Actuators A* **48**(2), 157–165 (1995)
533. K.R. Udayakumar, P.J. Schuele, J. Chen, S.B. Krupanidhi, L.E. Cross, Thickness-dependent electrical characteristics of lead zirconate titanate thin films. *J. Appl. Phys.* **77**(8), 3981–3986 (1995)
534. J. Chu, T. Itoh, C. Lee, T. Suga, K. Watanabe, Novel high vacuum scanning force microscope using a piezoelectric cantilever and the phase detection method. *J. Vac. Sci. Technol. B* **15**(4), 1551–1555 (1997)
535. I. Kanno, S. Fujii, T. Kamada, R. Takayama, Piezoelectric properties of c-axis oriented PZT thin films. *Appl. Phys. Lett.* **70**(11), 1378–1380 (1997)
536. J.F. Shepard, F. Chu, I. Kanno, S. Trolier-McKinstry, Characterization and aging response of the d_{31} piezoelectric coefficient of lead zirconate titanate thin films. *J. Appl. Phys.* **85**(9), 6711–6716 (1999)
537. V.V. Felmetser, P.N. Laptev, R.J. Graham, Deposition of ultrathin AlN films for high frequency electroacoustic devices. *J. Vac. Sci. Technol. A* **29**(2), 021014 (2011)
538. X.L. Feng, C.J. White, A. Hajimiri, M.L. Roukes, A self-sustaining ultrahigh-frequency nanoelectromechanical oscillator. *Nat. Nanotechnol.* **3**(6), 342–346 (2008)
539. J.J.E. Gragg, Silicon pressure sensor. U.S. Patent 4,317,126, 23, 1982
540. P. Gieschke, Y. Nurcahyo, M. Herrmann, M. Kuhl, P. Ruther, O. Paul, CMOS integrated stress mapping chips with 32 n-type or p-type piezoresistive field effect transistors, in *Proceedings of IEEE MEMS*, pp. 769–772, 2009
541. M. Doelle, D. Mager, P. Ruther, O. Paul, Geometry optimization for planar piezoresistive stress sensors based on the pseudo-Hall effect. *Sens. Actuators A* **127**(2), 261–269 (2006)
542. J. Creemer, F. Fruett, G.C.M. Meijer, P.J. French, The piezojunction effect in silicon sensors and circuits and its relation to piezoresistance. *IEEE Sens. J.* **1**(2), 98–108 (2001)
543. B. Puers, L. Reynaert, W. Snoeys, W.M.C. Sansen, A new uniaxial accelerometer in silicon based on the piezojunction effect. *IEEE Trans. Electron Devices* **35**(6), 764–770 (1988)
544. F. Fruett, G.C.M. Meijer, A test structure to characterize the piezojunction effect and its influence on silicon temperature sensors, in *Proceedings of the European Conference on Solid-State Transducers*, pp. 53–56, 1999
545. R.C. Jaeger, J.C. Suhling, R. Ramani, A.T. Bradley, J.P. Xu, CMOS stress sensors on (100) silicon. *IEEE J. Solid-St. Circ.* **35**(1), 85–95 (2000)
546. G.C.M. Meijer, Integrated circuits and components for bandgap references and temperature transducers. Ph.D. dissertation, Delft University of Technology, 1982
547. F. Fruett, G.C.M. Meijer, *The piezojunction Effect in Silicon Integrated Circuits and Sensors* (Kluwer Academic Publishers, Norwell, 2002)
548. T. Ivanov, T. Gotszalk, T. Sulzbach, I. Chakarov, I.W. Rangelow, AFM cantilever with ultra-thin transistor-channel piezoresistor: quantum confinement. *Microelectron. Eng.* **67–8**, 534–541 (2003)
549. G. Shekhawat, S.H. Tark, V.P. Dravid, MOSFET-embedded microcantilevers for measuring deflection in biomolecular sensors. *Science* **311**(5767), 1592–1595 (2006)